Investigation of the influence of the process parameters on the microstructure and fracture behavior of a i20wt.%Cr alloy produced by Laser owder Bed Fusion

Sélia Benmabrouk

Normandie Université

INSA INSTITUT NATIONAL DES SCIENCES APPLIQUÉES ROUEN NORMANDIE

THÈSE

Pour obtenir le diplôme de doctorat

Spécialité **MECANIQUE DES SOLIDES, GENIE MECANIQUE, PRODUCTIQUE, TRANSPORT ET GENIE CIVIL**

Préparée au sein de l'**INSA Rouen Normandie**

Investigation of the influence of the process parameters on the microstructure and fracture behavior of a Ni20wt.%Cr alloy produced by Laser Powder Bed Fusion

Présentée et soutenue par

SELIA BENMABROUK

Thèse soutenue le 18/10/2024

devant le jury composé de :

M. BENOIT VIEILLE	PROFESSEUR DES UNIVERSITÉS - INSA Rouen Normandie (INSA)	Directeur de thèse
M. ERIC CHARKALUK	DIRECTEUR DE RECHERCHE - Ecole Polytechnique, Palaiseau	Président du jury
M. ERIC HUG	PROFESSEUR DES UNIVERSITÉS - Université de Caen Normandie (UCN)	Co-directeur de thèse
MME LAURINE CHOISEZ	CHARGE DE RECHERCHE - Université catholique de Louvain, Belgique	Membre
M. CLEMENT KELLER	PROFESSEUR DES UNIVERSITÉS - Université de Technologie de Tarbes	Membre
M. JONATHAN CORMIER	PROFESSEUR DES UNIVERSITÉS - ENSMA	Rapporteur
MME ANNE-FRANÇOISE GOURGUES-LORENZON	PROFESSEUR DES UNIVERSITÉS - Ecole nationale supérieure des mines de Paris - PSL	Rapporteur

Thèse dirigée par **BENOIT VIEILLE** (GROUPE DE PHYSIQUE DES MATERIAUX) et **ERIC HUG** (Laboratoire de cristallographie et sciences des materiaux (Caen))

ED 591 PSIME

GPM Groupe de Physique des Matériaux

Remerciements

Quiconque me connait bien dira que je suis très bavarde en face à face, et je pense bien que mes remerciements ne feront pas exception. Car des personnes à remercier, je suis reconnaissante de pouvoir dire que j'en ai rencontré beaucoup (vraiment beaucoup) au cours de ces 3 dernières années.

Tout d'abord, je tiens à remercier les trois principales institutions qui m'ont donné l'occasion de travailler sur ce sujet de thèse : le Centre National de la Recherche Scientifique (CNRS), le laboratoire Groupe de Physique des Matériaux (GPM), et l'Institut National des Sciences Appliquées (INSA) de Rouen. Je me dois également de remercier le laboratoire de Cristallographie et Sciences des Matériaux (CRISMAT) pour m'avoir accueillie à de nombreuses reprises et avoir fabriqué mes éprouvettes, ainsi que le Labex EMC3 pour avoir financé mes travaux de thèse.

Je remercie bien sûr les membres de mon jury pour avoir accepté d'évaluer mes travaux de thèse : tout d'abord Anne-Françoise Gourgues-Lorenzon et Jonathan Cormier, pour leur lecture attentive de mon manuscrit, nos discussions enrichissantes et leur bienveillance à mon égard. Merci également à Eric Charkaluk pour avoir accepté de présider ma soutenance dans la bonne humeur, et d'avoir été aussi pédagogue vis-à-vis de mes proches sur son déroulement. Merci beaucoup à Laurine Choisez pour avoir accepté d'examiner minutieusement ma thèse, et pour nos échanges toujours chaleureux. Un grand merci à Clément Keller pour m'avoir offert des discussions pertinentes tout au long de ma thèse et m'avoir aiguillée à de nombreuses reprises. Enfin, merci à Ronan Henry, qui a ouvert le côté plus exploratoire de ma thèse et avec qui j'ai eu un grand plaisir à travailler. Merci pour ton temps et tes encouragements, ton recul sur mon travail m'a permis de prendre réellement confiance en moi en 3^{e} année et je t'en suis très reconnaissante.

Evidemment, un grand merci va à mes très chers directeurs de thèse : Benoit Vieille et Eric Hug. Très complémentaires sur beaucoup d'aspects, vos deux expertises et vos deux approches de la thèse m'ont été chacune d'une grande aide et m'ont permis d'évoluer au cours de ces 3 ans. Benoit, merci beaucoup pour ta disponibilité, ton écoute et ta réactivité ; j'ai énormément aimé travailler avec toi. Tu m'as toujours guidée sans jamais me brider, et ce même lorsque tu étais moins convaincu (petite pensée pour la préfi haha !). Tu as su valoriser mon travail et mes efforts de sorte que je prenne confiance en moi, tout en me rassurant lorsque mon côté plus anxieux me faisait douter. Eric, merci beaucoup pour tes retours toujours pertinents, honnêtes et constructifs sur mon travail ; tu m'as constamment poussée à faire mieux et à

travailler le fond. Même si je sais que j'ai encore beaucoup à apprendre, tu m'as donné envie de toujours garder cette rigueur et cette curiosité scientifique dans ce que j'entreprendrai, et de prendre le temps pour faire un travail qualitatif. Je suis très reconnaissante d'avoir eu la chance de travailler sur ce sujet avec vous deux.

Je souhaite ensuite remercier tout le personnel et les collègues qui m'ont permis de mener cette thèse à bien, de près ou de loin, et la liste est très longue. Côté UFR, merci tout d'abord à notre directeur de laboratoire Xavier Sauvage, pour m'avoir permis de travailler dans les locaux du GPM et avoir échangé avec moi à de nombreuses reprises au cours de ces 3 ans. Merci à Béatrice pour m'avoir souvent aidée et guidée pour la préparation de mes échantillons, et à Charlie pour avoir pris le temps d'usiner mes porte-échantillons. Merci également à Fabien et Emmanuel pour leur aide récurrente avec le MEB et leurs précieux conseils (et les matchs de badminton !). Merci à Antonella pour sa bonne humeur, son aide et sa gentillesse sans limites (et ses supers conseils de mise en page haha). Merci à Marie-Ange et David pour nos discussions toujours sympathiques. Merci à tous mes collègues et amis doctorants que j'étais heureuse de croiser quand je passais de longues journées à préparer et observer mes échantillons : Joséphine, Morgane, Samba, Aissatou, Simo, Alexandre, Loic, Kylian, Jules, toute la team des pauses café… Et puis merci à Linda, ma très chère figure maternelle du GPM ! tu sais bien que je ne pouvais pas ne pas te mentionner ici. Mille fois merci pour ta gentillesse, ta bienveillance et toutes nos discussions interminables. Tes vannes et tes piques me manqueront énormément, tu étais l'une de mes plus grandes motivations pour traverser la rue. Enfin, je ne peux pas terminer sans remercier ta chère rivale : Isabelle (aka ma Bibim !). Bibim, je te dois beaucoup sur l'aspect émotionnel de cette thèse. Merci d'avoir toujours cru en moi quand je ne faisais que douter, merci de m'avoir écoutée me plaindre 100 fois du même petit problème, et merci d'avoir été une amie aussi précieuse autant pendant les moments de joie que les moments plus difficiles.

Côté INSA, j'aimerais remercier notre chère secrétaire Elisabeth pour sa bonne humeur, Agnès pour m'avoir toujours gentiment renseignée, David du CCU pour avoir usiné un nombre vertigineux d'éprouvettes (plus de 200 !), Christelle de la reprographie pour sa disponibilité et sa gentillesse, notre très cher coach de sport Jérôme dont l'absence se fera ressentir, ainsi que toute la team sport du mardi et jeudi qui a rythmé mes semaines. Merci à Vincent pour avoir été mon binôme de badminton du mercredi pendant ma 2e année (le dernier survivor !). Merci également à Laurent pour avoir géré toutes mes bourdes informatiques en 1e année, et sa bonne humeur toujours égale lorsqu'on se croisait dans les couloirs. Un très grand merci à ma Hanani et toute l'équipe de la cafétéria qui m'a toujours donné le sourire à chacun de mes passages pour un café ou un sandwich. Hanani, tu as été un vraie grande sœur pour moi et je t'en remercie. Une petite dédicace aux méca de la promo 2024, qui restent dans mon cœur la meilleure des

promos ever ! J'ai beaucoup aimé vous avoir en cours et je garde un très bon souvenir de ma mission d'enseignement grâce à vous. Je vous souhaite tout le meilleur !

Un grand merci à toute l'équipe ERMECA (même si ce nom est devenu désuet je le sais) : Tanguy (merci pour tous les gâteaux et ta gentillesse), Fabrice (toujours de bon conseil), Alain (ce fut un plaisir de faire les cours avec toi), Mouldi (merci de t'être toujours assuré que la porte ne grinçait plus haha) et Meher (merci pour le gâteau d'anniversaire que je ne méritais clairement pas hihi…). Merci à tous les anciens de l'équipe qui m'ont chaperonnée lors de mes premiers pas dans l'équipe : mon premier et cher co-bureau David Boubou, qui a supporté toutes mes questions naïves et mes pics de stress de jeune doctorante. Bien sûr, l'incontournable Yan (Lemeilleur mais pas « le meilleur » héhé), qui m'a formée sur toutes les machines, donné tous les meilleurs tuyaux, et offert les débats les plus enflammés (si tu étais un chien, je serais un chat !). Même si je râle souvent, ça a été vraiment rassurant de t'avoir avec moi pendant ces 3 ans. Un grand graaaand merci à celle qui a été mon modèle et mon inspiration au GPM, Amandine, pour m'avoir formée sur les analyses microstructurales (et qui m'a surnommée la reine des facettes), pour m'avoir initiée à plein de sports, et m'avoir écoutée radoter encore et encore... Nous étions les deux seules filles de l'équipe lorsque nous sommes arrivées, et ça a été une très grande chance de t'avoir auprès de moi dans mes débuts. Merci également à mon ancien co-bureau David Philippe qui m'a gracieusement prêté ses livres de solfège, Mathieu que je remercie pour son accueil lorsque je suis arrivée, Alireza pour sa très grande gentillesse (et les chocolats !), and of course thank you Shubham for all our interesting discussions, your help on my work, and your endless availability. Merci aussi à nos petits stagiaires, avec une pensée particulière pour ma petite Pauline que j'ai été heureuse de recroiser. Petite dédicace à notre petit nouveau Paul, qui m'aura faite beaucoup rire sur ces dernières semaines de thèse, et que je regrette de ne pas pouvoir côtoyer davantage ! Et pour terminer, merci à mes deux adorables co-bureaux qui m'ont accompagnée pendant cette fin de thèse : Yanis et Julie. Yanis, merci pour tous tes cadeaux adorables, tes lettres, toutes nos discussions intéressantes, tous les snacks chinois que tu me ramenais parce que tu savais que j'adorais ça, et ta gentillesse en générale. J'étais triste de perdre David Boubou, mais j'ai retrouvé une personne toute aussi géniale que lui. Ma Julie, le petit poussin de ma 3^{e} année, merci de m'avoir donné mon quota de sucre quand je stressais (et merci à mamie Julie au passage haha !), merci pour nos pauses café le matin, pour m'avoir accompagnée au sport quand je me suis retrouvée seule, et pour avoir toujours été disponible quand je te demandais de l'aide. Ça m'a fait plaisir de te voir évoluer jusqu'à ton début de 2^{e} année, et je vous souhaite tout le meilleur à toi et Yanis pour la suite de vos thèses (même si vous allez tout déchirer, je le sais).

Enfin pour terminer le volet collègues et doctorants, je voudrais remercier les amis et collègues des autres laboratoires : au CRISMAT, je voudrais remercier Jade qui a été ma co-pilote à Caen pendant ces 2 dernières années, ainsi que Lydie et Rémy pour le temps

incalculable qu'ils ont passé à fabriquer mes éprouvettes. Merci également à Cendrine Folton pour avoir partagé avec moi son expertise, avoir répondu à mes questions, et m'avoir aidée dans cette fin de thèse. Côté CORIA, merci à Artémis dont j'ai longtemps entendu le nom mais que j'ai rencontré trop tardivement : j'ai beaucoup aimé aller à la piscine avec toi et acheter des pâtisseries sur le chemin du retour haha. Au LMN, je remercie du fond du cœur Carole dont le sourire a toujours été contagieux, ainsi que bien sûr mes grandes amies : Nouha et Oumaima. Toutes les deux, vous avez rempli ma fin de thèse de rires, de tajines, d'olives et d'affection, tout en partageant avec moi les doutes qui envahissent tous les doctorants de 3e année. Sans vous, ma thèse n'aurait pas été la même, et je suis reconnaissante qu'on ait pu vivre ça ensemble toutes les trois. Vous allez terriblement me manquer.

A ce stade des remerciements, je vois de loin tous mes amis se demander si leur nom apparaitra un jour (s'ils n'ont pas déjà fait un CTRL+F pour se trouver haha), et bien sûr je ne les oublie pas, loin de là. Merci à tous mes amis de l'école d'ingénieur : Sarah et Vicky, mes parents de l'ENSMA, qui m'ont toujours soutenue à fond, parfois même plus excités que moi pour mes projets. Merci à mes amis docteurs dont j'essaie de suivre les traces : Lisa et Thomas. Lisa ma binôme de toujours, tu as été un soutien inconditionnel pour moi et tu as répondu à mes questions incessantes sans jamais perdre patience ; pour ça je te remercie. C'est drôle quand même, on doutait d'être de bonnes ingénieures pendant les TP à l'ENSMA, et nous voilà aujourd'hui docteures toutes les deux. Thomas, merci beaucoup pour tes encouragements (autant pour ma thèse que pour mes compétences sur LOL hihi), je pense aujourd'hui pouvoir te défier à nouveau pour te montrer qui est la cheffe héhé. Merci aussi à ma Basmou et ma Isabella, qui m'ont toujours hypée malgré la distance et leurs journées très chargées, et qui prenaient le temps d'écouter mes audios dignes de vrais podcasts. Thank you à toi Aron, mon cher ami canadien, pour tes encouragements même à des milliers de kilomètres ! Merci à la famille El-Hamdani, le backbone de ces deux dernières années à Rouen, pour leur gentillesse illimitée, leur bienveillance, et l'accueil à bras ouverts dans leur famille dont ils m'ont gratifiée. Khali Mohamed, Khalti Khadija, ma Basmalou (et pas Basmati lol), ma Firda… du fond du cœur, merci merci merci. Merci à toi ma Douniazad, même si on n'a toujours que trop peu l'occasion de se voir, je sais que tu as toujours une pensée pour moi où que tu sois. Un grand merci aussi à ma cousine et petite sœur, ma Linouche, pour m'avoir soutenue et avoir toujours pris de mes nouvelles pour s'assurer que je survivais. Et bien sûr le meilleur pour la fin, une gratitude toute particulière à ma meilleure amie, ma sœur de cœur, qui m'a vue évoluer du CP jusqu'à ma dernière année de thèse, et qui n'a jamais douté ni failli : merci à toi ma Ann-kelly, ma K-chou. Je ne sais pas à quoi ressemblerait ma vie sans une personne aussi formidable que toi, tu es mon safe-space, celle qui m'a toujours dit « *oui* » quand j'entendais « *non* », et si je ne me canalisais pas, je pourrais t'écrire un chapitre entier. Tu es la meilleure de toutes, et cette thèse, tu y as ton emprunte marquée au fer blanc.

Pour clôturer ces remerciements monstrueusement longs (pas faute d'avoir prévenu), j'aimerais dédier ce paragraphe à ma famille : les Benmabrouk. Mon soutien infaillible ces 3 dernières années, mais aussi les 9 dernières, et même les 27 dernières. Merci à mes neveux (Elias, Adel, Raïs, Aron, Eden) et ma nièce (Ryem) pour toujours m'avoir redonné le sourire et le moral chaque fois que je rentrais sur Paris, j'espère être une tata dont vous pourrez être fiers. Merci également à mes adorables belles-sœurs, Lilouche et Zihati, qui m'ont toujours encouragée, réconfortée, et se sont soucié de moi comme de leur propre sœur. Un grand merci à « *mes frèèèères !* », Hazize et Abid, qui ont su me taquiner et me faire rire toute ma vie tout en me poussant à aller toujours plus loin. Vous m'avez accompagnée dans chaque déménagement (même en plein covid !), vous êtes venus me voir à Rouen quand j'allais moins bien, et peu importe mon besoin, vous avez toujours été là. Je me souviendrais toujours de ta phrase qui m'a décidée à faire une thèse Hazize : « *Tant qu'à faire, tu es arrivée jusque-là, autant aller au bout* ». Merci à ma grande sœur d'amour, Rabiouche, mon inspiration de toujours, que je ne saurais honnêtement pas remercier avec des mots. Tu as été mon journal intime, mon pilier, mon bras droit… tu as suivi tous les détails fastidieux de ma thèse même quand tu comprenais moins, car tu savais que ça me tenait à cœur. Tu es la meilleure de toutes. Papa, maman, merci pour votre soutien inconditionnel pendant mes longues années d'études, et vos allers-retours incalculables pour vous assurer que je ne manquais jamais de rien. Neuilly-Paris, Neuilly-Rouen, Neuilly-Poitiers, Neuilly-Canada… Il y en eu, et vous avez toujours répondu présents.

Les Benmabrouk, merci pour tout votre amour. Je vous aime, du fond du cœur.

Papa, l'exemple de ma vie, cette thèse je te la dédie. Elle est le fruit de toutes ces années que tu as passé à me soutenir et à t'investir dans mes projets, et de toute la confiance que tu m'as accordée. Encore une fois merci pour tout, mon père adoré.

« *La vraie générosité envers l'avenir consiste à tout donner au présent.* »

Albert Camus

TABLE OF CONTENTS

INTRODUCTION

Additive manufacturing (AM), most commonly known as “3D printing”, is a recent technology that enables the production of three-dimensional parts with complex shapes, usually difficult to achieve with conventional methods. The technique emerged during the 1980s and has become widely popular in numerous industrial sectors, including automotive [1], aeronautics and aerospace [2], medical [3], and food industries [4] (Figure 1a), as a wide range of materials is compatible with this process: polymers, metals, ceramics, etc. As illustrated in Figure 1b, the AM market value has known a rapid growth since 2008, reflecting the increasing demand around this technology.

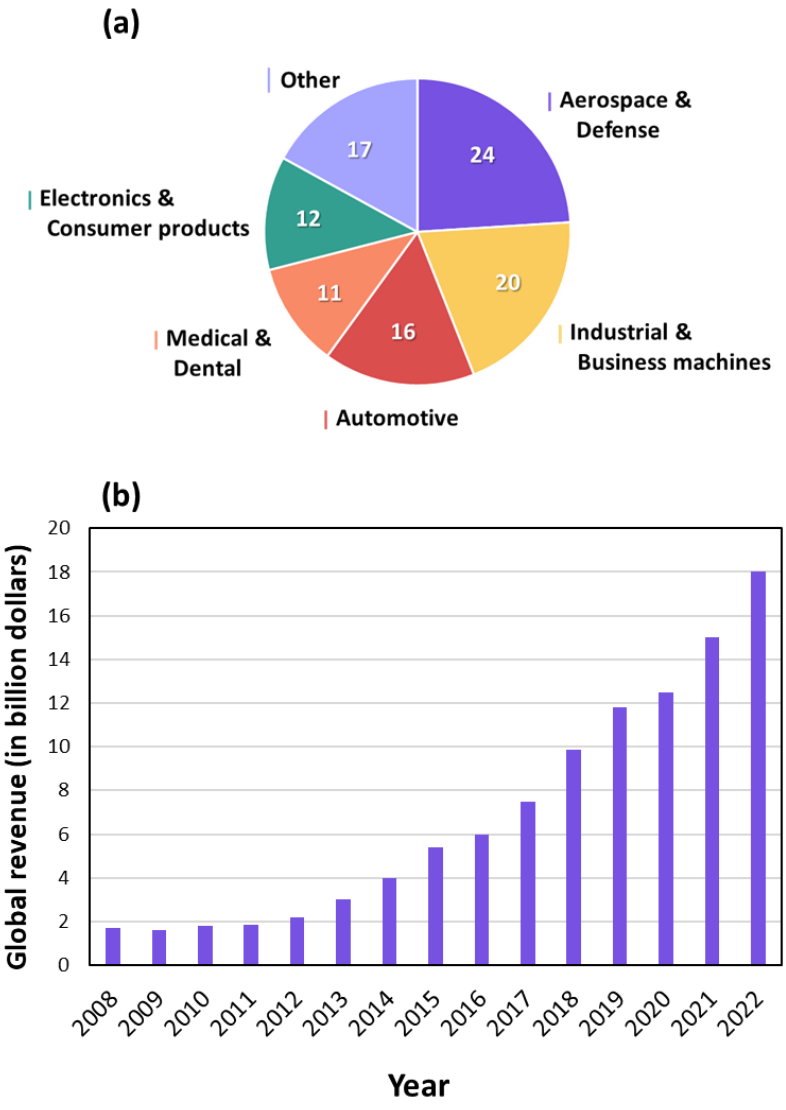

Figure 1 : Overview of the additive manufacturing market
(a) Parts of industrial sectors in metal AM in 2018 (adapted from [5])
(b) Global revenue for AM manufacturing from 2008 to 2022 (adapted from [6])

Its exponential rise during the past decades foreshadows for many experts the start of the 4th industrial revolution [7]. As a result, it has become a great focus for researchers, particularly in the field of metallic materials which were introduced to AM processes later, during the 2000s. Nowadays, a large range of AM methods can be considered to manufacture metallic materials, as shown in Figure 2: Material Extrusion, Direct Energy Deposition, Binder Jetting, etc. However, one category is maturing the fastest to face the current industrial challenges: Laser Powder Bed Fusion (L-PBF). This technique is commonly used to produce metallic parts, found at the core of aeronautical, aerospace, and biomedical applications. It is much appreciated for its speed, but especially for its precision which remains superior to other similar processes in metal AM [8]. Therefore, it is currently the most prevalent method for producing metallic parts, as visible in Figure 2.

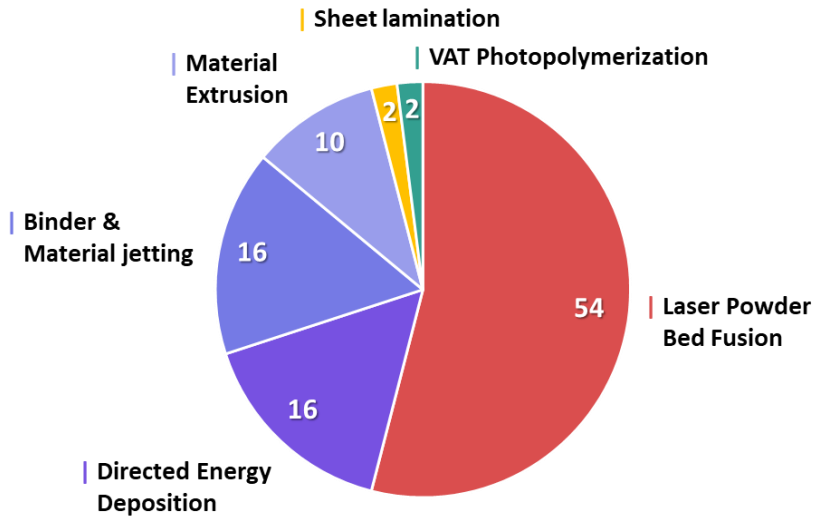

***Figure 2: Proportion of AM processes in metallic AM (adapted from** [9])*

Following this dynamic, numerous studies have been initiated in France on this subject in recent years, particularly in Normandy with the creation of two AM platforms: FAN for polymer materials, and METINNOV for metallic materials. Among metallic materials, one alloy has attracted particular interest for L-PBF manufacturing due to the expertise already developed at the CRISMAT laboratory in Caen: the Ni20wt.%Cr (Ni20Cr) alloy. The first significant contribution on this material is the PhD work carried out by M. Lelievre from 2018 to 2021, which allowed the determination of several optimal process parameters resulting in dense specimens. The tensile behavior was also investigated. This study paved the way for two projects, each composed of two PhDs as shown in Figure 3. The first one is the NICHROFAB

project launched in 2020, focused on improving the mechanical, electrochemical, and electrical properties of the L-PBF Ni20Cr alloy. S.S. Joshi's PhD investigated the deformation mechanisms under monotonic and cyclic loading, while L. Mas's PhD examined the resistance to corrosion. The second one, MIFASOL, started in 2021, assesses the influence of the resulting L-PBF microstructures on the resistance to irradiation and fracture. A. Dujarrier's PhD is centered on the impact of irradiation, while the current work investigates the fracture behavior of the Ni20Cr L-PBF alloy.

The choice to study this L-PBF alloy extensively is supported by several factors. Conventional Ni-based superalloys are usually challenging to characterize due to their complex microstructure, which often leads to the formation of precipitates and several phases [10–14] and can influence the mechanical behavior. Hence, the understanding of the interactions between the microstructure and the mechanical properties gets hindered by so many factors to consider. In contrast, the Ni20Cr alloy is often used as a model material, as it constitutes the main metallurgical base for many widely used Ni-superalloys (Inconel, Hastelloy...), but presents a simpler single-phase system. It is also widely used in industries for its advantageous properties at high temperatures, and as already mentioned, a high expertise has already been acquired on this material at the CRISMAT laboratory. The research on L-PBF Ni20Cr aims to expand further its industrial use.

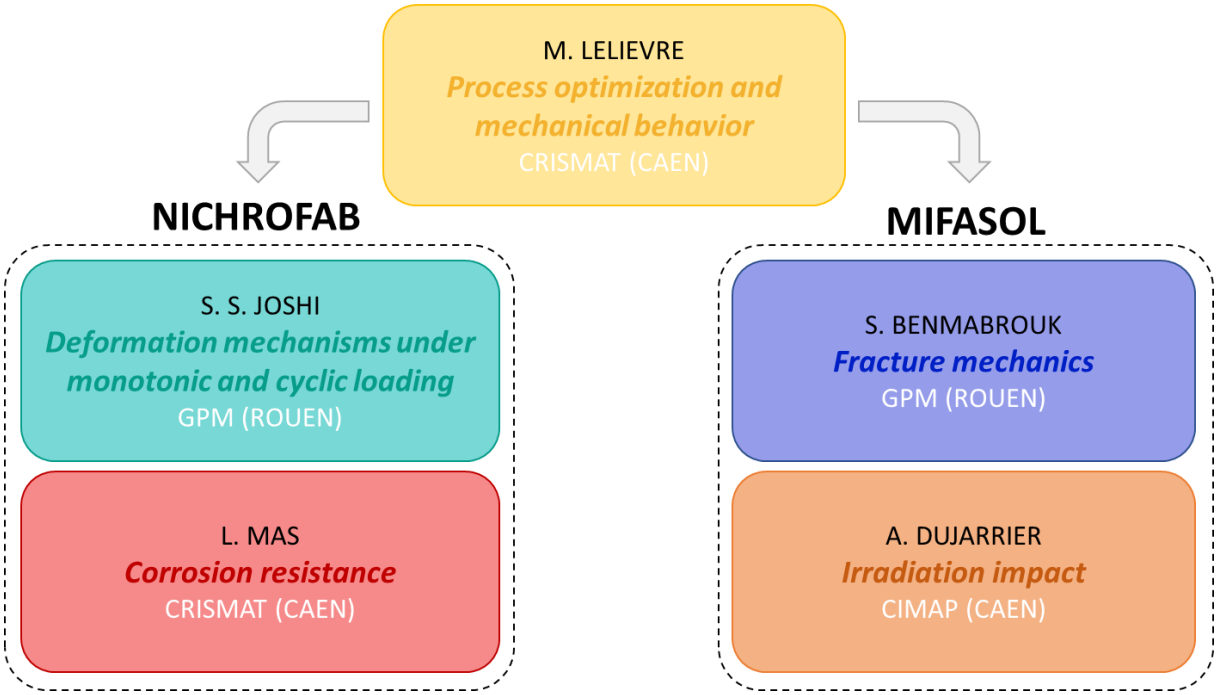

Figure 3: Organizational chart presenting the PhD works on the Ni20Cr L-PBF alloy

Among many concerns around the industrial applications for AM alloys, understanding the fracture behavior appears as a key issue for safety, operational cost, and industrial maintenance, and has yet to be addressed thoroughly in the literature. The fracture behavior of conventionally processed alloys (casting, forging…) has already been studied for decades to prevent unexpected failure of structures. However, the complex and out-of-equilibrium microstructure resulting from the very high cooling rates of L-PBF processes limits the application of current knowledge to AM materials. It is in this vast context of research, and for the reasons listed above, that the current work proposes to characterize the fracture behavior of the L-PBF Ni20Cr alloy.

Many studies have highlighted the effect of the processing parameters on both the microstructure and mechanical behavior of L-PBF alloys: the laser power and laser speed [15–18], the building orientation [19–22], the scanning strategy [23–25], etc. As a result, similar questions can be raised regarding their impact on the fracture behavior. The focus of the current work is hence put on the influence of three main L-PBF manufacturing parameters: the building orientation (horizontal or vertical), the rotation angle between layers (67° or 90°), and the volumetric energy density considered (60 J/mm^3 or 90 J/mm^3). The study is divided into six main chapters:

The first chapter establishes the state of the art, introducing the general principles of additive manufacturing, and reviewing the different families of alloys commonly found for metallic AM. The characteristic microstructures, mechanical properties, and fracture mechanisms described in the literature are also discussed, with a brief overview of the data reduction methods recommended by crack propagation test standards.

The second chapter presents the material of interest, the Ni20Cr, before describing in detail the manufacturing strategies (building orientations, rotation angles, and volumetric energy densities) considered, as well as the experimental methods implemented throughout the study. Experimental methods considered go from the preparation and characterization of the specimens both initially and post-mortem, to the mechanical testing and the post-processing of the experimental data.

The third chapter deals with the initial characterization of the specimens (density, microhardness, microstructure…) and the tensile properties of the Ni20Cr alloy resulting from

the considered printing strategies. The relationship between the initial microstructure and the tensile properties is discussed, to identify the most influential processing parameters and pave the way to understand better the fracture properties.

The fourth chapter investigates the effect of the manufacturing strategies on the fracture behavior observed during fracture testing. Profilometry analysis, fractographic images, and post-mortem microstructure observations are presented to understand the role of the plastic deformation, and which microstructural features are ruling the fracture behavior. Results are correlated to both the initial and post-mortem microstructures, as well as the tensile properties. The role of the different microstructural scales (meltpools, grains, dendrites…) on the fracture behavior is addressed.

The fifth chapter gives an overview of the first results obtained for two side problematics pursued during this PhD work: the first one aims to characterize the influence of the loading rate on the fracture behavior through impact tests (Charpy), as the Ni20Cr alloy presents a strong viscoplastic behavior, which can also be amplified at higher temperatures. The second problematic concerns the size effects on the fracture behavior of L-PBF Ni20Cr. As L-PBF manufacturing is associated with several interfaces observed at different scales (meltpool boundaries, grain boundaries, dendrite walls…), this raises questions on the influence of these interfaces on the fracture behavior and mechanisms resulting from different specimen sizes. Both aspects are discussed to the best of the current knowledge acquired on these matters.

Finally, the sixth and last chapter summarizes the main results of the PhD research and discusses future prospects to follow in the wake of what has been investigated so far.

CHAPTER 1:
State of the art

This first chapter introduces the general concepts of additive manufacturing, before diving deeper into one in particular: Laser Powder Bed Fusion. The various families of alloys concerned by this manufacturing method are presented, with a highlight on their tensile properties. Finally, the literature results regarding their microstructure and fracture behavior are presented.

I. An introduction to Additive Manufacturing (AM)

Additive Manufacturing (AM) is defined by the French standard (NF E 67-001) as a process "enabling parts to be manufactured using successive layers of material based on a digital model" (Figure 4).

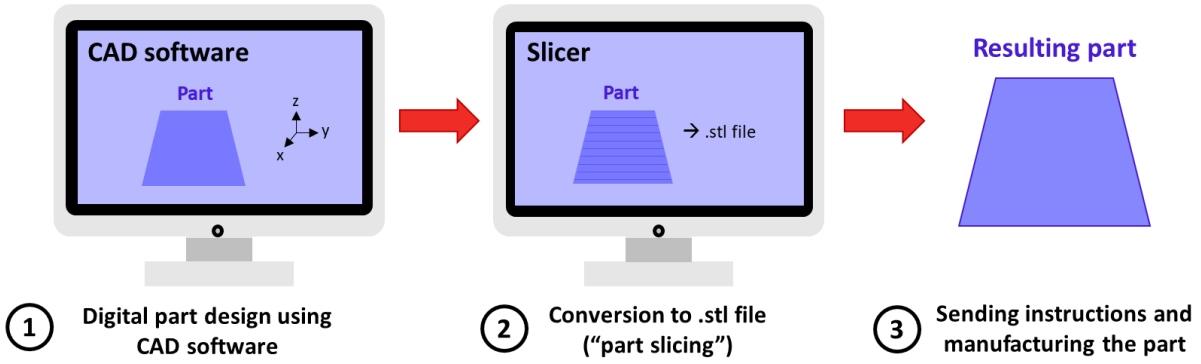

Figure 4: Steps of an AM process

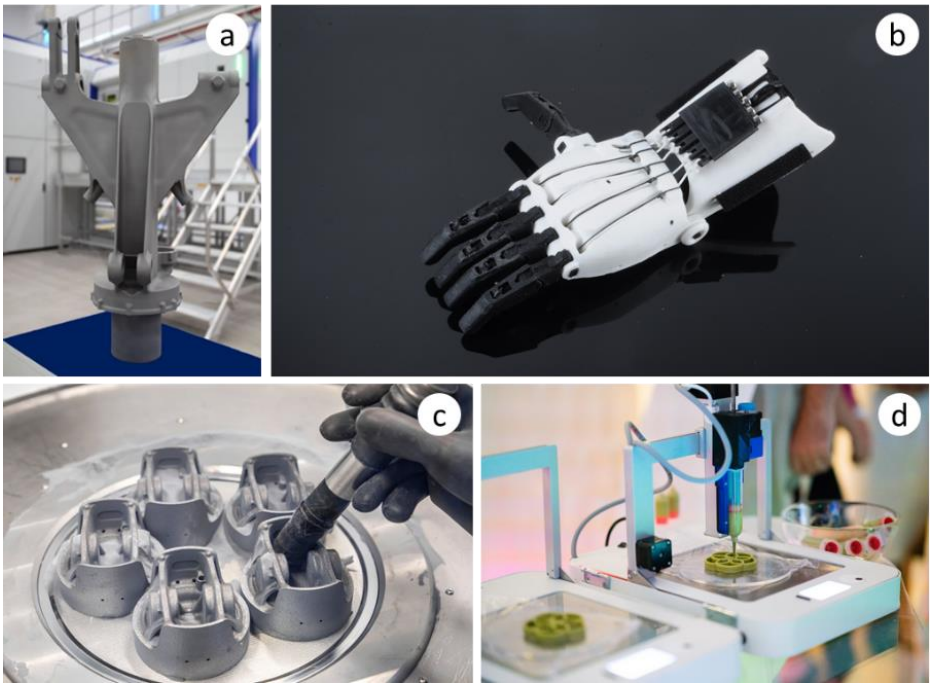

Figure 5: Examples of AM parts
(a) Landing gear [26] (b) Hand prosthesis [27] (c) Porsche pistons [28] (d) Food printers [29]

Due to its various assets, this manufacturing method is revolutionizing several industrial sectors including aeronautics, medicine, automotive, and food industries, as shown in Figure 5a to d. It is for instance a highly flexible process, enabling the design of parts with complex geometries which would be impossible using conventional methods, without additional tooling

or assembly steps. This flexibility also limits the number of stages required to manufacture a part, thereby reducing costs and production time. Furthermore, unlike subtractive manufacturing where the part is produced by removing material, it generates much less waste by using only the quantity of material required to manufacture the part.

"Additive Manufacturing" is a general term that can be subdivided into seven sub-families, each differentiated by the method implemented to apply the layer and the material used. They are defined by the ISO/ASTM 52900 standard [30] as follows: Binder Jetting, Direct Energy Deposition, Material Extrusion, Material Jetting, Powder Bed Fusion (or Sintering), Sheet Lamination, and Vat Photopolymerization (Figure 6). This list is not exhaustive, given how fast the field is evolving. Each family of AM is generally compatible with a specific range of materials. For example, Direct Energy Deposition will not be suitable for printing polymers and ceramics, just like Vat Photopolymerization cannot be applied to metallic materials. For the latter, several processes are possible, but one in particular is widely used in both industry and academia: Powder Bed Fusion (PBF). This process was the one considered throughout this PhD work and will be detailed in the next section.

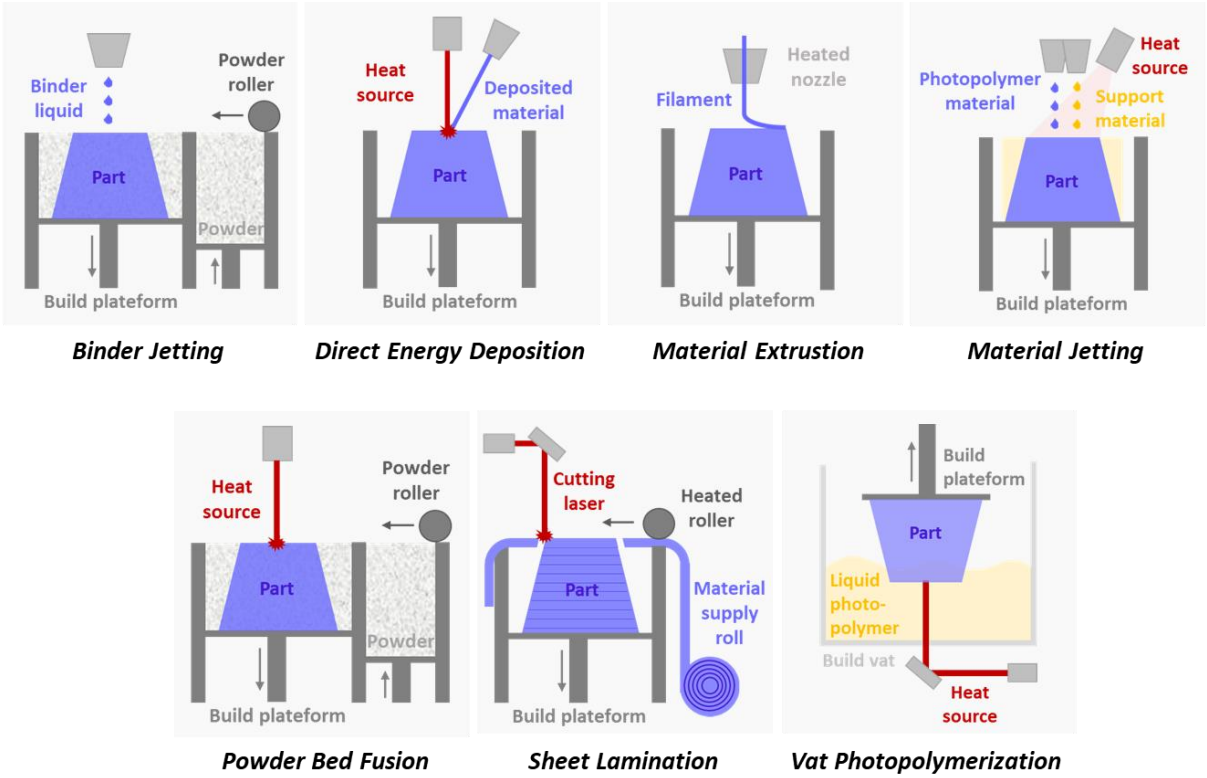

Figure 6: The seven AM families according to the ISO/ASTM 52900 standard *[30]*

II. Powder Bed Fusion (PBF)

II.1. Principle

Powder Bed Fusion (PBF) is an AM process based on the following principle: a bed of metal powder is deposited on a plate (usually heated) and a heat source, such as an electron beam or laser, selectively melts portions of this powder bed. The plate is then lowered, a new bed of powder is deposited, and the process is repeated until, layer after layer, the final part is completed. The whole process is illustrated in Figure 7. The part can then be recovered once the whole apparatus has cooled down and the surrounding unmelted powder has been cleaned. The unmelted powder can generally be reused after sieving. The entire process takes place in a heated closed chamber, filled with an inert gas such as argon or in a vacuum, depending on the heat source considered. This allows the control of the atmosphere in which the manufacturing process takes place, and thus prevents the powder from interacting with moisture or oxygen, which can either degrade the quality of the print or present an explosion hazard.

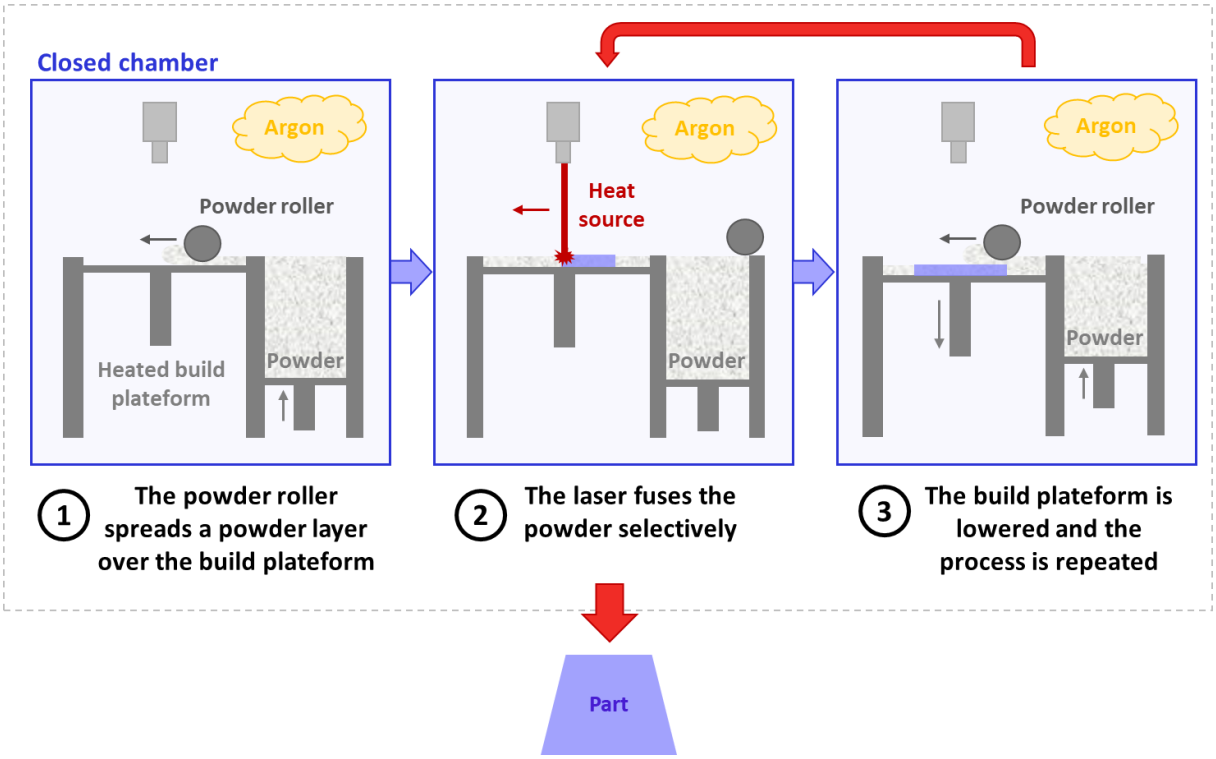

Figure 7: Principle of the Powder Bed Fusion (PBF) process

PBF is the most widely used AM process nowadays for the production of metal parts in the industrial sector, and is highly researched in the academic world [7,9,31]. It is particularly

appreciated for its reproducibility and precision in terms of part dimensions, which remain unmatched [8]. This process can be divided into two sub-processes depending on the heat source chosen: electron beam or laser.

II.2. Electron Beam Powder Bed Fusion (E-PBF)

Electron Beam Powder Bed Fusion (E-PBF) uses an electron gun as a heat source to melt the powder bed. It works as follows: a filament, usually made of tungsten, is heated to recover electrons. The electrons are then accelerated by applying a voltage, and a set of electromagnetic lenses act as a guide to concentrate and project them onto the bed of metal powder to fuse the powder. The powder bed is generally heated to avoid excessive thermal gradients [8], and the chamber is kept in a vacuum to prevent the atmosphere from reacting with the electrons or the powder.

This method is appreciated for its undeniable manufacturing speed of up to 10^2 m/s, permitted by the use of coils to control the electron beam, which is therefore free of any inertia [8]. It is quite commonly used in the aerospace and medical fields, especially for titanium, chrome-cobalt, and nickel alloys [32,33]. However, electron beam melting requires coarser powder (50 to 100 μm) than laser melting (15 to 45 μm) in order not to be too sensitive to electrostatic effects [34], which induces poorer surface finish and lower quality precision. In addition, it only works with a fairly restricted range of materials [32], and offers less freedom in terms of modifying the processing parameters [8]. Therefore, Laser Powder Bed Fusion is more appreciated and considered.

II.3. Laser Powder Bed Fusion (L-PBF)

II.3.1. Principle

Laser Powder Bed Fusion (L-PBF) is currently the most industrially mature metal AM process, with a growing number of machines on the market [8]. It is more specifically already implemented in the aeronautic industry for parts certified as safe for flights [35]. As mentioned, the heat source used is a laser, and the chamber is filled with an inert gas, such as argon or nitrogen.

II.3.2. Key manufacturing parameters

The processing parameters have a considerable impact on the mechanical behavior of parts produced by L-PBF, given their direct role in the formation of the various microstructures [36–40]. They are generally optimized to produce dense parts with few defects (which are defined in the next section), good surface finish, and good mechanical properties [41]. A large number of studies are conducted to benefit as much as possible from this flexibility, by obtaining microstructures directly suitable for different geometries and applications [23,42–44].

However, determining an optimum set of parameters can be challenging, given the interdependence between them. A large number of variables directly influential to the final manufacturing result can be listed, but some might not be as impactful as others depending on which ones are considered. They are therefore classified, and the most predominant ones are called 'first order' parameters and are illustrated in Figure 8. This category includes laser power P (W), laser speed v (mm/s), powder layer thickness t (mm), hatch spacing h (mm), and laser beam diameter s (mm), which has a direct impact on the distance h [35].

Such a large number of variable parameters complexifies the comparison of several combinations. A more global criterion is therefore generally considered: the energy density E. There are three possible approaches to this parameter in the literature: linear density E_l [45,46], surface density E_s [47], and volumetric density E_v [48] (also more commonly noted VED). Each of these respectively describes the energy required to form a bead, several beads, or a material volume. Each is expressed as follows:

$$E_l = \frac{P}{v} \tag{1}$$

$$E_s = \frac{P}{v.h} \tag{2}$$

$$E_v = VED = \frac{P}{v.t.h} \tag{3}$$

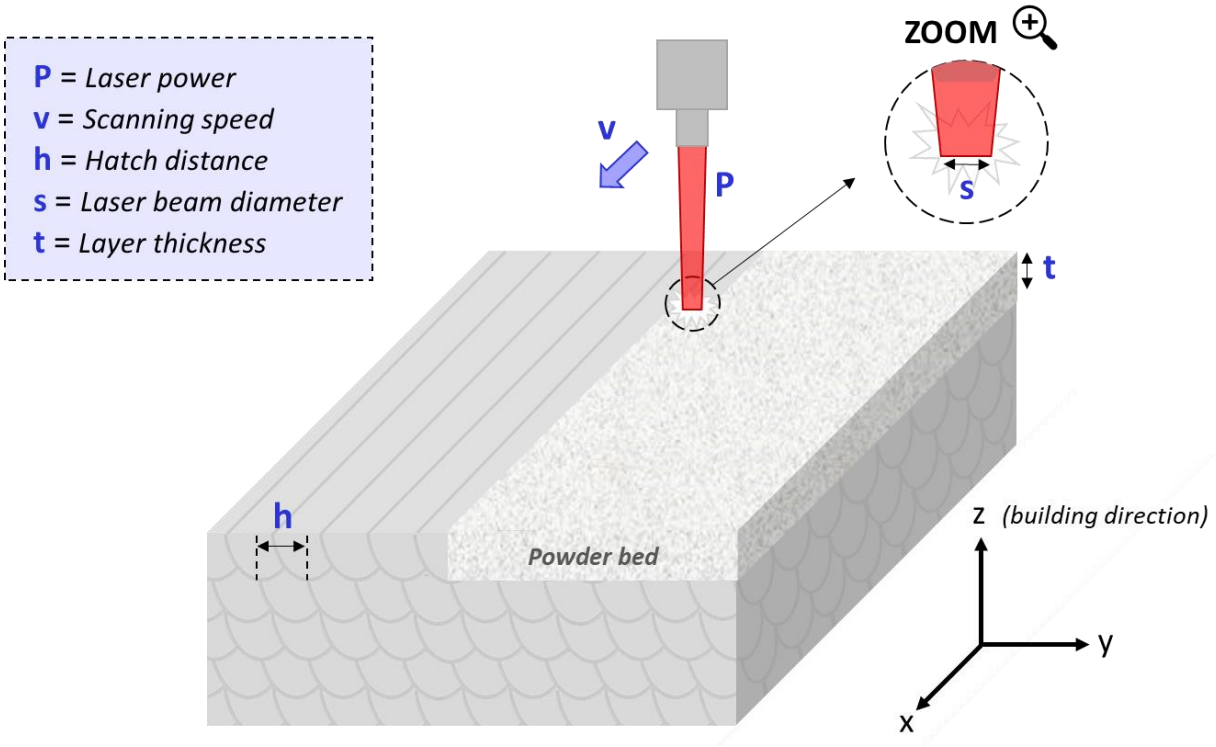

***Figure 8: First order manufacturing parameters (adapted from** [49])*

As done in many works on the influence of processing parameters, the comparison criterion adopted in the present study is the Volumetric Energy Density, denoted VED. However, it is important to note that despite the practical and synthetic aspects of this parameter, comparing two similar volumetric energy densities is not equivalent to comparing the same set of parameters. In addition, it is not suitable for describing complex physical phenomena such as those that can be observed in meltpools [50], and a critical eye must be kept regarding this matter.

In addition to the parameters of the process itself, the manufacturing strategy also plays an important role in the resulting properties, and is described as a ‘second order’ parameter [35]. It is subdivided into two parts: the scanning strategy and the layer-stacking strategy. The scanning strategy defines the laser path followed by the laser, while the stacking strategy describes the angle of rotation between each layer. For both strategies, an unlimited number of possibilities are available, and only the most commonly implemented techniques mentioned in the literature to date are illustrated in Figure 9. For the stacking strategy, the 67° angle is generally considered to maximize density and minimize the anisotropy effects already present [24,38,51].

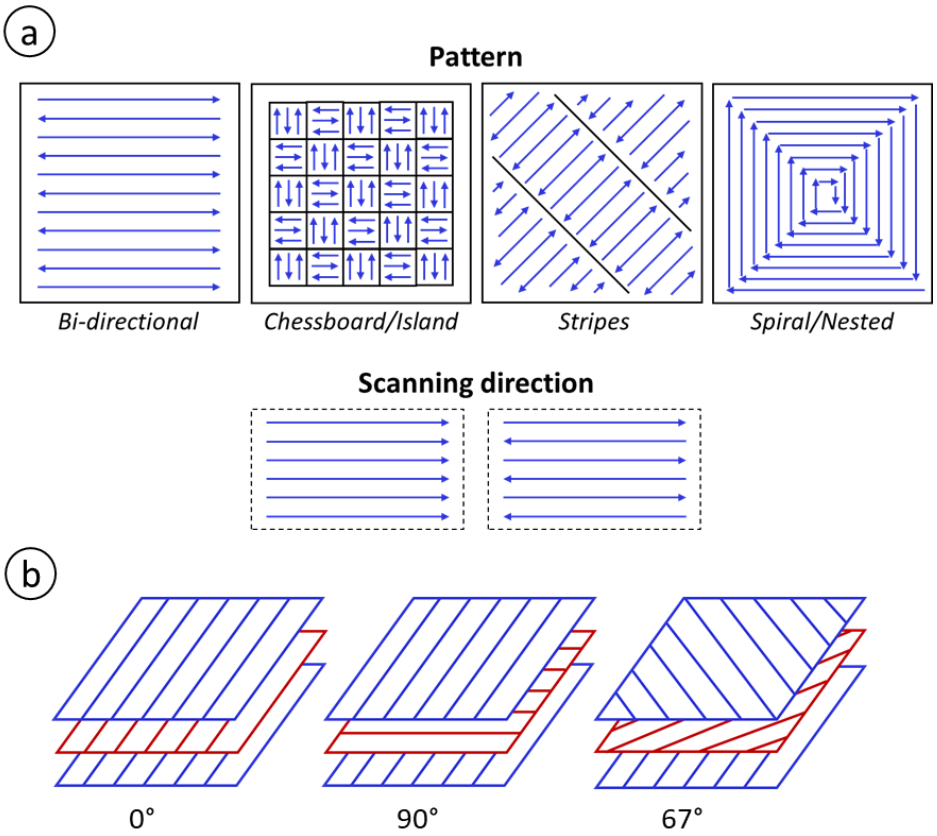

***Figure 9: Examples of manufacturing strategies (adapted from** [35])*
(a) Scanning strategy (path) (b) Stacking strategy (rotation angle)

Finally, other parameters can also play an important role such as the heating temperature of the plate, which will influence the thermal gradient during solidification, the direction of the gas flow, the substrate considered, or the geometry of the support, just to name a few. In order to stay consistent with previous works and allow relevant comparisons, the parameters considered in the current study are the same as those set in M. Lelievre's PhD work on L-PBF Ni20Cr [36].

II.3.3. L-PBF specific defects

Although promising, the L-PBF process is not exempted from the presence of defects within the structures it produces. If an as-fabricated part that has not undergone any post-processing is considered, microstructural defects can be divided into two main categories: defects due to the powder, and those due to laser-material interactions during manufacturing [8]. Other types of machine-related defects exist, such as those resulting from the poor distribution of the powder bed by the leveling roller.

Microstructural defects caused by the powder generally depend on the process used to obtain it, which determines its quality: granulometry, morphology, density, flowability, etc [52]. Hence if defects are observed in the powder, they will be reflected in the manufactured part. In particular, this can lead to the presence of oxidized particles, or porosity due to either occluded gases or specific coating defects. If these are too large and/or irregular in shape, they can quickly become crack initiation sites [53–55], raising once again questions on the overall resistance to crack initiation and propagation.

Regarding the defects induced by the manufacturing process itself, several studies on the matter carried out on various materials [8,15,56–58] have led to the creation of maps to guide the choice of the manufacturing parameters. Generally, the main parameters of interest are the laser power and the laser speed considered. Four areas have been identified: Keyhole, LOF (Lack Of Fusion), Balling-up, and the ideal processing window, as illustrated in Figure 10. The associated defects are shown in Figure 11.

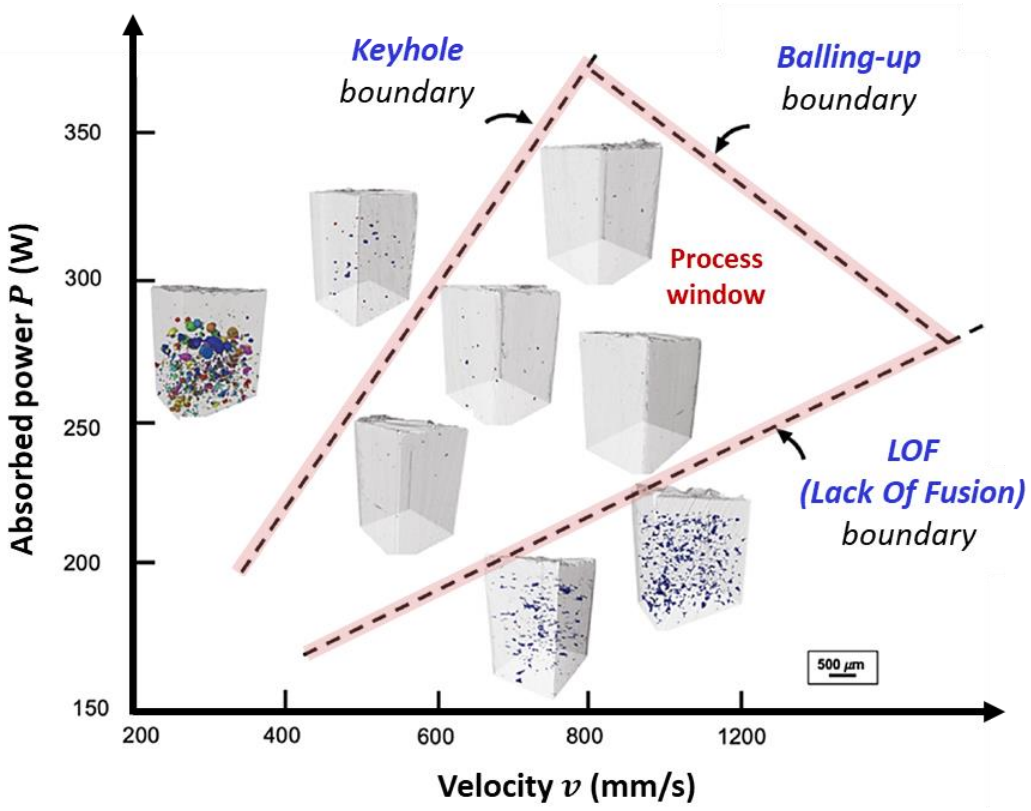

Figure 10: L-PBF defects morphology according to the set of power-speed chosen (adapted from** [58] **and** [8]**)

The Keyhole domain corresponds to a case where the laser power is too high in relation to the laser speed, causing gas to get trapped and resulting in the formation of cavities known as "keyholes", as illustrated in Figure 11c. Conversely, the LOF (Lack Of Fusion) domain represents the case where the laser speed is too high for a laser power that is too low: complete fusion does not have time to occur and porosities are generated (Figure 11a). In the "balling-up" range, the speed and power are so high that they cause particles to be ejected and deposited on the layer (Figure 11b). The manufacturing window defined in Figure 10 therefore corresponds to the optimum power-velocity range to limit the appearance of these defects as much as possible, and result in the highest density achievable.

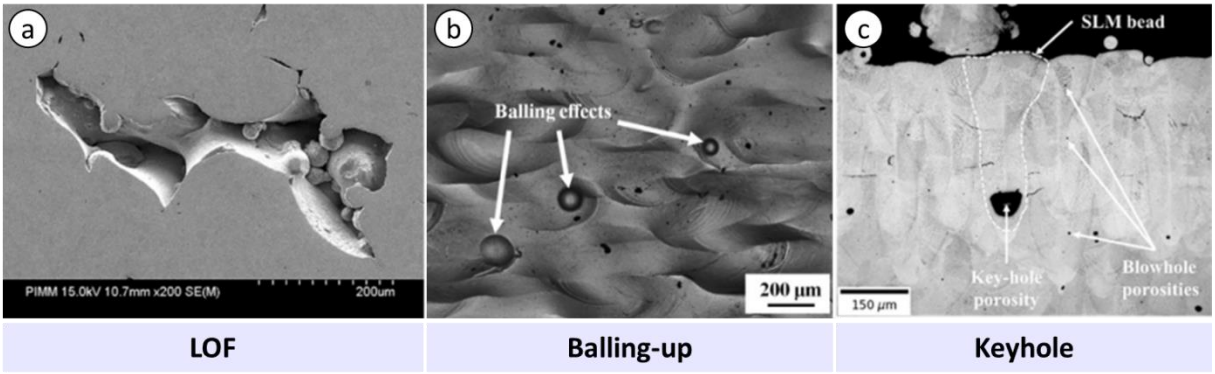

Figure 11: Characteristic L-PBF defects for 316L alloy and pure Titanium (adapted from** [59] **and** [60]**)
(a) LOF (316L) (b) Balling-up (Titanium) (c) Keyhole (316L)

III. An overview of the main L-PBF alloys

L-PBF is highly appreciated for the wide range of metallic materials it is compatible with. Among them, nickel, titanium and aluminum-based alloys, as well as steels, constitute the vast majority. The aim of this section is to summarize the main results obtained in the literature on these materials, in order to determine whether there are any trends specific to metallic AM materials in terms of microstructure evolution and mechanical behavior. To do so, the focus is put on the most commonly used and investigated alloys: Ti6Al4V for titanium alloys, AlSi10Mg for aluminum alloys and 316L for steels. As the study was carried out on a nickel-based alloy, a wider range is considered in this case: Inconel 718, Inconel 625 and Hastelloy X.

III.1. Microstructure of L-PBF alloys

The diverse and complex microstructure of L-PBF alloys is highly dependent on the manufacturing process, due to high cooling rates (10^5-10^7 K/s) and solidification rates (0.1-1 m/s) which can result in a large range of microstructures with columnar or equiaxed grains [61–63], specific precipitation characteristics [10,63,64], high dislocation densities [65], as well as significant residual stresses [66,67] and various types of elaboration defects [8]. In addition, the layer-by-layer manufacturing process induces remelting of the material during the process, resulting in microstructural characteristics specific to the process.

Two parameters govern the morphology and size of these microstructures: the temperature gradient G, and the solidification interface velocity R. The G/R ratio determines the morphology, while the $G \times R$ product influences the size. For L-PBF manufacturing, the solidification structure generally remains fine, with both a columnar and cellular microstructure as shown in Figure 12.

Despite the differences that can be observed between several alloys and printing strategies, the L-PBF microstructure at different scales can generally be described as follows: meltpools (meso/microscale), grains elongated along the building direction (microscale), cell dendrites (sub-microscale) and interdendritic regions (nanoscale) (Figure 13).

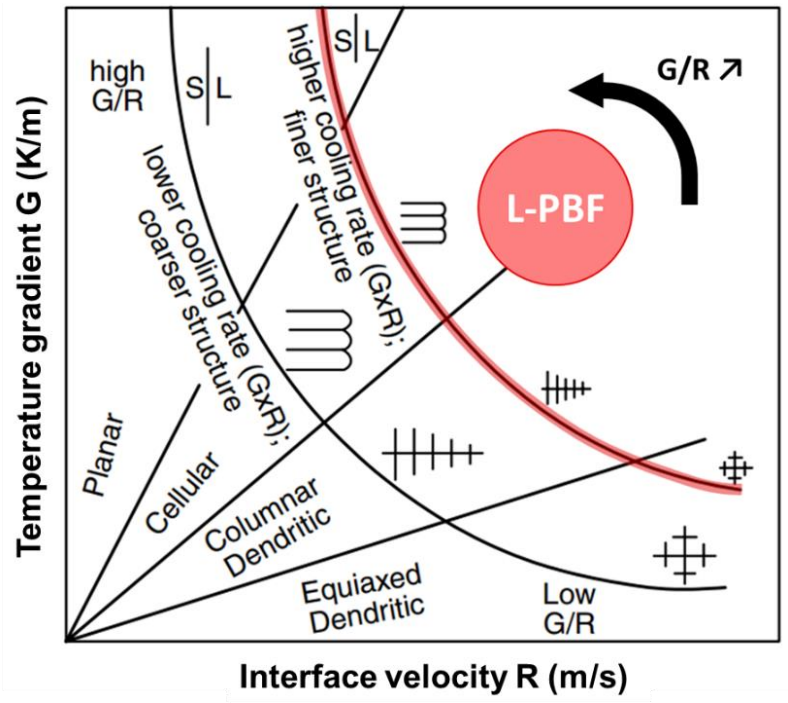

Figure 12: Map displaying the influence of the temperature gradient G and the interface velocity R on the size and morphology of microstructures during solidification (adapted from** [68] **and** [69]**)

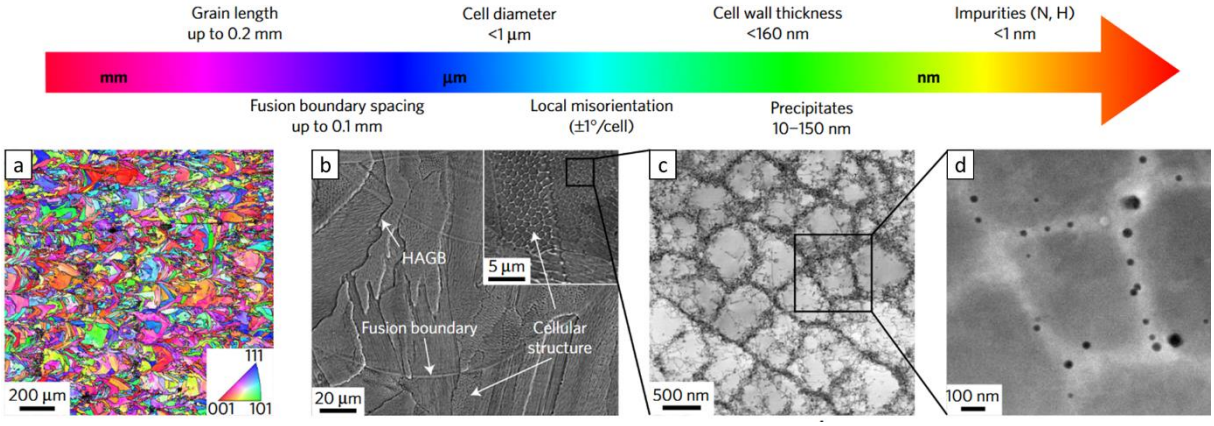

Figure 13: Characteristic microstructure of L-PBF 316L SS alloy (adapted from** [70]**)
(a) Grains (b) Meltpools (c) Cellular structure (dendrites) (d) Nano-particles at the cell walls

These microstructural features are heavily influenced by the process parameters considered, especially the "first and second" order parameters such as the laser power, the laser speed, the scanning strategy, or the layer-stacking strategy. The literature already provides plenty of examples regarding the influence of those parameters on the microstructure of various well-known alloys. A set of parameters particularly interests us throughout this PhD work: the building orientation, the scanning strategy between layers, and the VED considered.

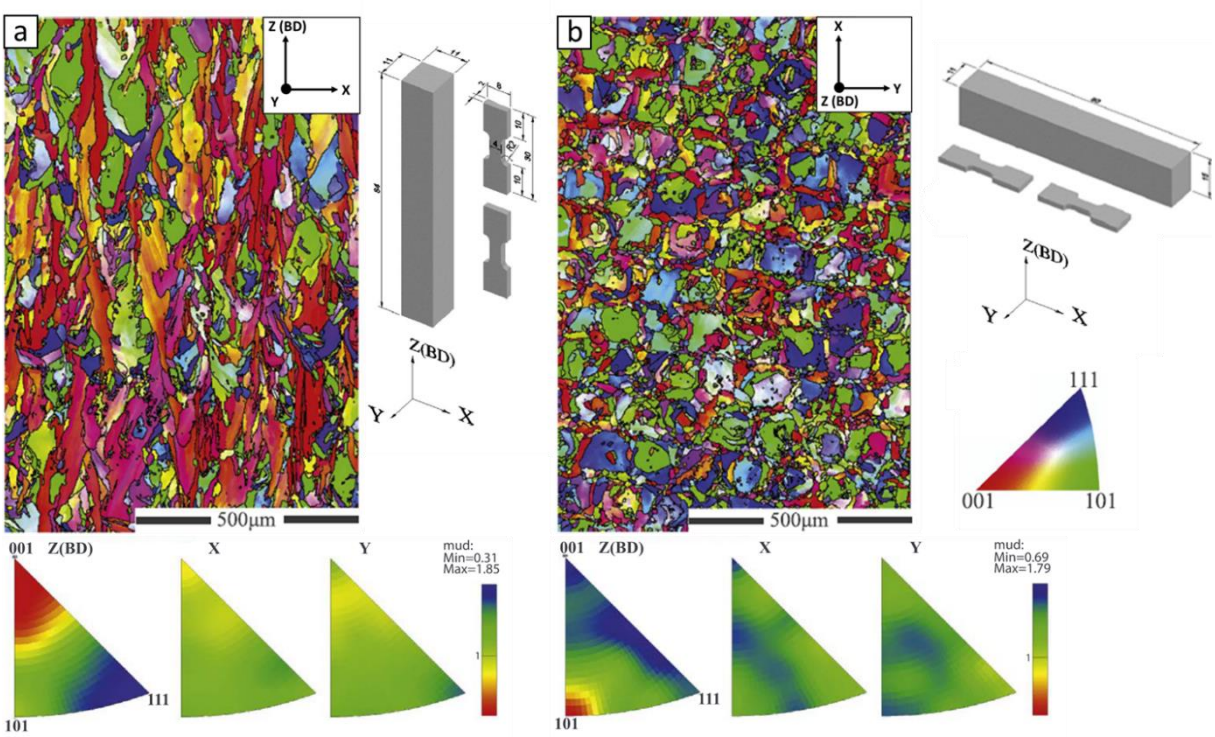

Figure 14: Influence of the building orientation on the microstructure of L-PBF Inconel 718 alloy
(a) 'Horizontal' orientation (b) 'Vertical' orientation (adapted from [68])

The building orientation has already been extensively investigated, demonstrating the high anisotropy of L-PBF microstructures [19–22,68,71–74]. A common observation of the differences between the faces respectively parallel and perpendicular to the building direction is shown in Figure 14. Grain size and morphology are greatly impacted, with a columnar structure along the building direction, and an equiaxed one on the face perpendicular to it. A high difference in crystallographic texture index can also be induced for a given observation plane due to the difference in geometry orientation, directly impacting the heat dissipation within the specimen [19].

The rotation angle and scanning strategy also hold a significant influence on the resulting microstructure, impacting the meltpool and grain size, morphology, and texture [17,23–25], as shown in Figure 15. The overlapping of several melting tracks generally generates more regular and uniform microstructure with higher texture for 0° and 90° angles, while minimizing the contact surface between them will result in a more complex crystallographic orientation as shown with the 67.5° angle. This is due to the influence of the rotation angle on the temperature gradient: with successive overlapping of the melting tracks, such as what is observed for 0° and 90° angles, the maximum temperature gradient tends to be

oriented perpendicular to the center of the meltpool boundary, inducing more unidirectional grains. On the opposite, for an angle of 67.5° the orientation of the temperature gradient varies constantly from one layer to another, resulting in more random grain orientations [75].

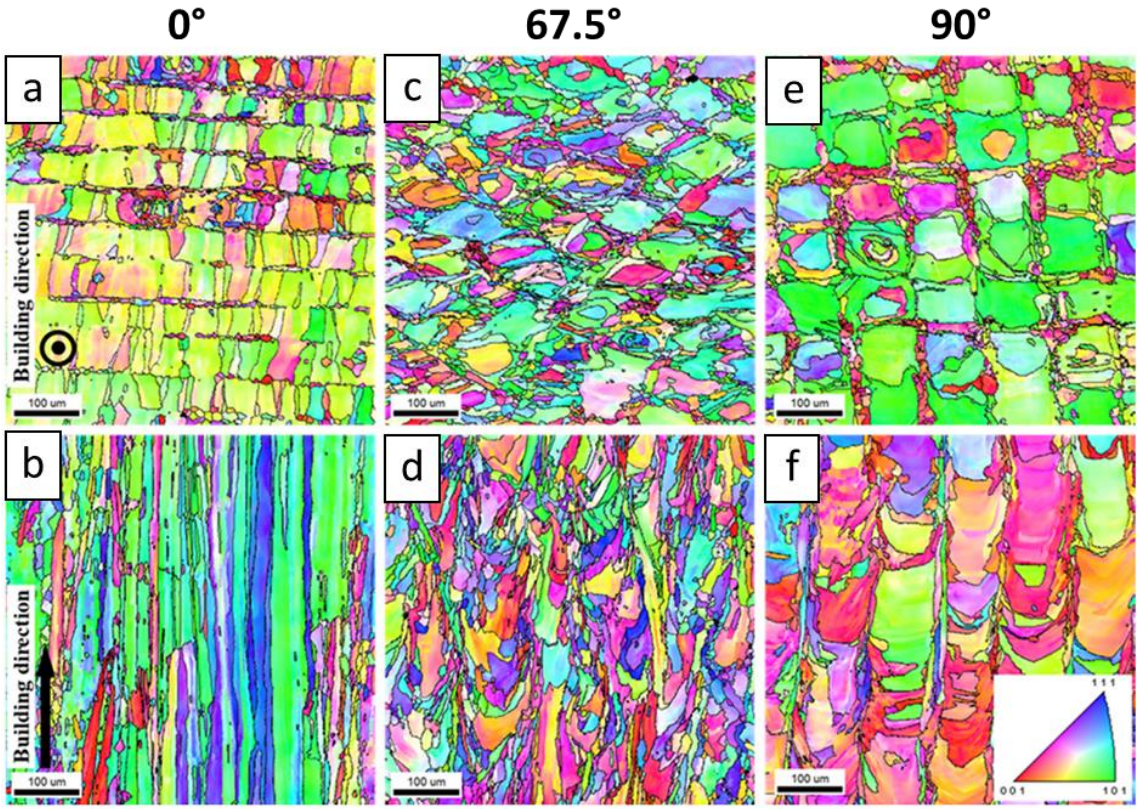

***Figure 15: Influence of the rotation angle on the microstructure of L-PBF 316L SS alloy (adapted from** [25])*
(a, b) XY and XZ planes for a 0° angle (c, d) XY and XZ planes for a 67.5° angle
(e, f) XY and XZ planes for a 90° angle

Finally, the VED is usually mainly responsible for the resulting solidification mode (cellular, columnar dendritic, equiaxed dendritic…) [15,17,18,76,77], as shown in Figure 16. Within a range providing relatively dense specimens (relative density > 98%), lower VEDs usually induce smaller meltpools, finer sub-microstructures, and more equiaxed microstructures overall (Figure 16a, c and e). On the other hand, higher VEDs generate wider and shallower meltpools, with wider dendrites as well, and notable columnar microstructures elongated along the building direction. However, as mentioned previously, the VED is a parameter that should be approached with caution as different laser power-laser speed couples can result in virtually identical VEDs, but significant differences in precipitation, grain size, morphology, or growth direction [77]. While the observations shown in Figure 16 are representative of frequently observed patterns, they should not be generalized.

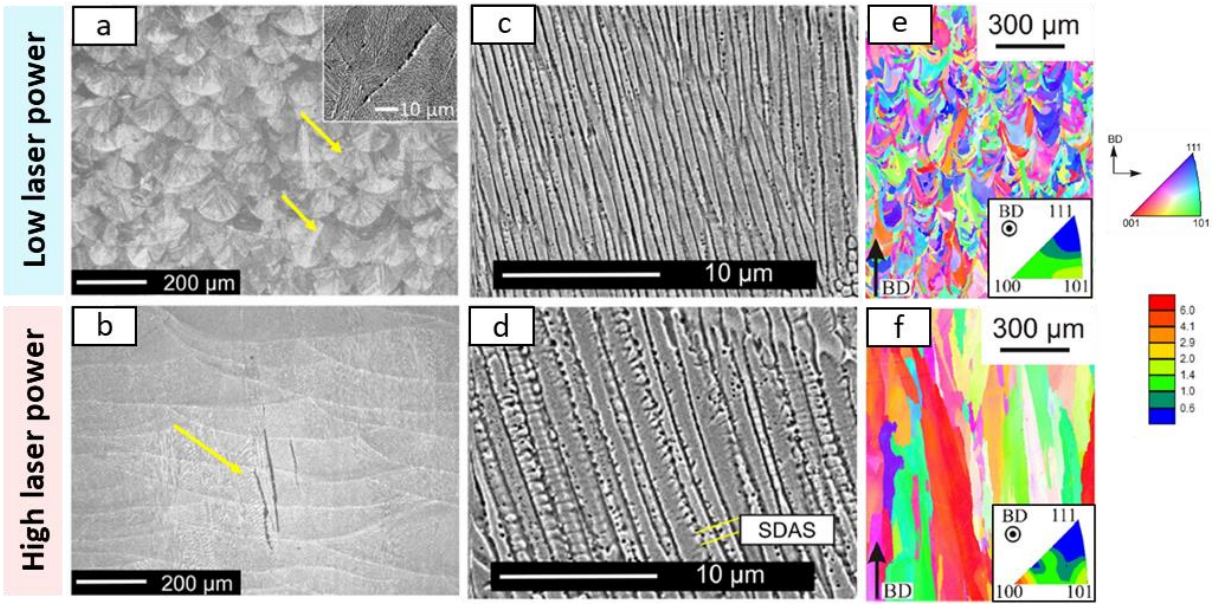

***Figure 16: Influence of the laser power on the meltpools, dendrites and grains on L-PBF Hastelloy X alloy (low and high laser power) (adapted from** [78])*

(a, b) Meltpools optical observation (c, d) Dendrites observation (e, f) grains observation

Therefore, it has been demonstrated that the key processing parameters of the current study (building orientation, rotation angle, and VED) have a considerable influence on the microstructure at different scales (meso, micro, and sub-micro). Hence, it is likely to be highly influential to the mechanical behavior as well, since the two are intrinsically related. The impact on the tensile behavior is discussed in the following section.

III.2. Tensile behavior of L-PBF alloys

As previously demonstrated, the manufacturing parameters have a direct influence on the microstructure, and therefore most likely the overall mechanical behavior (tensile, fatigue, fracture…). Several studies dealing with the impact of the process parameters on the tensile behavior have been gathered and displayed in Figure 17. The objective of this small review is to observe whether any trend emerges in terms of tensile properties, considering the three most commonly found tensile parameters: yield stress σ_{YS}, ultimate tensile stress σ_{UTS}, and elongation A (at ultimate tensile stress or breaking point). Results for each alloy representative of the main metallic L-PBF families are shown, with at least three nickel-based materials as they relate the most to the Ni20Cr alloy investigated. The alloys considered for this study are the following: Hastelloy X [23,76,78–80], Inconel 718 [71,81–87], Inconel 625 [88–90], 316L [91–95], Ti6Al4V [22,43,96–99] and AlSi10Mg [73,100–105].

The main comparison criteria are the building orientation and the VED, which is systematically calculated from the data available in the references. Second and third-order parameters specific to the manufacturing strategy (rotation angle, scanning strategy, building plate heating temperature…) are not taken into account, and are quite variable from one study to another. No post-heat treatment is considered as well, and different tensile specimen geometries and conditions are shown (dogbone and cylindrical, as-built or extracted from a L-PBF bulk…). The presented results relate to two of the most commonly found specimen building orientations: horizontal (principal axis perpendicular to the building direction) represented by circles, and vertical (principal axis parallel to the building direction) represented by triangles. The typical values resulting from conventional manufacturing methods (casting, forging, etc.) are indicated by a continuous line on the plots associated with each alloy. These reference values are provided by the ANSYS Granta Materials database, and the value considered was always the highest within the range provided. However it is important to note that these reference values can be subjected to discussion, as they can be quite variable between wrought or cast alloys, and dependent on whether they were subjected to any heat treatment or strain hardening.

This review indicates that, for a given VED, a horizontal building orientation generally results in higher yield and ultimate tensile stresses, but lower ductility compared to a vertical one. This trend may not be very noticeable in Figure 17, but is systematically observed for a given study presenting both building orientations, among those listed for each alloy. The only exceptions are Ti6Al4V and AlSi10Mg alloys, for which the conclusions are more nuanced. This may be due to their distinctive microstructural features (grain morphologies, phases, particles…) compared to steels and nickel-based alloys. The differences between the two orientations are often attributed to the resulting temperature gradients, which produce distinct textures and induce anisotropic tensile properties [106].

Although the reference values taken for conventional manufacturing can be highly variable, the literature highlighted that yield and ultimate tensile stress values for metallic L-PBF specimens are at least equal or superior to the values obtained with conventional manufacturing methods. However, the elongation at ultimate tensile stress A is generally higher in the case of conventional specimens, due to their higher ductility.

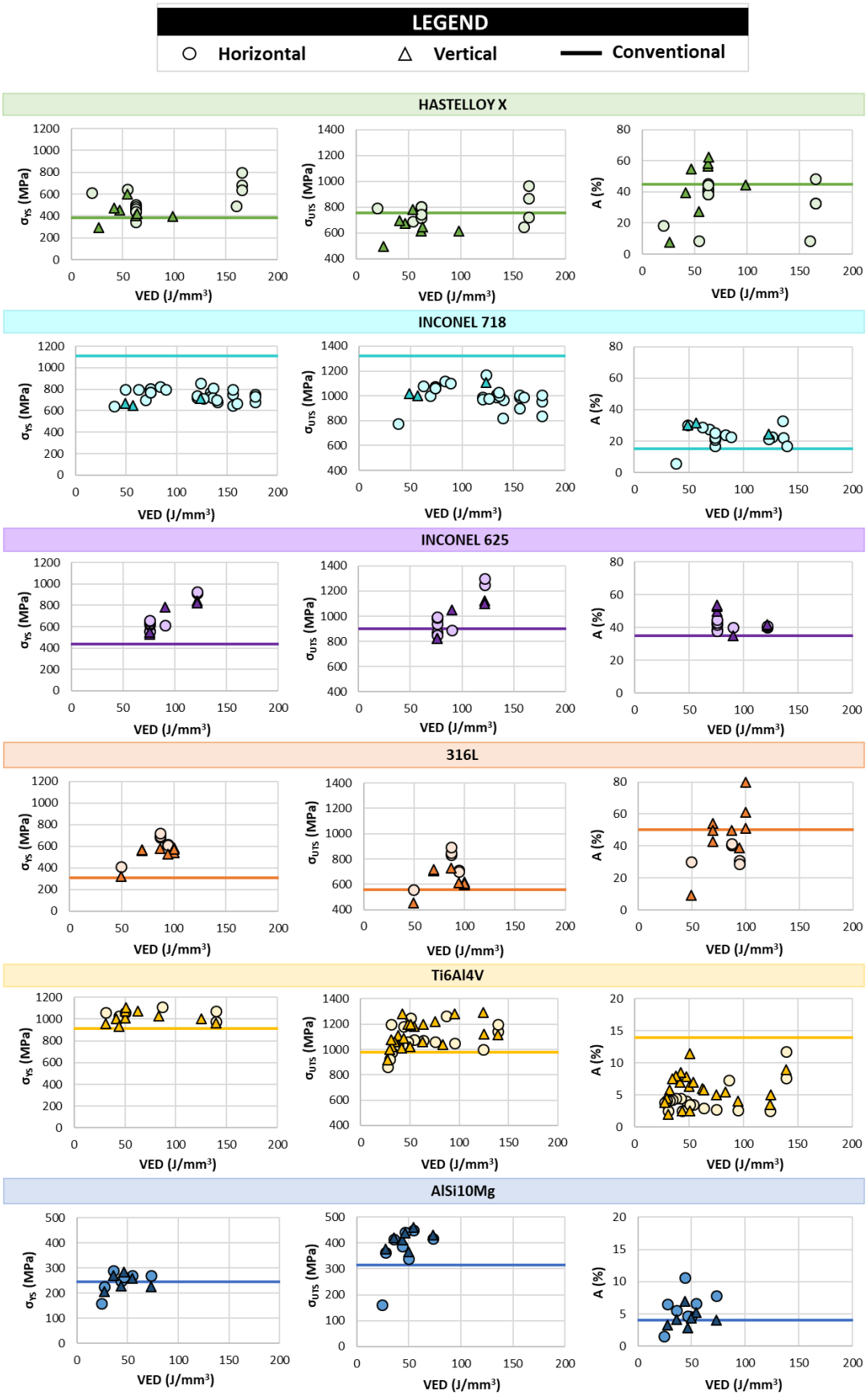

***Figure 17: Tensile properties (Yield stress σ_{YS}, Ultimate tensile stress σ_{UTS} and Elongation A) for alloys representative of metallic L-PBF: Hastelloy X** [23,76,78–80], **Inconel 718** [71,81–87], **Inconel 625** [88–90], **316L** [91–95], **Ti6Al4V** [22,43,96–99] **and AlSi10Mg** [73,100–105]*

No specific trend can be noted for the different VEDs from this review, probably because many other manufacturing parameters are variable and should be taken into account. It also has been mentioned previously that the use of the VED to compare different sets of parameters has known limits, as virtually equal VEDs with different laser power and laser speed for instance, could result in different microstructures and mechanical properties [77]. The literature demonstrates that the influence of the VED lies mostly on the solidification structure generated, and on the type and proportion of defects it can induce if specimens are not fully dense (LOF for low VEDs, and keyholes for high VEDs). The different resulting precipitation kinetics also highly influence the mechanical properties, and will be variable from one alloy to another [77,107]. Finally, it can also impact the temperature gradient, and hence the texture of the specimens [106].

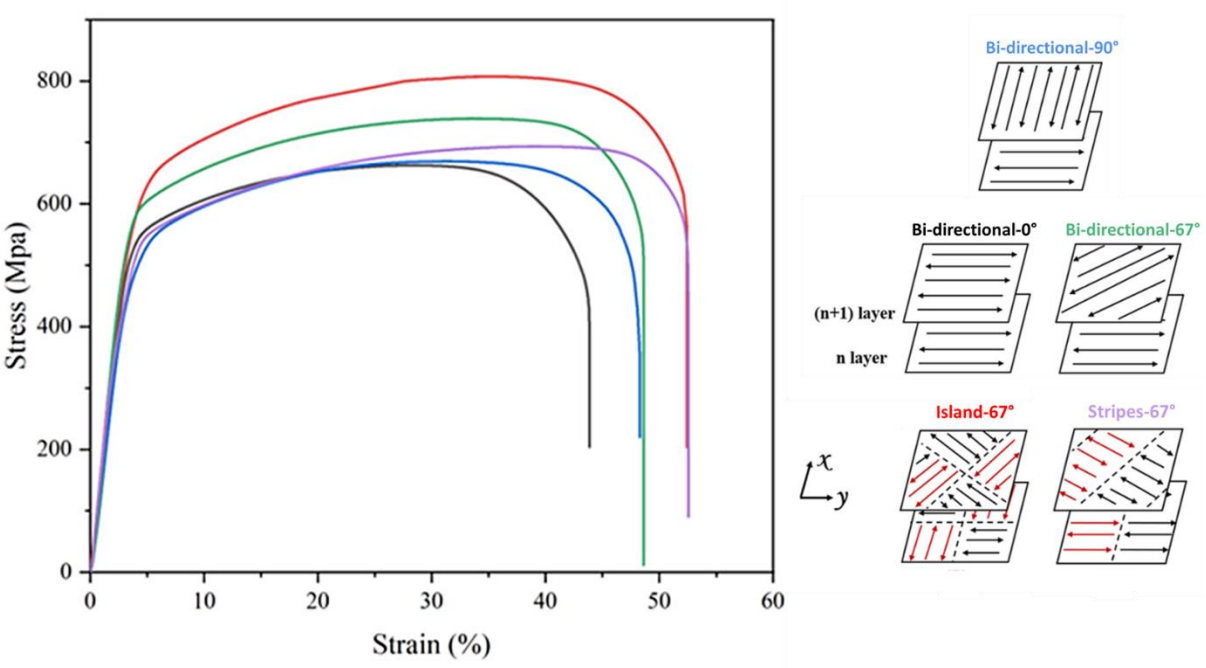

***Figure 18: Influence of the rotation angle and the scanning strategy on the tensile properties of L-PBF 316L SS alloy (adapted from** [24])*

Regarding the influence of the rotation angle, and the scanning strategy overall, the strategy chosen can improve or degrade the mechanical properties as illustrated by Figure 18, as it affects the amount and type of defects generated by the different layer overlapping processes. A rotation angle of 67° will for instance usually improve the mechanical properties (more dense, and less textured specimens) as opposed to one of 0°, as fewer defects are likely to be generated between layers during the process [24]. As for the building orientation and the VED, the scanning strategy also directly impacts the anisotropy of the tensile properties due to its influence on the texture [106].

As hinted by the conclusions on the impact of the manufacturing parameters on the microstructure, the tensile properties of L-PBF alloys are also highly dependent on the processing parameters. Therefore, this raises questions about their influence on another critical aspect of the mechanical behavior: the fracture properties.

III.3. Fracture behavior of L-PBF alloys

Before diving deeper into the discussion on the fracture behavior provided by the literature regarding L-PBF alloys, a brief overview of the main concepts of fracture mechanics based on references [108] and [109] is presented below.

III.3.1. Key basics of fracture mechanics

III.3.1.1. Main concepts of fracture mechanics

Fracture mechanics aims at preventing the failure of parts or structures containing a defect during service conditions to ensure safety. Initially, the approach was limited to elastic materials where plastic deformation is confined to the crack tip: it is known as Linear-Elastic Fracture Mechanics (LEFM). It was later extended to materials with significant ductile behavior, for which plasticity is not confined to the crack tip anymore, leading to the development of Elastic-Plastic Fracture Mechanics (EPFM). Both LEFM and EPFM are discussed below.

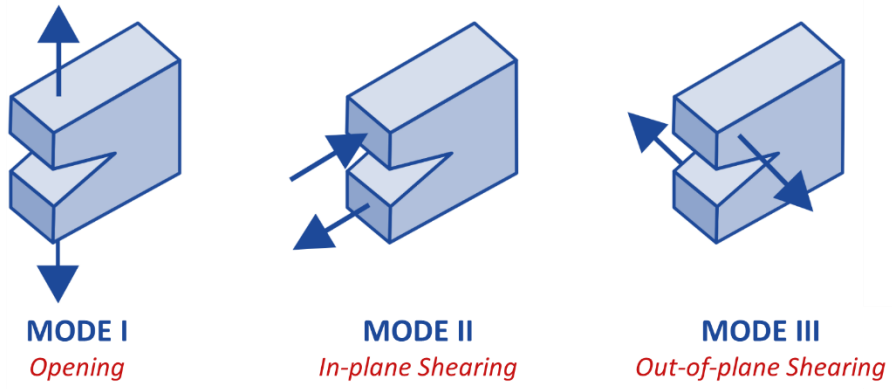

Figure 19: Primary loading modes of a cracked structure *[110]*

For a structure containing a crack, different loading modes occur as illustrated in Figure 19. For the following overview of the main concepts presented, only mode I (the most damaging) is considered.

A singularity (via an initial notch or a crack) within a specimen or a structure induces stress concentration, which results in local heterogeneity of the stress field and complex stress states. In the case of a mode I failure observed on a specimen with a single notch and subjected to a tensile stress, the distribution of the axial stress $\sigma_y(r,\theta)$ depends on the material behavior, as shown in Figure 20.

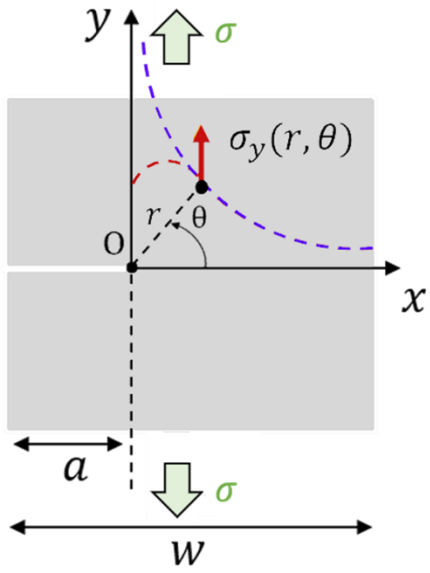

Figure 20: Single notched specimen loaded in tension

Evolution of axial stress $\sigma_y(r,\theta)$ in the vicinity of the notch in a specimen in finite dimensions
(In blue elastic-brittle behavior, in red elastic-plastic behavior)

For a material with an elastic-brittle behavior (in blue in Figure 20), the overstress tends towards infinity at the notch tip, and decreases to the stress value σ applied to the edges of the specimen when moving away from it. The value of this overstress is conditioned by the geometry of the specimen, its characteristic dimensions but also the radius of curvature at the notch tip. For a material with elastic-plastic behavior (in red in Figure 20), the overstress profile will be clipped due to the dissipation of mechanical energy via plastic deformation mechanisms. The plastic deformation zone is more or less extended around the crack tip depending on the mechanical loading conditions. The extent of plastic deformation depends on the yield strength of the material, its ductility (function of temperature), but also the thickness of the test specimen.

For an elastic-brittle material (LEFM) loaded in mode I, Irwin [111] provided a first solution to calculate the stress field at the vicinity of the crack tip, given by the following formulas in plane strain conditions (in polar coordinates r and θ) :

$$\sigma_{xx} = \frac{K_I}{\sqrt{2\pi r}} cos\frac{\theta}{2}\left(1 - sin\frac{\theta}{2} sin\frac{3\theta}{2}\right) \quad (4)$$

$$\sigma_{yy} = \frac{K_I}{\sqrt{2\pi r}} cos\frac{\theta}{2}\left(1 + sin\frac{\theta}{2} sin\frac{3\theta}{2}\right) \quad (5)$$

$$\sigma_{xy} = \frac{K_I}{\sqrt{2\pi r}} cos\frac{\theta}{2} sin\frac{\theta}{2} cos\frac{3\theta}{2} \quad (6)$$

$$\sigma_{zz} = \nu\left(\sigma_{xx} + \sigma_{yy}\right) \quad (7)$$

With ν the Poisson ratio. K_I is referred as the stress intensity factor, and depends on the crack length and loading. It is a key parameter in LEFM to characterize the stress field at the crack tip, but also the fracture behavior of elastic-brittle materials. The previous equations enable the determination of a critical value, noted K_{Ic}, called the fracture toughness of the material, and representative of the resistance to crack initiation. It is generally expressed as follows:

$$K_{Ic} = \sigma\sqrt{\pi a}Y \quad (8)$$

Where σ is the applied stress, a the crack length, and Y a function of the specimen geometry and the crack length.

Griffith considered a different approach, taking the variation of the elastic energy within the studied structure as a criterion for crack propagation. If the elastic energy provided is sufficient to overcome the materials resistance, crack propagation occurs. The parameter of interest here is noted G, and called the energy release rate. Therefore, crack propagation occurs when G reaches a critical value noted G_{Ic}. In plane strain state, G_{Ic} can be related to K_{Ic} by the following equation:

$$G_{Ic} = \frac{{K_{Ic}}^2(1 - \nu^2)}{E} \quad (9)$$

With E the Young's Modulus.

In order to determine the fracture toughness for ductile materials, a parameter equivalent to the energy release rate G was considered: the Rice integral, denoted J [112]. This is a concept first introduced by Rice to enable the study of isotropic metallic materials exhibiting non-linear elastic behavior. It has then been extended to ductile materials when subjected to monotonically increasing loading, to account for the significant plastic deformation. This curvilinear integral is based on the principle that the value of J does not depend on the shape of the contour chosen (Figure 21). The J-integral is expressed as follows:

$$J = \int_{\Gamma} \left(W dy - \vec{t} \frac{\partial \vec{u}}{\partial x} dS \right) \tag{10}$$

With:

- Γ: arbitrary contour defined around the crack tip
- W: strain energy density
- $\vec{t}$: traction vector at a given point of the contour
- $\vec{u}$: displacement vector at a given point of the contour
- dS: a length increment along the contour

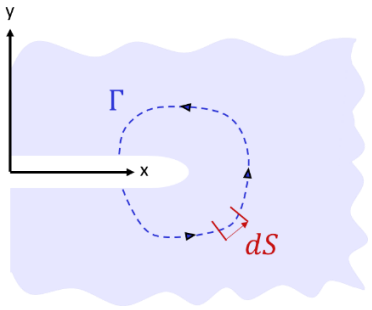

Figure 21: Contour defined around the crack tip for J calculation

The main property of the J-integral is that it is independent of the contour chosen around the crack tip. This property remains valid as long as the following conditions are respected: time-independent process, small strains, homogeneous hyper-elastic material, and plane stress-strain field. The parameter J allows to describe more accurately the strain and stress fields around the crack tip for plastic materials. For elastic-brittle materials, and under plan strain conditions, the critical value J_{Ic} for which crack initiation occurs can be related K_{Ic} and G_{Ic} using the expression below:

$$J_{Ic} = G_{Ic} = {K_{Ic}}^2 \left(\frac{1 - \nu^2}{E} \right) \tag{11}$$

Depending on the type of behavior encountered (brittle with small scale plasticity, or ductile with large scale plasticity), the suitable parameter (K, G, or J) is considered to investigate the fracture behavior of a material. The size of the plastic zone around the crack tip is therefore a point of the utmost interest, as it determines the choice of the parameter to consider. For small scale yielding, Irwin's correction [111] allows to calculate the size of this plastic zone r_p and accounts for the plasticity occurring at the crack tip:

$$r_p = \frac{1}{2\pi}\left(\frac{K_I}{\sigma_{YS}}\right)^2 \tag{12}$$

Where σ_{YS} is the yield stress. However, it is relevant to note that the coexistence of several phenomena complicates the study of fracture behavior and the difficulty is to use methods (experimental and/or numerical) to dissociate the share of mechanical energy associated with these different dissipative phenomena.

The next section presents a concise summary of the methods provided by test standards to determine the fracture parameters of interest: the fracture toughness J_{Ic} (resistance to crack initiation) and the tearing modulus T (resistance to crack propagation).

III.3.1.2. Test standards and influential parameters to fracture toughness

The experimental determination of the fracture toughness for plastic materials is codified through test standards such as ISO 12135 [113], ASTM E1820 [114], or BS 7448 [115]. The guidelines provided by all three of them are considerably similar, but with different constitutive models for the determination of the fracture parameters that might be more suitable for some materials than others [116]. Only an overview of the test standard ISO 12135 [113], considered in the present study as the most suitable, is presented below.

ISO 12135 test standard [113] provides several specimen geometries to carry out crack propagation tests in order to determine a material's fracture properties. The most common configurations considered are Compact Tension (CT) and Single Edge Notch Bend (SENB) specimens, shown in Figure 22. The dimensions are given to ensure a plane strain state at the core of the specimen. The fracture toughness value J_{Ic} is calculated from the test assuming that

the J-integral value J could be decomposed as the sum of an elastic component J_{el} and a plastic component J_{pl} ($J = J_{el} + J_{pl}$).

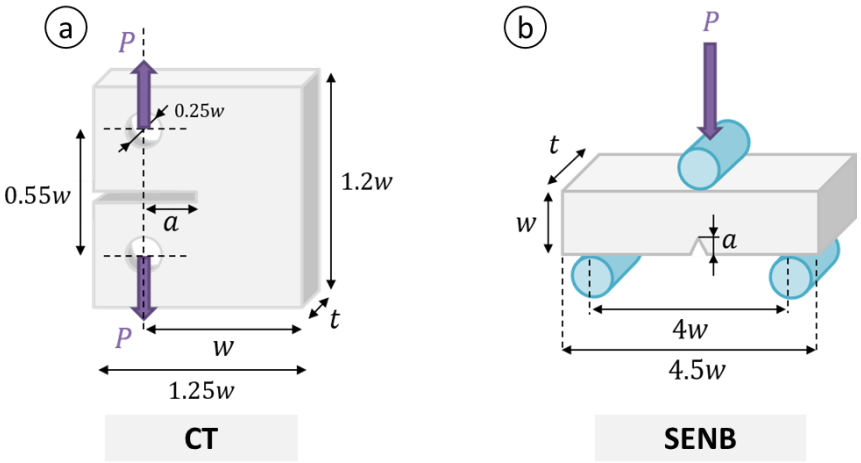

Figure 22: Illustration of the standard specimen geometry proposed by ASTM E1820 *[114]*
(a) "Compact Tension" (CT) (b) "Single Edge Notch Bend" (SENB)
(In this illustration, w is the height, t the thickness, a the notch length, and P the load applied)

The monitoring of the crack extension Δa and the calculation of the parameter J at different times of the test, allow the obtention of the main curve of interest: the resistance curve, illustrated in Figure 23. Each phase of the curve can be associated with a physical phenomenon during the test: the starting point of the curve corresponds to the initial sharp notch. The first slope, called the 'blunting phase', is representative of the plastic deformation occurring at the crack tip, which becomes rounder to accommodate the mechanical load before it reaches the critical limit to initiate. The change in the curve trend corresponds to the crack initiation, while the last phase is related to the crack propagation, stable for the material considered in this study. The zone around the crack tip is called the Fracture Process Zone (FPZ), and gathers all the dissipative mechanisms occurring due to both crack propagation and plastic deformation.

Two main fracture parameters can be identified from the resistance curve: the fracture toughness denoted J_{Ic}, related to the resistance to crack initiation, and the tearing modulus T, representative of the resistance to crack propagation. The fracture toughness J_{Ic} is denoted this way because it represents the critical J value for a mode I loading, corresponding to a load perpendicular to the crack plane. The entire procedure for the calculation of these two parameters is detailed in Chapter 2.

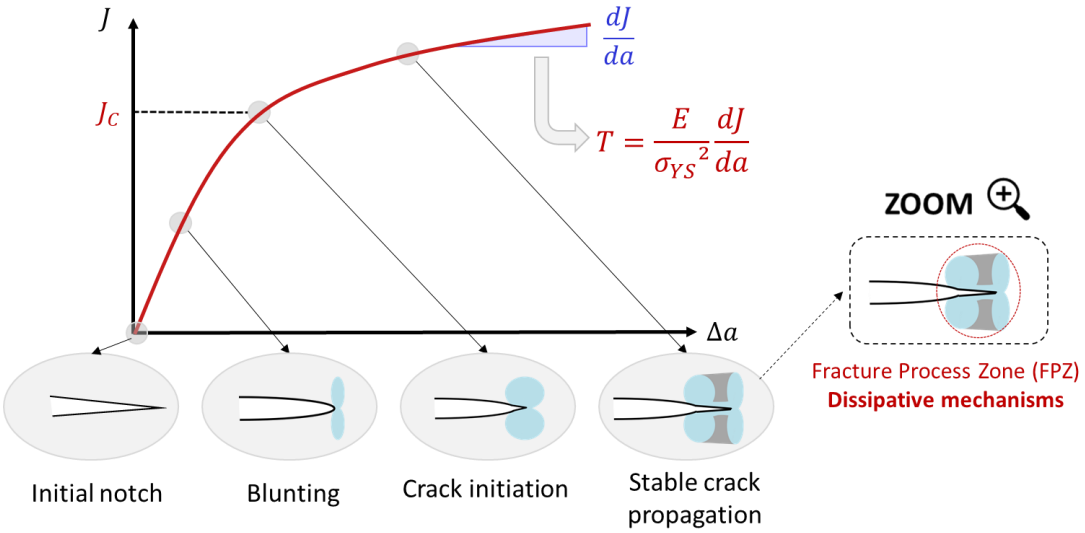

Figure 23: Illustration of the resistance curve, and the different steps of crack propagation

The fracture toughness is not an intrinsic material parameter, hence it is essential to keep a critical eye on two aspects in particular to assess it: the thickness of the specimen, and the temperature (Figure 24). These two key factors can greatly affect the measured value, and potentially lead to overestimate it if they do not comply to the test standard recommendations. In many cases, if the thickness is too thin, the plane stress state will be predominant and the specimen will exhibit a more ductile behavior, leading to an overestimation of the fracture toughness. Therefore, ensuring a plane strain state is critical to obtain size-independent fracture toughness values, which requires sufficient specimen thickness. Similarly, as the ductility of the material increases with the temperature, the measured fracture toughness also tends to rise, underlying the importance of conducting experiments at appropriate temperatures to get reliable results.

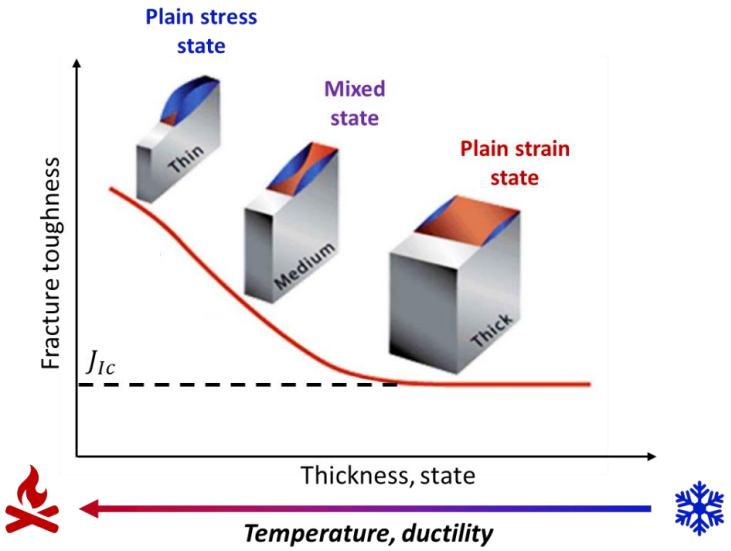

Figure 24: Influence of specimen thickness and temperature on the fracture toughness

III.3.1.3. Propagation mechanisms

A quick overview of the fracture mechanisms is given in this section, from a more experimental point of view. It is of the utmost importance to differentiate the macroscopic and the microscopic behaviors, as the relationship between both scales is not trivial, and can be subjected to brittle or ductile fracture behavior independently. Relevant examples of ductile or brittle mechanical behaviors associated with different microscopic fracture mechanisms are provided by [108], and shown in Figure 25a (ductile-ductile), b (brittle-ductile), c (ductile-brittle) and d (brittle-brittle).

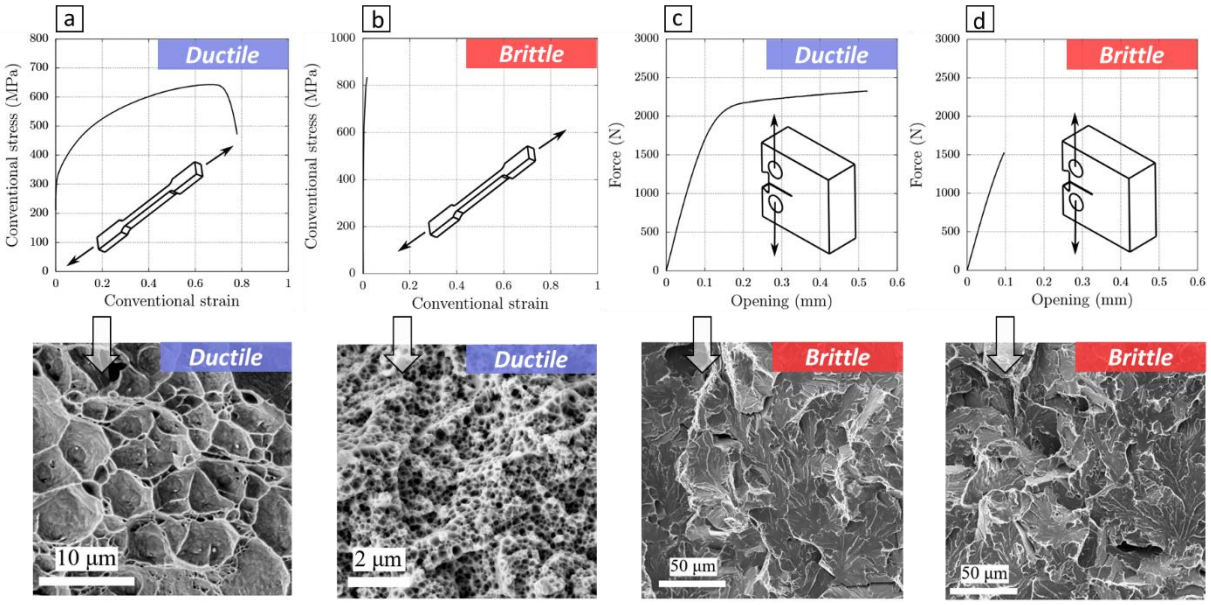

Figure 25: Examples of associated macroscopic and microscopic behaviors (ductile or brittle) for different alloys subjected to tensile or fracture tests (adapted from** [108]**)
(For each case, the stress-strain curve and associated SEM images are presented)
(a) Ductile macroscopic behavior and ductile microscopic fracture mechanisms (austenitic stainless steel at room temperature) (b) Brittle macroscopic behavior and ductile microscopic fracture mechanisms (highly irradiated austenitic stainless steel at room temperature) (c) Ductile macroscopic behavior and brittle microscopic fracture mechanisms (low-alloy steel at high temperature) (d) Brittle macroscopic behavior and brittle microscopic fracture mechanisms (low-alloy steel at low temperature)

Therefore if the material is known to have a ductile macroscopic behavior, the behavior at the microscopic scale is not assured to be ductile as well. Among brittle or ductile fracture mechanics, different categories exist and are presented in Figure 26. For brittle fracture, two mechanisms can be found: transgranular cleavage (Figure 26a) and intergranular decohesion (Figure 26b). For ductile fracture, four mechanisms have been identified: transgranular void

nucleation, growth and coalescence (Figure 26c), transgranular void growth and coalescence (Figure 26d), intergranular void nucleation, growth and coalescence (Figure 26e), and ductile shearing (Figure 26f).

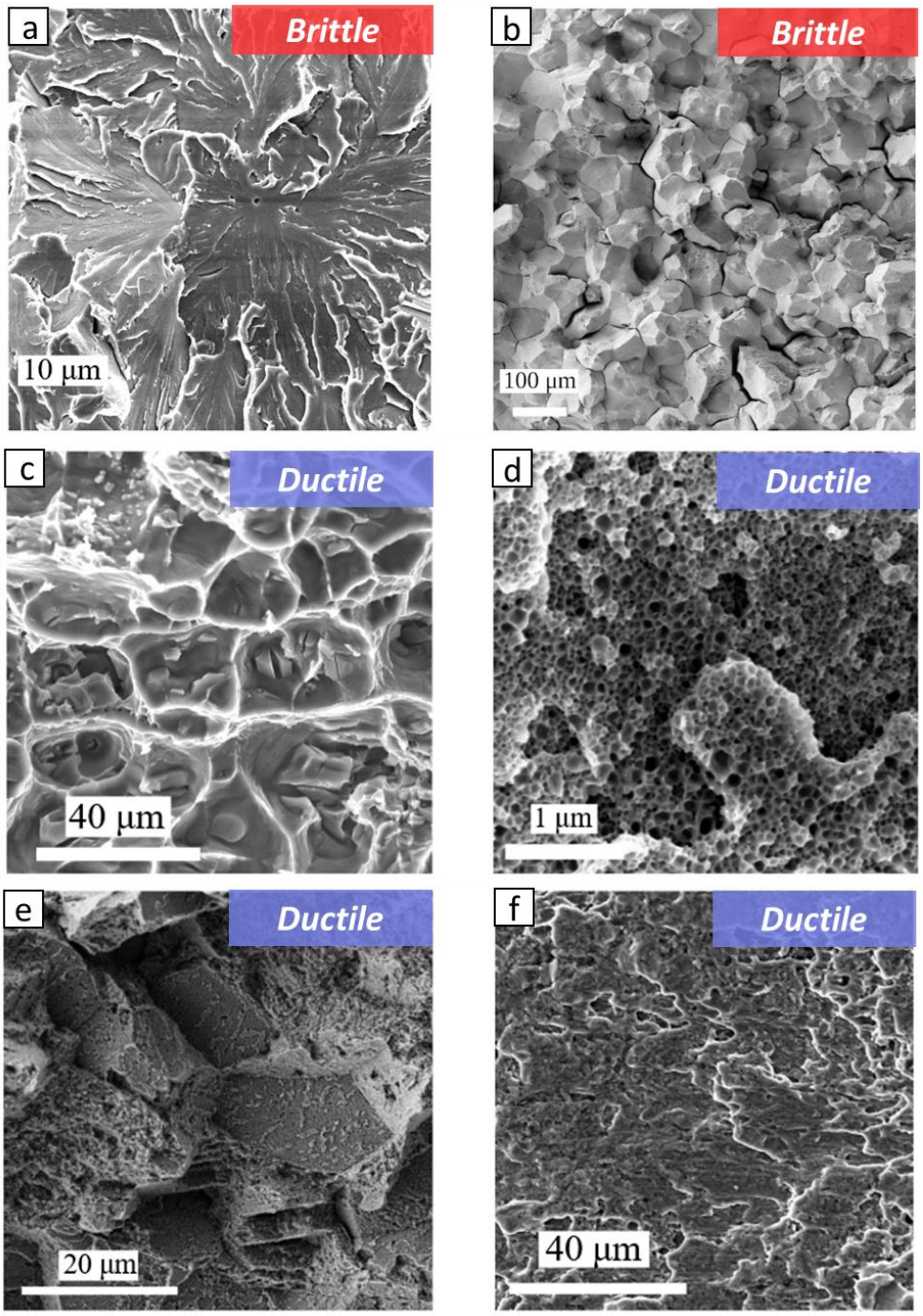

***Figure 26: Brittle and ductile fracture mechanisms in metal alloys (adapted from** [108])*
(a) Transgranular cleavage (brittle, low-alloy steel) (b) Intergranular decohesion (brittle, stainless steel) (c) Transgranular void nucleation, growth and coalescence (ductile, aluminum alloy) (d) Transgranular void growth and coalescence (ductile, austenitic steel) (e) Intergranular void nucleation, growth and coalescence (ductile, austenitic steel) (f) Ductile shearing (ductile, low-alloy steel)

III.3.2. Fracture properties and mechanisms of L-PBF alloys

This section aims to summarize the results available in the literature on the fracture behavior of metallic L-PBF alloys.

III.3.2.1. Fracture behavior for cyclic loading (fatigue)

The majority of studies on the fracture behavior of L-PBF alloys investigate the fatigue crack propagation behavior [117–127]. Several aspects like the building orientation, the VED, or stress relieving heat treatments are studied, using both unnotched or notched specimens, to assess their influence on the fatigue crack growth. Comparison with conventional manufacturing methods is also carried out. The Paris-Erdogan law defined in equation (13) was used to quantify the crack propagation in these materials. In this equation, a is the crack length, N the number of cycles, and ΔK the stress intensity factor range. C and m are the fitting parameters of the law.

$$\frac{da}{dN} = C(\Delta K)^m \tag{13}$$

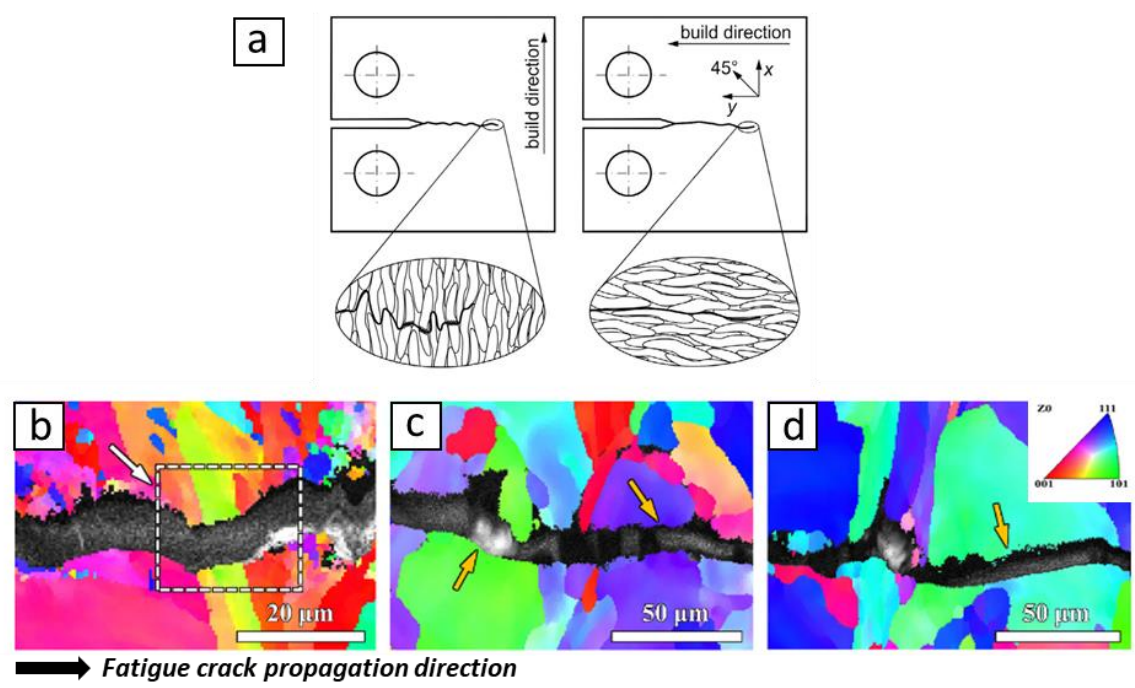

Figure 27: Investigation on the fracture mechanisms occurring during fatigue crack propagation for the L-PBF 316L SS alloy

(a) Illustration of the dependence on the grain orientation and morphology [125]

(b, c, d) EBSD maps showing the transgranular path for different heat-treatment conditions [120]

Initial and post-mortem microstructure characterizations were performed in order to identify the fracture mechanisms ruling the crack propagation as shown in Figure 27. Mostly transgranular crack propagation is observed for most of the fatigue crack propagation studies found. However, cyclic and monotonic loadings can result in very different outcomes. Few studies have yet been carried out on the determination of fracture toughness using established test standards, which require monotonic loadings.

III.3.2.2. Fracture behavior for monotonic loading

As far as monotonic loading is concerned, both quasi-static and dynamic, there is a noticeable knowledge gap in the literature regarding the fracture properties of L-PBF alloys for industrial applications.

The studies found for a quasi-static loading (three-point bending, or compact tension…) have attempted to investigate the influence of key processing parameters (sample building orientation, scanning strategy…) on widely used alloys such as 316L SS [128], Inconel 718 or 625 [129,130], Hastelloy X [131], AlSi10Mg [132]... An overview of the various conclusions highlights that the fracture behavior is highly dependent on the considered material and the chosen processing parameters, as they directly affect the criticality of an interface for crack propagation. Three different scales could be identified as detrimental to crack initiation and propagation: the meltpool boundaries [129,130,132,133], the grain boundaries [130–132], and the oxide/matrix interfaces (often located in the interdendritic region) [130,134,135]. An illustration is given in Figure 28, with both the meltpool and grain boundaries acting as potential crack path depending on the building orientation. However, the contribution of each of the aforementioned microstructural features on crack propagation is yet to be investigated thoroughly for all L-PBF alloys. The fracture mechanisms observed are often a mix between intergranular and transgranular fractures.

The building orientation has been the most investigated parameter in these studies, yet no definitive trend could be identified regarding the most efficient one to consider to obtain the best resistance to crack initiation and propagation. For highly ductile alloys (316L, Hastelloy X), the vertical building orientation results in better resistance to crack initiation and propagation than a horizontal one. Yet the opposite is observed for less ductile alloys like AlSi10Mg (Figure 28), where horizontal specimens are more resistant than vertical ones.

Moreover, unlike what is generally observed for conventional manufacturing methods, for L-PBF titanium and aluminum alloys no correlation could be established between fracture toughness and tensile properties, especially ductility [136].

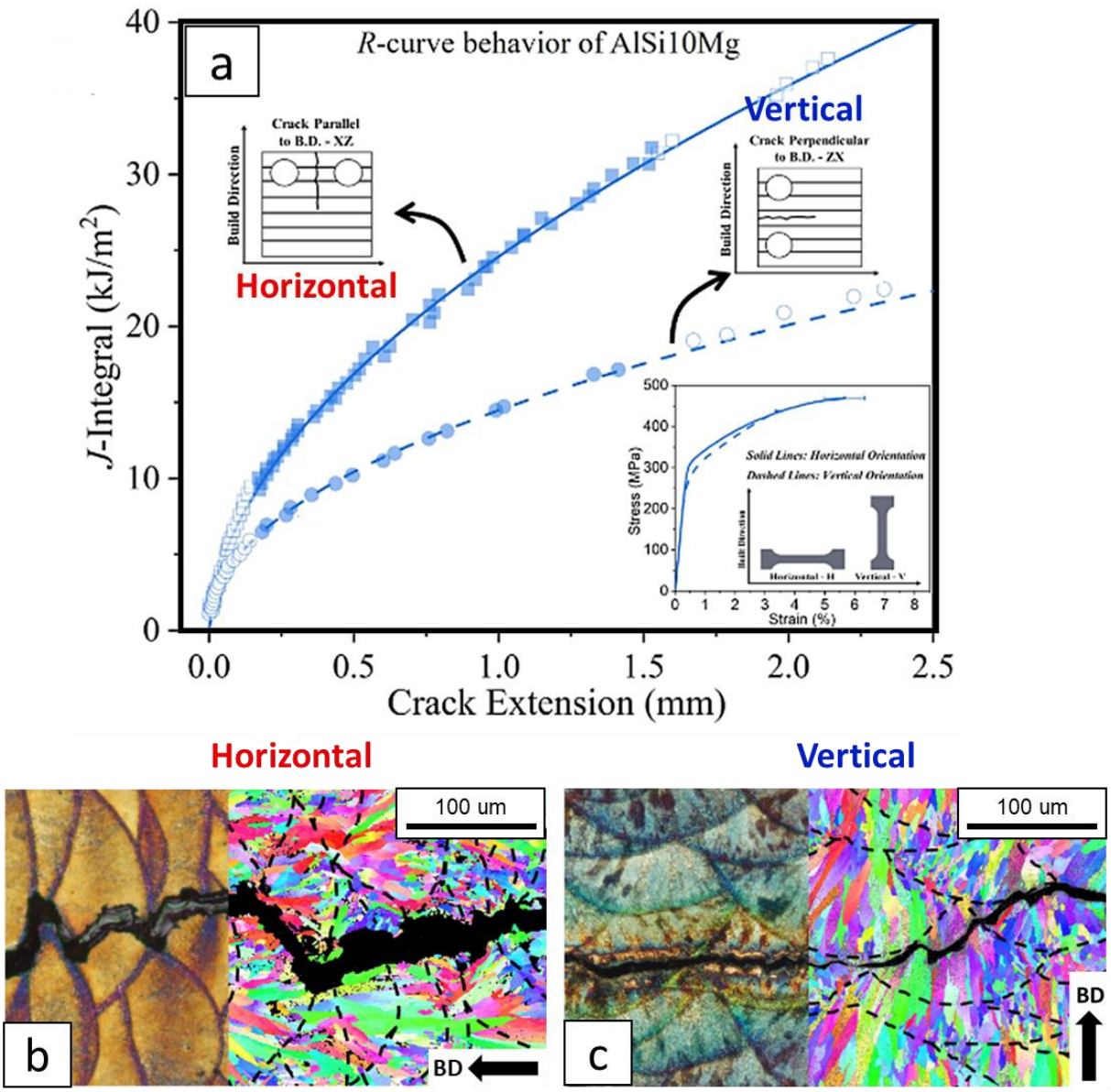

***Figure 28: Example of the influence of different interfaces (grains' and meltpools' boundaries) on the fracture behavior of a L-PBF AlSi10Mg alloy (adapted from** [132,136])*
(a) Resistance curve (b) Crack path for the horizontal specimen (c) Crack path for vertical specimen

For dynamic tests such as Charpy impact tests [130,134,137,138], not much difference was noted in terms of critical interfaces (meltpool boundaries, grain boundaries, interdendritic regions…), or fracture modes (mixed between transgranular and intergranular), as illustrated in Figure 29. One study on 316L [134] carried out tests under both quasi-static and dynamic loading demonstrated that no significant differences were observed on this aspect between the

two. For both studies considered, vertical specimens exhibited better resistance to crack propagation than the horizontal ones. The fracture mode was also a mixed one between intergranular and transgranular.

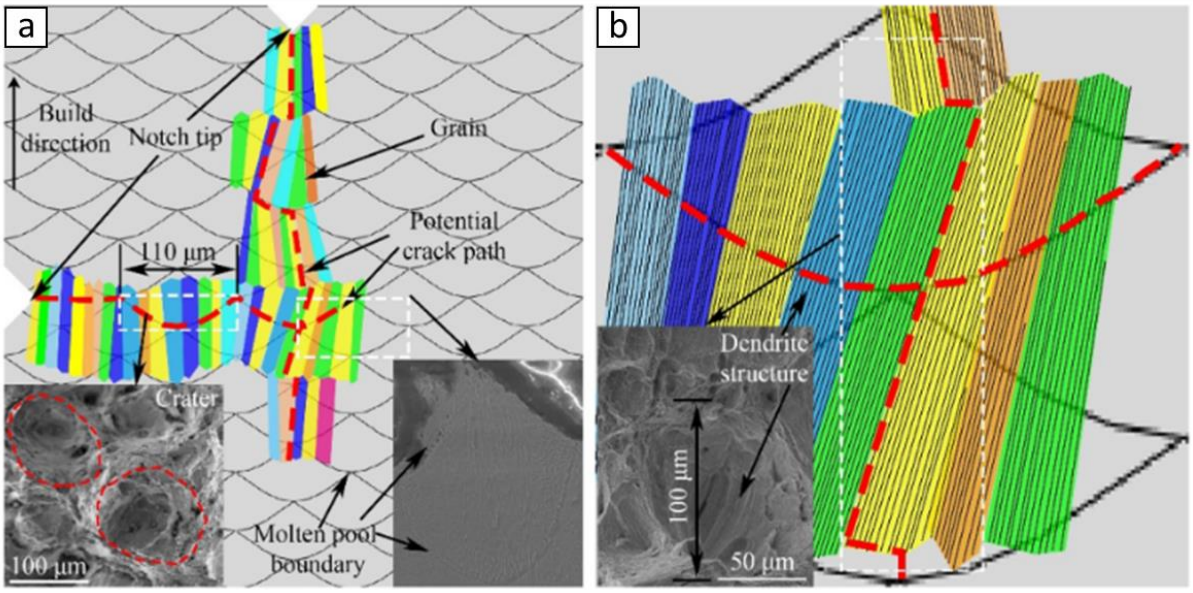

Figure 29: Schematic illustration of the different possible crack paths identified after Charpy impact tests performed on a L-PBF GH3536 alloy *[130]*
(a) Crack propagation along the grains' and/or meltpools' boundaries
(b) Crack propagation along the interdendritic regions

Finally, this last section concludes on the importance to characterize the fracture behavior for a given L-PBF alloy, with a given set of manufacturing parameters, as the resulting properties could tremendously vary from one configuration to another. It has also been demonstrated that a correlation with tensile properties like strength or ductility was questionable for L-PBF alloys, and hence conducting experiments following standard guidelines seems the most suitable method to obtain reliable results and conclusions.

CHAPTER 2:
Materials, manufacturing strategies & experimental methods

This chapter introduces the material of interest, Ni20Cr. The general properties of conventionally produced Ni20Cr are presented, as well as literature results regarding L-PBF Ni20Cr manufacturing, microstructure, and mechanical behavior. The manufacturing strategies and experimental methods implemented throughout this PhD work are also detailed.

I. Introduction to Ni20Cr alloy

I.1. General properties of conventionally manufactured Ni20Cr

The Ni20wt.%Cr (Ni20Cr) alloy, also commonly called Nichrome, is a non-magnetic binary alloy often investigated for its remarkable properties at high temperatures: good resistance to electrochemical corrosion [139,140], irradiation [141,142], high-temperature oxidation [143], creep behavior [144], etc. Its high resistivity and oxidation resistance make it a relevant choice for producing electronic components and heating elements like electric ovens, toasters, electronic cigarettes, etc [140,145–148]. Its general properties are listed in Table 1.

Table 1: General properties of conventionnally produced Ni20Cr (ANSYS Granta Materials database)

Young's modulus	205-220 GPa
Yield stress	365-450 MPa
Hardness (Vickers)	160-200 HV
Density	8,3-8,5 g/cm^3
Melting point	1390-1430°C
Electric resistivity	102-114 μΩ.cm
Specific heat capacity	430-450 J/kg.K

Another asset of Ni20Cr is the fact that it is a base alloy, meaning many widely used superalloys like Inconel alloys (718, 625, 600) or Hastelloy alloys (X, C-276) derive from it. Conventional Ni-based alloys usually present various phases and precipitations that hinder the understanding of the relationship between the microstructure and the mechanical behavior [149–154]. Ni20Cr matrix-chromium content falls in the same range as those, but with a much simpler system: it is a single-phase alloy with a single FCC structure, displaying no formation of intermetallic compounds for the considered thermodynamic solidification conditions. Hence, it is often considered as a model material (from a microstructural standpoint) to study coupling mechanisms occurring in these more complex alloys [143,144]. The phase diagram of the Ni-Cr system at equilibrium is presented in Figure 30. The red dotted line indicates the position of Ni20Cr. For 20% of Cr in substitution in a pure Ni matrix, the only existing phase for a rapid solidification above 500°C is a Ni solid solution, which is stable until approximately 1400°C.

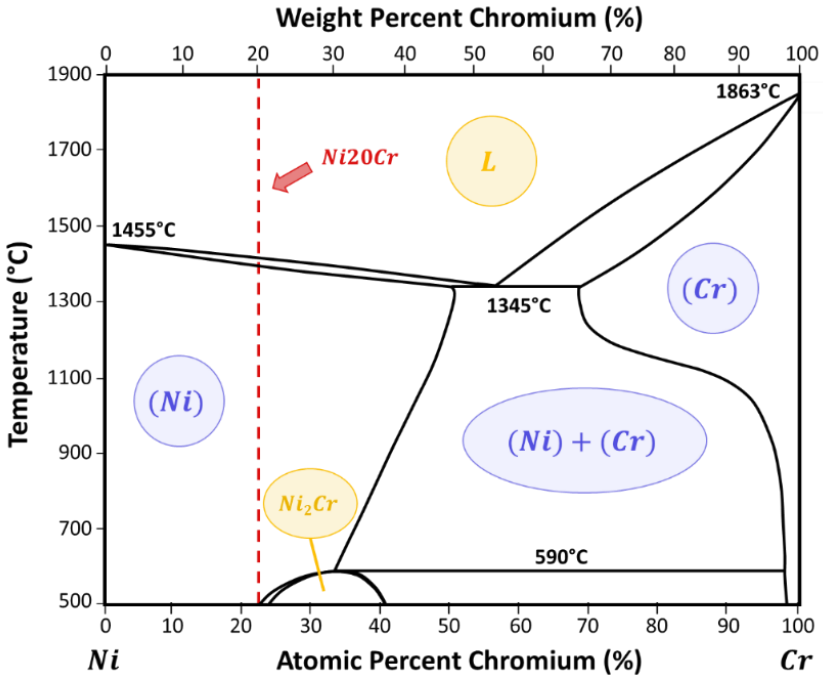

***Figure 30: Phase diagram of the Ni-Cr system (adapted from** [155])*

I.2. Overview of L-PBF Ni20Cr

Until very recently, Ni20Cr alloy received very little attention when it comes to additive manufacturing, with only one study available in the literature [156]. Most of the latest research conducted on the matter was carried out by two recent PhD works [36,157]. The results obtained in terms of optimal processing parameters, microstructure, and mechanical properties are summarized below.

I.2.1. Manufacturing process

The first investigations on L-PBF Ni20Cr specimens were conducted by Song et al. [156]. The laser power and laser scanning speed allowing the complete formation of dense parts were specifically addressed. It was demonstrated that for a layer thickness of 50 µm and a hatch spacing of 40 µm, complete fusion of the powder was achievable for a power of 100 W and a scanning speed between 100 and 300 mm/s. Based on this range of processing parameters, parts relative density was estimated between 98%-99% using the Archimedes' method. Surface roughness analyses and SEM micrographs, shown in Figure 31, exhibited that the surface roughness increased with the scanning speed, with larger balls and splashing occurring during the manufacturing process.

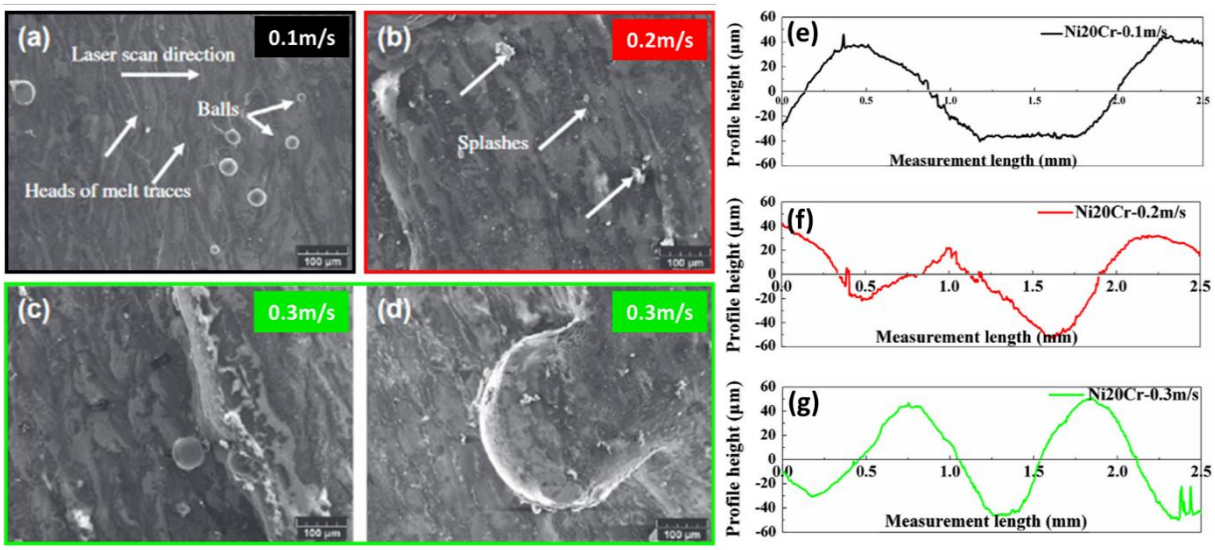

***Figure 31: Surface roughness analyses of L-PBF Ni20Cr specimens (adapted from** [156])*
(a, b, c, d) SEM micrographs of the specimens surface for 0.1, 0.2 and 0.3 m/s scanning speed
(e) Profilometry analysis for 0.1, 0.2 and 0.3 m/s scanning speed

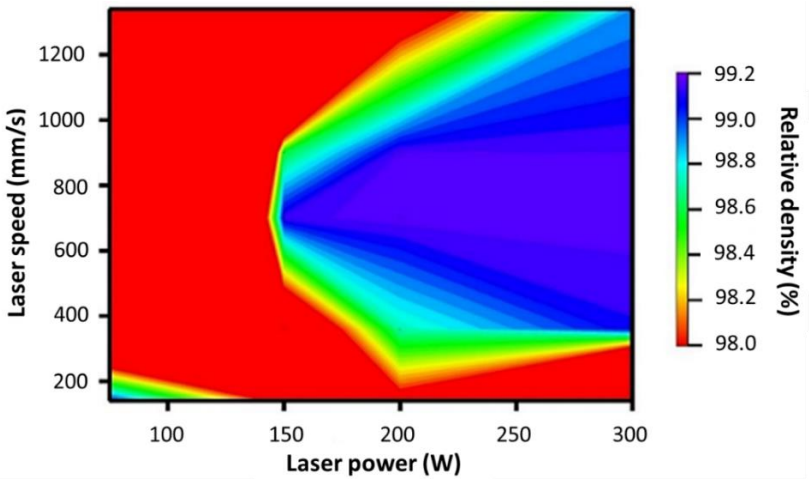

***Figure 32: Printability map laser power versus scan speed** [36]*

Hug et al. and Lelievre [36,37] tested a wider range of VEDs to print dense specimens. Only the laser speed and laser power were varied, with layer thickness and hatch spacing set at 30 and 120 µm respectively. Density measurements following the Archimedes' principle and porosity analyses were conducted to characterize the relative density and possible defects associated with each VED (Figure 32 and Figure 33). Observations from both methods were in good agreement, as well as with the literature results: lower-end VEDs generally resulted in LOF-type defects, whereas higher-end VEDs generated keyholes. Both extreme cases increased the specimen porosity. A processing window was established to visualize which power-speed combination fosters the highest relative density. A range of 60 to 120 J/mm^3 was determined as

suitable to print dense L-PBF Ni20Cr specimens (relative density higher than 99.2%), and was considered in the present work.

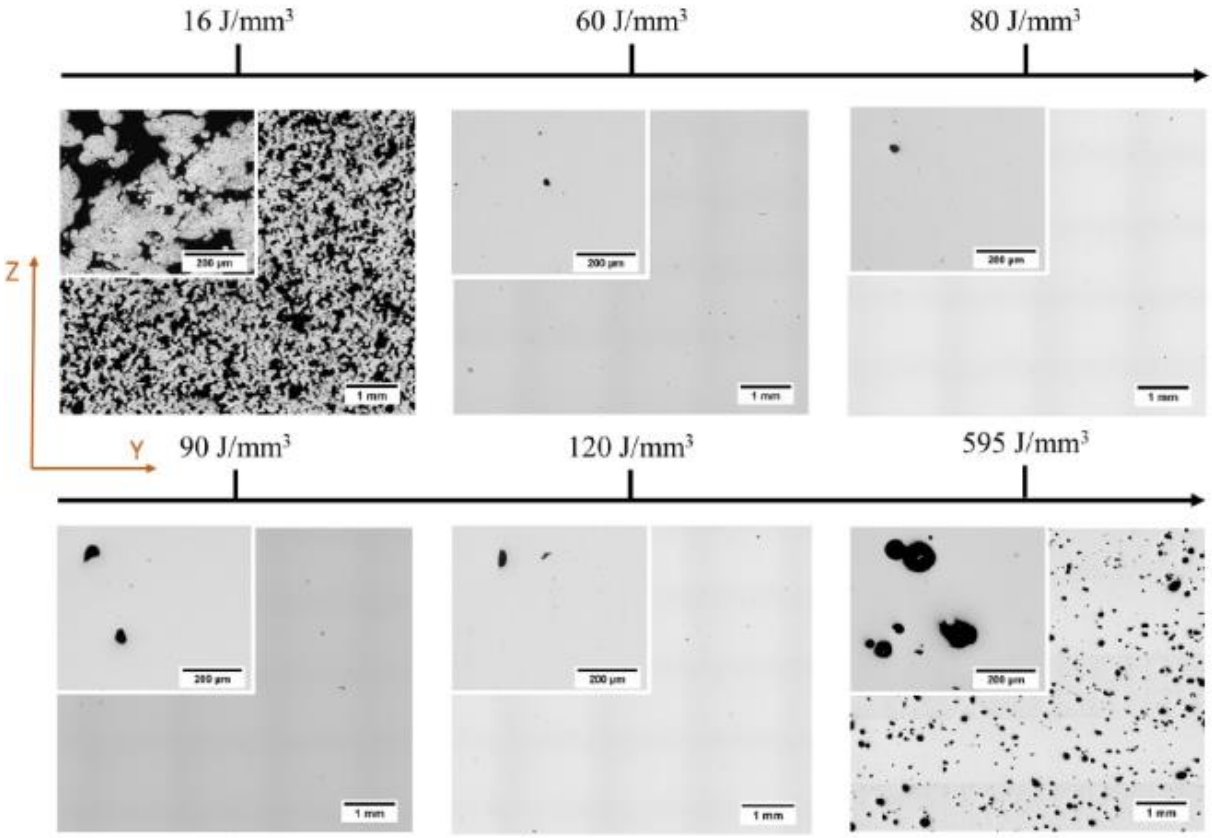

Figure 33: Optical microscope analysis of the pores observed for different VEDs *[37]*

I.2.2. Microstructure

L-PBF Ni20Cr specimens exhibit the typical multi-scale microstructure of L-PBF alloys already discussed in Chapter 1, as shown in Figure 34. Meltpools are observed at the mesoscale, whereas grains are found at the microscale and cellular dendrites at the sub-microscale. Though precipitation is not expected in conventional Ni20Cr generally subjected to moderate or low cooling rates, Cr-rich nano-precipitates were observed in interdendritic walls when built by L-PBF [158].

In the case of L-PBF microstructure, it is of the utmost importance to point out that the morphology of each of these sub-structures highly depends on the processing parameters, in particular the first order parameters (laser speed, power, etc.) represented by the VED. To characterize this, Hug et al. and Lelievre [36,37] considered three different VEDs within the

range resulting in dense specimens: 60, 90 and 120 J/mm^3. The rotation angle was set at 67°, with a lasing strategy in stripes. At mesoscale, they proved that both meltpools width and depth observed on the XZ plane increase with the VED (Figure 35a, b and c). The strip bands observed on the XY plane, representative of the meltpools, follow the same tendency (Figure 35d, e and f).

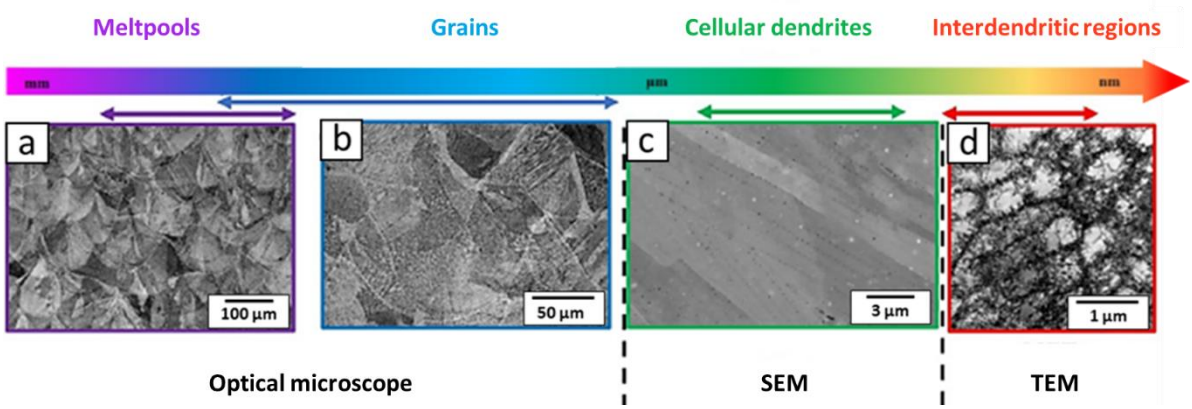

Figure 34: Illustration of the different length scales observed in Ni20Cr *[36]*

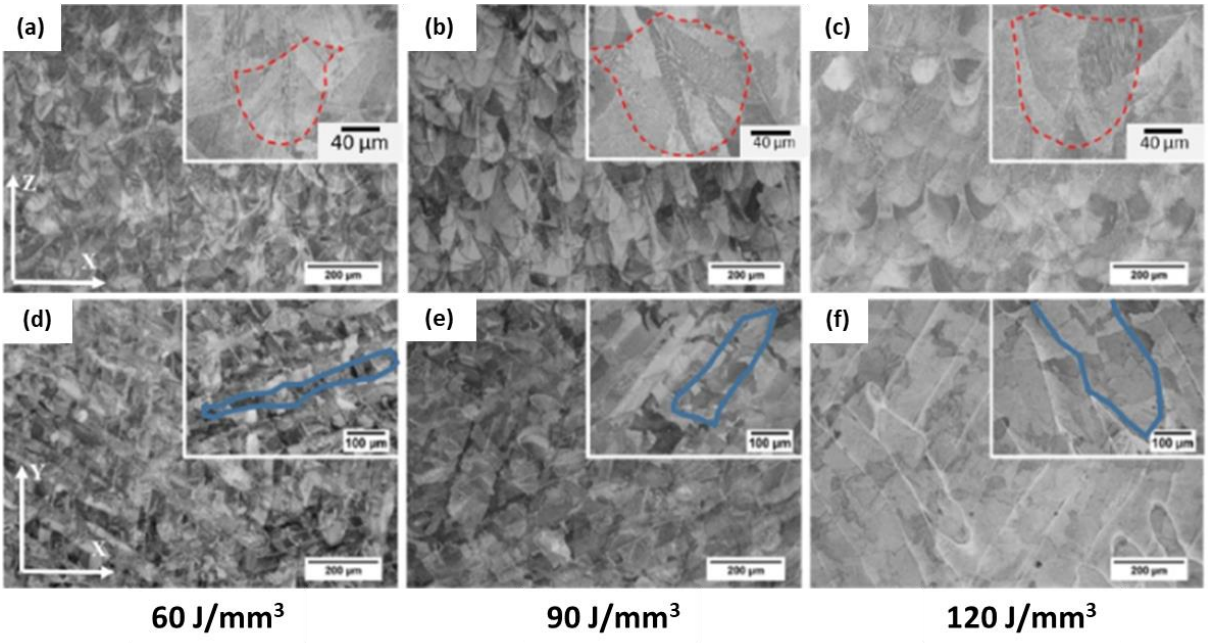

Figure 35: Meltpools morphology for different VEDs (adapted from *[37])*
(a, b, c) On the XZ plane (parallel to building direction)
(d, e, f) On the XY plane (perpendicular to the building direction)

At microscale, both grain morphology and crystallography are strongly influenced by the VED as shown in Figure 36a, b and c. An evolution from an equiaxed to columnar microstructure was observed for a VED ranging from 60 to 120 J/mm^3, with grains gradually

growing on both the XY and the XZ planes, and getting more elongated along the building direction. Higher maximum intensity values are also observed at higher VEDs, also revealing more pronounced textures. Overall, the study highlights the anisotropic nature of the Ni20Cr L-PBF microstructure considering the differences observed in both planes in terms of grain morphology and orientation.

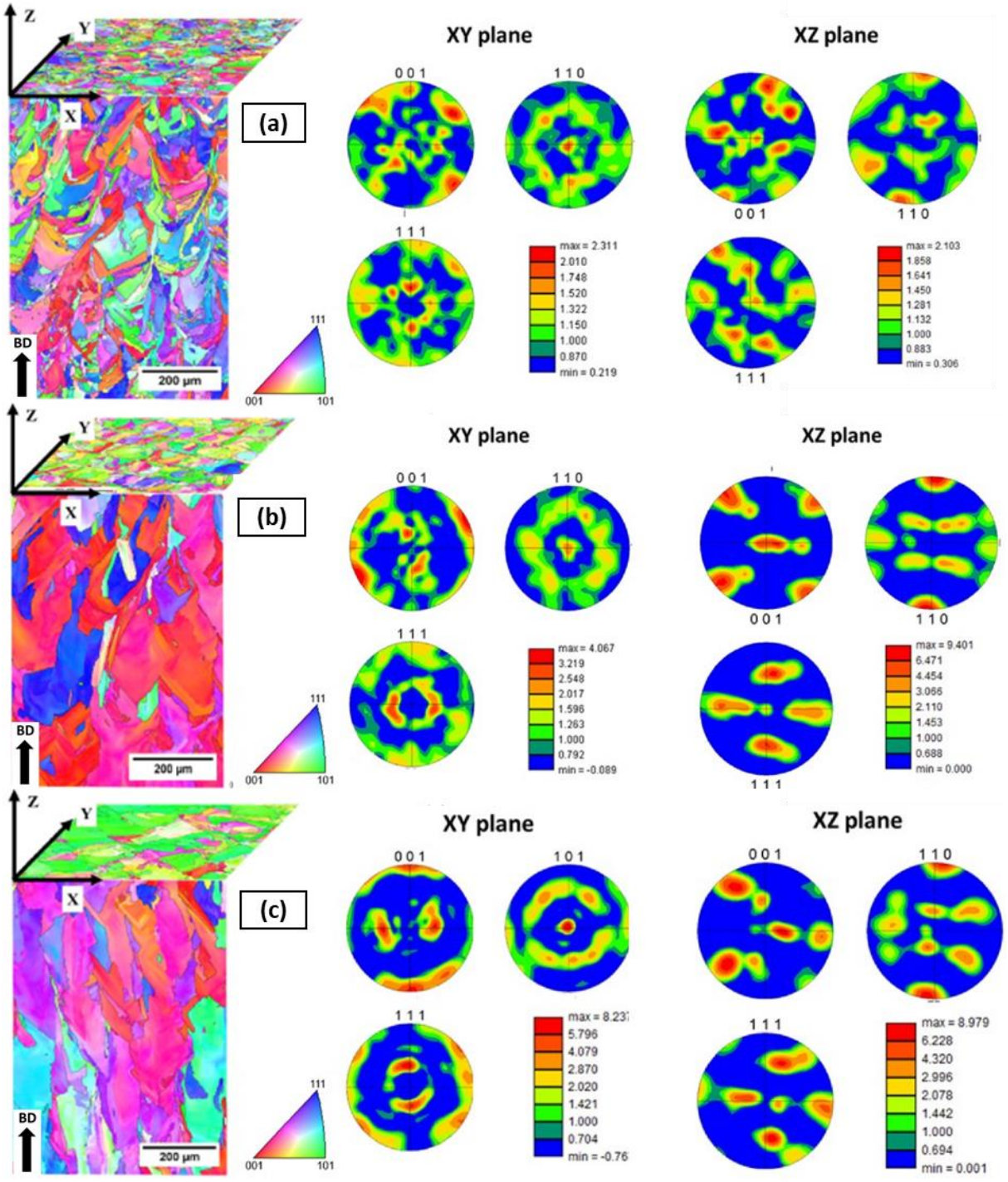

Figure 36: EBSD grain orientation maps and Pole Figures resulting from different VED values
(a) 60 J/mm^3 (b) 90 J/mm^3 (c) 120 J/mm^3

I.2.3. Tensile behavior

It has been shown that the choice of process parameters does not only significantly influence the resulting microstructure, but also the mechanical behavior. Song et al. [156] investigated the influence of the scanning speed on the mechanical properties, showing that for their set of parameters, tensile properties (yield and ultimate tensile stresses) increase with the scanning speed (and therefore a decreasing VED).

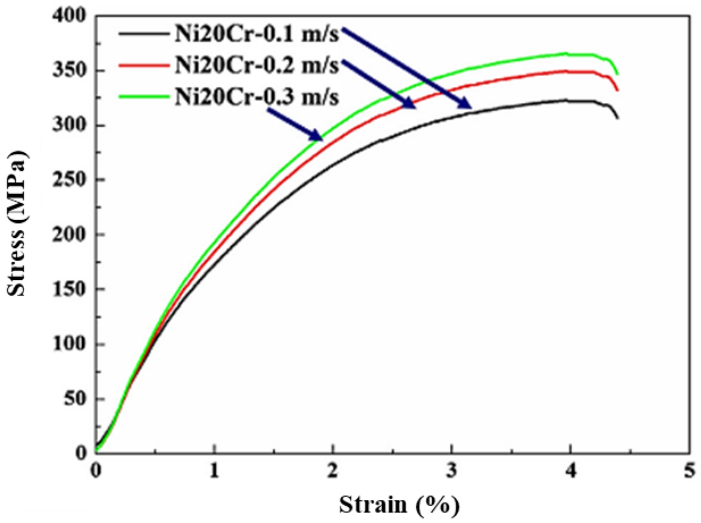

Figure 37: Engineering tensile curves of L-PBF Ni20Cr specimens for different laser scanning speeds *[156]*

The same results were observed by Hug et al. and Lelievre [36,37], with in addition an increase in ductility for higher VEDs. They also tried to correlate the yield stress evolution with the dendrites arm spacing, as the peculiar grain geometry in L-PBF complexifies the use of the Hall-Petch law. It was shown that a relation could be identified between the yield stress, and the inverse of the square root of the smaller primary arm dendrite. Dendritic arm spacing size is directly related to the cooling rate, meaning that higher cooling rate resulted in an increased yield stress.

Joshi et al. confirmed these results by studying the microstructure of a wider range of VEDs (46 to 230 J/mm^3) [159]. A comparison with cast & wrought materials [158] was also carried out to analyze the differences on both the microstructure and the tensile behavior, as shown in Figure 39. The results exhibited significant differences in terms of microstructures and tensile behaviors between the two manufacturing processes. In this study, cast & wrought specimens were characterized by large equiaxed grains, with a more homogeneous distribution

of the grain size and morphology, and a higher texture compared to L-PBF specimens. The tensile behavior also indicated very different strain hardening trends and significant ductility for cast & wrought specimens compared to their L-PBF counterparts. These differences hence foreshadow a need to characterize the influence of the manufacturing process parameters on the overall mechanical behavior, including the fracture properties of L-PBF Ni20Cr which has been little studied in the literature.

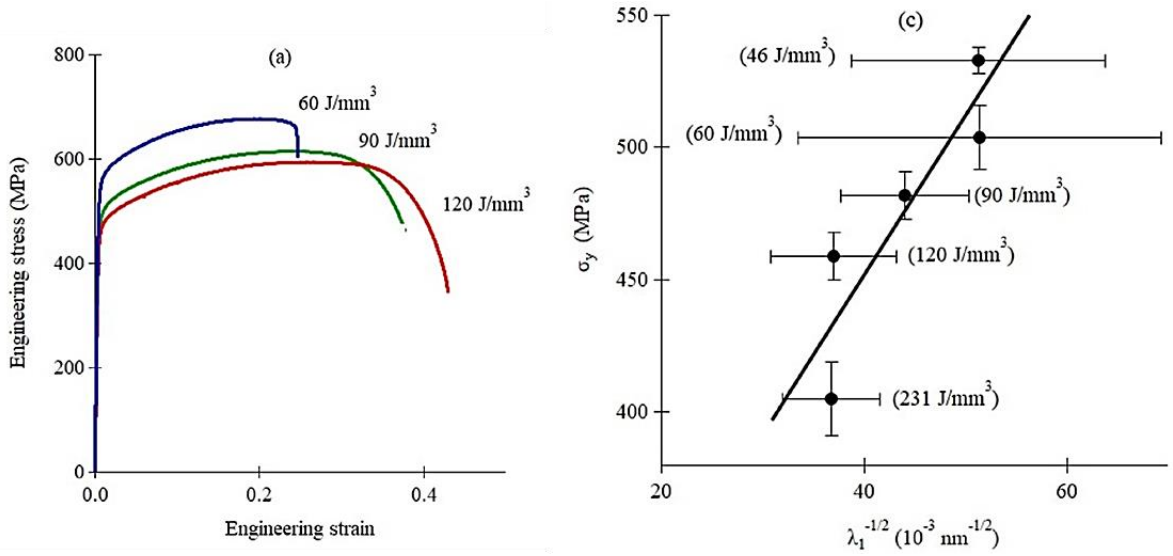

***Figure 38: Comparison of the tensile properties of L-PBF Ni20Cr specimens for different VEDs values (60, 90, and 120 J/mm^3) (adapted from** [36,37])*

(a) Engineering tensile curves (b) Relationship between yield stress and primary arm dendrite spacing

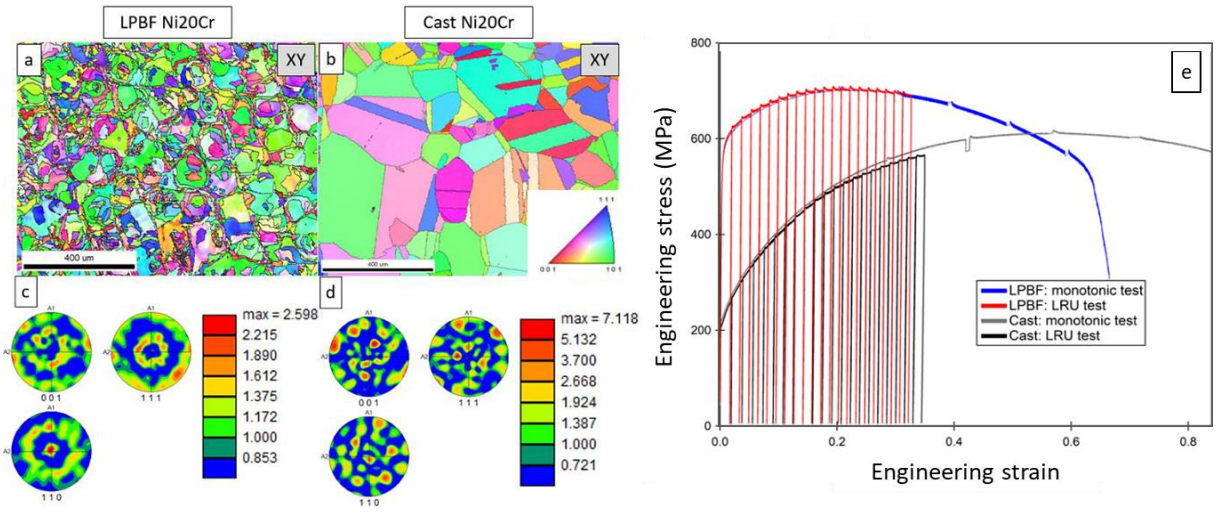

***Figure 39: Comparison between L-PBF (VED = 62 J/mm^3) and cast & wrought specimens (adapted from** [158])*

(a, b) EBSD maps (c, d) Pole Figures (e) Engineering Stress-Strain curves (Monotonic curves and Loading-Relaxation-Unloading curves)

II. Manufacturing strategies

During this study, samples with two sets of dimensions (length×height×width) were considered: 120mm×15mm×5mm for tensile specimens, and 65mm×10mm×10mm for fracture specimens.

To account for conventional manufacturing methods, a set of samples was machined from a 200mm×200mm×10mm cast & wrought plate provided by Innov'metor society (France), by means of Electrical Discharge Machining (EDM). The chemical composition was estimated by EDS (Energy Dispersive x-ray Spectroscopy) analysis and is given in Table 2. To ensure homogeneous microstructure, machined specimens were subjected to a recrystallization heat treatment of 1150°C for 10h.

On the other hand, L-PBF specimens were produced using a commercial Ni-20 wt.%Cr gas atomized powder, provided by Höganäs AB company (Sweden). The feedstock was already thoroughly investigated in previous studies [36,37]: chemical composition was obtained by means of Inductively Coupled Plasma Spectroscopy (ICP-OES) and presented in Table 2. Additionally, X-Ray Diffraction (XRD) was considered to analyze the presence of possible secondary phases or impurities, as both Silicium and Aluminum were reported during feedstock characterization. However, none was observed. Finally, particles size (~ 30-40µm) and morphology (spherical) were assessed through SEM and Laser Diffraction to assure the good flowability of the powder.

Table 2: Chemical composition of L-PBF powder and cast & wrought plate (in wt.%)

	Cr	**Fe**	**Si**	**Mn**	**Al**	**C**	**O**	**Ni**
Cast & wrought plate	19.9	1.6	-	0.9	-	trace	trace	bal.
L-PBF powder [37]	19.9	0.0222	0.035	<0.0002	0.047	-	-	bal.

Figure 40a presents the general system of the SLM 125 HL machine from SLM Solutions (Germany) used to manufacture L-PBF specimens. For this machine the powder alimentation comes from above, as illustrated in both Figure 40a and b, which is not common for this process. As O_2 content is known to be detrimental to parts qualities and properties during L-PBF manufacturing [160–162], the building chamber was filled with Argon to

maintain percentage below 0.1%. A 400 W Yb-fiber laser with a beam focus diameter of 60 µm was used to fuse the powder, and the Inconel building plate was preheated at 200°C in order to minimize the residual stresses induced during the building process. To compare the different manufacturing strategies of interest, the Volumetric Energy Density (VED), was considered throughout this work:

$$VED = \frac{P}{hvt} \tag{14}$$

with P the laser power, h the hatch distance, v the scanning speed and t the powder layer thickness. Stripes pattern was chosen for the scan strategy, with 10 mm wide stripes. h and t are constants provided by SLM Solutions as the optimized values for Nickel-based alloys. All processing parameters, listed in Table 3, were chosen according to previous work [36,37] to produce specimens with an optimal relative density higher than 99.2%. To improve the roughness of the specimens, an external ring with 0.22 mm border vectors was added during L-PBF manufacturing.

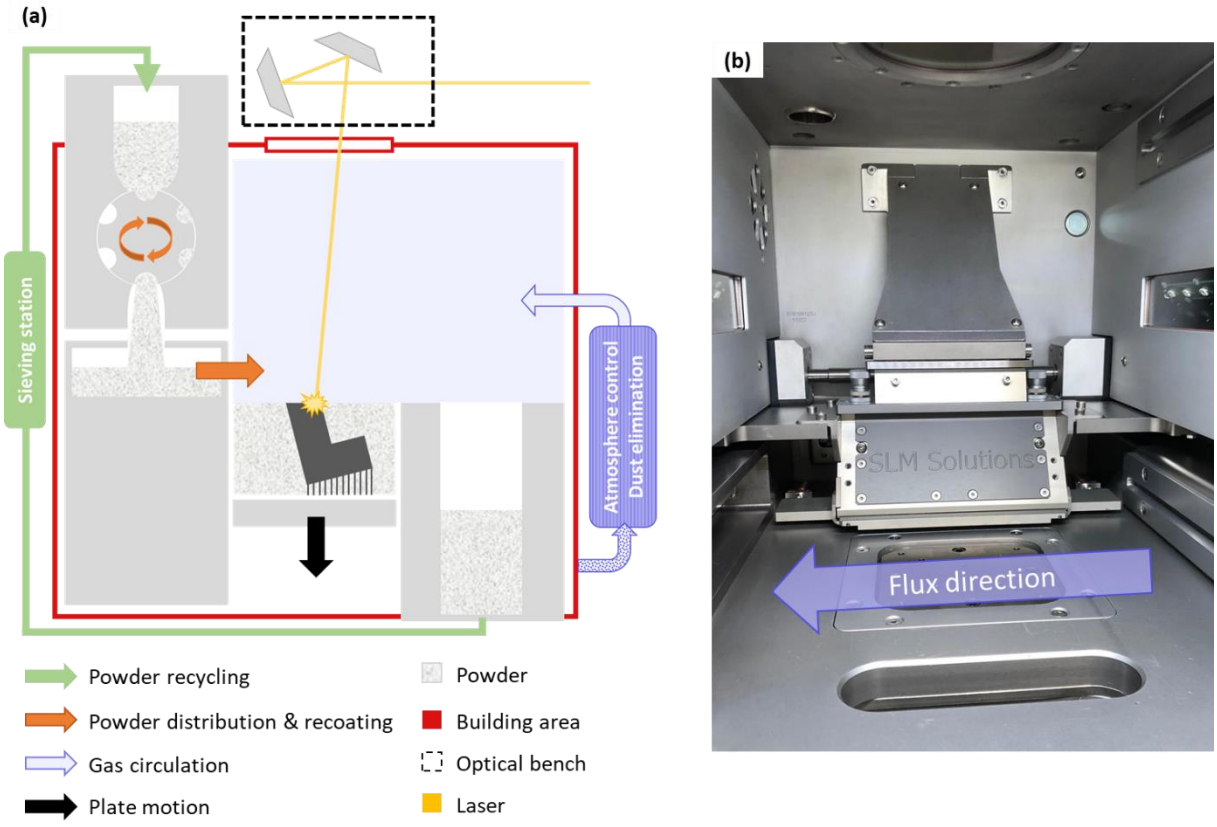

Figure 40: Presentation of the SLM 125 HL machine used to produce L-PBF specimens
(a) Illustration of the machine system (Credit to C. Folton) (b) Photo of the processing chamber

Table 3: L-PBF manufacturing parameters (SLM 125 HL)

Volumetric energy density VED	Laser power *P*	Hatch spacing *h*	Laser speed *v*	Layer thickness *t*
60 J/mm^3	150 W	0.12 mm	700 mm/s	0.03 mm
90 J/mm^3	300 W	0.12 mm	900 mm/s	0.03 mm

To investigate the influence of the manufacturing strategy on the microstructure and mechanical properties of L-PBF Ni20Cr, the present work focuses on three parameters that were previously discussed as key factors: the sample building orientation (horizontal or vertical), the VED (60 and 90 J/mm^3), and the rotation angle between layers (67° or 90°). All parameters are illustrated in Figure 41. Regarding the building orientation, specimens printed with their principal axis along the X direction are referred to as 'horizontal' specimens, and those printed along the Z direction are referred to as 'vertical' specimens. For comparison purposes, color-coded nomenclatures were given to each printing strategy, and are summarized in Table 4.

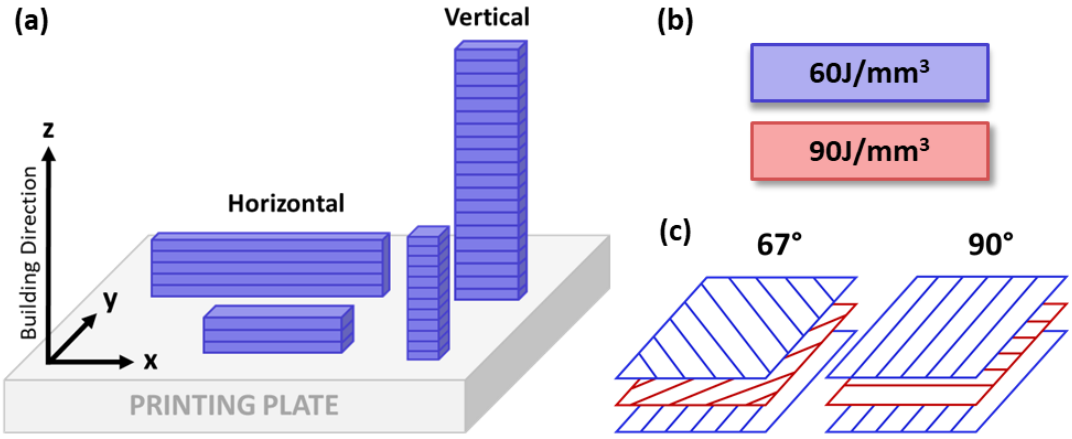

Figure 41: Illustration of the L-PBF manufacturing strategies
(a) Horizontal and Vertical orientations (b) 60 and 90 J/mm^3 VED values
(c) 67° and 90° rotation angles between layers

All in all, seven configurations were considered in this work, with six sets of printing parameters for L-PBF specimens, and one set of cast & wrought specimens (noted C&W). L-PBF specimens were labelled using the 'building orientation-VED-rotation angle' order as follows: H9067, V9067, H9090, V9090, H6067, and V6067 (Table 4).

Table 4: Color-coded nomenclatures of all manufacturing configurations

Manufacturing	Building orientation	VED (J/mm^3)	Rotation angle (°)	Nomenclature
L-PBF	Horizontal	90	67	**H9067**
L-PBF	Vertical	90	67	**V9067**
L-PBF	Horizontal	90	90	**H9090**
L-PBF	Vertical	90	90	**V9090**
L-PBF	Horizontal	60	67	**H6067**
L-PBF	Vertical	60	67	**V6067**
Cast & wrought	-	-	-	**C&W**

III. Experimental methods

III.1. Density and porosity characterization

Though the printing parameters were chosen to achieve dense specimens [36,37], a density analysis was carried out for each configuration to ensure that all configurations have the same density in the present work, regardless of the manufacturing parameters. In this regard, Archimedes' principle was used to quantify the samples density. The Archimedes' principle relies on the determination of the dry and wet weight of a specimen in order to determine its density. The dry weight m_d is obtained by weighing the specimen in air, whereas the wet weight m_w is determined by weighing the specimen immersed in distilled water. The density ρ was calculated using the following formula:

$$\rho = \left(\frac{m_d}{m_d - m_w} * (\rho_w - \rho_a) \right) + \rho_a \quad (15)$$

with ρ_a and ρ_w the densities of water and air respectively at room temperature. The shape and dimensions of the specimens measured, corresponding to fracture test specimens, will be further described.

Porosity analysis was also performed at the specimen core using an optical microscope, with a magnification of 200x and a resolution of 1 pixel/µm. At least two surfaces of 10mm×10mm were considered in each case, using an assembly tool to merge all the images taken from a single surface. The porosity was calculated based on the ratio of the pores area over the area of the zone observed. It is important to note that this technique may be sensitive to the observation zone considered.

III.2. Microhardness testing

To get a first glance at the influence of the manufacturing strategy on the material, microhardness tests were carried out on at least one fracture specimen (dimensions 65mm×10mm×10mm) per configuration. For L-PBF specimens, it also allowed to assess a possible difference induced by the significant temperature gradients during the manufacturing

process. To get a representative analysis, specimens were cut at both ends and along the principal axis of the specimens, and each section was subjected to microhardness testing (Figure 42).

Tests were carried out using a semi-automatic PRESI HZ50-4 hardness tester with a Vickers indenter. A load of 0.3 kgf was applied for 10 seconds. Distances between each indent was calculated to be at least three times bigger than the indent diagonals (~300 µm) to avoid mutual influences of the indents plastic zone [163]. All test parameters are given in Table 5.

Table 5: Microhardness test parameters

Indents matrix	Load (kgf)	Time (s)	X distance between indents (µm)	Y distance between indents (µm)
8×8	0.3	10	1100	1050
5×30	0.3	10	1800	1800

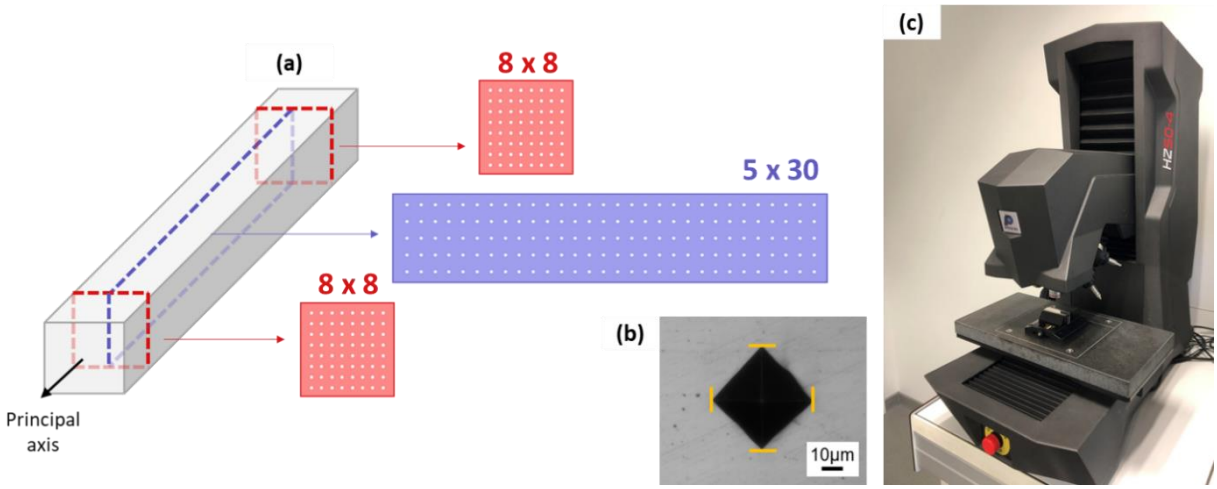

Figure 42: Illustration of microhardness testing
(a) Position of the indented surfaces (b) Indent example (Vickers) (c) Hardness machine

Results were automatically analyzed by the PRESI software, using the following formula to calculate the Vickers hardness:

$$HV = \frac{2F \times \sin(136°/2)}{9.80665 \times d^2} \tag{16}$$

with F the load (in N), and d (in mm) the mean value between the two indent diagonal lengths.

III.3. Tensile testing

All mechanical tests were performed using a MTS hydraulic machine equipped with a 100 kN load cell, and the repeatability of the results was ensured by considering at least five specimens in every configuration.

Tensile tests were carried out at room temperature to assess the monotonous mechanical properties associated with each printing strategy. Flat dogbone-shaped specimens were used, as prescribed in the ISO 6892-1 tensile test standard [164]. Machining was done by means of EDM, and the dimensions are given Figure 43. Tests were carried out in displacement-controlled mode, with a displacement rate of 2 mm/min, equivalent to an average standard strain rate of 10^{-3} s^{-1}. The axial strain was measured with a blade extensometer with a 12 mm gage length.

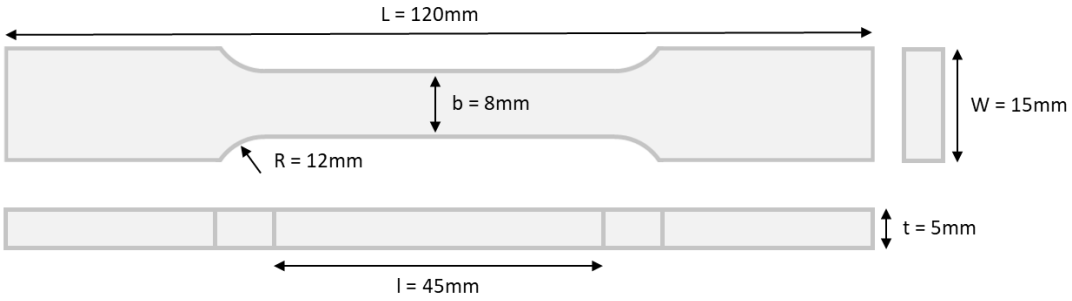

Figure 43: Geometry and dimensions of tensile specimens

The Young's modulus E, the yield stress σ_{YS}, the ultimate tensile stress σ_{UTS}, and the elongation at necking A were determined as shown in Figure 44. The ductility was also characterized more locally by another parameter: the fracture strain ε_f. The fracture strain ε_f is approximated by measuring the ultimate section of the broken specimen A_f and using the following equation:

$$\varepsilon_f = \ln\left(\frac{A_0}{A_f}\right) \times 100 \qquad (17)$$

With A_0 the initial section of the tensile specimen.

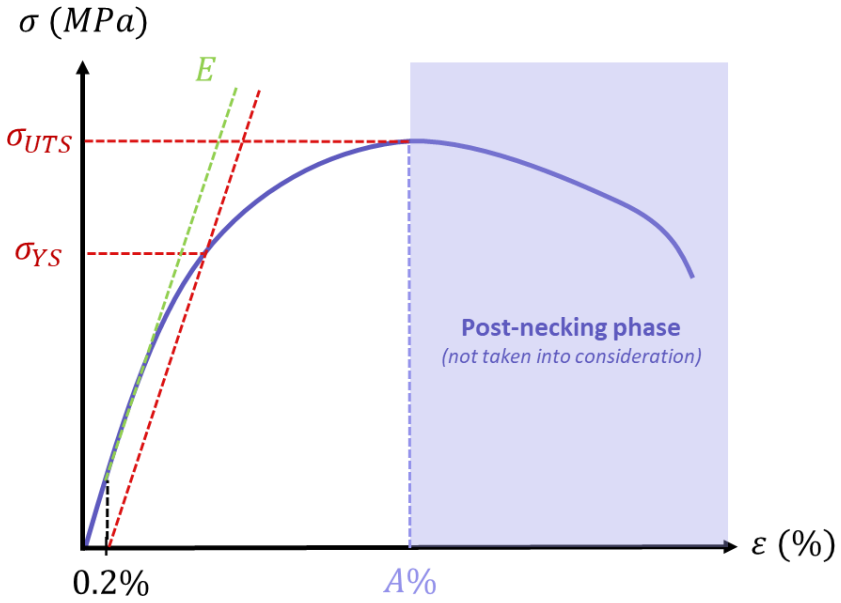

Figure 44: Illustration of tensile parameters identification

Additionally, the Hollomon strain hardening coefficients n_H and k_H were determined from the true stress-true strain curves from the following expression:

$$\sigma_t = k_H {\varepsilon_t}^{n_H} \tag{18}$$

with σ_t and ε_t respectively the true stress and true strain calculated from engineering stress and strain values σ and ε:

$$\sigma_t = \sigma(1+\varepsilon) \tag{19}$$

$$\varepsilon_t = \ln(1+\varepsilon) \tag{20}$$

III.4. Fracture testing

III.4.1. Three-point bending tests

Quasi-static fracture tests were performed using three-point bending specimens, also known as Single-Edge Notched Bending (SENB) specimens (Figure 45a). Samples dimensions and experimental set-up are specified in Figure 45. For fracture toughness estimation, test standard ISO 12135-21 [113], suitable for ductile materials loaded in opening mode I, served

as a guideline for the testing procedure. Tests were carried out using a monotonic loading in a displacement-controlled mode, with a displacement rate of 1 mm/min.

Initial notch was machined by means of EDM, with a thread of 0.25 mm resulting in a width of 0.33 mm. As recommended by test standards [113,114], fatigue pre-cracking was then conducted to obtain the most critical configuration for crack initiation (Figure 45b). Pre-cracking was performed under load control at a frequency of 20 Hz, the highest achievable, with a constant load ratio of R = 0.1. The pre-crack length was approximated on the outer surface of the sample by optical microscope observations, and recalibrated using post-mortem observations. The final initial crack length a_0 is taken as the sum of the notch length and the pre-crack length.

A high-speed monochromic Grasshopper® camera with a 2.3 Mpix resolution was used to perform in-situ monitoring of the crack propagation at the surface. The acquisition frequency was set to 20 Hz. To ease crack tip identification, the specimen surface was painted in white prior to the test, and a high intensity light source was used to increase the image contrast.

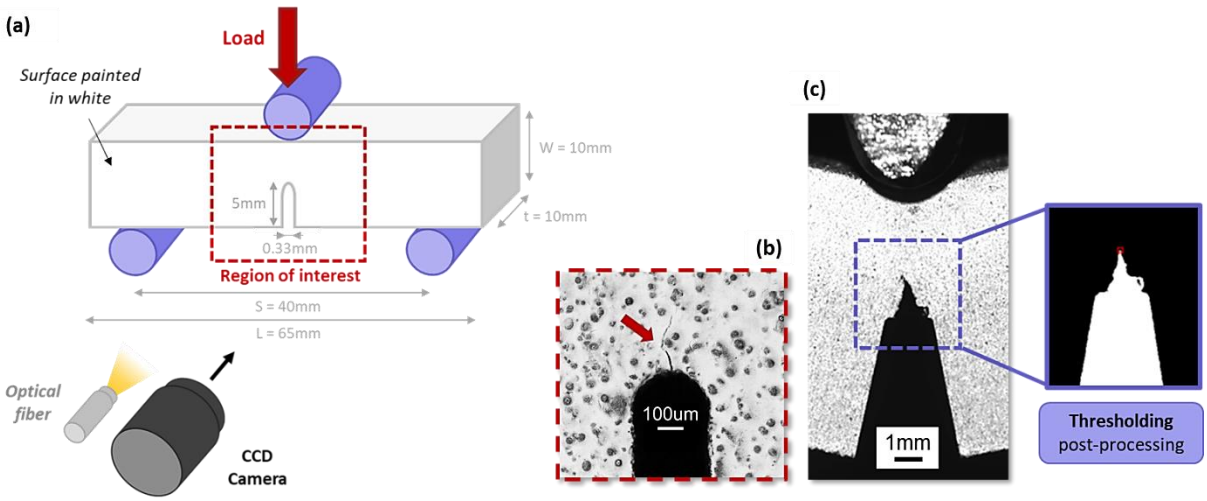

Figure 45: Three-point bending testing
(a) SENB specimen dimensions and experimental set-up
(b) Fatigue pre-crack (c) Post-mortem MATLAB crack monitoring

The test data were then reduced using a custom MATLAB script provided in Appendix A, and the crack path identified by means of a thresholding-based algorithm using the recorded digital images (Figure 45c).

Though the stress state is not homogeneous in the specimen due to the notch and crack propagation, an estimation of the bending strain ε_b and stress σ_b of the specimen was performed using the formulas given by ISO 178 [165] for standard bending tests:

$$\varepsilon_b = \frac{6W}{S^2} \tag{21}$$

$$\sigma_b = \frac{3FS}{2Wt^2} \tag{22}$$

where W is the specimen height, S the distance between the supporting cylinders, and F the applied load. The parameter t, generally corresponding to the specimen thickness, was taken here as the length of the remaining ligament throughout the test. The bending strain ε_b and stress σ_b are considered here to normalize the data and ease the comparison between the different configurations when crack propagation occurs.

Two key parameters were considered to analyze the fracture behavior: the fracture toughness J_{Ic}, and the tearing modulus T. The fracture toughness J_{Ic} characterizes the amount of energy per surface unit needed to initiate a crack, while the tearing modulus T is representative of the energy per surface unit required to propagate the crack. Both are complementary to characterize the plastic fracture behavior.

The fracture toughness value J_{Ic} (also denoted $J_{0.2}$) was calculated assuming that the J-integral value J is the sum of an elastic and a plastic components, both computed iteratively from the experimental data for each time i, according to the following formulas:

$$J = J_{el} + J_{pl} \tag{23}$$

$$J_{el(i)} = \frac{{K_{(i)}}^2(1-\nu^2)}{E} \tag{24}$$

$$J_{pl(i)} = \frac{\eta A_{pl(i)}}{B b_0}\left[1 - \gamma\left(\frac{a_{(i)} - a_{(i-1)}}{b_0}\right)\right] \tag{25}$$

with K the stress intensity factor for a given load, ν = 0.3 the Poisson ratio, E the Young's modulus, η = 1.9 and γ = 0.5 plastic factors specified in ISO 12135-21 [113] for SENB

specimens. A_{pl} corresponds to the area under the load-plastic displacement curve. B is the specimen thickness, a the crack length, and $b_0 = W - a_0$ the initial unbroken ligament length. The critical J-integral value $J_{0.2}$ (J_{Ic}), corresponding to the fracture toughness at crack initiation, was estimated using the compliance method described in ISO 12135-21 standard [113]. The method implemented corresponds to the case where no experimental compliance could be evaluated. No valid $J_{0.2}$ value could be determined from the resistance curve $J - \Delta a$ using the standard criteria provided by both ISO 12135-21 ($J_{0.2} = 3.75\sigma_{UTS}(\Delta a - 0.2)$) [113] and ASTM E1820 ($J_{0.2} = 2\times0.5(\sigma_{YS} + \sigma_{UTS})(\Delta a - 0.2)$) [114]. Data could not be fitted properly during the blunting phase, leading to significant overestimation of the fracture toughness. To get more representative values, linear regression of the blunting phases was carried out on all resistance curves $J - \Delta a$, and the mean value for each manufacturing configuration was taken to determine $J_{0.2}$ (J_{Ic}) values. The fracture properties are illustrated in Figure 46.

When test standard ISO 12135-21 [113] is considered for fracture testing, the $J_{0.2}$ value estimated is usually considered as valid if it does not exceed a value J_{limit} defined as follows:

$$J_{limit} = min(B, b_0, a_0)\frac{\sigma_Y}{10} \tag{26}$$

with σ_Y the flow stress, taken as the average of the yield stress and the ultimate tensile stress. This value ensures that the size of the Irwin plastic zone remains small enough compared to the specimen size. In the present work, J_{limit} is always reached as specimen dimensions are known as too small to comply with the plane strain conditions imposed by test standard ISO 12135-21 [113]. Therefore, it is important to note that the $J_{0.2}$ values presented in this study are used only for comparison purposes, and not as design values.

The tearing modulus T [166] was also computed to better quantify the resistance to crack propagation:

$$T = \frac{E}{{\sigma_{YS}}^2}\frac{dJ}{da} \tag{27}$$

Finally, regarding the validity of crack initiation identification at the surface of the specimen, a heat tint was performed at 550°C for 4h on one specimen in order to observe if any

difference is noted compared to crack initiation at the core of the specimen. The three-point bending test was stopped once crack initiation was spotted at the surface, and fatigue crack propagation was carried out until the specimen was fully broken. Fractographic observations were then conducted to evaluate the gap between the core and the surface of the specimen.

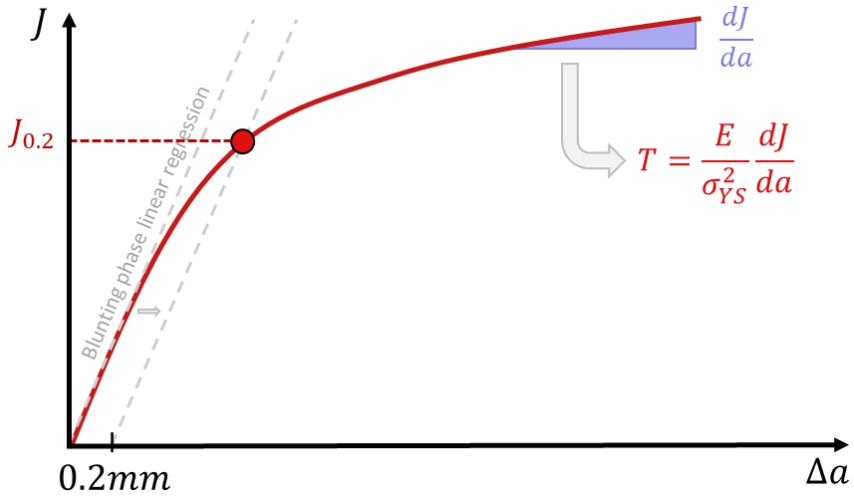

Figure 46: Identification of fracture toughness J_{Ic} $(J_{0.2})$ and tearing modulus T

III.4.2. Impact toughness tests

Many alloys, like Inconel 718 and 316L, are characterized by a time-dependent strain behavior, which result in the mechanical properties varying with the loading rate considered [167–169]. The Ni20Cr alloy studied exhibits a high ductility, which plays a major role in the quasi-static fracture tests mentioned in the previous section. It is hence of utmost interest to analyze the possible influence of the loading rate on the fracture behavior, considering that higher loading rates may reduce plastic deformation at the crack tip. From an industrial standpoint, high loading rate tests like impact tests are commonly used, as experiments are easier, faster and less expensive to conduct than quasi-static fracture tests [170].

Therefore it seems relevant to characterize the influence of the time-dependent behavior on the fracture properties of L-PBF Ni20Cr. Charpy tests were carried out using an instrumented Testwell PW 30/15 impact test machine with a 300 J capacity, shown in Figure 47a and b. Specimens considered were identical to quasi-static fracture specimens (Figure 47c), and were also pre-cracked in fatigue to get similar initial conditions. At least 5

specimens were tested for each configuration. The start angle θ considered was 54°, and the potential energy can be calculated using the following equation:

$$E_p = mgL(1 - cos\theta) \tag{28}$$

With m the mass of the hammer (13 kg), g the gravity acceleration (9.80665 m/s²), and L the length of the pendulum arm (0.8 m). In the present case, the initial potential energy E_p for an initial angle of θ = 54° is 42 J.

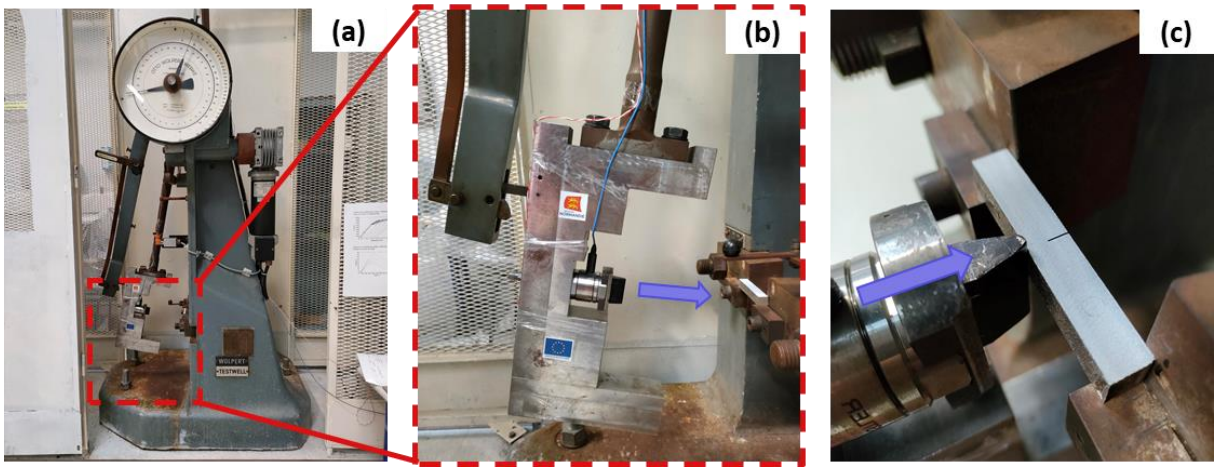

Figure 47: Impact test apparatus
(a) Charpy pendulum hammer (b) Zoom on the instrumented hammer
(c) Striker and three-point bending specimen
(The blue arrow indicates the direction of the impact)

Due to significant oscillations induced during impact tests, data from the load-displacement curves were filtered using the moving average method as recommended in [171]. Three parameters were identified from the impact tests: the load corresponding to the start of the plastic behavior F_{gy}, the maximum load F_{max} and the corresponding maximum displacement d_{max}. Both F_{max} and d_{max} are associated with the crack initiation. It is important to note that the crack initiation time is not precisely determined, due to data smoothing as well as difficulties to observe a clear peak value. Therefore, the values obtained should only be considered as a first approximation.

The area under the load-displacement curve represents the total fracture energy, denoted KV. It can be decomposed as follows:

$$KV = KV_i + KV_p \tag{29}$$

With KV_i the energy associated with the crack initiation (calculated between $d = 0$ and $d = d_{max}$), and KV_p the energy corresponding to the crack propagation (calculated between $d = d_{max}$ and the end of the test)

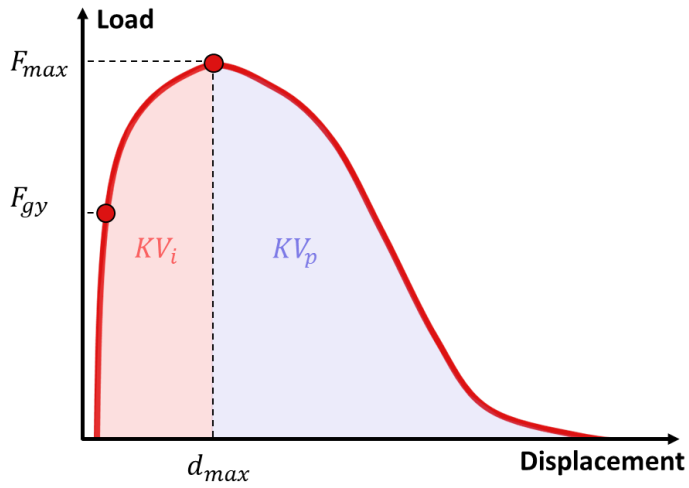

Figure 48: Illustration of the Charpy test parameters identification

In addition, dynamic J-R resistance curves were determined from experimental data, using the method proposed by [171], and further applied on different alloys [130,172]. The principle relies on the compliance changing rate $\Delta C/C_{el}$, calculated as follows:

$$\frac{\Delta C}{C_{el}} = \frac{C - C_{el}}{C_{el}} \tag{30}$$

with C the compliance, defined as the inverse of the slope $\Delta d/\Delta F$ calculated between the original loading point and any point on the load-displacement curve. C is assumed linear. C_{el} is the initial compliance calculated from the start of the test to F_{gy}. During the test, a noticeable change in compliance changing rate $\Delta C/C_{el}$ occurs and allows to the load associated to crack initiation F_{ini} to be determined, as shown in Figure 49. However in the present study, the slope change was not clear enough to determine the crack initiation precisely. Thus the estimated load

would often slightly exceed F_{max}, which is physically unlikely. Therefore, it was considered that F_{max} is assumed as the load where crack initiation occurs, as defined previously.

The next step of the method consists in fitting the load-displacement data between F_{gy} and F_{max} by the following power law:

$$\frac{FW}{b_0^2} = k\left(\frac{d_{pl}}{W}\right)^m \tag{31}$$

$$d_{pl} = d - C_{el}F \tag{32}$$

where W and b_0 are still respectively the specimen height and initial ligament length, and F the load. k and m are fitting parameters, and d_{pl} is the plastic displacement calculated from the displacement d, the load F and the elastic compliance C_{el} as shown above.

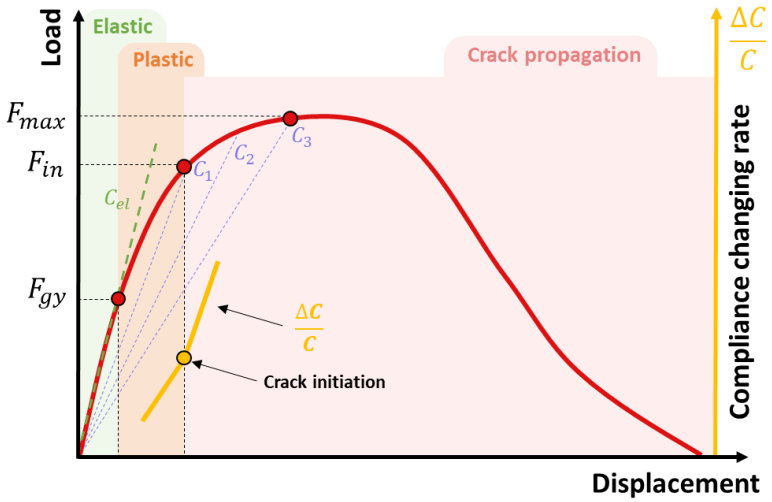

Figure 49: Parameter identification with the compliance changing rate method (adapted from** [130]**)

Once the power law constants k and m are determined, they are used to extrapolate the ligament values b from the load-displacement curve. The crack extension values Δa are then derived from b, as detailed in the following equations:

$$\frac{FW}{b^2} = k\left(\frac{d_{pl}}{W}\right)^m \tag{33}$$

$$b = \sqrt{\frac{FW^{m+1}}{k(d_{pl})^m}} \tag{34}$$

$$\Delta a = b_0 - b = b_0 - \sqrt{\frac{FW^{m+1}}{k(d_{pl})^m}} \tag{35}$$

The dynamic fracture toughness can then be determined from the relationship proposed by Rice et al. [173] for pure bending, corrected with the Garwood's formula [174]:

$$J_i = J_{i-1}\frac{W - a_i}{W - a_{i-1}} + \frac{2U_i}{B(W - a_{i-1})} \tag{36}$$

with U_i the area under the experiment load-displacement curve between d_i and d_{i-1}. The dynamic fracture toughness, denoted J_d, is taken as the value corresponding to the load F_{max} where crack is initiated.

III.4.3. Microbending tests

Given the key role of the interfaces between the different microstructural features (meltpool boundaries, grain boundaries, dendrite walls, nano-oxides/matrix interface…) spread over different scales, miniaturized fracture tests were considered as an attempt to assess their individual influence on the fracture behavior. Considering really small specimens, and therefore really small notches, may allow a better investigation of the interfaces observed at really small scales (micro to sub-micro scale), compared to the macro-specimens presenting a 0.33 mm wide initial notch. The tests presented in this section have been carried out in collaboration with a research engineer from the GPM laboratory, Ronan HENRY.

Bending tests were carried out on micro-cantilever specimens, machined by means of a FIB (Focused Ion Beam) with notched rectangular cross-section. Two ranges of beams were prepared as shown in Figure 50: the 'small' beams, machined using a Gallium FIB (Helios 5UX, ThermoFisher Scientific) with $B{\times}W{\times}L$ dimensions of approximately 20µm×4µm×4µm (Figure 50a and b), and 'large' beams prepared with a plasma FIB (Helios5 PFIB CXe, ThermoFisher Scientific) with $B{\times}W{\times}L$ dimensions of approximately 100µm×30µm×30µm

(Figure 50c and d). As achieving a high machining precision at such small scales is a complex matter, all dimensions obtained are detailed in Table 6.

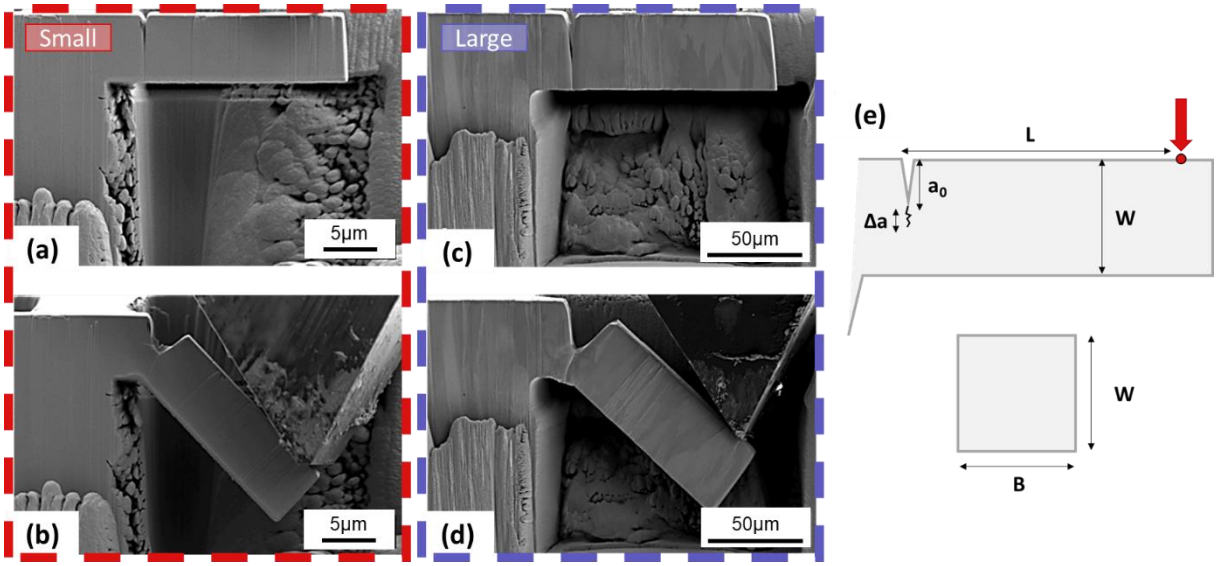

Figure 50: Test specimens before and after loading
(a, b) Small single bending specimens (c, d) Large single bending specimens
(e) Micro-cantilever specimen dimensions

Table 6: Dimensions of the micro-cantilever specimens obtained

	Small cantilevers				Large cantilevers				
	S1	**S2**	**S3**	**S4**	**L1**	**L2**	**L3**	**L4**	**L5**
***L* (µm)**	28.0	9.2	14.9	16.0	95	84	90	94	94
***B* (µm)**	5.0	3.5	2.8	3.3	22	17	29	35	34
***W* (µm)**	4.3	3.9	5.5	5.7	30	30	39	38	41
a_0 (µm)	1.6	1.0	1.8	1.8	12.5	14.0	22.2	22.2	21.2

The specimens were loaded in-situ by means of a SEM (XB540, Zeiss), combined with a nano-indentation system with a wedge tip (PI87R, Brucker). Tests were conducted in displacement-controlled mode, at a rate chosen to correspond to a bending strain rate $\dot{\varepsilon}$ of around 0.0005 s^{-1}, standard for microbending tests, and calculated as follows:

$$\dot{\varepsilon} = 1.5\,\frac{dW}{L^2} \tag{37}$$

In order to monitor the crack propagation directly, the specimen was placed in front of the SEM column. A video of the test provided a continuous monitoring, but with poor image

resolution. Therefore, a three-phase step load was considered instead (Figure 51): the first phase consisted in a 3s loading step, the second one by a 10s plateau where displacement was kept constant, and the last was a 3s partial unloading set at 50% of the displacement of the first step (Figure 51a).

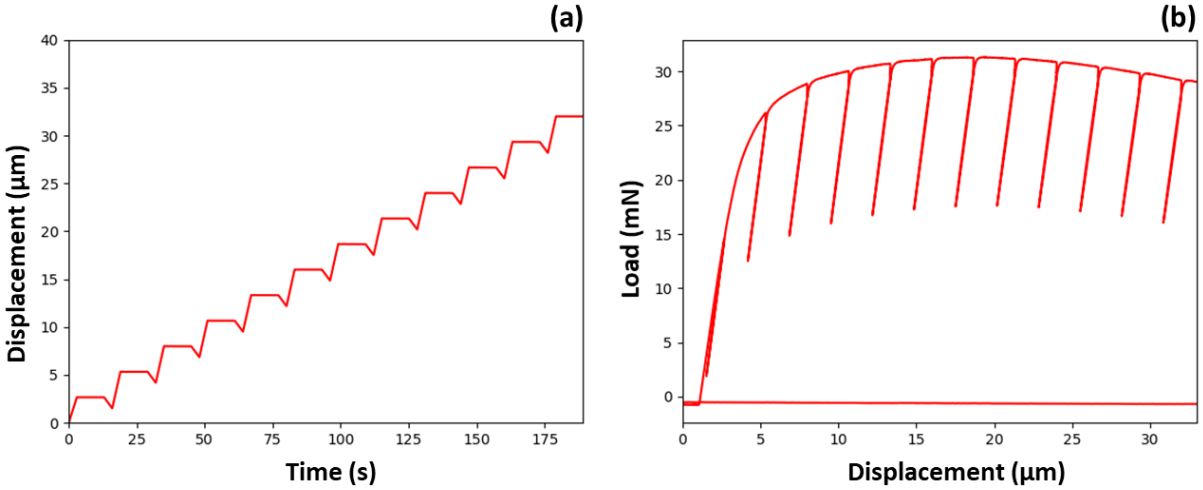

Figure 51: Experimental curves from microbending tests

(a) Example of applied load during specimen bending (b) Example of force-displacement curve obtained during a micro-cantilever bending, with partial discharges clearly visible.

During every 10s plateaus, a good-resolution SEM image was taken using a secondary electron sensor, an electron acceleration voltage of 5 kV, and an integrating noise reduction mode, with an acquisition time of around 8s per image. The field of view encompassed the entire specimen to observe the onset of wedge tip slippage during bending. Partial unloadings were used to estimate specimen stiffness (Figure 51b). Thus, the data associated with the unloadings were extracted, and a linear regression was performed on these portions of the load-displacement curve; the compliances k_i (in N/m) were thus calculated for each unloading i. Force and displacement data were measured continuously, unlike the compliance k and the crack extension Δa. Hence, load and displacement data were reduced to one point per step, with force and displacement values taken in the middle of each step.

III.5. Microstructural and fractographic analyses

The initial microstructure of the specimens was characterized using a Keyence VHX-5000 optical digital microscope, and a JEOL 79000F Scanning Electron Microscope (SEM) coupled with Electron BackScattered Diffraction (EBSD). Both the plane parallel (XZ) and

perpendicular (XY) to the building direction (XZ) were observed to characterize a possible anisotropy, as shown Figure 52.

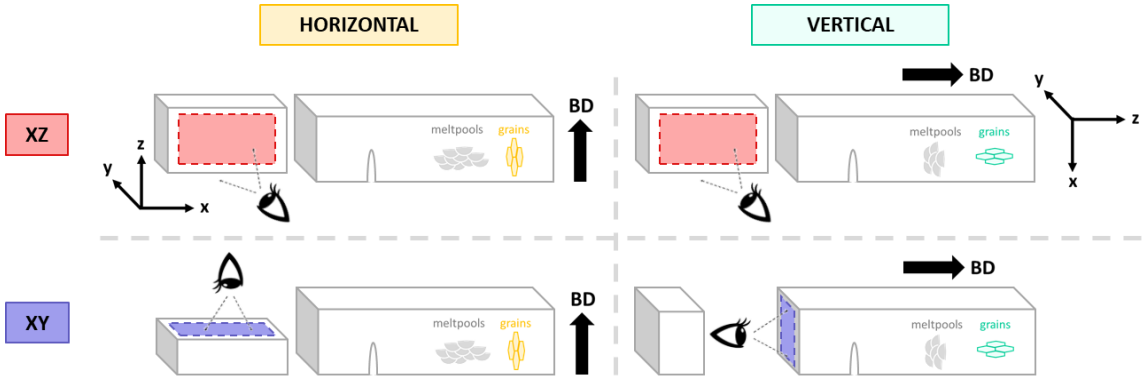

Figure 52: Planes of interest for microstructural characterization

For SEM-EBSD analyses, specimens were mechanically polished using SiC paper up to 2400 grit grades, and then colloidal diamond solutions (6 to 1/4 µm grades). The surface preparation was finalized using a colloidal silica suspension (OP-U) to obtain optimal surface quality. Steps of 0.7 and 2 µm were considered for EBSD acquisitions, and all data were processed using EDAX OIM software to obtain Inverse Pole Figures (IPF) and Pole Figures (PF). The detection limit for grain boundaries is set at 15°, and the grain size is taken as the equivalent diameter computed from the grain area value. Specimens were then etched using a Struers A2 electrolyte at 10 V for 5s to allow meltpools and dendrites observation.

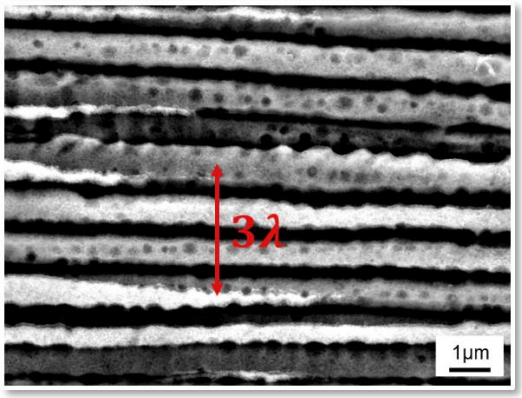

Figure 53: Determination of the interdendritic arm spacing distance using SEM images

The interdendritic arm spacing λ was measured using images of dendrites parallel to the observation plane, by plotting a line perpendicularly to the dendrites' growth direction, as

shown in Figure 53. The distance measured was divided by the number of interdendritic spaces observed.

Additionally, a few specimens were broken after fracture testing to visualize the crack propagation at the core. Specimens surface were also examined, and the plastic deformation was characterized using the optical microscope profilometry tool to quantify their magnitude.

CHAPTER 3:
Influence of the manufacturing strategy on the initial microstructure and tensile behavior

This third chapter presents the initial characterizations (density, microhardness tests, microstructure…) and the tensile behavior resulting from the various manufacturing conditions. The influence of the different processing parameters is discussed, as well as the relationship between the microstructure and mechanical properties observed.

I. Initial characterization

I.1.1. Density and porosity analysis

The results from density measurements and porosity analysis are displayed in Table 7. For L-PBF specimens, both methods show little to no difference between the different manufacturing strategies. Only the H9067 configuration exhibits a higher surface porosity than other printing configurations, due to an isolated more porous section. However, porosity values remain low overall, and literature results also indicate that no significant difference should be induced by the building orientation [85,93,175] or rotation angle [24] in terms of porosity content, for the given VEDs [37]. All density values obtained for L-PBF specimens are close to bulk Ni20Cr density, usually ranging between 8.3 to 8.5 g/cm^3 according to ANSYS Granta Materials database. Cast & wrought specimens on the other hand exhibit lower density values, but are proven as dense as L-PBF specimen by porosity analysis. This result can be explained by the difference in chemical composition already noted in Chapter 2 (p. 46), which influences the specimen's density.

Table 7: Specimens estimated volumetric masses (density) and porosity

	H9067	**V9067**	**H9090**	**V9090**	**H6067**	**V6067**	**C&W**
Density (g/cm^3)	8.38 (±0.01)	8.38 (±0.02)	8.41 (±0.02)	8.37 (±0.01)	8.39 (±0.01)	8.40 (±0.01)	8.35 (±0.01)
Porosity (%)	0.21 (±0.32)	0.02 (±0.01)	0.02 (±0.02)	0.03 (±0.03)	0.02 (±0.01)	0.03 (±0.02)	0.02 (±0.01)

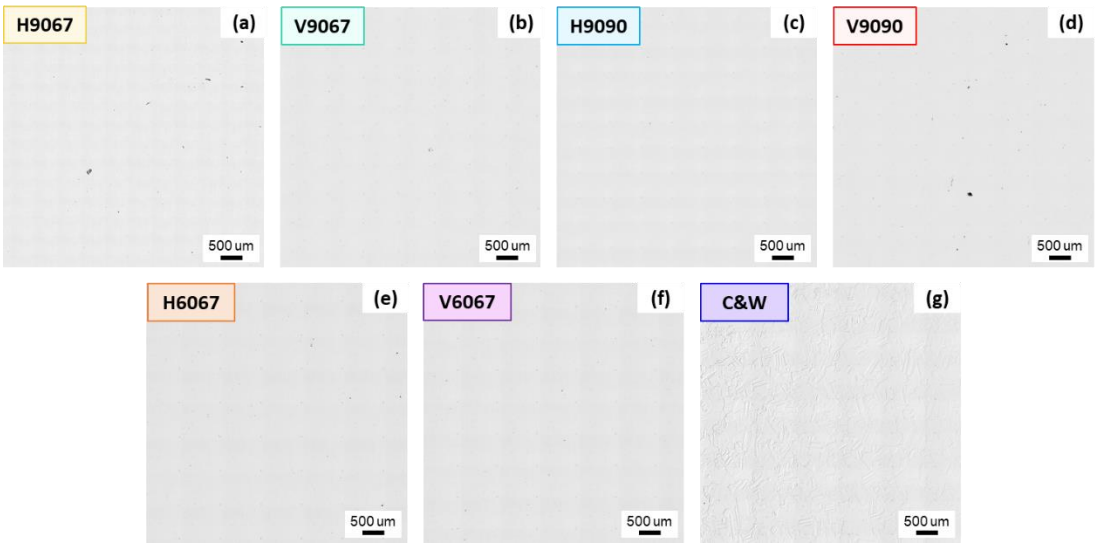

Figure 54: Optical microscope observations of pores (10mm×10mm section)
(a) H9067 (b) V9067 (c) H9090 (d) V9090 (e) H6067 (f) V6067 (g) C&W

I.1.2. Microhardness tests

Figure 55 and Table 8 respectively show the microhardness maps and values of all the specimens obtained for the different manufacturing configurations. As detailed in Chapter 2, three sections were considered in order to be representative: two transversal sections (one at the top and one at the bottom, in red) of 10mm×10mm, and one longitudinal section (in blue) of roughly 55mm×10mm.

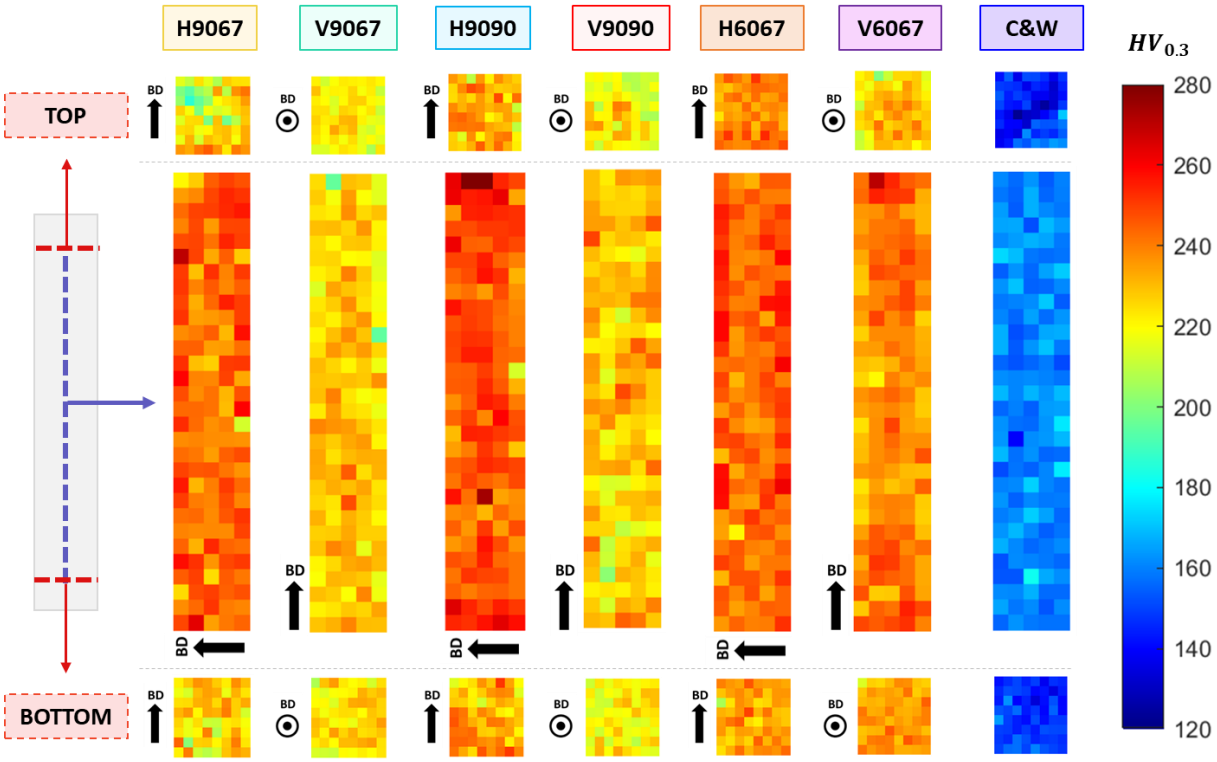

Figure 55: Microhardness maps for each manufacturing configuration at the bottom, in the middle and at the top of the specimens
(The Building Direction (BD) is systematically indicated by an arrow)

Table 8: Microhardness values for each configuration
(at the bottom, in the middle and at the top of the specimens)

	H9067	V9067	H9090	V9090	H6067	V6067	C&W
Top ($HV_{0.3}$)	221 (±13)	221 (±5)	232 (±9)	220 (±8)	239 (±6)	227 (±8)	145 (±10)
Middle ($HV_{0.3}$)	244 (±8)	227 (±7)	248 (±10)	229 (±8)	245 (±7)	239 (±8)	160 (±6)
Bottom ($HV_{0.3}$)	226 (±9)	224 (±7)	233 (±9)	221 (±6)	234 (±7)	235 (±4)	148 (±6)

All specimens display microhardness variations due the known microstructure inhomogeneity, and the variation of the amplitudes are similar for all. No noticeable difference is observed between the bottom and the top surfaces, indicating an absence of gradient along the building direction regardless of the manufacturing conditions. Therefore, no matter the location taken for microstructural analysis, most sections observed can be considered representative of the specimen.

As it is the largest and contains more indents, the middle-section (in blue) is considered as the most representative one to discuss the differences between the manufacturing conditions. As shown in Figure 55, the lowest microhardness values among L-PBF specimens are obtained for the V9067 and V9090 configurations with around 230 $HV_{0.3}$. The highest are observed for the H6067, H9067, and H9090 configurations, with 245-250 $HV_{0.3}$. Hence specimens with a horizontal building orientation overall display higher microhardness values than vertically built specimens. This result was already reported in the literature [86,176–178] and attributed to the different thermal history between horizontal and vertical building orientation. Depending on the specimen geometry considered, one may induce finer or bigger microstructures, and therefore impact microhardness values.

The rotation angle on the other hand does not influence the microhardness values, with similar values for both horizontal specimens (H9067, H9090) and vertical specimens (V9067, V9090). The same result was observed with the VED for horizontal specimens (H9067, H6067), however a slight increase was noted for vertical specimen with a VED of 60 J/mm^3 (239 $HV_{0.3}$) compared to 90 J/mm^3 (227 $HV_{0.3}$).

Finally regarding cast & wrought specimens, microhardness values are much below L-PBF specimens, with 160 $HV_{0.3}$. This can be explained by the significant difference in microstructure between both manufacturing strategies that has been discussed in Chapter 1, and will be further discussed in the following sections.

I.1.3. As-built microstructures

As-built L-PBF microstructures are known to be complex and spread over several scales (Chapter 1), hence this section focuses on offering an overview of each of them: the macro/mesoscale (the meltpools), the meso/microscale (the grains) and the sub-micro/nanoscale (dendrites/nano-oxides). In order to cover the microstructure inhomogeneity, two planes are observed as well: the plane parallel to the building direction (denoted XZ), and the plane perpendicular to the building direction (denoted XY). The objective is to characterize every possible interface that could act as a weak bond and influence the crack path, and overall fracture behavior.

I.1.3.1. Macro/mesoscale (meltpools)

Figure 56 presents optical microscope images of the meltpools along the XZ plane for all the manufacturing conditions. A more in-depth characterization was already performed for V9067 and V6067 configurations in previous studies [37,179] by considering a single scan track to obtain accurately the width and depth of the resulting meltpools. In the present investigation, only a qualitative approach is considered, by analyzing the overall meltpools morphology between the different configurations. Rough width ranges are also given in Table 9.

Regarding the influence of the processing parameters, the building orientation does not significantly influence the meltpool size and morphology (Figure 56a, b and e, f), except for the H9090 specimens that display narrower meltpools than the V9090 specimens (Figure 56c and d). In contrast, a rotation angle of 90° is associated to both deeper and narrower meltpools compared to one of 67°, as observed in Figure 56a, c and b, d. Regarding the VED, at 60 J/mm^3 slightly narrower and deeper meltpools are induced compared to 90 J/mm^3, even though it appears less impactful than the rotation angle. However comments on the meltpools depth should be taken with caution if based solely on these observations, as the overlapping and successive remelting of the layers may distort the actual depth evolution with respect to the processing parameters. Finally, no meltpools are observed for cast & wrought specimens due to the difference in manufacturing methods, nevertheless Figure 56g allows a size comparison between the visible grains and the meltpools.

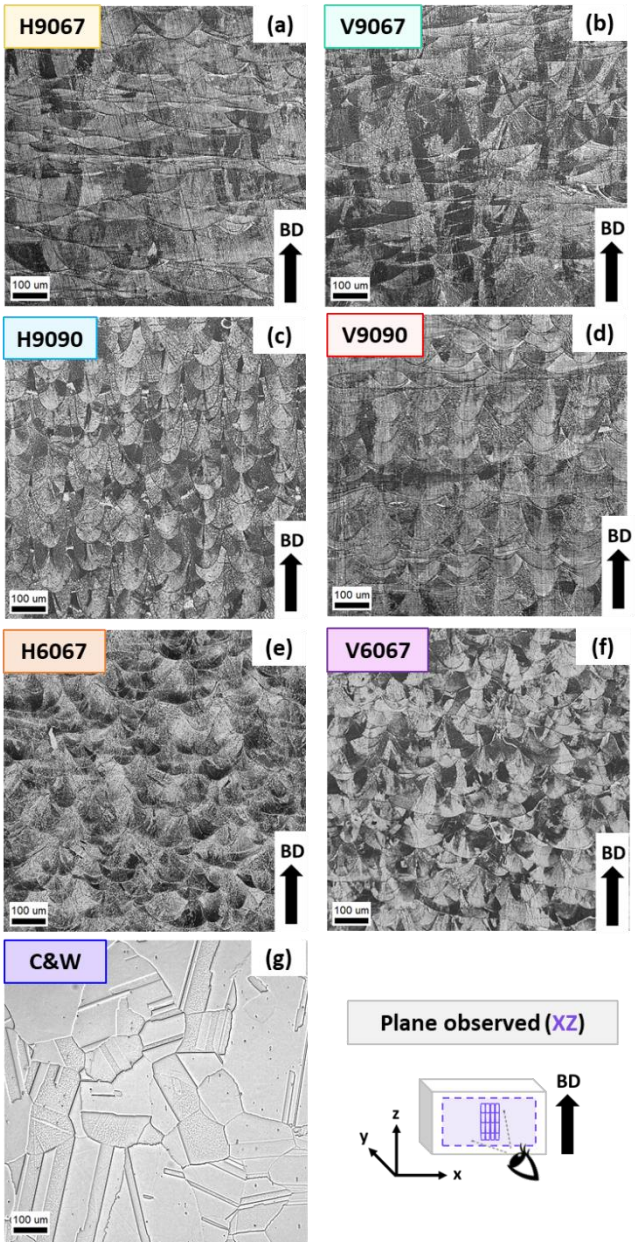

Figure 56: Optical microscope observations of L-PBF and cast & wrought specimens

Meltpools observations for (a) H9067 (b) V9067 (c) H9090 (d) V9090 (e) H6067 (f) V6067 (g) Grains observations for C&W

Table 9: Influence of the manufacturing parameters on the meltpools width

	H9067	V9067	H9090	V9090	H6067	V6067
Meltpools width range (µm) (XZ plane)	50-350	50-350	50-130	50-200	50-180	50-200

The same investigation on the meltpools morphology was conducted on the XY plane, and is shown in Figure 57. For this plane, no estimation of the bead width could be obtained, as poor etching quality for some manufacturing conditions made the comparison more difficult and less reliable. No significant difference is visible regarding the influence of the building orientation, except for Figure 57c and d: the rotation of 90° between the top layer and the previous layer is clearly visible for the H9090 specimen, whereas the presence of the previous layer is almost completely erased for the V9090 specimen. The bead width does not seem noticeably impacted by the rotation angle (Figure 57a, c and b, d), however a notable decrease is observed for a lower VED (Figure 57a, e and b, f).

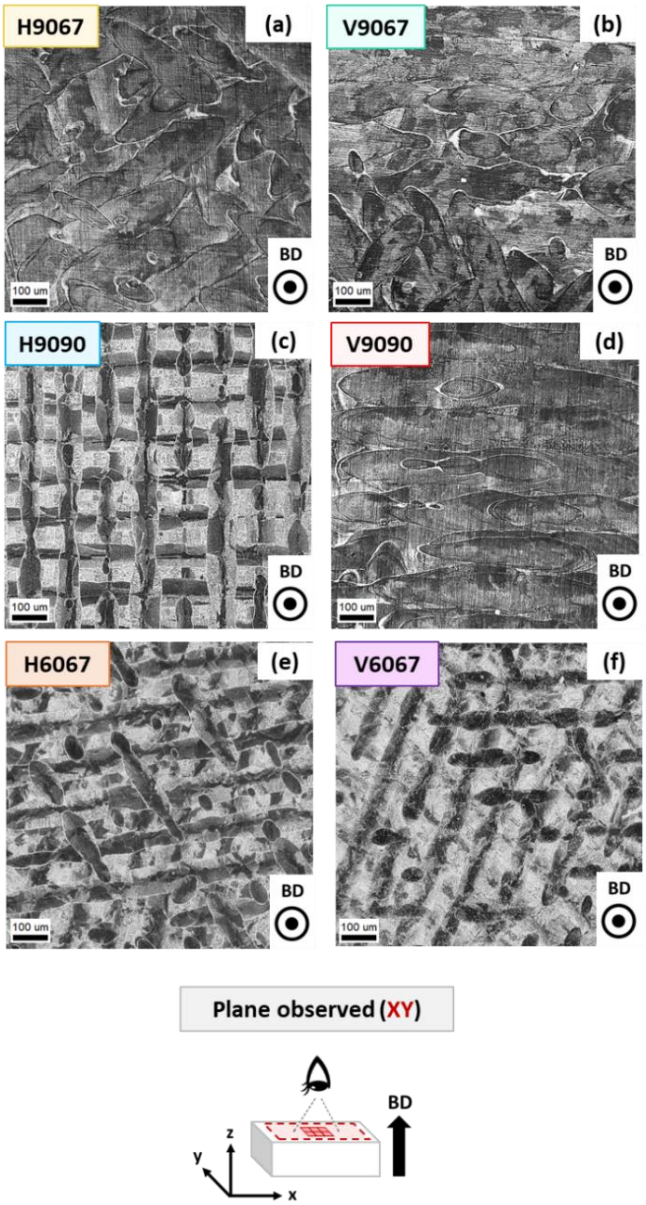

Figure 57: Optical microscope observations of meltpools (XY plane)
(a) H9067 (b) V9067 (c) H9090 (d) V9090 (e) H6067 (f) V6067

I.1.3.2. Meso/microscale (grains)

The SEM-EBSD observations conducted are first presented for the XZ plane: IPF and PF maps are shown in Figure 58, and the grain sizes are given in Table 10. L-PBF specimens are characterized by columnar grains oriented parallel to the building direction, and very heterogeneous grain sizes (Figure 58 and Table 10). Two parameters influence the most the grain morphology in the current study: the VED and the rotation angle. A higher VED (90 J/mm^3) promotes a more columnar microstructure compared to a lower one (60 J/mm^3) (Figure 58a, e and b, f), whereas a rotation angle of 90° results in more unidirectional and organized grain morphology than one of 67° (Figure 58a, c and b, d). The building direction only affects the grain size (taken as the equivalent diameter calculated from grains area) for a VED of 90 J/mm^3, with on average bigger grains for the vertical specimens (220-230 µm) and finer ones for the horizontal ones (120-130 µm). At 60 J/mm^3, no difference is observed between the two, with really fine grains for both (60-70 µm). The grain size is overall really heterogeneous, with a high number fraction of really small grains, but a high area fraction of bigger grains (Table 10).

Regarding the crystallographic texture, the building orientation seems to hold a noticeable influence at a VED of 90 J/mm^3, with more pronounced crystallographic texture noted for vertically built specimens (Figure 58a, b and c, d). The maximal intensity ranges between 5 to 10 M.R.D (Multiple Random Distribution) for a vertical orientation, and remains below 5 for a horizontal one. A rotation angle of 67° tends to erase any preferential orientation, with a lower crystallographic texture compared to an angle of 90° (Figure 58b and d). Vertical configurations both display hints of clear preferential orientations that should be further confirmed with the XY plane observations: for V9067, both ⟨001⟩ and ⟨110⟩ directions are emerging from the Pole Figures (Figure 58b), whereas for V9090, only ⟨001⟩ is clearly visible along the building direction (Figure 58d). Regarding both H9067 and H9090, no defined texture can be identified. For a VED of 60 J/mm^3, no significant difference is noted between the two building orientations (Figure 58e and f), as well as no distinct crystallographic texture. The maximum intensity was the lowest obtained, at 2 to 3 M.R.D.

Finally, when compared to L-PBF specimens, cast & wrought specimens display a totally different microstructure with equiaxed grains, and several annealing twins, as shown in Figure 58g. Significant grain size is observed with an average of 155 µm (Table 10), as well as a relatively high annealing texture at approximately 7 M.R.D.

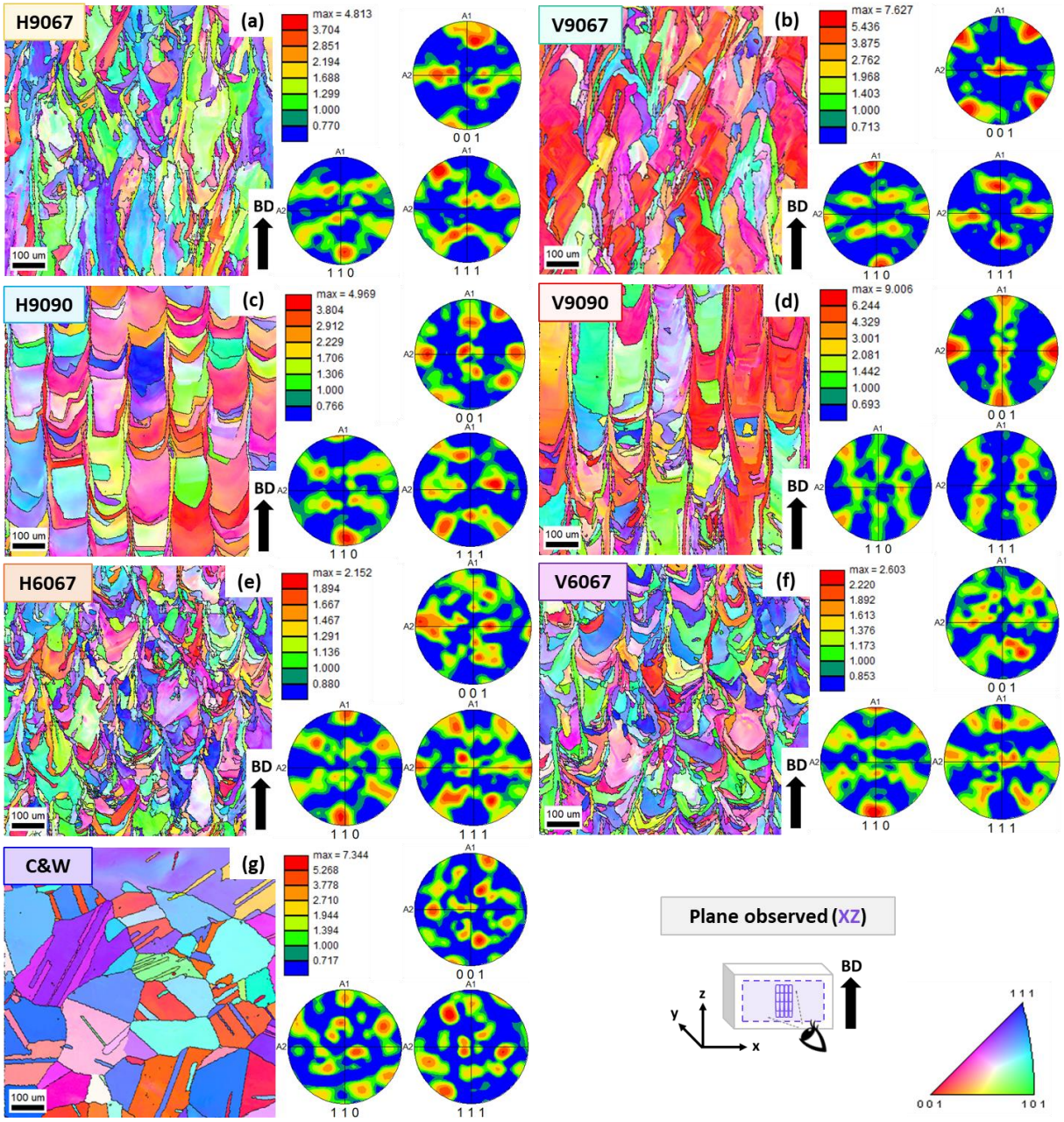

Figure 58: SEM-EBSD Inverse Pole Figures (IPF) and Pole Figures (PF) (XZ plane)
(a) H9067 (b) V9067 (c) H9090 (d) V9090 (e) H6067 (f) V6067 (g) C&W

Table 10: Grain size (area and number fractions) for all the manufacturing conditions (XZ plane)

		H9067	V9067	H9090	V9090	H6067	V6067	C&W
Grain size (µm) (diameter)	Area fraction	124 (±70)	232 (±156)	132 (±69)	219 (±131)	63 (±34)	67 (±37)	155 (±87)
	Number fraction	29 (±34)	30 (±46)	44 (±46)	28 (±45)	22 (±20)	23 (±22)	46 (±51)

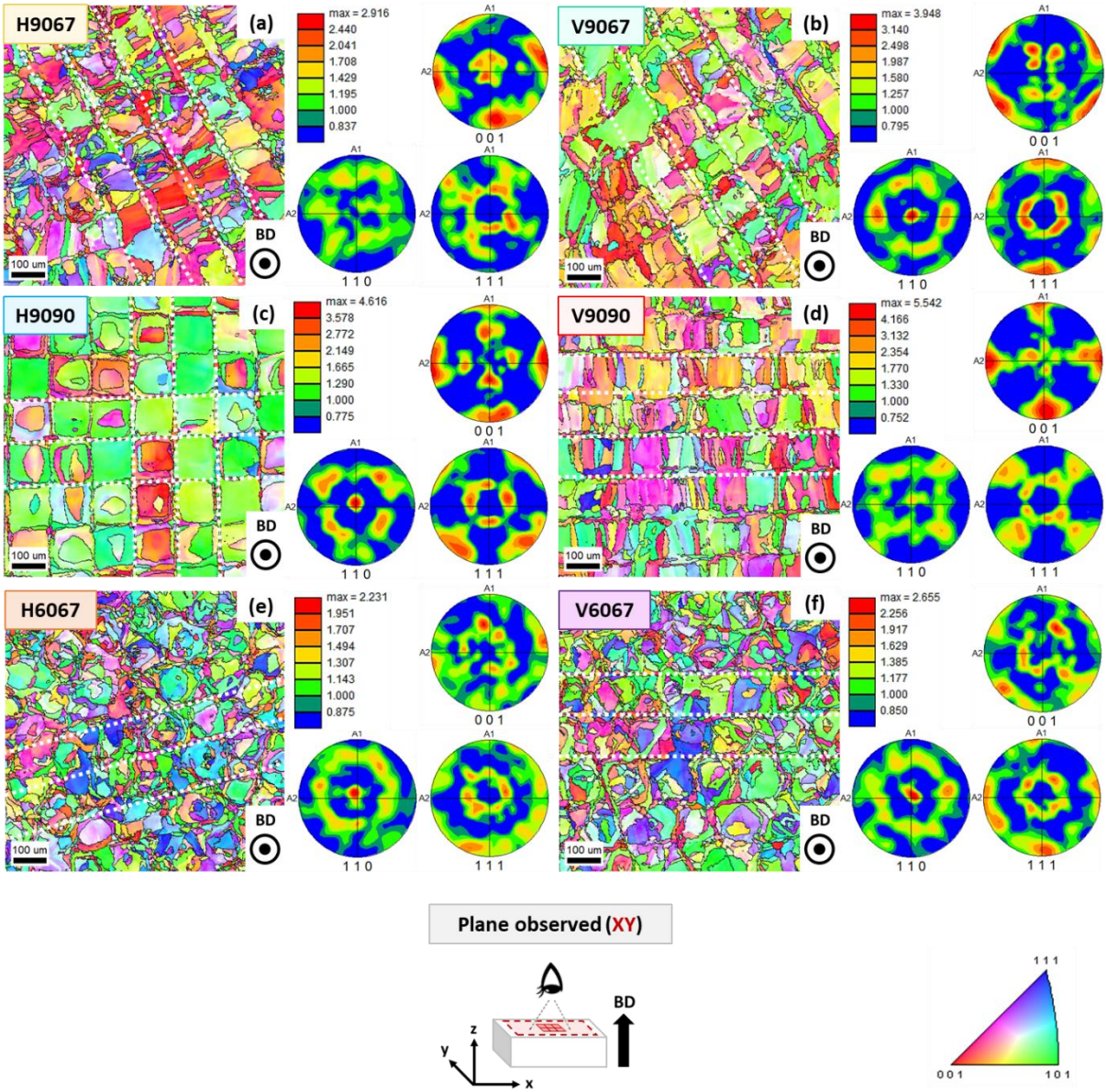

Figure 59: SEM-EBSD Inverse Pole Figures (IPF) and Pole Figures (PF) (XY plane)
(a) H9067 (b) V9067 (c) H9090 (d) V9090 (e) H6067 (f) V6067
(Meltpools' borders are highlighted by the white dotted lines)

Table 11: Grain size (area and number fractions) for all the manufacturing conditions (XY plane)

		H9067	V9067	H9090	V9090	H6067	V6067
Grain size (µm) (diameter)	Area fraction	62 (±45)	112 (±83)	102 (±56)	108 (±77)	47 (±30)	51 (±28)
	Number fraction	18 (±17)	24 (±28)	26 (±30)	24 (±27)	18 (±15)	20 (±17)

The same microstructural analysis was conducted on the XY plane: associated IPF and PF maps are shown in Figure 59, and the grain sizes are given in Table 11. As discussed, the grains morphology and size is much different from the one observed on the XZ plane, due to the anisotropic nature of the L-PBF microstructure. The laser beads and the laser direction are easily visible on Figure 59, and highlighted in white.

For this observation plane, two grain morphologies can be observed: the first one for a VED at 90 J/mm^3 (Figure 59a, b, c, and d), with rectangular grains, larger at the center of the meltpool, and smaller at the interfaces between two meltpools. In the case of the H9090 specimens (Figure 59c), both the laser beads from the top layer and the previous layer are visible, giving a square shape to the larger grains. The difference between H9090 and V9090 specimens show the difference in thermal history that both building orientations can generate. For all four configurations (H9067, V9067, H9090, V9090), the grains' growth is perpendicular to the laser direction. The second type of grain morphology is observed at 60 J/mm^3, for which no particular grain shape is noted, as well as no preferential grain growth (Figure 59e and f). Smaller grains are still observed at the border between two meltpools, while the bigger grains remain at the center. Specimens produced with a VED of 90 J/mm^3 present the larger grains, with an average of 100-110 µm (still considering the equivalent diameter calculated from grains area), except for H9067 specimens which present finer grains (~ 60 µm). A VED of 60 J/mm^3 results in an average grain size of 50 µm for both H6067 and V6067 configurations (Table 11). Overall, the VED has the most influence on the grains' size and morphology on the XY plane. The building orientation has little influence on the grain morphology, except for a slight decrease in the grain size. The rotation angle on the other hand impacts noticeably the grain morphology, as an angle 90° result in a more organized grain morphology compared to 67°.

In terms of crystallographic texture, the maximum intensity value does not exceed 5 M.R.D, and is obtained for the V9090 configuration. All other manufacturing conditions fall between 2 to 4 M.R.D, indicating the absence of substantial crystallographic texture on this plane. Considering observations conducted on both XZ and XY planes, V9067 specimens exhibit a GOSS $\{110\}\langle001\rangle$ texture (Figure 58b and Figure 59b), while V9090 is characterized by a cubic texture $\{110\}\langle001\rangle$ (Figure 58d and Figure 59d). Contrary to what was observed for the XZ plane, the crystallographic texture is here not only dependent on the VED and building orientation, but also on the rotation angle.

For this section, no comparison with cast & wrought specimens is made as its microstructure is independent from the plane of observation considered.

I.1.3.3. Sub-micro/nanoscale (dendrites and nano-oxides)

Figure 60 presents the SEM observations performed on all the specimens, in order to analysis both the dendrites and nano-oxides. An estimation of the primary dendrite arm spacing is also given in Table 12.

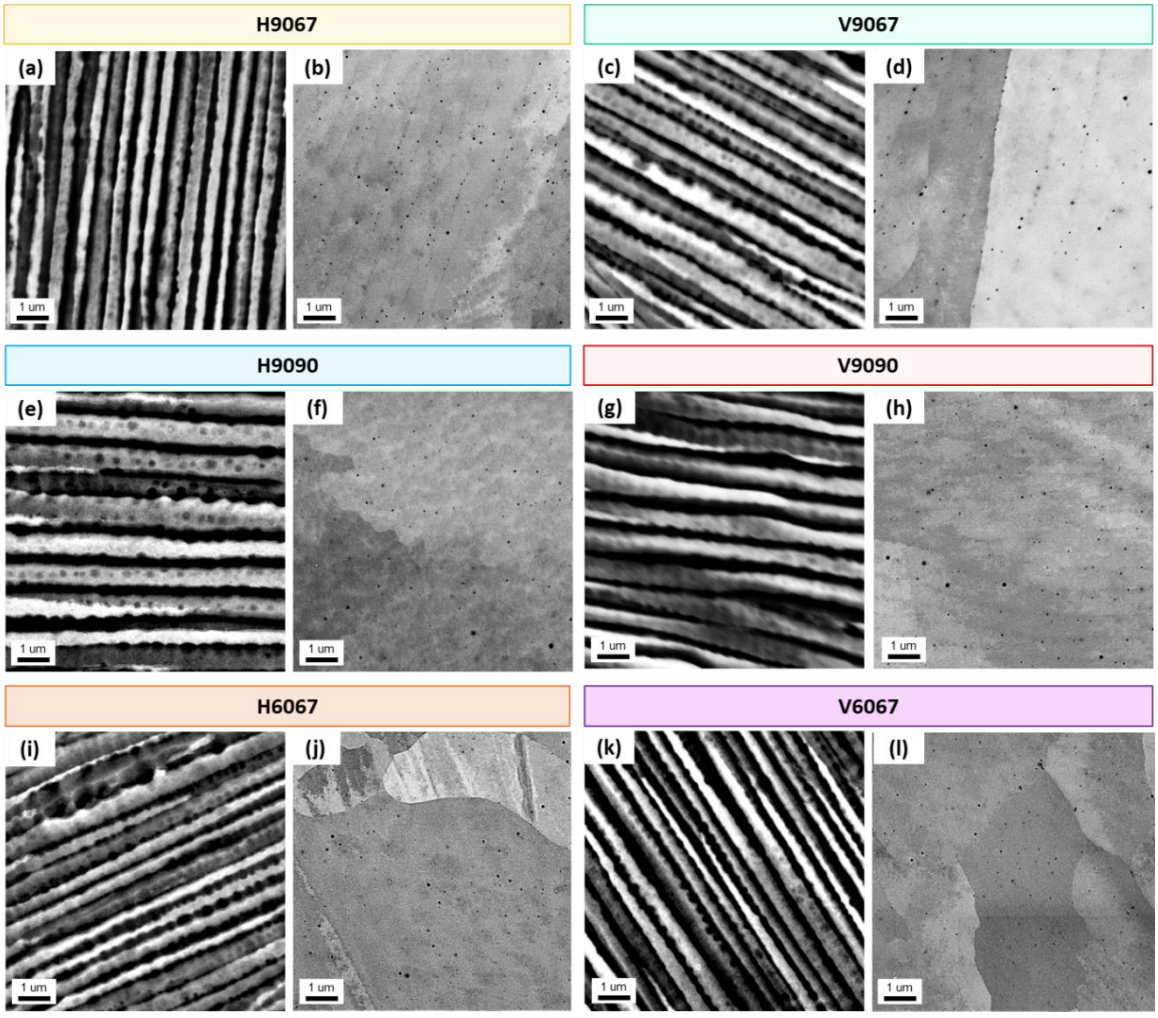

Figure 60: SEM dendrites and nano-oxides observation
(a, b) H9067 (c, d) V9067 (e, f) H9090 (g, h) V9090 (i, j) H6067 (k, l) V6067

Table 12: Influence of the manufacturing parameters on the primary dendrite arm spacing size

	H9067	V9067	H9090	V9090	H6067	V6067
Primary dendrite arm spacing (nm)	587 (±37)	544 (±72)	783 (±245)	853 (±199)	551 (±146)	547 (±176)

The first observations tend to point out the rotation angle as the most influential processing parameter on the dendrites. The average primary dendrite arm spacing goes from

587 nm for H9067 to 783 nm for H9090, and from 544 nm for V9067 to 853 nm for V9090 (Table 12). The heterogeneity is also much higher for an angle of 90° than for one 67° at a VED of 90 J/mm^3, reaching a standard deviation of 200-250 nm for 90° against 40-70 nm for 67°. A set of several dendrites' images illustrating this point are shown in Appendix B. For a 67° angle, a VED of 60 J/mm^3 results in average sizes close to those obtained at 90 J/mm^3, with the exception that the heterogeneity is once again much higher (150-180 nm). However, a previous study demonstrated that the dendrite size usually increases with an increasing VED [159]. For all cases, the building orientation did not play a significant role, except for H9090 that displayed a lower mean value than V9090 specimens. However, given the huge standard deviation obtained, it is of utmost importance to remember that the representativity of the primary dendrite arm spacing sizes presented is limited. Given the scale observed, the number of images taken should be higher to obtain a good statistical approach. This number was limited by both the time available to perform this analysis, and the number of dendrites observed that were oriented parallel to the observation plane.

Regarding the presence of nano-oxides, Figure 60 shows that they were systematically observed, regardless of the manufacturing parameters considered. Different precipitate morphologies were also observed and are shown Appendix B. An extensive analysis of the size and nature of these precipitates was not performed in this study, however it was already demonstrated that they tend to increase in size with an increase in VED [159].

I.2. Conclusion

The first part of this chapter aimed at presenting an initial physical and microstructural characterizations of the specimens for all the manufacturing methods considered in this study.

It was demonstrated that the resulting specimens are dense, and that the microstructures presented are not dependent on the spot considered within the specimen. As expected from the literature review, the anisotropic nature of the L-PBF microstructure was demonstrated through the observation of both the XZ and XY planes. Characteristic lengths were given at the macro/mesoscale (meltpools), meso/microscale (grains) and sub-micro/nanoscale (dendrites and nano-oxides) in order to better identify which one is the most influential during post-mortem observations for both tensile and fracture tests. The anisotropy observed at the different scales of the microstructure also hints at possible anisotropy of the mechanical behavior.

II. Influence of the manufacturing process on tensile properties

The present section aims at characterizing the influence of the processing parameters on the tensile properties of the specimens. Hence, tensile results presented below are centered around one parameter at a time: the building orientation (horizontal or vertical), the rotation angle (90° or 67°), and the VED (60 J/mm^3 or 90 J/mm^3). For each configuration presented, at least five specimens were considered. The continuous lines are the experimental curves, and the dotted lines the mean curves calculated from them. A discussion on the overall results is provided at the end of the chapter.

II.1. Influence of the manufacturing parameters

II.1.1. Building orientation

In order to discuss the influence of the building orientation, Figure 61 presents the three sets of parameters for which two building orientations were tested: A VED of 90 J/mm^3 with a rotation angle of 67° (Figure 61a), a VED of 90 J/mm^3 with an angle of 90° (Figure 61c), and a VED of 60 J/mm^3 with an angle of 67° (Figure 61e). Figure 61b, d and f represent the zoomed-in elastic zone of the tensile test.

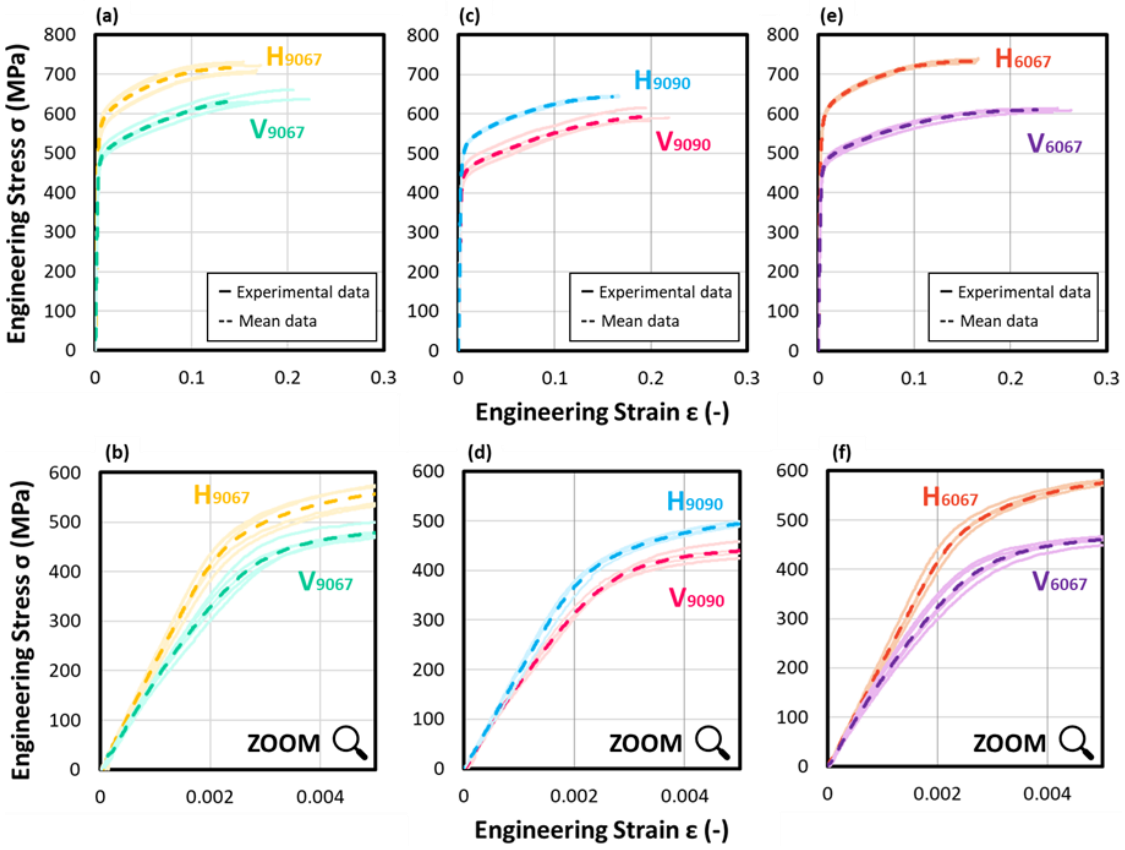

Figure 61: Influence of the building orientation (horizontal and vertical) on the tensile properties *(a, b) VED = 90 J/mm^3 and 67° (c, d) VED = 90 J/mm^3 and 90° (e, f) VED = 60 J/mm^3 and 67°*

Regardless of the set of parameters considered, horizontally built specimens exhibit higher tensile properties (Young's modulus E, yield stress σ_{YS}, and ultimate tensile stress σ_{UTS}) than vertically built specimens. This is a result often encountered in the literature and already discussed in Chapter 1. Vertical specimens also appear overall slightly more ductile than horizontal specimens. Even though the microstructure analyses conducted on both H6067 and V6067 specimens appear fairly identical, the discrepancy between both building orientations seems the most important between them. On the opposite, the tensile properties appear less affected when specimens are built with a VED of 90 J/mm^3 and a rotation angle of 90° (H9090 and V9090 specimens).

II.1.2. Rotation angle

Figure 62 presents the influence of the rotation angle (67° and 90°) on two sets of parameters: specimens oriented horizontally and vertically. The VED is the same in both cases, set at 90 J/mm^3. Figure 62b and d represent the zoomed-in elastic zone of the tensile tests.

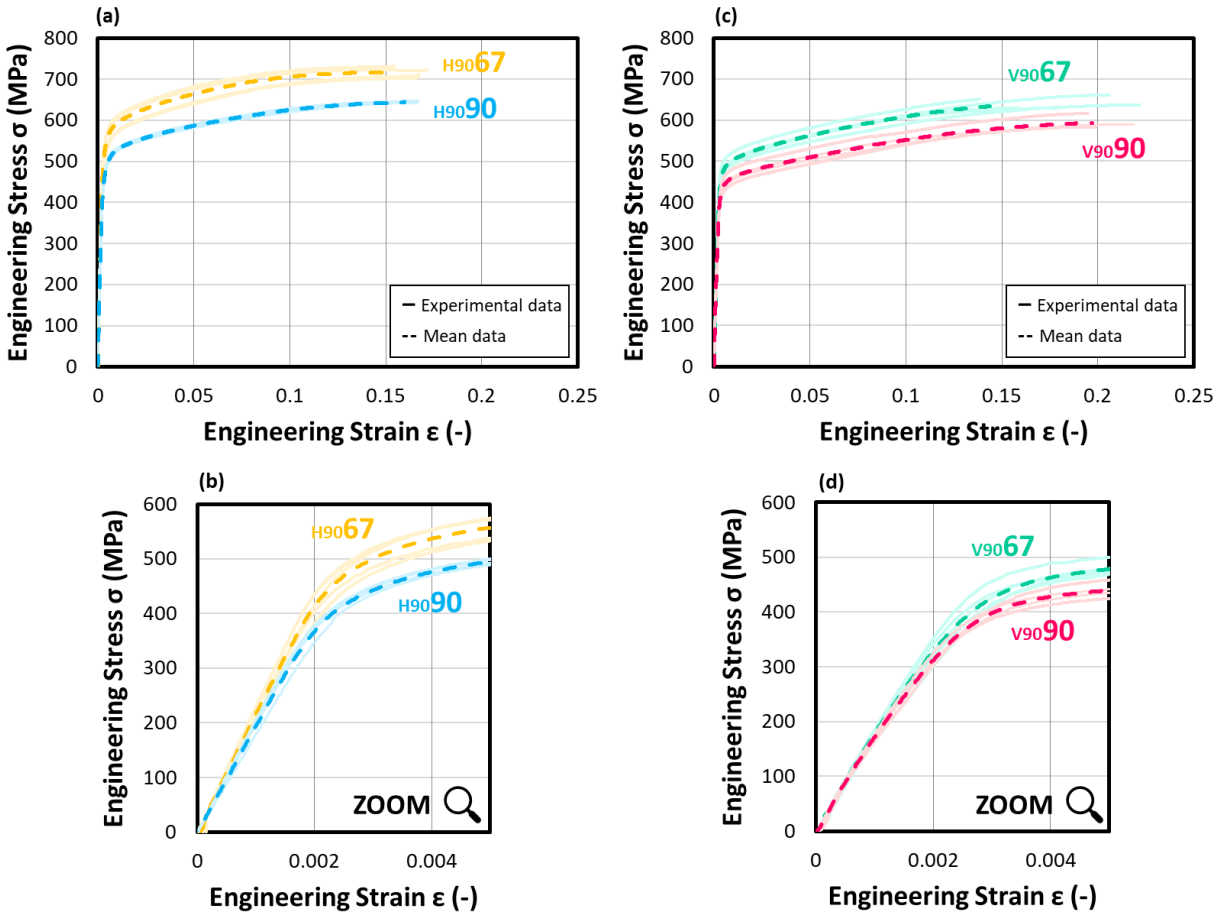

Figure 62: Influence of the rotation angle (67° and 90°) on the tensile properties
(a, b) VED = 90 J/mm^3 and horizontal orientation (c, d) VED = 90 J/mm^3 and vertical orientation

For both the horizontal and vertical building orientation, a rotation angle of 90° results in a noticeable decrease in yield stress σ_{YS} and ultimate tensile stress σ_{UTS}. The gap between the two rotation angles is wider between H9067 and H9090 (Figure 62a) than between V9067 and V9090 (Figure 62b). On the other hand, the Young's modulus E seems slightly less affected no matter the set of parameters, with especially very little difference for a vertical orientation as shown in Figure 62d. No significant influence on the ductility was noted in both cases.

II.1.3. VED

The effect of the VED is exhibited in Figure 63. In this case the rotation angle is always 67°, and only the two building orientations are considered here as well: horizontal and vertical. Figure 63b and d represent the zoomed-in elastic zone of the tensile tests.

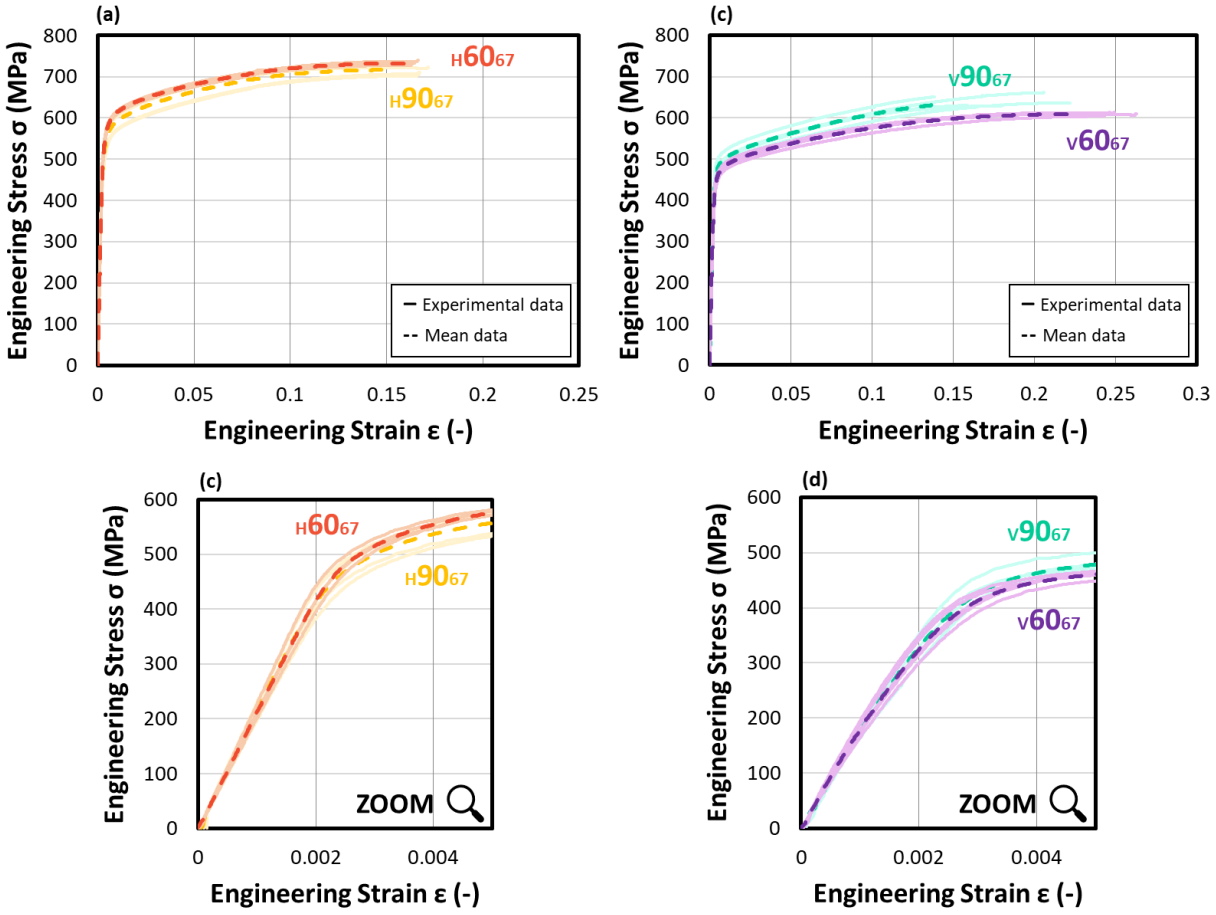

Figure 63: Influence of the VED (60 and 90 J/mm³) on the tensile properties
(a-b) Angle = 67° and horizontal orientation (c-d) Angle = 67° and vertical orientation

As demonstrated by Figure 63a and c, the VED has very little impact on the overall tensile properties for a given angle of 67°. A slight improvement is noted at a VED of 60 J/mm^3 rather than 90 J/mm^3 for a horizontal building orientation, while the contrary occurs for a vertical building orientation. The Young's modulus remains the same regardless of the VED considered as shown in Figure 63c and d. The ductility is not impacted either for a horizontal building orientation (Figure 63c), whereas a VED of 60 J/mm^3 results in higher values compared to 90 J/mm^3 for vertically built specimens (Figure 63d).

II.1.4. Comparison with cast & wrought material

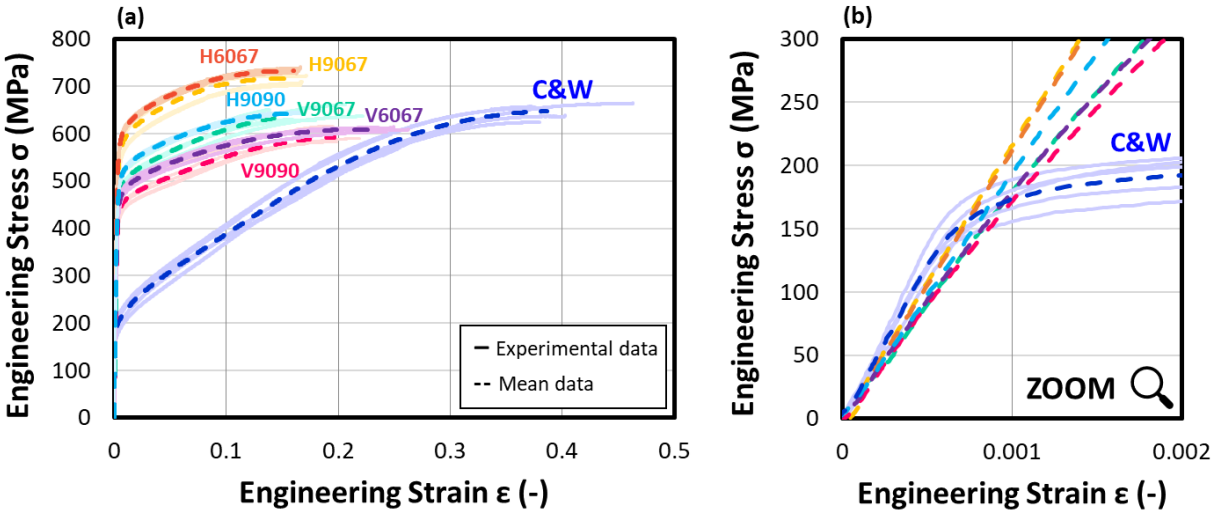

Figure 64: Tensile properties comparison between cast & wrought specimens and L-PBF specimens
(a) Stress-Strain curves (b) Zoom-in on the elastic domain
(Only the mean curves are represented for L-PBF specimens in the elastic domain)

Finally, Figure 64 demonstrates the significant difference in tensile properties between cast & wrought and L-PBF specimens. As shown in Figure 64a, the yield stress σ_{YS} of L-PBF specimens is at least twice as superior as the one of cast & wrought specimens. The ultimate tensile stress σ_{UTS} resulting from conventional manufacturing is equal or superior to the one of L-PBF specimens, except for horizontal specimens that are higher by approximately 100 MPa. On the other hand, Figure 64b exhibits a higher Young's modulus for cast & wrought specimens. They also exhibit a significant ductility compared to their L-PBF counterparts, and a noticeably different strain hardening behavior. The last point can be explained by the differences in initial dislocation structures between both [158], which influences significantly the strain hardening mechanisms occurring during the test.

II.2. Discussion

Table 13 presents all the tensile parameters evaluated from the tensile tests data. The four commonly found tensile parameters are presented: The Young's Modulus E, the yield stress σ_{YS}, the ultimate tensile stress σ_{UTS}, and the maximum elongation at necking A. The ductility was also characterized more locally by another parameter, which is often related to fracture properties: the fracture strain ε_f. Finally, the table also presents the strain hardening exponent n_H and the strength coefficient k_H. They are calculated as defined in Chapter 2 using the Hollomon law, in order to discuss the influence of the manufacturing parameters on the strain hardening behavior of the manufacturing configurations.

Table 13: Tensile properties evaluated for all manufacturing conditions

	H9067	**V9067**	**H9090**	**V9090**	**H6067**	**V6067**	**C&W**
E **(GPa)**	217 (±11)	184 (±10)	196 (±12)	184 (±3)	213 (±8)	201 (±11)	243 (±22)
σ_{YS} **(MPa)**	549 (±18)	468 (±15)	486 (±4)	435 (±14)	571 (±5)	451 (±7)	191 (±19)
σ_{UTS} **(MPa)**	723 (±11)	645 (±18)	648 (±2)	595 (±14)	737 (±4)	613 (±3)	649 (±13)
A **(%)**	16 (±2)	19 (±3)	17 (±0.1)	20 (±2)	16 (±1)	25 (±1)	39 (±4)
ε_f **(%)**	58 (±4)	69 (±7)	62 (±2)	63 (±7)	64 (±2)	85 (±4)	52 (±2)
n_H **(-)**	0.16 (±0.01)	0.23 (±0.03)	0.19 (±0.01)	0.25 (±0.02)	0.16 (±0.00)	0.22 (±0.01)	0.63 (±0.03)
k_H **(MPa)**	1145 (±26)	1149 (±62)	1066 (±18)	1093 (±54)	1156 (±10)	1060 (±20)	1858 (±49)

The results discussed previously indicate that the three manufacturing parameters considered could be classified from the most to the least influential to the tensile properties as follows: the building orientation, the rotation angle and the VED. Obviously, this is a simplistic approach, as many manufacturing configurations are missing to assure this trend no matter the building orientation, the angle and the VED chosen. Still, quantitative values displayed in Table 13 support that the tensile behavior is the most sensitive to the building orientation, regardless of the rotation angle and the VED considered.

The Young's modulus values computed from the initial slope of the tensile curves appear systematically lower for vertical specimens with a VED of 90 J/mm^3 (V9067 and V9090). This may be explained by the more pronounced crystallographic texture observed along the building direction compared to horizontal specimens (Figure 58). The difference between both building orientations is less noticeable at 60 J/mm^3 for which no texture was observed, with close Young's modulus values for H6067 and V6067 configurations. The same observation is made for the rotation angle and the VED, where few differences are notable in case of similar textures between the manufacturing conditions. These results are coherent with what was already reported in the literature [106,180], indicating that the Young's modulus decreases with a more pronounced texture for Ni alloys. When crystals are mainly oriented along one direction, some directions become more or less densely packed compared to others, leading to variations in resistance under different loading directions. This can result in an anisotropic Young's Modulus, as observed in the present case.

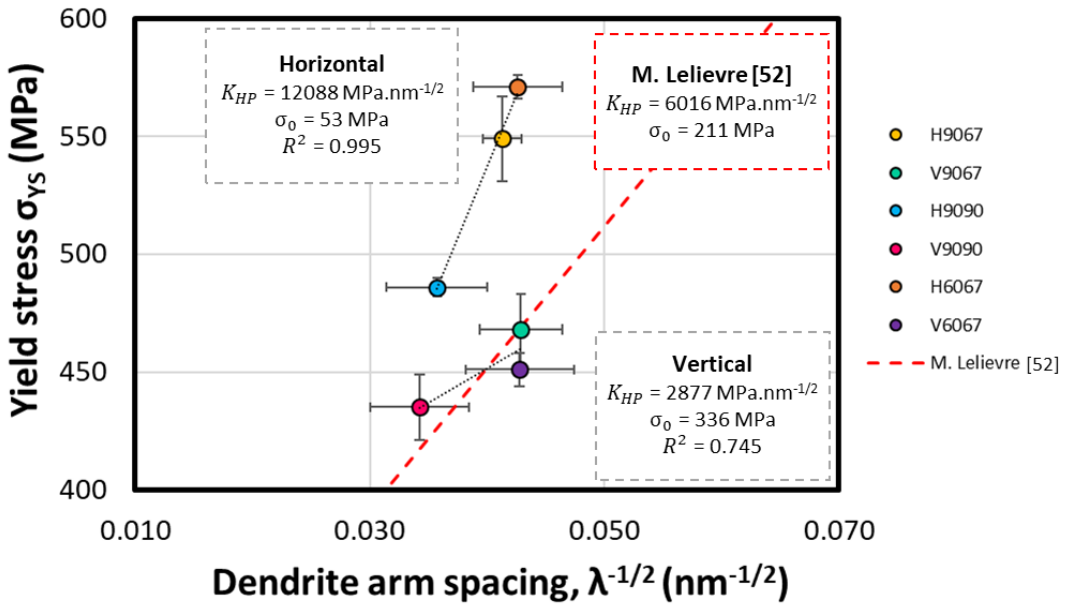

Figure 65: Evolution of the yield stress values with the size of the dendrite arm spacing

Previous work [36] already discussed the fact that due to the complex and anisotropic nature of microstructure of L-PBF alloys, the Hall-Petch equation defined below was not suitable to describe the evolution of the yield stress σ_{YS}:

$$\sigma_{YS} = \sigma_0 + \frac{K_{HP}}{\sqrt{d}} \tag{38}$$

With σ_0 a constant, K_{HP} the Hall-Petch slope, and the d the average grain diameter. Instead, previous studies [37,181] suggested to consider the dendrite arm spacing as a parameter to

describe the evolution of the yield stress. Despite the significant standard deviation observed for the interdendritic space sizes, Figure 65 exhibits an attempt made to correlate the yield stress σ_{YS} to this parameter in the present study.

Taking the mean yield stress σ_{YS} and dendrite arm spacing values λ for all the different configurations, no linear trend could be observed. However, if the data are separated according to the building orientations considered (horizontal or vertical), two laws are identified in Figure 65. The K_{HP} slopes for horizontal and vertical specimens are respectively 382 MPa.µm$^{-1/2}$ (12088 MPa.nm$^{-1/2}$) and 91 MPa.µm$^{-1/2}$ (2877 MPa.nm$^{-1/2}$). The previous K_{HP} value identified for L-PBF Ni20Cr vertical specimens produced using different VEDs [36] was estimated at 190 MPa.µm$^{-1/2}$ (6016 MPa.nm$^{-1/2}$), and is plotted in Figure 65 (red dots). Regarding cast & wrought Ni20Cr [148], K_{HP} was equal to 935 MPa.µm$^{-1/2}$. For both studies on L-PBF Ni20Cr, L-PBF specimens exhibit lower values than cast & wrought specimens, hinting at a reduced strengthening effect from the dendritic cellular structures compared to the grain boundaries. Regarding the difference between the previous work and the current one on L-PBF Ni20Cr, a higher slope (twice as superior) was previously obtained for vertically built specimens compared to the current one, as shown in Figure 65. However, given the scattering and the fact that only two configurations were built vertically with a rotation angle of 67°, additional experiments should be carried out to confirm the trends.

When it comes to ductility, the elongation at ultimate tensile stress A shows that even though vertical specimen are overall more ductile compared to horizontal specimen, the values remain pretty similar. However, the fracture strain $\boldsymbol{\varepsilon_f}$ results sheds light on the fact that the V6067 exhibited a more intense local plastic deformation compared to all the other configurations with 85%, against a range of 60-65% for other specimens.

Finally, Figure 66 enforces the assumption that the building orientation is the most influential parameters, as the most notable differences in strain hardening behavior are between horizontal and vertical specimens. Compared to horizontal ones, vertical specimens present higher values in terms of strain hardening exponent n_H, with a range of 0.16-0.19 against 0.22-0.25. The difference is less noticeable for the strength coefficient k_H, except for a VED of 60 J/mm^3 where H6067 specimens are more resistant than V6067 specimens by up to 100 MPa. Except the previous point, the VED and the rotation angle display minimal influence on the strain hardening parameters. Qualitative observations from Figure 64a indicating a different strain hardening behavior for cast & wrought specimens are confirmed in Table 13, with very different values for both the strain hardening exponent n_H and the strength coefficient k_H.

In both cases, values resulting from conventional manufacturing are two to three times higher than the ones from L-PBF manufacturing.

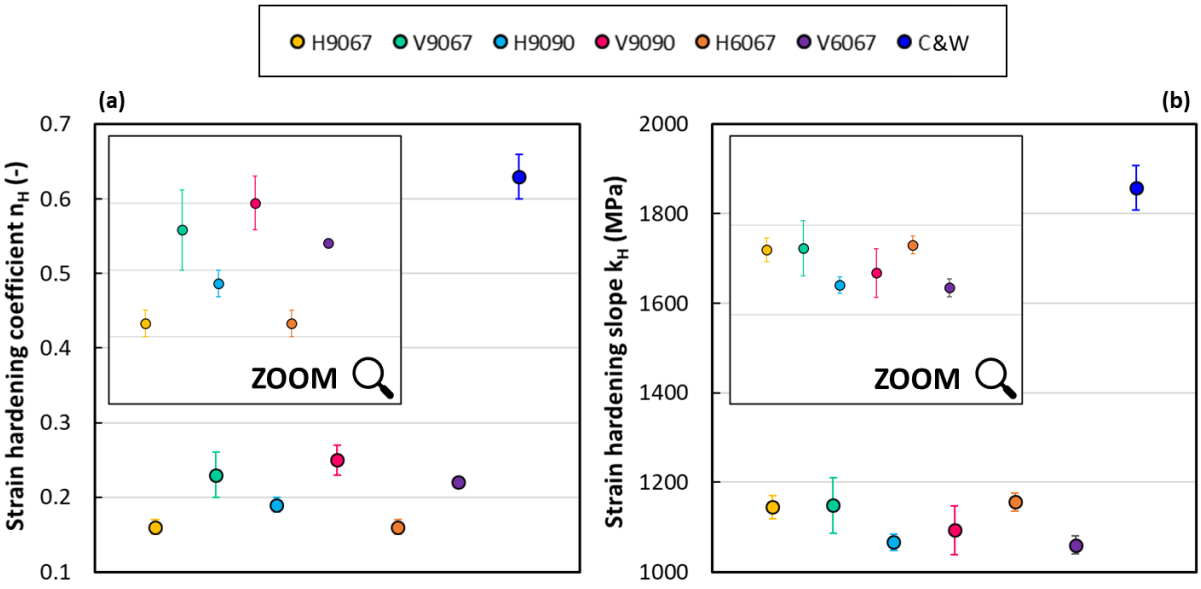

Figure 66: Strain hardening properties (Hollomon law) for all manufacturing configurations
(a) Strain hardening coefficient n_H (b) Strain hardening slope k_H

III. Conclusion

This chapter investigated the initial physical and microstructural properties of as-built Ni20Cr L-PBF specimens, as well as their tensile properties. A comparison with annealed cast & wrought specimens was also presented to discuss the differences between AM and conventional processes. The following conclusions were drawn:

- The resulting microstructure is highly dependent on the manufacturing parameters, for both the planes parallel and perpendicular to the building direction.

- The building orientation mainly influences the texture, with a more pronounced texture for vertical specimens compared to the horizontal ones. The rotation angle affects the grain morphology: an angle of 90° produces a more unidirectional and organized microstructure, while one of 67° tends to limit the influence of any preferential orientation. The VED has an impact on both aspects, with bigger grains elongated along the building direction and a higher crystallographic texture with an increasing VED.

- The tensile properties are overall mainly influenced by the building orientation, with still slight differences depending on the rotation angle or the VED.

- Horizontal specimens generally present higher Young's modulus, yield stress and ultimate tensile stress values, while vertical specimen are more ductile. The strain hardening behavior between both orientations is also different, with higher strain hardening exponents for vertical specimens compared to their horizontal counterparts. This could hint at different plastic deformation mechanisms occurring at the crack tip during fracture testing.

- It was demonstrated that the yield stress could be correlated to the dendrite arm spacing for a giving building orientation, but more investigation is yet to be made to confirm the trends discussed in this chapter.

CHAPTER 4:
Relationship between fracture behavior & microstructure

This fourth chapter presents the results obtained regarding the fracture behavior of the L-PBF Ni20Cr alloy, and which were published (for the most part) in the journal of Engineering Fracture Mechanics [182]. Test data, fractographic observations, profilometry analysis, and post-mortem microstructure are discussed. The influence of the manufacturing process on the trends noted is analyzed.

I. Fracture behavior

The results from the fracture tests are shown in the following figures, with again a focus on one manufacturing parameter at a time: the building orientation (horizontal or vertical), the rotation angle (67° or 90°), and the VED (60 J/mm^3 or 90 J/mm^3). To limit the number of plots discussed, only the crack extension versus time and the resistance curves are presented. The load-displacement and stress-strain curves for all the manufacturing configurations are presented in Appendix C. For each configuration presented, at least five specimens were considered. The continuous lines are the experimental curves, and the dotted lines the mean curves calculated from them.

I.1. Influence of the building orientation

Figure 67 presents the results for the sets of parameters with two different building orientations: A VED of 90 J/mm^3 with a rotation angle of 67° (Figure 67a and b), a VED of 90 J/mm^3 with an angle of 90° (Figure 67c and d), and a VED of 60 J/mm^3 with an angle of 67° (Figure 67e and f).

At a given displacement rate (1 mm/min), the crack extension occurs at the same speed regardless of the building direction for both (90 J/mm^3-67°) and (60 J/mm^3-67°) configurations, as shown in Figure 67a and e. Only the (90 J/mm^3-90°) configuration displays a significant speed gap, with H9090 specimens subjected to much faster crack propagation than V9090 specimens.

Despite the similar crack propagation rate for two out of three manufacturing conditions, all resistance curves exhibit an overall better resistance to crack propagation for vertically built specimens compared to horizontally built ones: more energy is hence needed to propagate the crack at the same speed for (90 J/mm^3-67°) and (60 J/mm^3-67°) configurations. The (90 J/mm^3-90°) set displays a significant gap between horizontal and vertical specimens (Figure 67d). Less difference is noted for the two other sets of parameters, nevertheless specimens built at a VED of 60 J/mm^3 still present a wider gap than the ones with a VED of 90 J/mm^3. The manufacturing conditions can be classified from the most to the least impacted by the building orientation as follows: (90 J/mm^3-90°), (90 J/mm^3-67°), and (60 J/mm^3-67°).

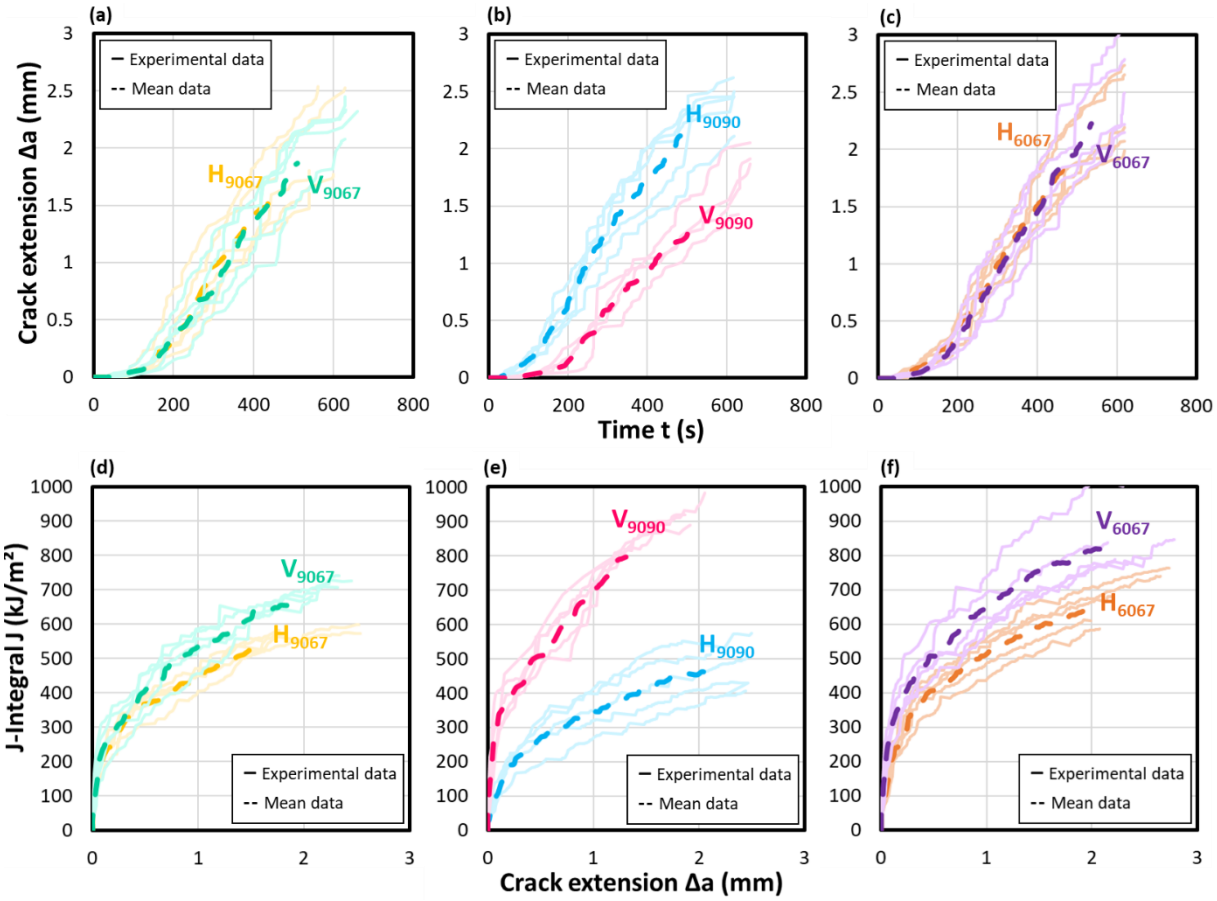

Figure 67: Influence of the building orientation (horizontal and vertical) on the fracture behavior (crack extension versus time, and resistance curve)

(a, b) VED = 90 J/mm^3 and Angle = 67° (c, d) VED = 90 J/mm^3 and Angle = 90°

(e, f) VED = 60 J/mm^3 and Angle = 67°

I.2. Influence of the rotation angle

The influence of the rotation angle is observed for both horizontal specimens (Figure 68a and b) and vertical specimens (Figure 68c and d) at a VED of 90 J/mm^3.

For both building orientations, the rotation angle has a notable effect on both the crack propagation speed and the overall resistance of the specimens. However, the trends obtained for each building orientation are opposing each other: for horizontal specimens, a rotation angle of 90° increases the crack propagation speed (Figure 68a) and hence decreases the resistance to crack propagation of H9090 specimens compared to H9067 specimens (Figure 68b). On the contrary, V9090 propagates the crack slower than V9067 (Figure 68c), which increases its overall resistance (Figure 68d).

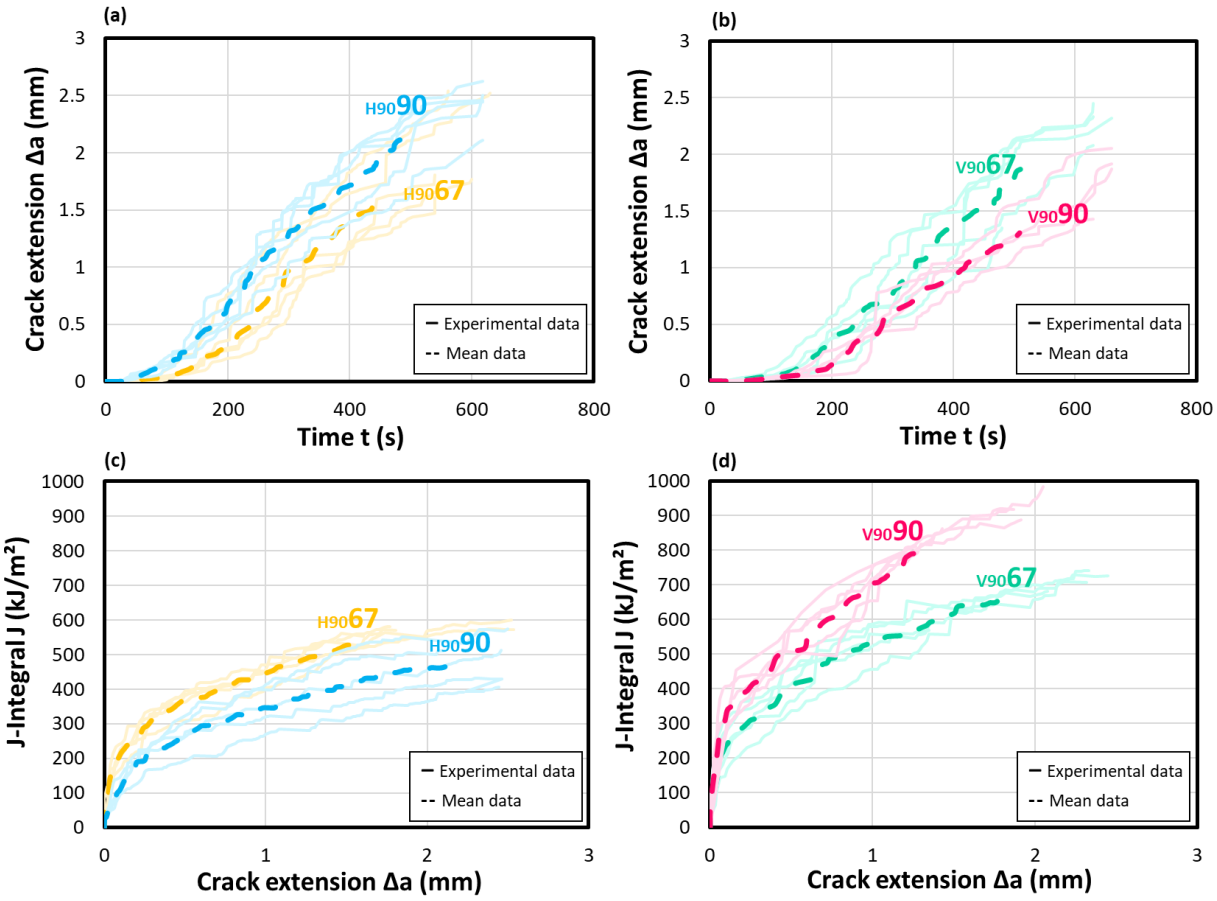

Figure 68: Influence of the rotation angle (67° and 90°) on the fracture behavior (crack extension versus time, and resistance curve)

(a, b) VED = 90 J/mm^3 and horizontal orientation (c, d) VED = 90 J/mm^3 and vertical orientation

I.3. Influence of the VED

Figure 69a, b and c, d exhibit the effect of the VED for a given rotation angle (67°) and building orientation.

Figure 69a and c show that regardless of the building orientation, the crack propagation rate is similar at both 90 J/mm^3 and 60 J/mm^3, though a slight increase of the mean curve is noted for a VED of 60 J/mm^3. The difference between the two VEDs is more noticeable on the resistance curves, with a wider gap for vertically built specimens compared to horizontally built ones. In both cases, a VED of 60 J/mm^3 improves the resistance to crack propagation compared to a VED of 90 J/mm^3.

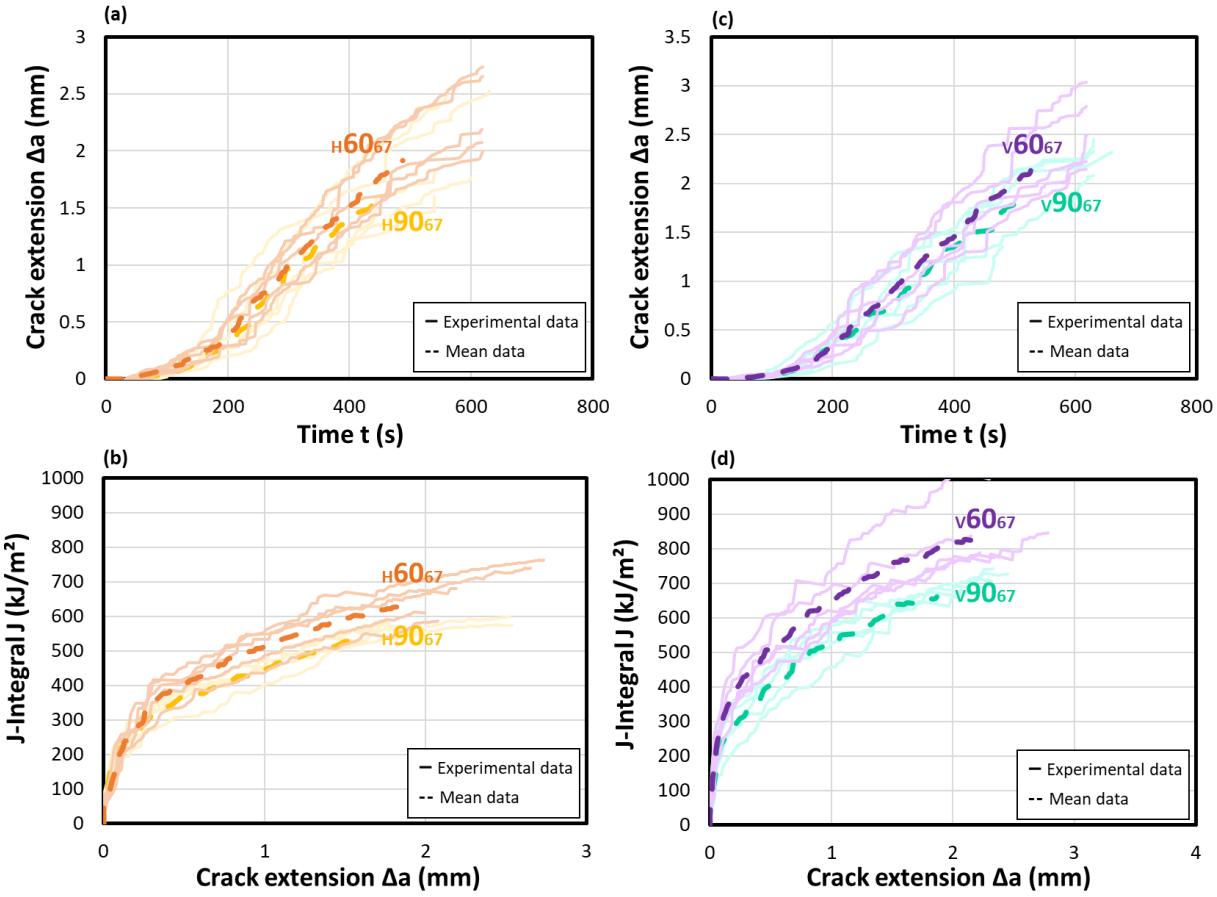

Figure 69: Influence of the VED (60 and 90 J/mm^3) on the fracture behavior (crack extension versus time, and resistance curve)

(a, b) Angle = 67° and horizontal orientation (c, d) Angle = 67° and vertical orientation

I.4. Comparison with cast & wrought material

A comparison between L-PBF and cast & wrought specimens is done in Figure 70a and b. For the sake of simplicity, only the mean curves of the L-PBF specimens are displayed.

Cast & wrought specimens exhibit a tremendously better resistance to crack propagation than L-PBF specimens, with a much slower and smaller crack propagation as shown in Figure 70a, as well as an overall resistance far above the other configurations (Figure 70b), especially regarding the tearing modulus.

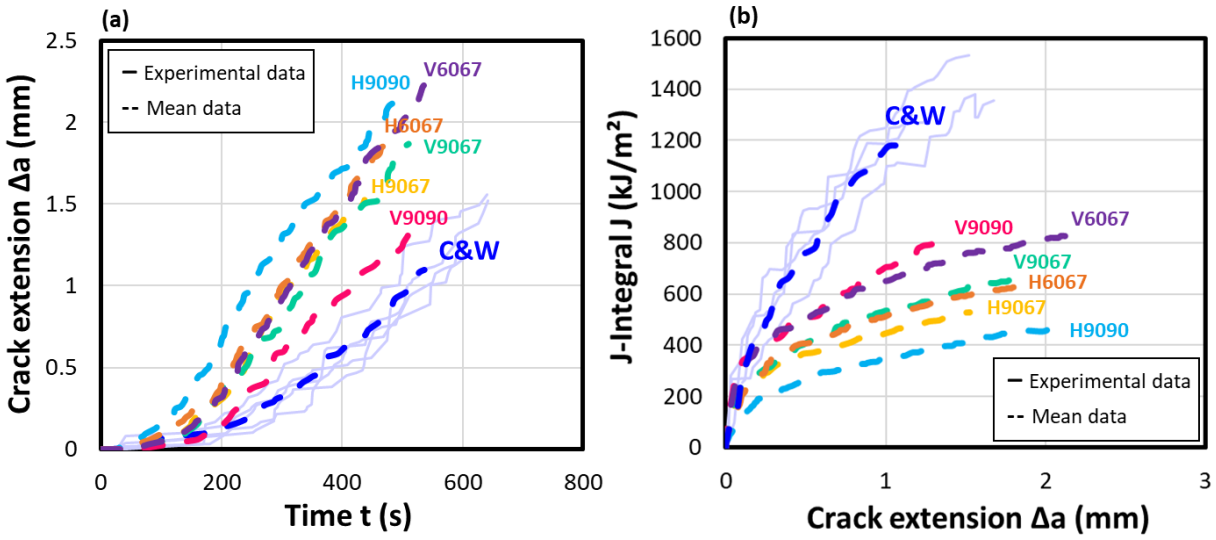

Figure 70: Fracture properties comparison between cast & wrought and L-PBF specimens
(a) Crack extension versus Time (b) Resistance curves
(Only the mean curves are represented for L-PBF specimens)

I.5. Discussion

Table 14 and Figure 71 present the fracture properties obtained for all the manufacturing configurations: the fracture toughness J_{Ic}, the slope $\frac{dJ}{da}$ of the second phase of the resistance curve, and the tearing modulus T calculated from it.

Table 14: Fracture properties for all the manufacturing configurations

	H9067	V9067	H9090	V9090	H6067	V6067	C&W
J_{Ic} (kJ/m²)	315 (±32)	334 (±58)	252 (±51)	437 (±45)	402 (±48)	476 (±68)	593 (±77)
$\frac{dJ}{da}$ (MPa)	167 (±12)	259 (±81)	152 (±36)	364 (±39)	199 (±20)	262 (±43)	810 (±147)
T (-)	120 (±9)	221 (±69)	126 (±29)	361 (±39)	130 (±13)	259 (±43)	5411 (±986)

Regarding the fracture toughness, the building orientation alone is not the main factor resulting in the biggest discrepancies between the different sets of parameters, as shown in Figure 71a. Though a vertical building orientation results in overall better resistance to both crack initiation and propagation compared to a horizontal one, the amplitude of the gap between them is highly dependent on the rotation angle considered. For a VED of 90 J/mm^3, an angle of

90° compared to one of 67° tends to increase the fracture toughness for a vertical orientation (334 to 437 kJ/m²) whereas it degrades it for a horizontal one (315 to 252 kJ/m²), as shown in Figure 71a and b. On the other hand, an angle of 67° induces smaller changes at a VED of 60 J/mm^3 between H6067 (402 kJ/m²) and V6067 (476 kJ/m²) configurations, while very little difference is observed at a VED of 90 J/mm^3 between H9067 (315 kJ/m²) and V9067 (334 kJ/m²) specimens.

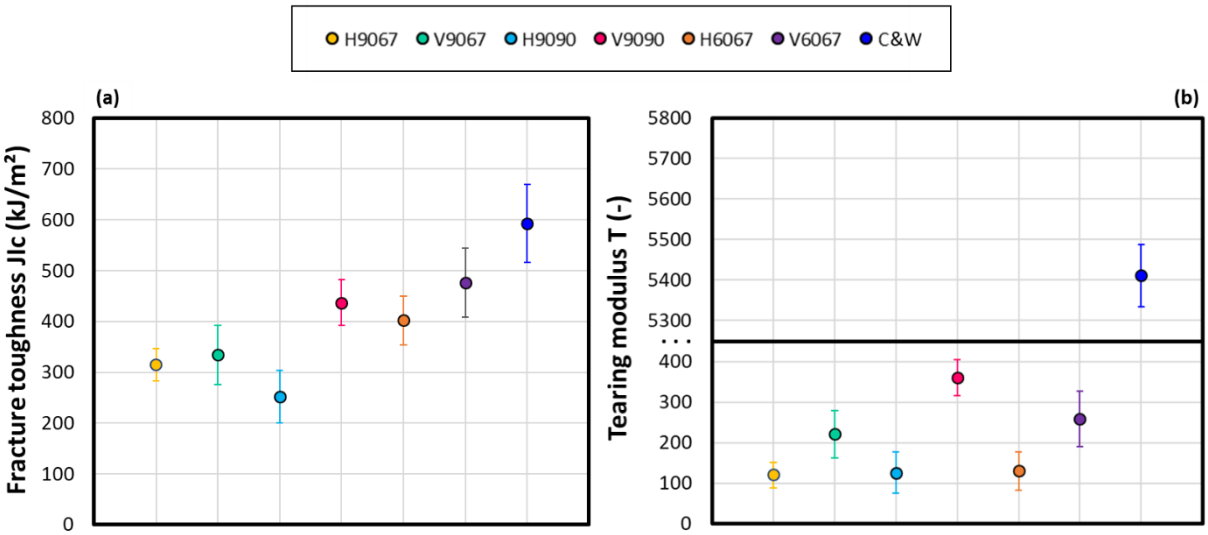

Figure 71: Fracture properties for all manufacturing configurations
(a) Fracture toughness (b) Tearing modulus

The influence of the building orientation on the tearing modulus is more noticeable, with values two to three times higher for vertical specimens compared to horizontal ones, regardless of the VED or rotation angle considered (Figure 71b). The gap is again wider between specimens manufactured with an angle of 90° (H9090 and V9090). Little difference is noted between the two rotation angles for horizontal specimens (H9067 and H9090), while an increase of 60% was noted for an angle of 90° (V9090) rather than 67° (V9067) for the vertical ones. Contrary to the fracture toughness, both 60 J/mm^3 and 90 J/mm^3 VEDs result in similar tearing modulus values.

To get a better understanding of the reasons behind the differences between the manufacturing conditions (ductility, strength, microstructure size, morphology, texture…) a post-mortem microstructural analysis and fractographic observations are presented in the next section.

II. Post-mortem fractographic observations

II.1. Fractographic observations

Post-mortem fractographic observations (optical microscope and SEM) of all the manufacturing conditions are shown below in Figure 72.

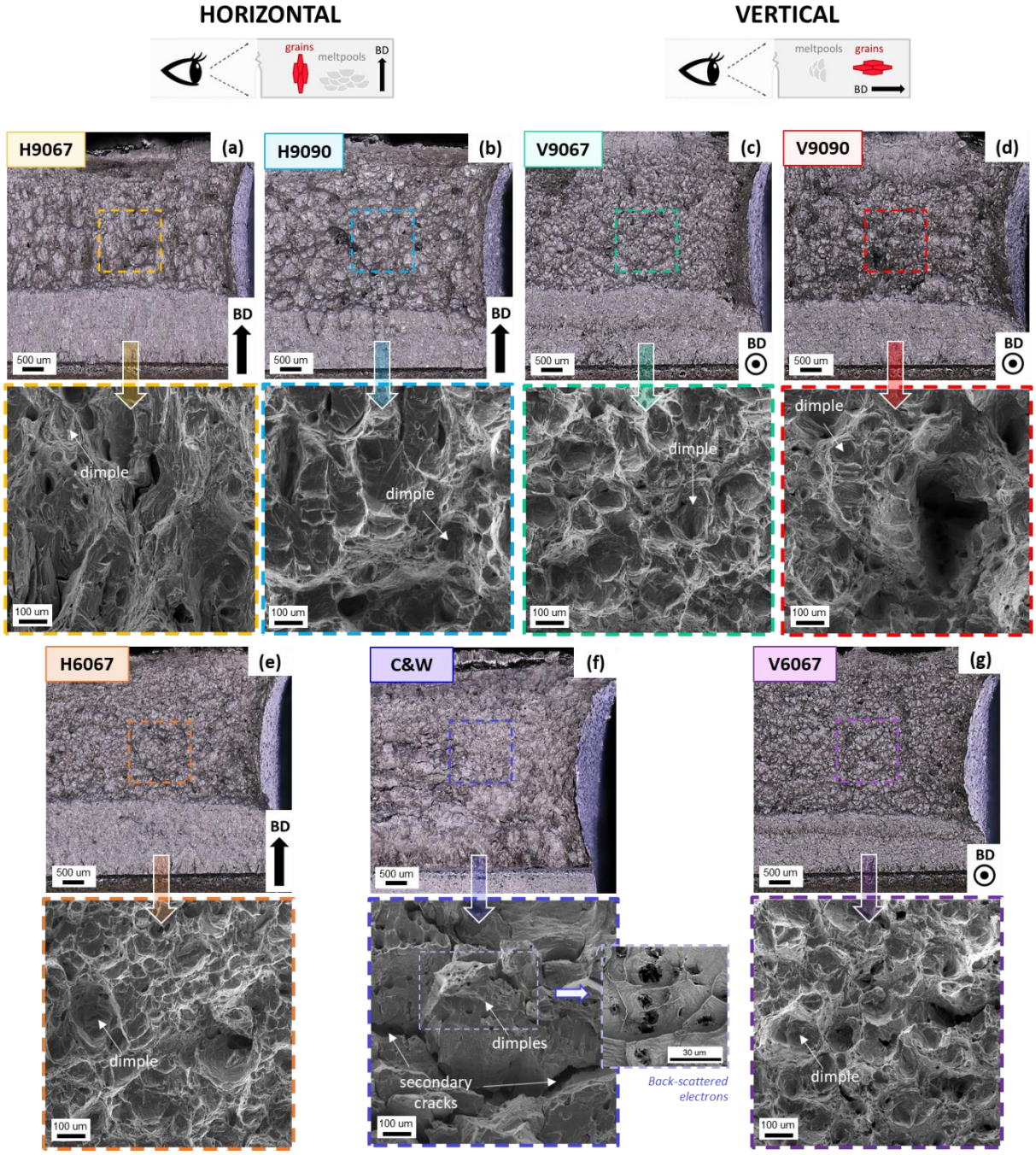

Figure 72: Fractographic observations (optical microscope, SEM) of the different configurations
(a) H9067 (b) V9067 (c) H9090 (d) V9090 (e) H6067 (f) C&W (g) V6067
(Examples of dimples and secondary cracks are pointed out by the white arrows)

L-PBF specimens all experience ductile fracture, with dimple sizes (indicated by white arrows in Figure 72) of the same order of magnitude as the grain sizes for the same observation plane: XZ plane for horizontal specimens, and XY for vertical ones. This suggests a possible influence from grain boundaries during crack propagation. No particle was observed inside the dimples, likely because they systematically fell off before observations were performed. However the dimples aspect seems to be associated with a transgranular void growth and coalescence type of fracture. All vertical specimens (V9067, V9090, and V6067) display dimples similar in size and morphology. Other fracture mechanisms were observed, but due to the lack of relevance in the discussion, they are presented in Appendix D.

Cast & wrought specimens on the other hand exhibit very different fracture surfaces. Very small dimples are present, with the presence of microparticles with a diameter of approximately 10 μm characterized with backscattered electrons (Figure 72f). In this case, mostly intergranular void nucleation is observed. A substantial number of secondary cracks in the plane perpendicular to the crack propagation plane are also noted, while none is found for L-PBF specimens. These secondary cracks may act as one of the main causes for the overall better fracture behavior of cast & wrought specimens, as propagating multiple cracks instead of a single one requires a lot more energy and hence slows down crack propagation.

II.2. Crack path and surface profilometry

Test standards for crack propagation [113,114] usually require a plane strain state at the core of the specimen, where the crack length is typically estimated post-mortem. However, the crack monitoring method used in this study relies on the specimen's outer surface observation, which is subjected to a plane stress state. Hence it is of utmost interest to characterize the out-of-plane plastic deformation with respect to the crack length. To do so, a profilometry study is conducted on the outer fracture surfaces of the broken specimens to assess the plastic deformation occurring near the crack tip, as shown in Figure 73. All crack paths identified during crack monitoring are also plotted in Figure 74, with images of the outer surfaces associated with each manufacturing condition.

Figure 73a shows the profiles along the compression zone, while Figure 73b displays the profile along the tension zone. Profile analyses are done on both outer surfaces of the

specimens (painted and not painted), but as few differences are noted, only one profile is shown for each configuration. Significant plastic deformation is observed for all specimens in the compression zone, with no remarkable differences between them, except cast & wrought specimens which exhibit prominent plastic deformation. These observations are in good agreement with both the microhardness and tensile properties estimated previously. For the profiles of the L-PBF specimens in the tension zone, only V9090 specimens undergo significant plastic deformation, whereas barely any is visible for other printing configurations. The height and width of the plastic zone are also really close to cast & wrought specimens, which is the only other configuration displaying important plastic deformation in the tension zone.

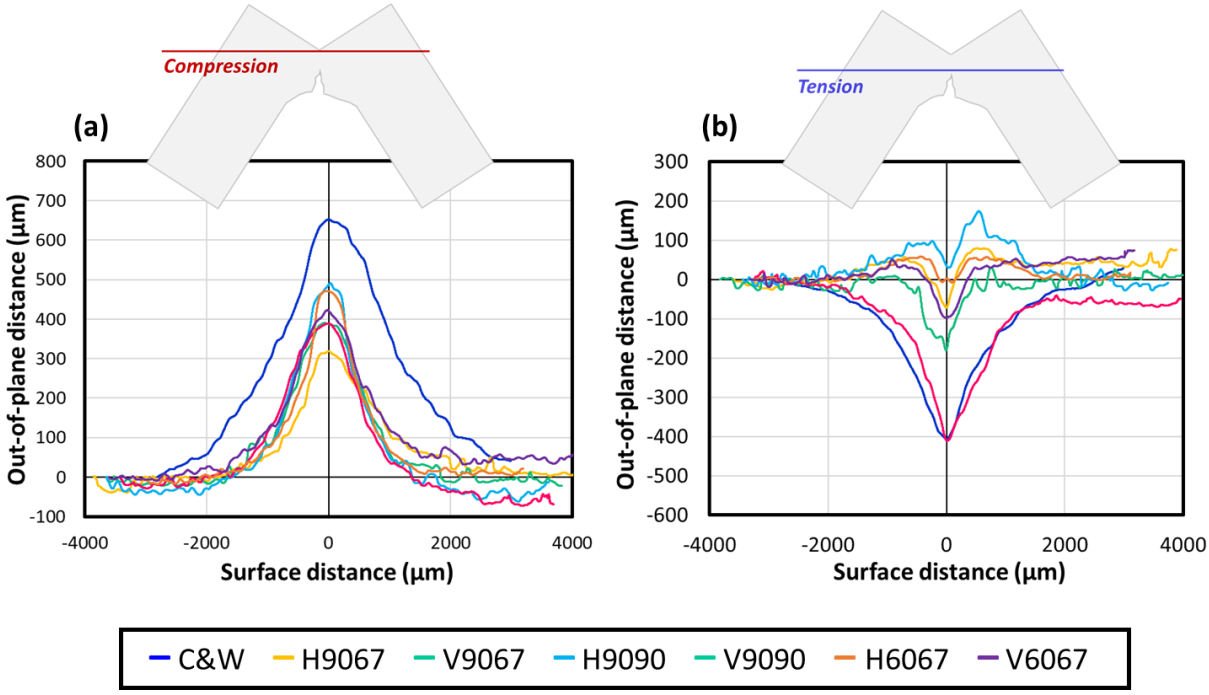

Figure 73: Post-mortem profilometry study on the specimen's outer surface for all configurations

(a) Local plastic deformation in compression area (b) Local plastic deformation in tension area

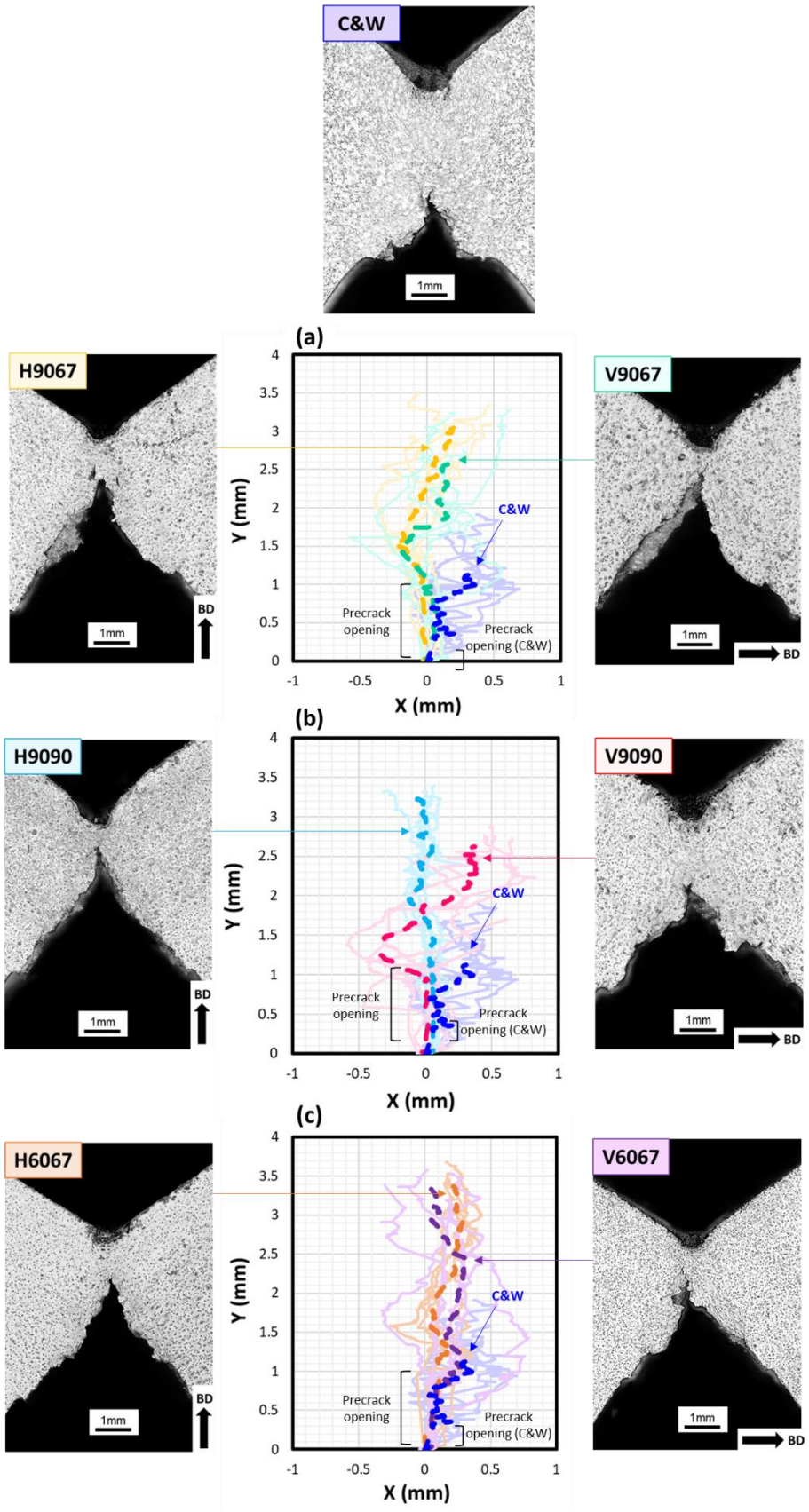

Figure 74: Post-mortem observations of the specimens grouped by building orientations (crack path and optical microscope observation of the outer surface)

(a) H9067 and V9067 (b) H9090 and V9090 (c) H6067 and V6067

(Cast & wrought specimen is plotted on every graphic for comparison purposes)

More generally, not much difference can be observed between all the other sets of parameters for L-PBF specimens. This highlights that for the V9090 manufacturing strategy, the crack tip is associated with a greater plastic deformation compared to the others. Thus, more energy is dissipated for plastic deformation compared to crack propagation, leading to higher crack propagation resistance for V9090 specimens. This hypothesis is supported by the tearing modulus values obtained in Table 14. However, the same result would be expected for V6067, which displayed both the highest fracture strain, and tearing modulus. Yet, no explanation can be provided as for now on this matter, and this point remains to be investigated.

More tortuous crack paths are observed for the V9090 as well (Figure 74b), supporting the fact that the energy required to grow the crack is more significant. Overall, vertical specimens exhibit more tortuous paths. In contrast, horizontal specimens follow a more linear crack path, especially H9090 specimens as shown in Figure 74b, suggesting that less mechanical energy is needed to propagate. This is in good agreement with the fracture properties observed in Figure 70, Figure 71 and Table 14.

II.3. Discussion on the crack initiation (heat tint)

In this study, it is a known fact that the crack estimated at the surface is late compared to the one occurring at the core of the specimens. An attempt to assess the amplitude of the difference in crack initiation has been conducted. However, only one specimen is investigated for this matter, due to the lack of specimens available for all manufacturing configurations. The specimen considered belongs to the V9090 configuration.

Figure 75a and b show the moment where the three-point bending is stopped after the visual identification of crack initiation at the surface. After a heat treatment of 4h at 550°C to oxidize the crack front, the specimen is completely broken in fatigue, and fractographic analysis is conducted and shown in Figure 75c.

From the fractographic analysis, the crack front at the core seems already advanced compared to the initiation noted at the surface. However, the time difference between what is observed at the surface and what is happening at the core may be reasonable.

This observation was already made by [129] using an acoustic device, where the crack initiation at the surface coincided with the initiation detected.

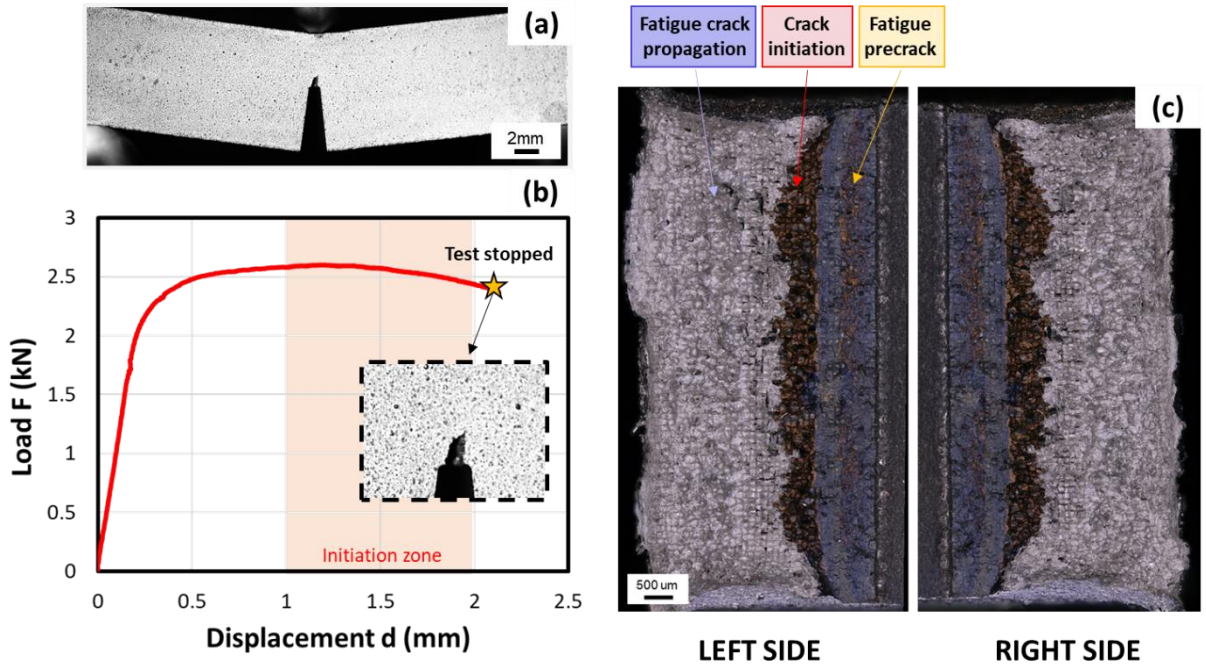

Figure 75: Heat tint performed on one specimen
(a) Specimen appearance at test stop (b) Load-displacement curve associated to the specimen (c) Fractographic observation of the heat tint

This study only serves a comparative purpose between the different configurations, hence the approximate crack initiation detection is considered sufficient. Nevertheless, it is important to note that to serve as any design basis, the accuracy of the crack initiation detection methods should be further worked on for the current alloy considered.

III. Post-mortem microstructure

To understand what is governing the crack path at the microscale, SEM observations and EBSD analyses were performed post-mortem on the XZ plane for the three scales of interest: macro/mesoscale (meltpools), meso/microscale (grains), and sub-micro/nanoscale (dendrites and nano-oxides). The results are discussed below.

III.1. Influence of the macro/mesoscale (meltpools)

Figure 76 exhibits SEM images of the meltpools (highlighted in white), and their position with respect to the crack path for each manufacturing condition.

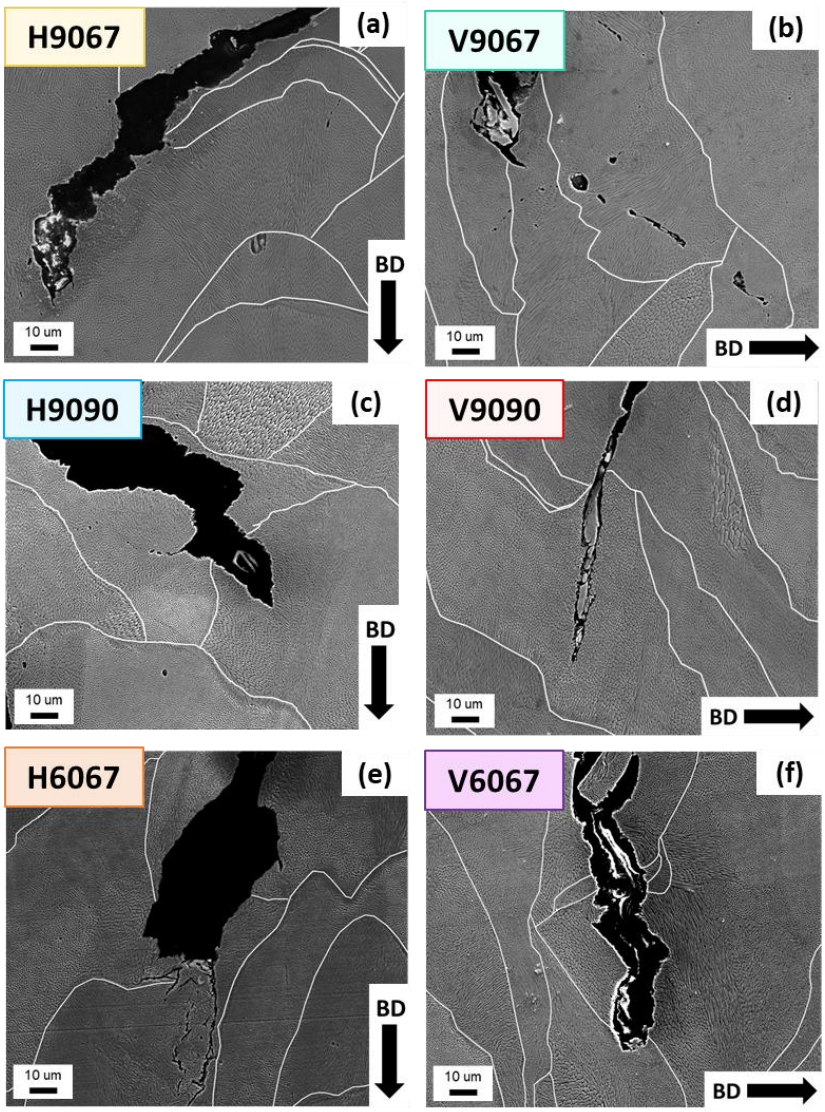

Figure 76: Observation of the meltpools influence on the crack propagation for the different manufacturing configurations (meltpools are highlighted in white)

Regardless of the manufacturing parameters considered, the interfaces between the meltpools do not influence the crack path. Therefore, in the context of this study, these interfaces are not considered as 'weak bonds' that could influence the crack propagation.

III.2. Influence of the meso/microscale (grains)

Figure 77, Figure 78 and Figure 79 offer a comparison of the post-mortem IPF maps for the two building orientations (horizontal or vertical), but fixed VED and rotation angle.

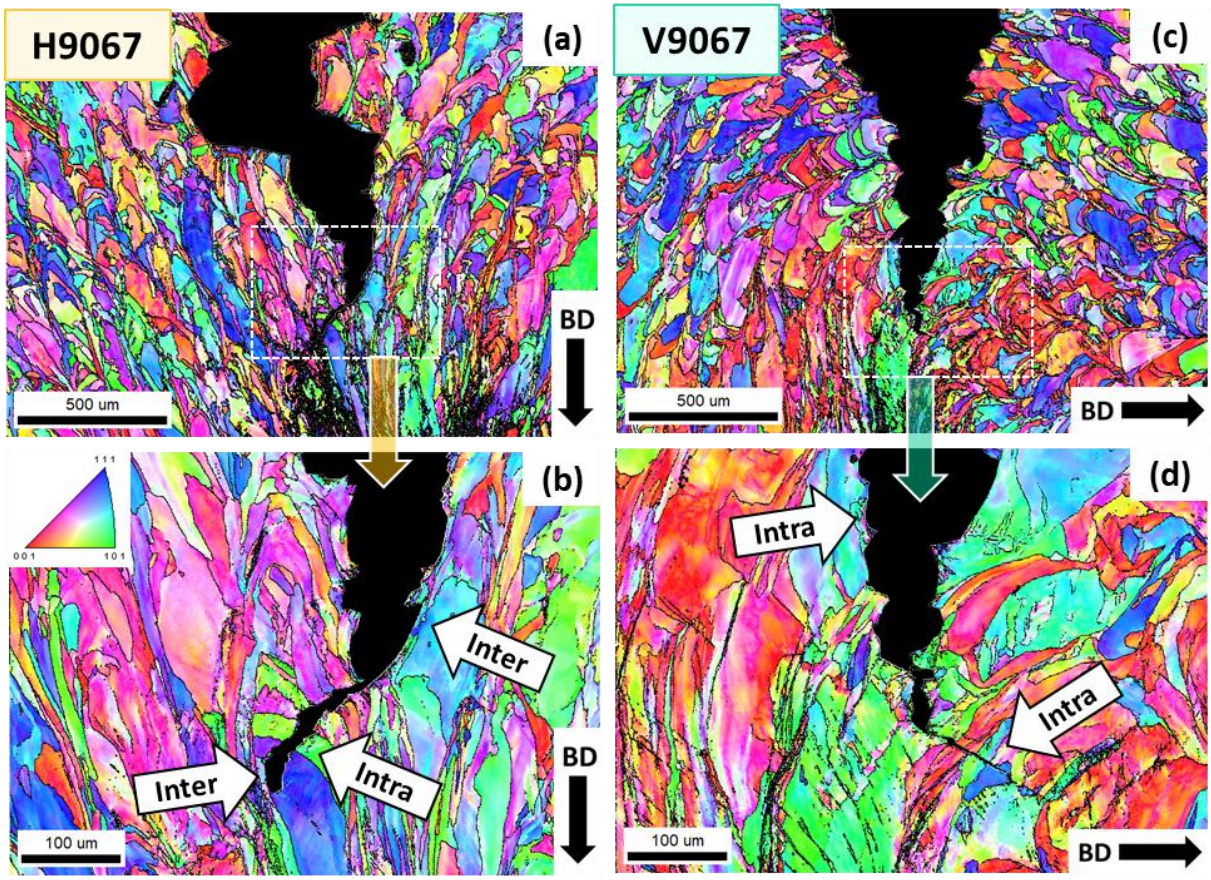

Figure 77: Post-mortem IPF maps at the crack tip at low and high magnifications (VED = 90 J/mm^3 and rotation angle of 67°)
(a, b) Horizontal orientation (c, d) Vertical orientation

All IPF images reveal a competition between intergranular and transgranular fracture modes no matter the configuration observed, as indicated by the arrows denoted 'inter' and 'intra' respectively. This mixed fracture mechanism was already mentioned in the literature by numerous studies on L-PBF alloys [128,130,131]. For horizontal specimens fabricated with a VED of 90 J/mm^3 (Figure 77a, b and Figure 78a, b), the propagation is primarily intergranular

and partially transgranular. The crack path seems to follow the grain boundaries oriented parallel to the propagation direction, due to a pronounced morphological texture. In Figure 77b, the crack crosses the green and blue grains, before the path seems to realign with the grain boundaries. For vertical specimens observed in Figure 77c, d and Figure 78c, d, mainly transgranular fracture is observed, with the crack going through the grains regardless of the crystallographic orientation. The difference between specimens with a VED of 60 J/mm^3 is much less visible as the grains are not as elongated along the building direction, erasing the influence of the grain's morphology on the crack path. The grains being smaller, it is also harder to identify the principal fracture mode.

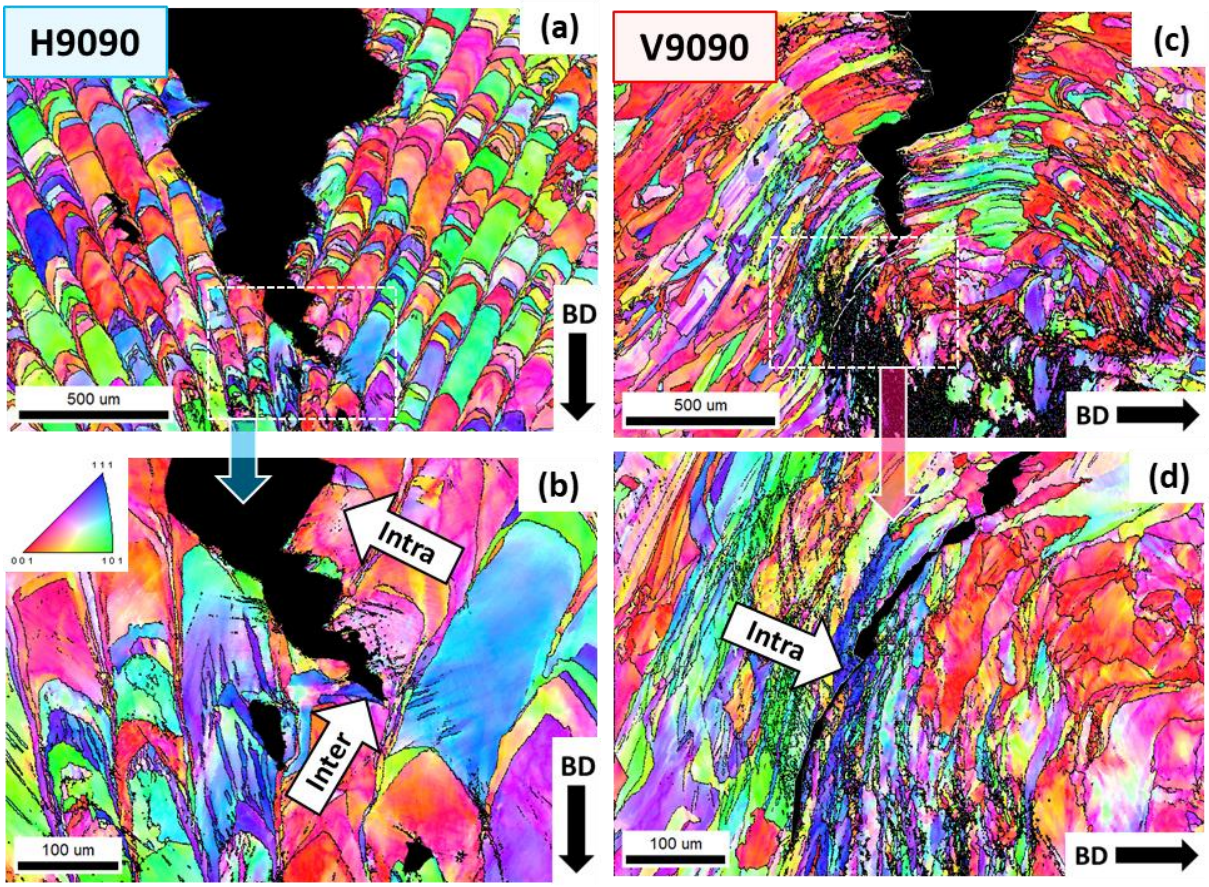

Figure 78: Post-mortem IPF maps at the crack tip at low and high magnifications (VED = 90 J/mm^3 and rotation angle of 90°)
(a, b) Horizontal orientation (c, d) Vertical orientation

As shown by both Figure 77 and Figure 78, as well as the fracture properties in Table 14, the rotation angle emphasizes the role played by grain boundaries in the case of 90° compared to 67°. Indeed, a higher proportion of grain boundaries aligned along the crack propagation direction is denoted for H9090, and less for V9090, compared to H9067 and V9067, respectively. Hence the propagation is harder for vertical specimens, resulting in higher

fracture toughness and tearing modulus compared to horizontal specimens. Overall, for a VED of 90 J/mm^3 the morphological texture appears to hold a key role in the deviation of the crack path when intergranular fracture occurs, as opposed to the crystallographic texture which is less influential.

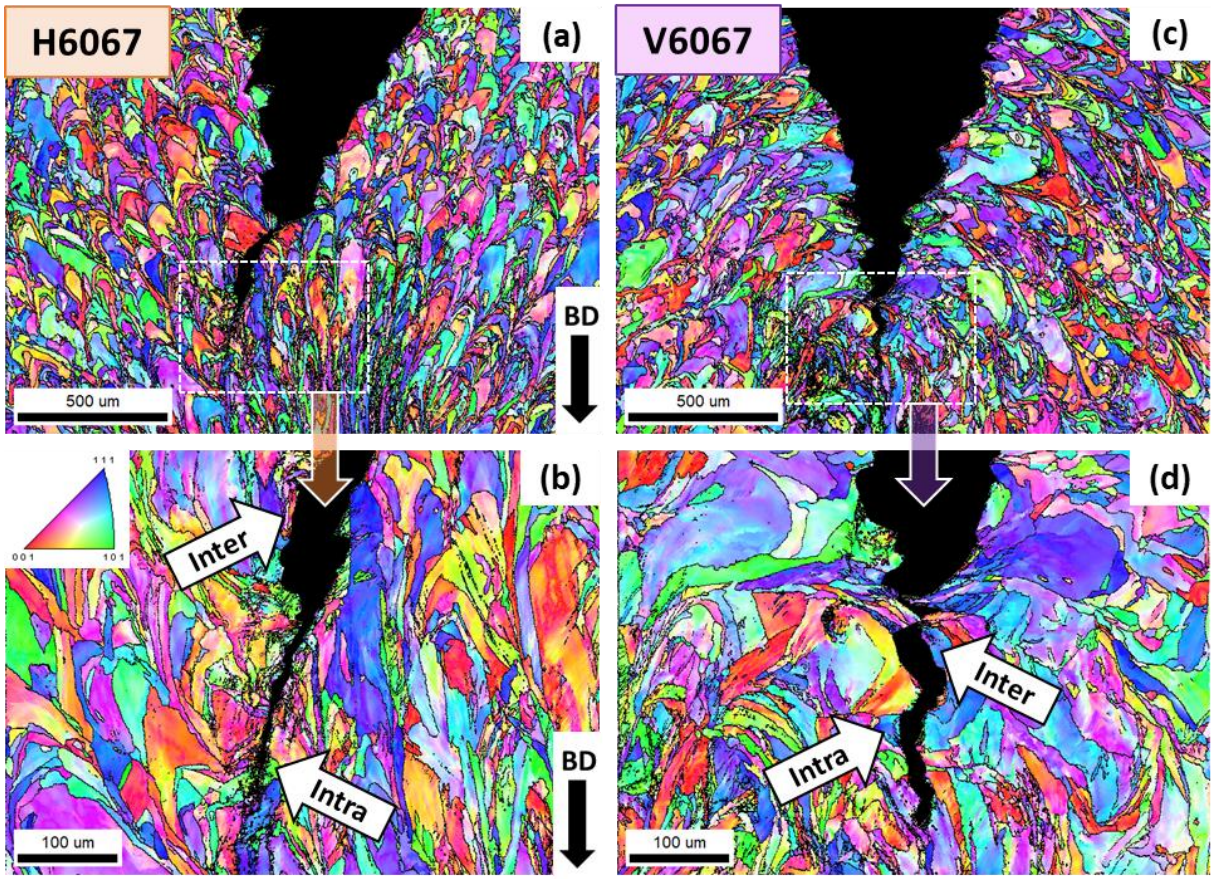

Figure 79: Post-mortem IPF maps at the crack tip at low and high magnifications
(VED = 60mm^3 and rotation angle of 67°)
(a, b) Horizontal orientation (c, d) Vertical orientation

On the other hand, differences between horizontal and vertical specimens produced with a VED of 60 J/mm^3 could hardly be explained thanks to post-mortem microstructure, due to the very few differences noted between the two. The only notable difference between the two manufacturing configurations is the tensile properties discussed in Chapter 3. Indeed V6067 specimens exhibit a much higher ductility, both globally with the elongation A, and locally with the fracture strain ε_f, than H6067 specimens.

Both H6067 and V6067 specimens (Figure 79) exhibit much more grain boundaries than H9067 and V9067 specimens (Figure 78), which means more interfaces to cross when a

transgranular fracture occurs, and hence more energy needed to propagate the crack. Therefore this point may explain why better fracture properties are obtained for specimens fabricated at 60 J/mm^3 compared to 90 J/mm^3.

III.3. Influence of the sub-micro/nanoscale (dendrites/nano-oxides)

Higher magnification images of the crack tip are displayed in Figure 80 to investigate the possible effect of the interdendritic regions and nano-oxides, as they are known to be influential to the fracture behavior [137] and might govern the crack propagation for transgranular fracture. Different behaviors were observed at the dendritic scale, and only some illustrative examples are presented in Figure 80. A more exhaustive overview is given in Appendix D.

Crack propagation along the dendritic arm spacings (Figure 80e, and h) or straight through it (Figure 80d) is commonly observed. As shown in Figure 80h, the cracks can also propagate between two different dendrite colonies, or within the same colony indifferently. Occasional debonding between dendrites far from the crack path can also be observed. Only observations carried out on V9067 and H9090 specimens highlight shear bands, as observed in Figure 80d, between two nucleation zones or near the crack path. However, further investigations are necessary to know whether this phenomenon is specific to these manufacturing configurations or not. These analyses suggest that nano-oxides located in the interdendritic spaces could contribute to the crack propagation. The debonding at the oxide/matrix interfaces has already been discussed in other studies to point out their influence on fracture properties [128], especially nano-oxides for L-PBF Ni-based alloys [137]. In the present case, further investigation on the size and proportion of these nano-oxides should be done to confirm how it affects the fracture behavior of each printing configuration.

As for now, no significant differences between the different configurations is noted on this aspect.

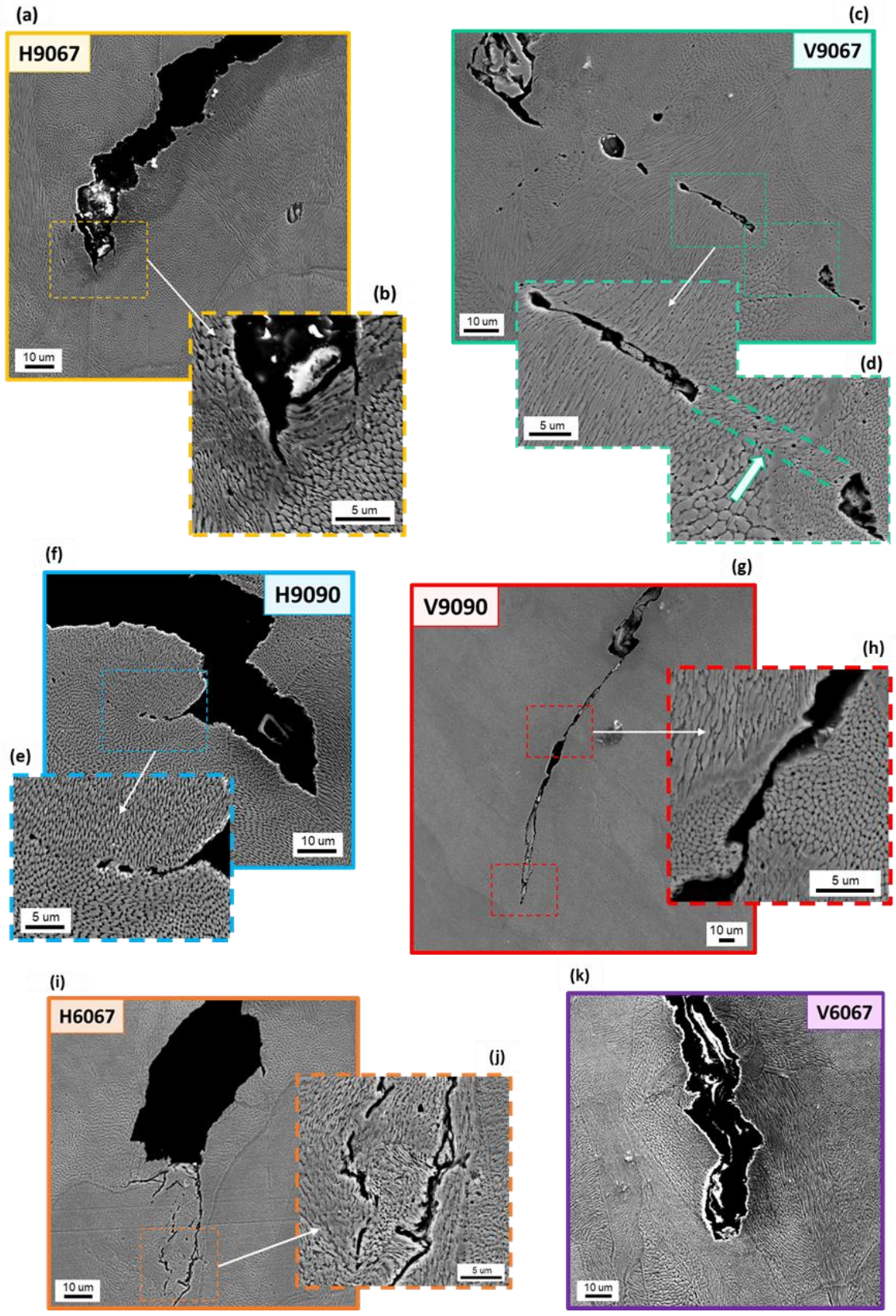

Figure 80: SEM observations at the crack tip for all the manufacturing configurations
(a, b) H9067 (c, d) V9067 (e, f) H9090 (g, h) V9090 (i, j) H6067 (k) V6067

III.4. Comparison with cast & wrought material

Figure 81 presents the post-mortem IPF maps for cast & wrought specimens.

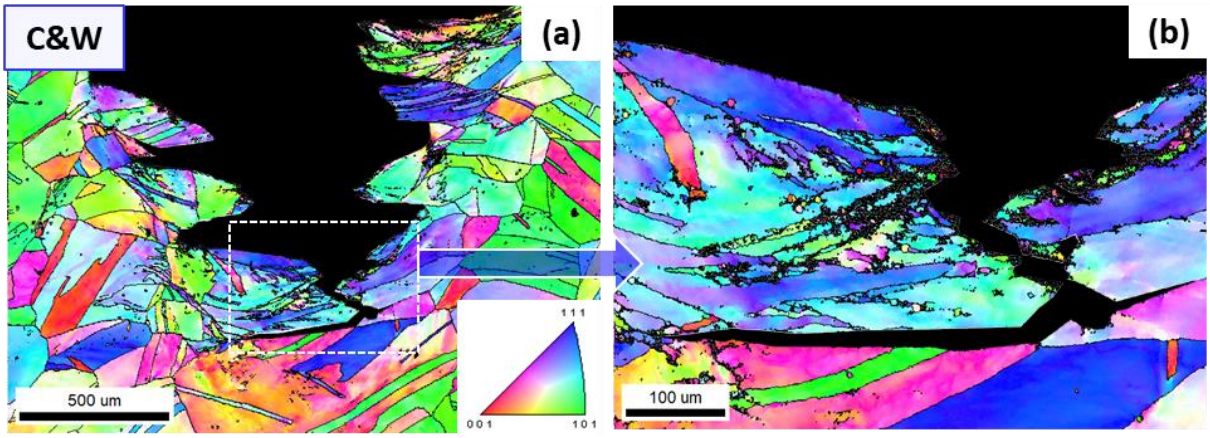

Figure 81: Post-mortem IPF maps at the crack tip at low and high magnifications (Cast & wrought specimens)

IPF images reveal that mainly intergranular fracture is occurring for cast & wrought specimens, with significant plastic deformation at the crack tip visible with the nuanced colors of the grains. The crack path appears tortuous, with secondary cracks along the way. These observations support the statement that the crack propagation appears harder for cast & wrought specimens, with a lot of energy dissipated by the plastic deformation and the propagation of secondary cracks. The presence of precipitates is also clearly visible everywhere on the specimen.

IV. Conclusion

In summary, the present section sheds light on the influence of the processing parameters on the fracture behavior of L-PBF Ni20Cr. The following conclusions were highlighted:

- As observed for the tensile behavior, the building orientation also holds an important role in the fracture behavior, however the amplitude of the gap between vertical and horizontal specimens is also highly dependent on the rotation angle and the VED.

- Specimens are dense enough for pores not to be detrimental to crack propagation, and the meltpool boundaries do not seem to affect the crack path either.

- In contrast, results indicate that grain orientation, size, and morphology are the most influential parameters on the fracture behavior for higher VEDs (elongated grains), while the tensile properties and especially the specimen's ductility have the most impact for lower VEDs (smaller grains).

- Crystallographic texture and nano-oxides display a more secondary impact on the fracture behavior, which should be further analyzed.

- The observations enabled to classify the impact of the different scales investigated on the fracture behavior of L-PBF Ni20Cr alloy, with the fracture properties being mainly governed by the meso/microscale and submicro/nanoscale.

CHAPTER 5:
Complementary experiments on the influence of the loading rate and the specimen size on the fracture behavior

This fifth chapter briefly presents the initial observations from both the impact and the microbending tests, carried out to characterize the fracture behaviors for respectively a dynamic loading, and miniaturized specimens. These investigations are still ongoing, and the results currently under discussion. Additionally, prospects regarding the remaining work are also discussed.

I. Impact tests

Fracture tests performed under a quasi-static loading highlighted the role of the plastic deformation on the fracture behavior of L-PBF Ni20Cr, with greater plastic deformation being associated with better fracture properties as observed with V9090 specimens. Considering the time-dependent behavior of the Ni20Cr, which presents a dependency to the loading rate, dynamic tests are conducted to investigate the influence of the loading rate behavior on the specimens. To do so, impact tests were performed using an instrumented Charpy pendulum. The objective is to observe whether a dynamic loading reduces the plastic deformation occurring, and hence alter the fracture behavior of the specimens. More generally, impact tests are often considered for materials used in the military and defense field to understand how to elaborate protective equipment [183–185], as well as space exploration [184] and aircraft turbines [186,187]. Among them, Charpy tests are often considered for they are simple and quick to perform.

This study has been initiated during the latter part of the PhD, and therefore could not be properly completed yet. Still, the preliminary results obtained so far are deemed relevant to discuss, and are presented below. Due to specimen's availability as well as a lack of time, only three L-PBF configurations were tested: H9067, V9067, and V9090.

I.1. Preliminary results

Figure 82 presents the smoothed load-displacement curves resulting from the impact tests for all the manufacturing conditions considered. In order to ensure a reliable comparison between dynamic and quasi-static tests, the specimens considered have the same geometry as their counterparts for quasi-static tests. They were also pre-cracked in fatigue using the same method, and subjected to three-point bending loading.

The tests appear more or less reproducible depending on the manufacturing configurations considered: H9067 (Figure 82a) and V9067 specimens (Figure 82b) display reproducible results, while V9090 specimens (Figure 82c) show significant scattering. The values for the fracture energy at initiation (KV_i), during propagation (KV_p), and in total (KV) are reported in Table 15.

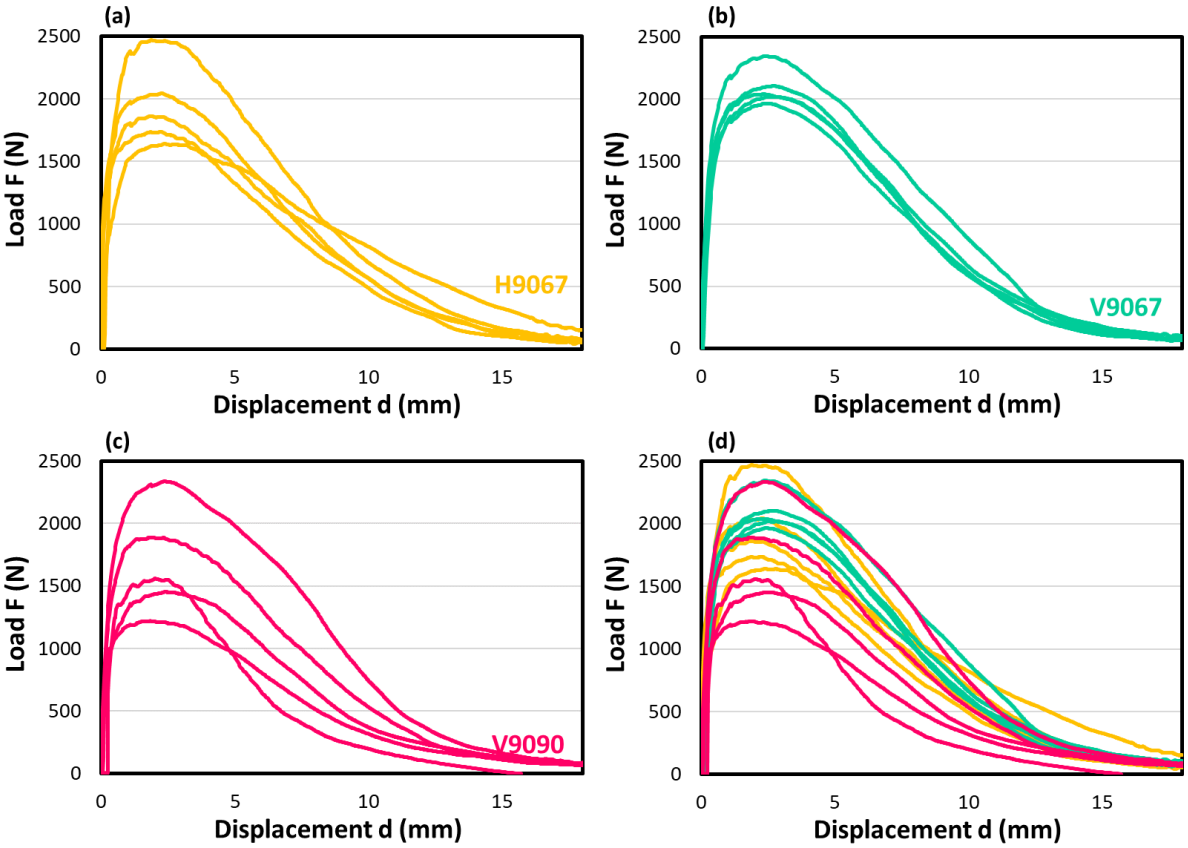

Figure 82: Load-displacement curves from the impact tests for all manufacturing conditions
(a) H9067 (b) V9067 (c) V9090 (d) Superposition of all configurations

Table 15: Fracture energies determined from the impact test load-displacement curves for all manufacturing conditions

	H9067	V9067	V9090
KV_i (J/cm²)	6 (±1)	7 (±1)	5 (±2)
KV_p (J/cm²)	11 (±2)	11 (±1)	9 (±3)
KV (J/cm²)	17 (±2)	18 (±2)	14 (±5)

Not much difference is noted in Table 15 regarding the energy required for crack initiation. Mean values of total fracture energy KV indicate that the V9067 and H9067 configurations result in the most resistant specimens, while the V9090 configuration is the weakest. However, given the scattering for V9090 specimens, more specimens need to be tested in order to ensure reliable results. Indeed, the dynamic nature of the loading makes impact tests

more sensitive to minor variations, imperfections, or even any inhomogeneity within the specimen, and hence implies a stronger statistical approach.

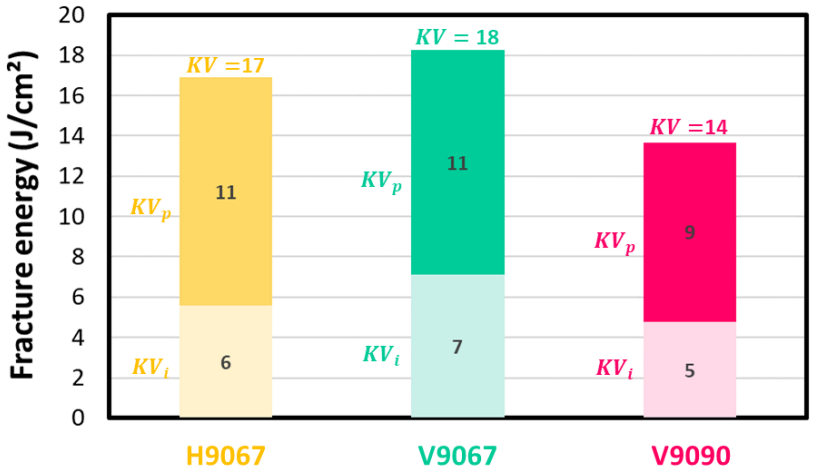

Figure 83: Mean fracture energies obtained during impact tests for all configurations
(Fracture energy at initiation KV_i, during propagation KV_p, and in total KV)

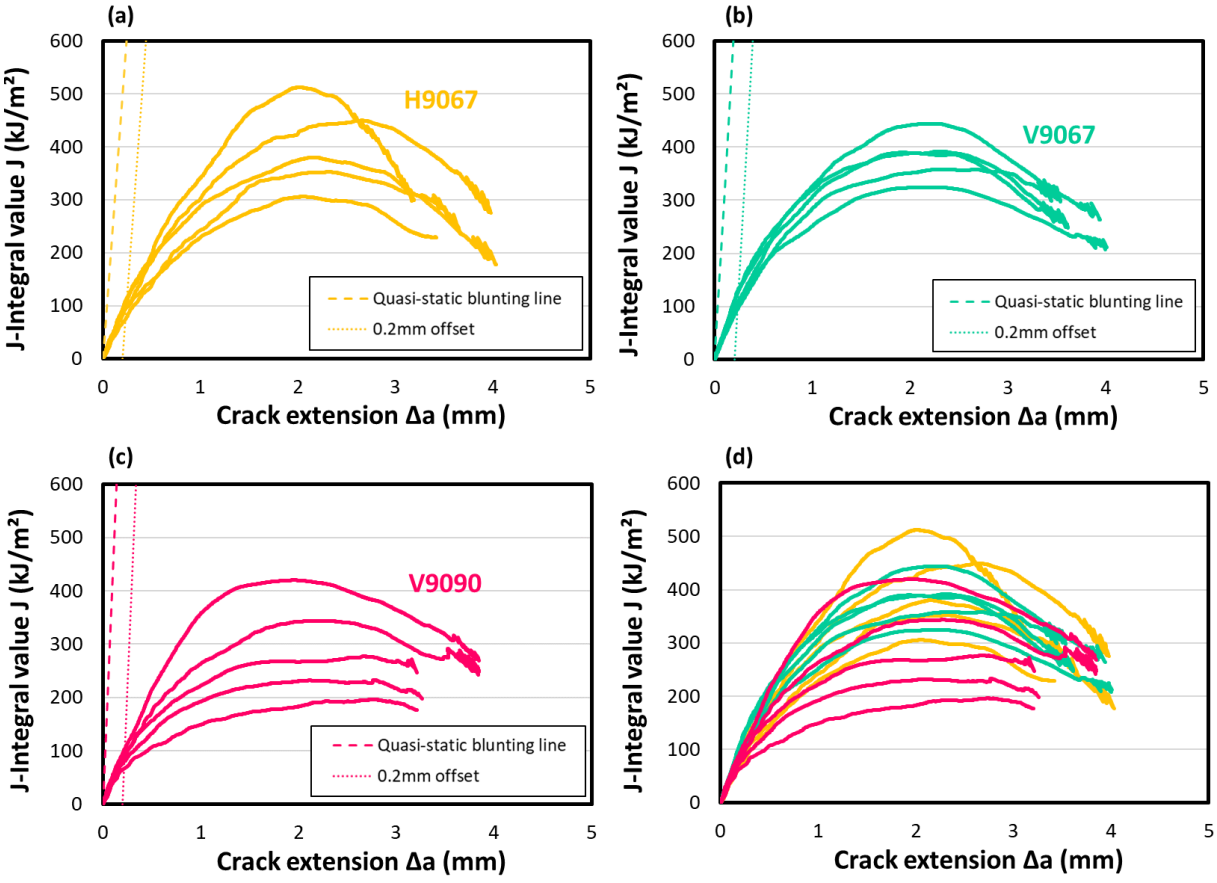

Figure 84: Resistance curves resulting from the impact tests for all the manufacturing conditions
(a) H9067 (b) V9067 (c) V9090 (d) Superposition of all configurations

Table 16: Estimation of the dynamic fracture toughness values J_d for all the configurations

	H9067	V9067	V9090
J_d (kJ/mm²)	98 (±19)	113 (±20)	84 (±13)

The dynamic J-R curves calculated using the method described in [130,188] are shown in Figure 84. The construction line and 0.2 mm offset lines determined from the quasi-static curves are also plotted, to serve as first criteria to assess the dynamic fracture toughness values J_d. No "blunting line" could be identified directly from the dynamic curves, as the initial phase of the test is not linear. It is important to note that the suitable method and criteria to determine meaningful dynamic fracture toughness and tearing modulus values from impact tests have yet to be investigated thoroughly. Still, a first estimation of the dynamic fracture toughness values J_d using the quasi-static blunting lines is reported in Table 16.

Using the same method as for quasi-static tests, dynamic fracture toughness values present the same trend as discussed previously: V9090 specimens appear as the weakest, while H9067 and V9067 specimens display a better resistance to crack initiation. Still taking these first observations cautiously, these results could be due to the impact test allowing less energy to be dissipated by plastic deformation, which was observed for V9090 quasi-static specimens. Hence the results tend towards a more brittle behavior, which is consistent with the influence of higher loading rates. The dynamic fracture toughness values are also all much lower than the ones calculated for quasi-static tests.

I.2. Discussion and perspectives

In summary, results drawn from the preliminary results remain debatable, hence it is still too early to make any conclusion on the observations from the impact tests. However, several points can be discussed, opening perspectives for what remains to be done:

- Additional specimens should be tested to improve the statistical approach and bring more reliable conclusions, as the reproducibility of the results can be questioned.
- The most relevant method to compute the dynamic fracture toughness and the tearing modulus should be investigated, as many key points differ from the quasi-static test.

- Fractographic and profilometry analyses should be conducted to identify if the fracture mechanisms are impacted by the loading rate, as well as if the plastic deformation at the surface is the same as the one observed during the quasi-static tests (especially for V9090 specimens).

- It would be interesting to carry out SEM and EBSD observations on the specimens to have a better idea of the crack path, and identify the microstructural interfaces responsible for the fracture behavior.

- Only three configurations have been tested so far in this work: H9067, V9067, and V9090. It would be of the utmost interest to investigate all the remaining manufacturing conditions already discussed during the quasi-static tests, including cast & wrought specimens.

II. Microbending tests

Considering the role of the microstructural interfaces highlighted in Chapter 4 (especially the grain boundaries and the oxides/matrix interface) on the fracture behavior of the L-PBF Ni20Cr alloy, microbending specimens were considered to investigate the influence of these interfaces at smaller scales (micro to sub-micro). However, this study also served another purpose: investigating the fracture behavior of miniaturized specimens. Macro-scale test standards are generally not suitable to study small-scale fracture mechanisms, like in micro-electro-mechanical systems (MEMS), hence miniaturized fracture toughness specimens are also exponentially studied in the literature [189–194]. In addition, the influence of the size effect, which is the dependency of a material's property on the measurement scale, is also a key topic in the scientific community. Studies on conventional brittle to semi-brittle alloys have been carried out to assess the influence of the specimen's dimensions on fracture toughness [194,194–196], but when considering ductile alloys, research on the matter becomes more scarce [197]. Therefore, a small part of this PhD has been dedicated to investigating the fracture behavior of L-PBF Ni20Cr miniaturized specimens.

The tests discussed in this section have been mainly performed and post-treated in collaboration with a research engineer from the GPM laboratory, Ronan HENRY, to whom most of the credit of this section goes. Contrary to the macroscopic tests presented in Chapter 4, the test standard considered in this work is ASTM E1820 [114], as this was the reference standard in the literature regarding microbending studies [193,194,198,199].

II.1. Preliminary results

The initial objective of the microbending tests was to assess the individual influence of the several microstructural interfaces spread at the different scales and understand which ones are the most critical to the fracture behavior of the L-PBF Ni20Cr alloy. Figure 85 illustrates the three main interfaces of interest: the meltpool boundaries, the grain boundaries, and the dendrite walls where the nano-oxides are located. Meltpools were previously demonstrated as not very influential to the fracture behavior, and hence were not the focus of the work presented here.

In order to investigate the influence of the microstructural features on the crack propagation, bending tests have been conducted on micro-cantilever specimens in addition to the three-point bending macro-specimens discussed previously in Chapter 4. In total, three

configurations were tested as illustrated in Figure 86: macroscale in red (Figure 86a and b), mesoscale in blue (Figure 86c and d), and microscale in yellow (Figure 86e and f). In this case, only one manufacturing configuration was considered: H9067. This choice was oriented by the fact that the notch was directly parallel to the grain boundaries, which is ideal to assess the influence of this interface.

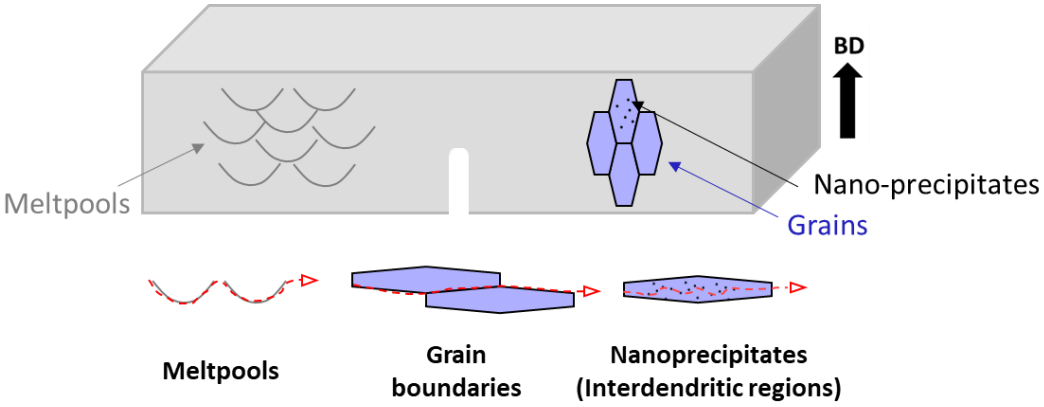

Figure 85: Illustration of the three main interfaces for crack propagation

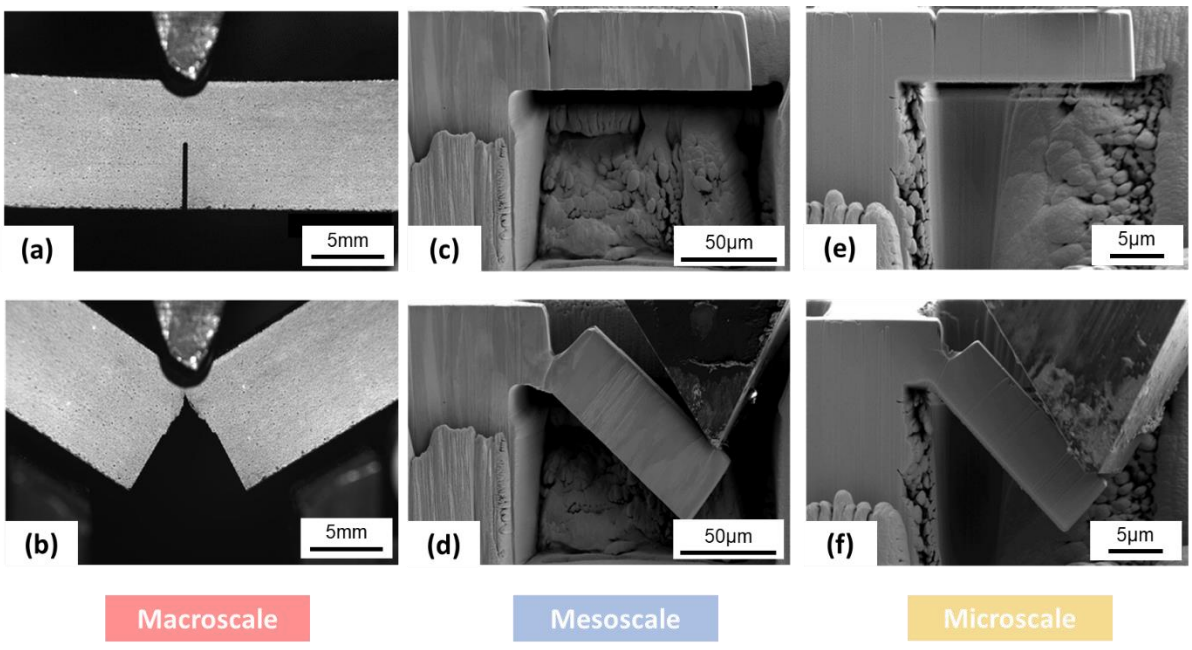

Figure 86: : Illustration of the three scales of interest (before and after bending)
(a, b) Macroscale (c, d) Mesoscale (e, f) Microscale

The main challenge of analyzing the role of each interface was locating the position of the initial notch with respect to the microstructure. The position of the notch was assessed post-machining by performing EBSD analyses, however many difficulties were faced to obtain good quality EBSD maps, as the precision over machining at such small scales is limited. Moreover,

Figure 87 indicates that the position of the notch is often debatable: the side view in Figure 87a displays a notch located at a grain boundary, whereas the top view in Figure 87b shows that the notch actually crosses several grains.

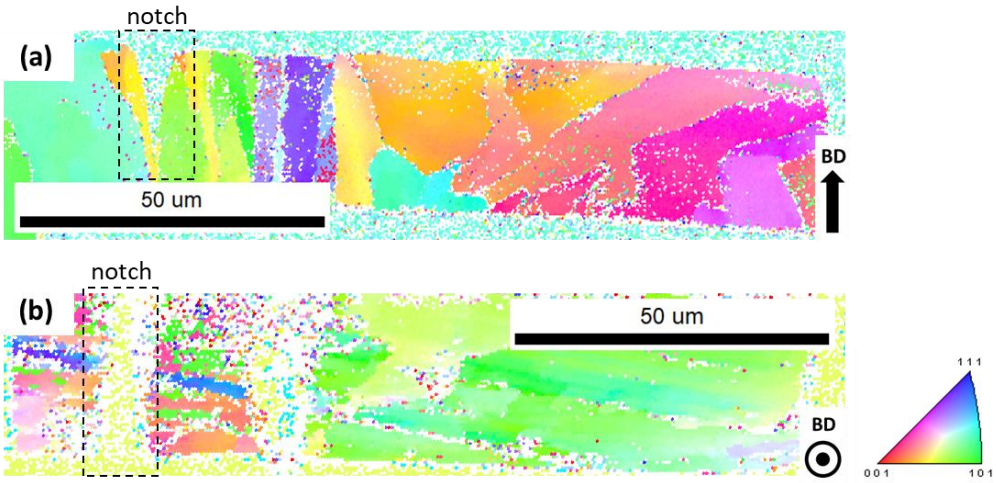

Figure 87: EBSD maps for one meso-specimen, showing the placement of the initial notch
(a) Side view (XZ plane) (b) Top view (XY plane)

The first post-mortem observations performed on meso and micro-specimens revealed that no matter the position of the notch with respect to the microstructure, no clear crack propagation occurs, and only ductile tearing is observed as shown by the example provided in Figure 88a. In addition, significant plastic deformation is noted at the crack tip as reported in Figure 88b and c.

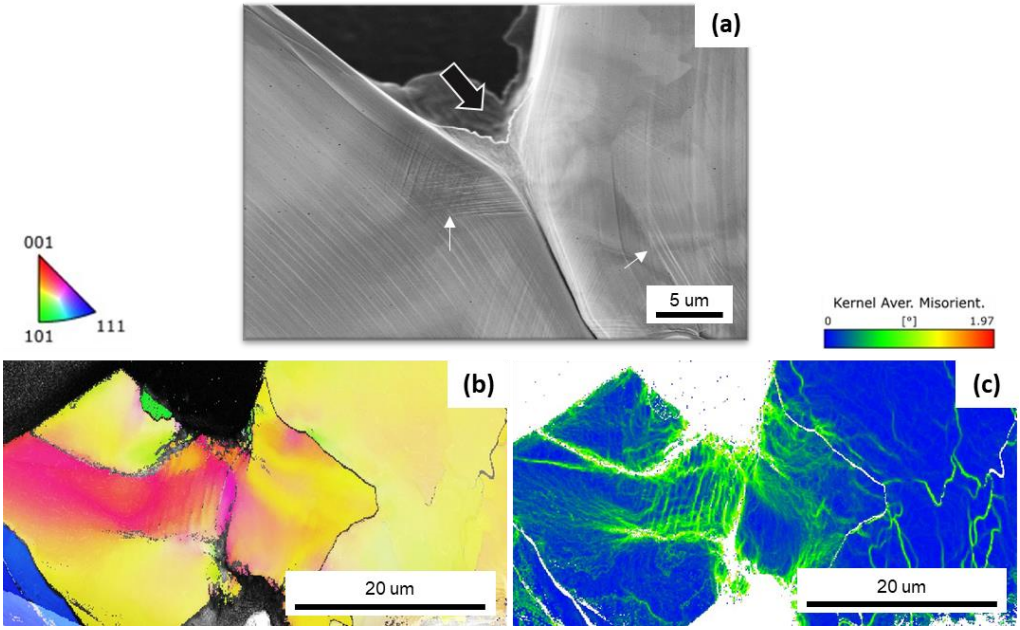

Figure 88: Ductile tearing observed post-mortem for a meso-specimen
(a) SEM image of the crack tip (ductile tearing pointed by the black arrow, and slip bands pointed by the white arrows) (b) EBSD map at the crack tip (c) Kernel Average Misorientation (KAM) image at the crack tip

Given the difficulties to identify the position of the notch and get actual crack propagation to identify a preferential path for both the meso and micro-specimens, another approach was considered to compare the three configurations: analyzing the specimens behavior and the different scales from a mechanical standpoint.

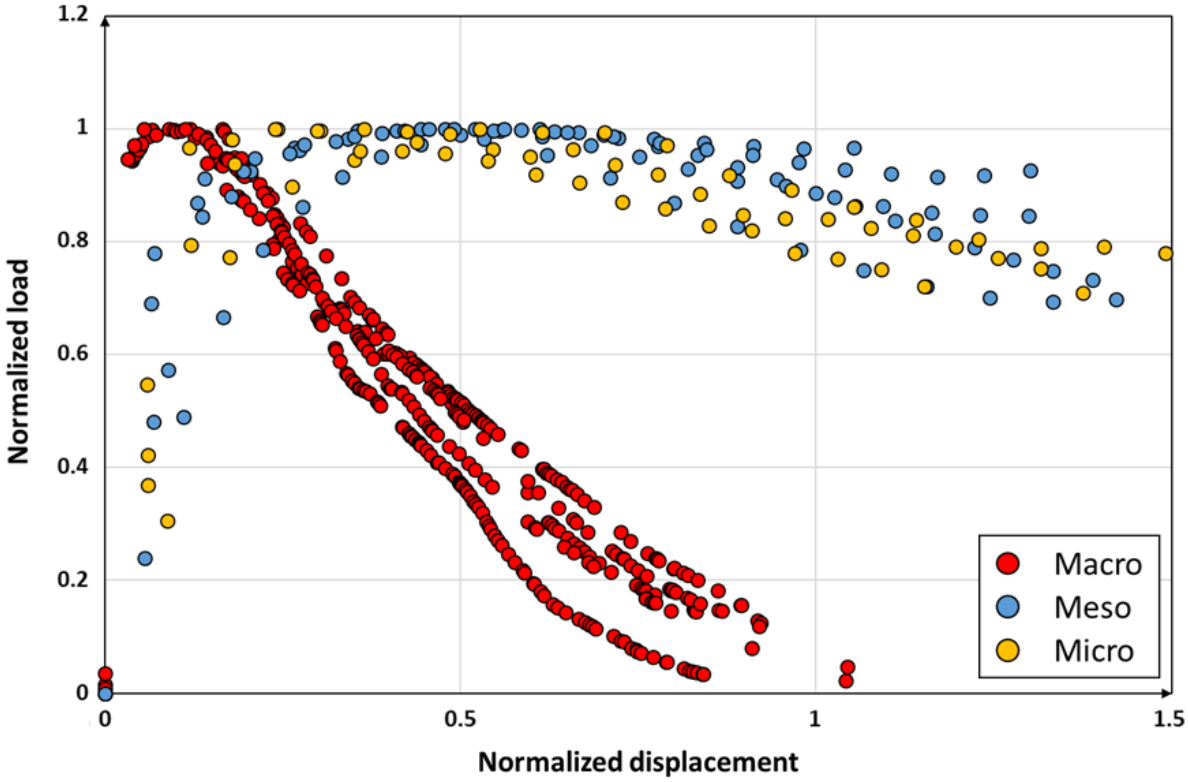

Figure 89: Normalized load-displacement curves for the three scales considered

Figure 89 shows the normalized load-displacement curves, as the sizes of the specimens considerably varies between the three scales. The behaviors between the meso and micro-specimens are pretty similar, while a drop in load is observed only for macro-specimens. The compliance plotted in Figure 90 follows the same trend, with an increase visible only for macro-specimens, while meso and micro-specimens display no variation. However, it is important to remind that the compliance of the macro-specimens has not been assessed experimentally due to the absence of unloadings, and has been computed empirically using formulas provided by the test standard ASTM E1820 [114]. Therefore, the comparison here is relevant, but still debatable.

Due to the absence of compliance evolution, measuring the crack extension using the compliance method is not possible for meso and micro-specimens. Instead, the same procedure as for macroscale three-point bending tests is implemented: monitoring the crack evolution (crack tearing) from the surface, using in-situ SEM images. However, it is important to note

that this method lacks precision due to the limited quality of the resolution and the small size of the specimens.

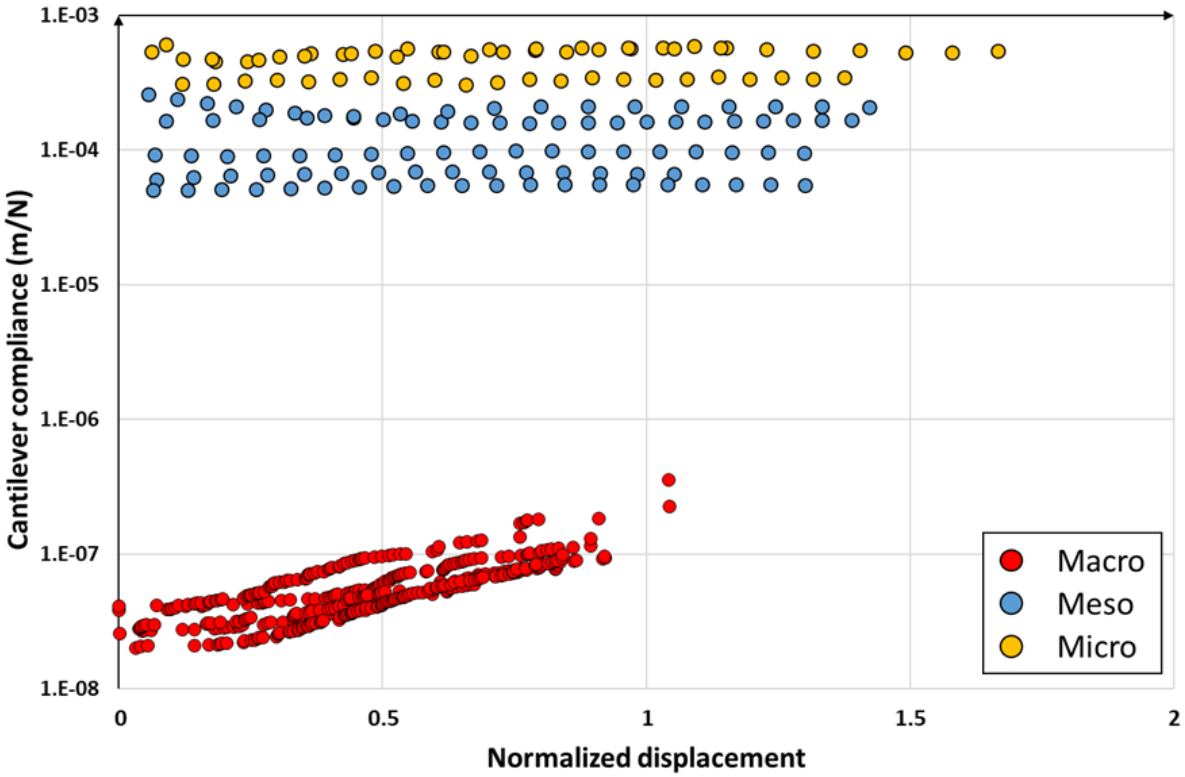

Figure 90: Compliance evolution for the three scales considered

Using ASTM E1820 [114] method, resistance curves were plotted for both meso and micro-specimens and are displayed in Figure 91. However, these curves also exhibit no change in trend to identify a fracture toughness value. Hence, another method is considered to identify a J-integral value at initiation: taking the J-integral value corresponding to the maximum load [200]. This J-integral value at initiation is noted J_{ini}. In the case of macro-specimens, the resulting values are not far from the ones determined using the slope change method [182]. The values obtained for J_{ini} using this method are reported in Table 17.

Table 17: Fracture toughness values determined for the three scales considered

	Macroscale					**Mesoscale**					**Microscale**			
Specimen	1	2	3	4	5	1	2	3	4	5	1	2	3	4
J_{ini} (kJ/m²)	310	302	294	310	256	2.19	1.25	1.75	2.20	2.47	0.24	0.14	0.27	0.50

The values computed show a significant size effect on the fracture properties, as the fracture toughness values evaluated drastically vary for each scale considered: a fracture

toughness of approximately 295 kJ/m² is obtained at the macroscale, against 2 kJ/m² at the mesoscale and 0.2 kJ/m² at the microscale. The low values for the meso and micro scales are not representative of the physical phenomena occurring, as the crack is actually very difficult to initiate at these smaller scales.

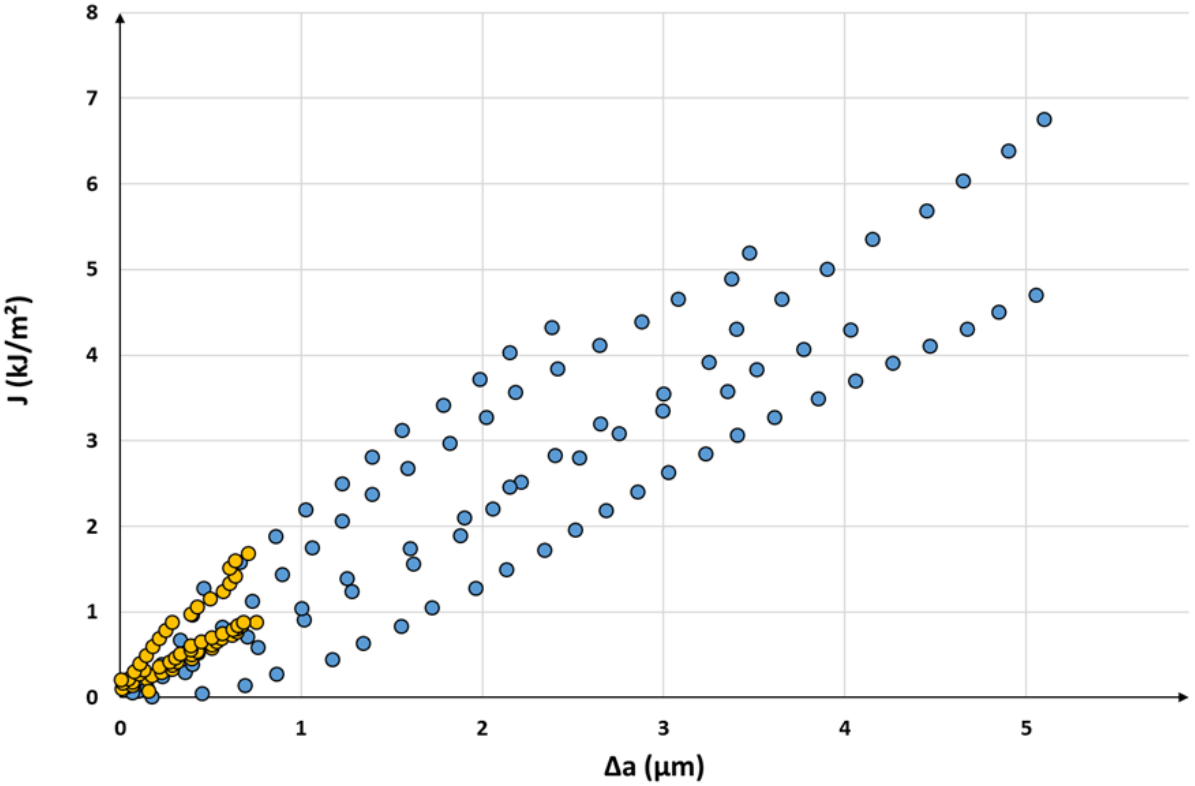

Figure 91: Resistance curves obtained for meso and micro specimens

In order to validate the usual method used to determine the J-integral value at initiation [114], the criterion given by equation (39) is used. This criterion ensures that the dimensions of the specimen considered are big enough to result in a plane strain state at the core of the specimen.

$$(W - a_0; B) > C \frac{J_{ini}}{\sigma_Y} \tag{39}$$

In this equation, W is the specimen width, a_0 the initial crack length, and B the thickness. σ_Y is the flow stress, taken as the mean value between the yield stress σ_{YS} and the ultimate tensile stress σ_{UTS}, and C is a coefficient which varies from 10 to 50 in the literature. In ASTM E1820 [114], it is set at 10.

In the present study, it is a well-known fact that this criterion is far from being validated, especially considering the small dimensions of the specimens and the high ductility of Ni20Cr. The focus of this work lies in comparing the influence of different specimen sizes. The literature indicates that to obtain reliable fracture toughness values, C should be set at 10. This value is related to the size of the Irwin plastic zone, and ensures that the plastic zone is sufficiently smaller than the specimen's size. The specimens from the macro, meso and micro scales considered in this work are associated with mean C values of respectively 0.003, 0.03 and 8. Except for the macro-specimens, which approach the criterion of 10, the values are significantly below the standard. Nonetheless, this provides an opportunity to investigate the relationship between the coefficient C and the specimen's size. As proposed by [201], C is plotted against the J_{ini} values in Figure 92. Results indicate that a dependence of the J_{ini} on the parameter C may exist, which means that the dissipated energy is a function of the specimen dimensions. For smaller specimens (lower C values), less energy is dissipated, and as a result lower J_{ini} values are determined. However, these values are not representative of the reality of the specimen, as the crack is actually not easier to initiate or propagate and is subjected to tearing and significant plastic deformation. Therefore, this reasoning cannot be applied to describe the physical phenomenon occurring.

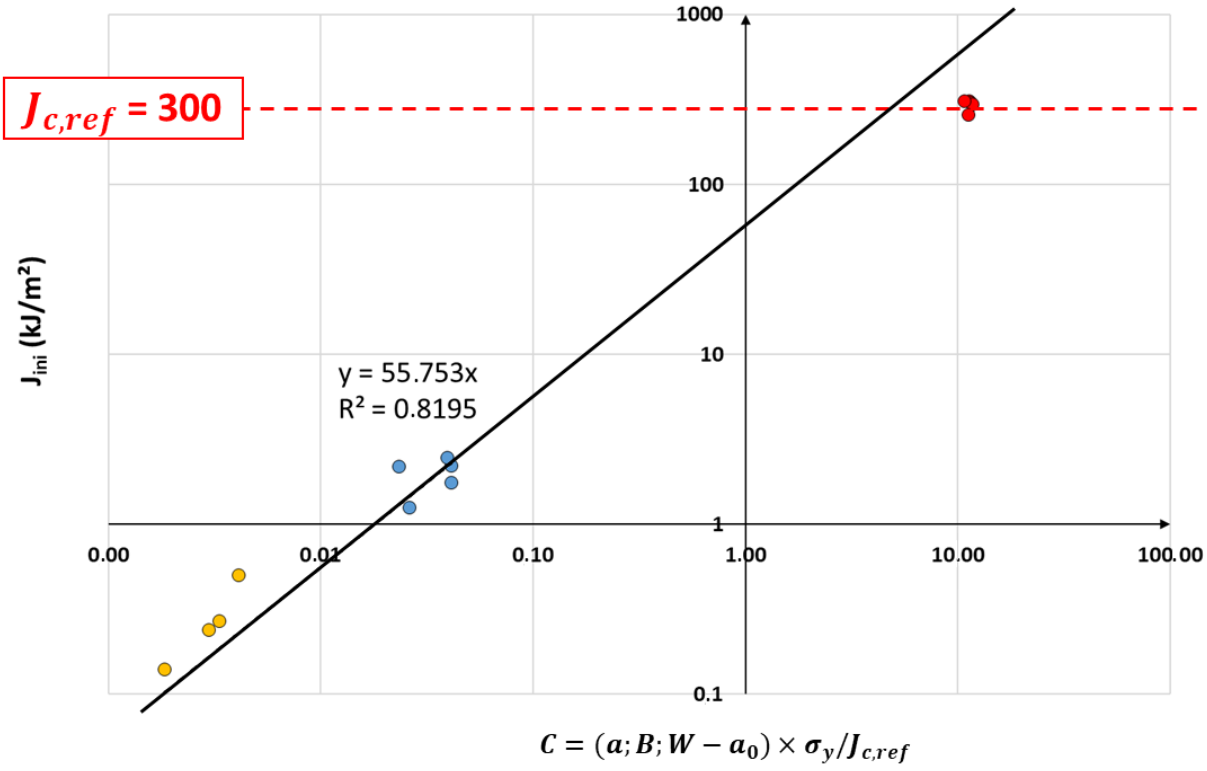

Figure 92: J_{ini} value as a function of the C coefficient
(The macroscopic J_{ini} value is given as a reference in red)

Instead, the interest of this process is shifted to see if a coherent J_{ini} value could still be extracted from the meso and micro scales results. Figure 92 displays a trend that could allow the determination of a threshold value to take for C, equals here to 4.4. This could mean that for a set value of C, the determination of the fracture toughness may be done by plotting J_{ini} as a function of C.

However, many points set back the discussion on this hypothesis, the first one being that nothing assures that the trend is linear here, as not enough data has been obtained so far. The reference value taken may not be correct as well, knowing it has been stated that the specimen's dimensions do not comply with the significantly larger dimensions recommended by the standards. Additionally, it is important to note the difference in geometry between macroscopic (three-point bending) and meso/microscopic (microcantilever) specimens, which may lead to significant differences in behavior. In particular, it is known that there is a much higher deformation gradient along the height of the specimen at both the meso and micro scales due to the size reduction. This gradient can greatly impact mechanical properties like the yield stress of the material due to the higher dislocation density induced. Finally, the method used in this study implies successive unloadings, which may induce phenomena like irreversible evolution of dislocation pile-ups and result in a bias during the crack propagation test [202,203]. A lot of aspects hence remain to be investigated in order to validate the trend observed.

II.2. Discussion and perspectives

In this section, an attempt to investigate the influence of the different interfaces on the fracture behavior of the L-PBF Ni20Cr alloy was presented. However, this initial objective was hindered by two main issues: the difficulties to locate the position of the notch with respect to the microstructure, and most importantly the significant plastic deformation that prevented any actual crack propagation. However, this work opened up the discussion on the size effects on the fracture properties of L-PBF Ni20Cr, and the possibility to determine valid fracture toughness values from small-scale specimens. The discussion has yet to be continued, however the following points may serve as prospects to investigate:

- Working on similar geometries at macro and meso/micro scales would be more representative and allow a better comparison.

- Introducing intermediate specimen sizes between meso and macro-specimens to expand the database to validate or invalidate the trend observed.

- Researching a way to avoid using unloading methods to avoid any bias on the crack propagation, by means of continuous dynamical testing [204]

- Investigating cast & wrought specimens to assess if there is a difference in behavior at the meso/microscale.

CHAPTER 6:
Conclusions & Perspectives

This PhD aimed at characterizing the influence of three main processing parameters on the microstructure and fracture behavior of the Ni20Cr L-PBF alloy: the building orientation (horizontal or vertical), the rotation angle (67° or 90°), and the VED (60 J/mm^3 or 90 J/mm^3). Another objective was also to compare the behavior of L-PBF specimens with annealed cast & wrought specimens. Figure 93 presents a graphical overview of the different aspects investigated in the current work. The main conclusions could be drawn from the results presented:

- Both the initial microstructure and the tensile properties are heavily influenced by all the processing parameters, as they have a significant impact on the heat dissipation of the specimens. The building orientation mainly influences the crystallographic texture, with vertical specimens usually more textured than horizontal ones, while the rotation angle affects considerably the grain morphology. The VED influences both, with more elongated grains and higher textures associated with an increasing VED.

- As a result of the microstructural features, tensile properties are also impacted, with a major influence from the building orientation. Vertical specimens usually display lower Young's Modulus, yield and ultimate tensile stress values, but improved ductility compared to horizontal specimens. They also display higher resistance to strain hardening. The differences between the rotation angles or VEDs are however less noticeable. A correlation between the yield stress and the inverse of the square root of the dendritic arm spacing has been identified, with two different trends depending on the building orientation which remain to be confirmed.

- The fracture behavior is also affected by the processing parameters, with overall better resistance to crack initiation and propagation for vertical specimens compared to horizontal ones. The discrepancies between both building orientations are increased or reduced depending on the rotation angle or VED considered.

- The post-mortem microstructure analyses revealed that the fracture behavior is governed by two aspects depending on the VED considered. For a VED of 90 J/mm^3,

the microstructure has the most influence, in particular the grain's size, morphology, and orientation. Even though a mixed fracture mode between intergranular and transgranular is observed, one can be promoted more than the other according to the building orientation. When grains are oriented parallel to the crack propagation direction (horizontal specimens), more grain boundaries are aligned with the crack path and the propagation tends to be intergranular. On the contrary, for a perpendicular orientation (vertical specimens), fewer grain boundaries are aligned with the crack path, and transgranular propagation is promoted. More energy is dissipated for vertical specimens, hence improving the specimen's overall fracture resistance. This phenomenon is accentuated by the more unidirectional grain distribution resulting from a rotation angle of 90° compared to one of 67°. On the other hand, at a VED of 60 J/mm^3, the microstructure is pretty similar for both building orientations. Therefore, the gap between the two building orientations is associated with the tensile properties, especially the difference in ductility. In all cases, the meltpool boundaries and the crystallographic texture did not play a significant role. The interdendritic arm spacing on the other hand is considered as a second-order influence on the fracture behavior, but should be more investigated for any statement to be made.

- Cast & wrought and L-PBF specimens were compared in terms of both microstructure and mechanical properties, and exhibited very different behaviors. Contrary to the columnar, anisotropic L-PBF microstructure, cast & wrought specimens present equiaxed grains with twins. The tensile behavior is also different with lower yield stress values, and a more prominent ductility and strain hardening behavior. As expected, the fracture behavior also differed drastically, with a much higher resistance to crack initiation and propagation, and an intergranular fracture mode. Its high ductility and tendency to form secondary cracks are coherent with its better resistance as more energy is dissipated during crack propagation. However, the difference in chemical composition with L-PBF specimens is to be taken with caution when comparison between specimens is made.

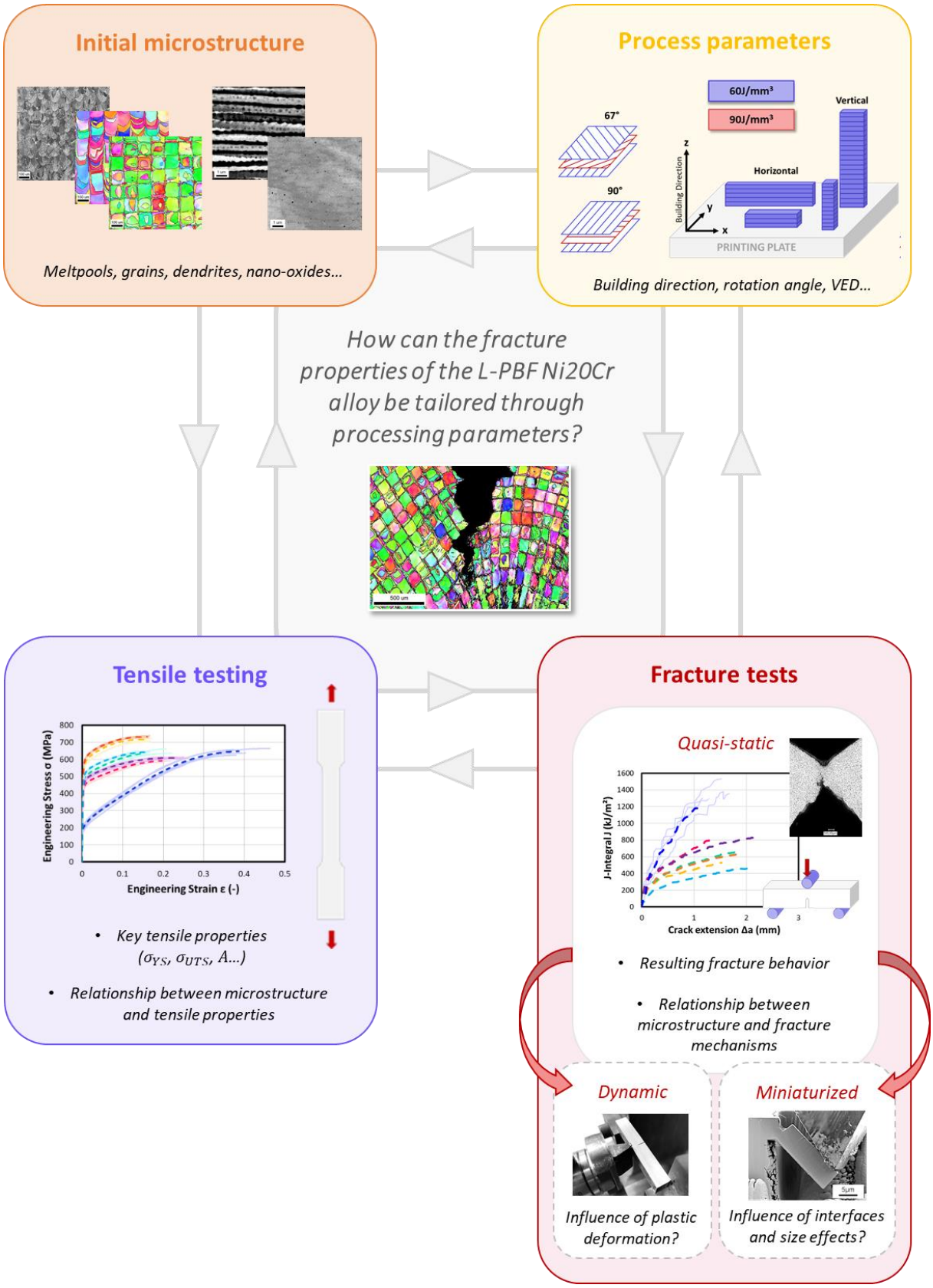

Figure 93: Graphical overview of the PhD objectives

This study opened up many prospects for future studies, as a lot of aspects remain to be uncovered regarding the fracture behavior of Ni20Cr L-PBF alloy. A few suggestions are listed below to pursue this work:

- An investigation of the highest VED resulting in dense specimens, 120 J/mm^3, should be carried out to get a wider panel of results regarding the microstructure and fracture behavior.
- On a similar note, as the key parameters improving the fracture resistance are a vertical building orientation, a 90° angle, and a VED of 60 J/mm^3, it would be interesting to investigate the fracture properties of this configuration to see if it can improve the fracture behavior compared to what has been observed so far.
- As conventionally made specimens pose issues in terms of reliable comparison with L-PBF specimens, it would be relevant to carry out a comparison with fully recrystallized L-PBF specimens. It would be closer in chemical composition to as-built L-PBF specimens, while presenting the typical microstructure of conventional Ni20Cr alloy.
- The studies on both the influence of the loading rate and the size effect on the fracture behavior are still under discussion, however considering the importance of plastic deformation and ductility on the fracture behavior, the first results support that both remain very relevant to pursue.
- Finally, it would be relevant to consider conducting crack propagation simulations on Zcrack to differentiate the energy required only to propagate the crack, from the energy dissipated by the plastic deformation occurring around the crack tip.

REFERENCES

[1] A. Charles, A. Hofer, A. Elkaseer, S. Scholz, Additive Manufacturing in the Automotive Industry and the Potential for Driving the Green and Electric Transition, in: Sustainable Design and Manufacturing, Springer, 2021: pp. 339–346. https://doi.org/10.1007/978-981-16-6128-0_32.

[2] B. Blakey-Milner, P. Gradl, G. Snedden, M. Brooks, J. Pitot, E. Lopez, M. Leary, F. Berto, A. du Plessis, Metal additive manufacturing in aerospace: A review, Materials & Design 209 (2021) 110008. https://doi.org/10.1016/j.matdes.2021.110008.

[3] M. Salmi, Additive Manufacturing Processes in Medical Applications, Materials (Basel) 14 (2021) 191. https://doi.org/10.3390/ma14010191.

[4] L. Bravi, F. Murmura, Additive Manufacturing in the Food Sector: A Literature Review, Macromolecular Symposia 395 (2021). https://doi.org/10.1002/masy.202000199.

[5] Wohlers Report 2018, Wohlers Associates (n.d.). https://wohlersassociates.com/product/wohlers-report-2018/ (accessed August 16, 2024).

[6] C. Scott, Wohlers Report 2023 Unveils Continued Double-Digit Growth, Wohlers Associates (2023). https://wohlersassociates.com/news/wohlers-report-2023-unveils-continued-double-digit-growth/ (accessed August 15, 2024).

[7] M. Armstrong, H. Mehrabi, N. Naveed, An overview of modern metal additive manufacturing technology, Journal of Manufacturing Processes 84 (2022) 1001–1029. https://doi.org/10.1016/j.jmapro.2022.10.060.

[8] A. Mostafaei, C. Zhao, Y. He, S. Reza Ghiaasiaan, B. Shi, S. Shao, N. Shamsaei, Z. Wu, N. Kouraytem, T. Sun, J. Pauza, J.V. Gordon, B. Webler, N.D. Parab, M. Asherloo, Q. Guo, L. Chen, A.D. Rollett, Defects and anomalies in powder bed fusion metal additive manufacturing, Current Opinion in Solid State and Materials Science 26 (2022) 100974. https://doi.org/10.1016/j.cossms.2021.100974.

[9] A. Vafadar, F. Guzzomi, A. Rassau, K. Hayward, Advances in Metal Additive Manufacturing: A Review of Common Processes, Industrial Applications, and Current Challenges, Applied Sciences 11 (2021) 1213. https://doi.org/10.3390/app11031213.

[10] F. Schulz, K. Lindgren, J. Xu, E. Hryha, Gamma prime formation in nickel-based superalloy IN738LC manufactured by laser powder bed fusion, Materials Today Communications 38 (2024) 107905. https://doi.org/10.1016/j.mtcomm.2023.107905.

[11] H. Liu, W. Cheng, Y. Sun, R. Ma, Y. Wang, J. Bai, L. Xue, X. Song, C. Tan, Effects of Process Parameters and Heat Treatment on Microstructure and Mechanical Characteristics of Laser Powder Bed Fusion Alloy Inconel 718, Coatings 13 (2023) 189. https://doi.org/10.3390/coatings13010189.

[12] D. Zhang, Z. Feng, C. Wang, W. Wang, Z. Liu, W. Niu, Comparison of microstructures and mechanical properties of Inconel 718 alloy processed by selective laser melting and casting, Materials Science and Engineering: A 724 (2018) 357–367. https://doi.org/10.1016/j.msea.2018.03.073.

[13] E. Hosseini, V.A. Popovich, A review of mechanical properties of additively manufactured Inconel 718, Additive Manufacturing 30 (2019) 100877. https://doi.org/10.1016/j.addma.2019.100877.

[14] G.M. Volpato, U. Tetzlaff, M.C. Fredel, A comprehensive literature review on laser powder bed fusion of Inconel superalloys, Additive Manufacturing 55 (2022) 102871. https://doi.org/10.1016/j.addma.2022.102871.

[15] G. Huang, K. Wei, J. Deng, M. Liu, X. Zeng, High-power laser powder bed fusion of 316L stainless steel: Defects, microstructure, and mechanical properties, Journal of Manufacturing Processes 83 (2022) 235–245. https://doi.org/10.1016/j.jmapro.2022.08.066.
[16] Q. Zhong, K. Wei, Z. Lu, X. Yue, T. Ouyang, X. Zeng, High power laser powder bed fusion of Inconel 718 alloy: Effect of laser focus shift on formability, microstructure and mechanical properties, Journal of Materials Processing Technology 311 (2023) 117824. https://doi.org/10.1016/j.jmatprotec.2022.117824.
[17] M.L. Montero-Sistiaga, M. Godino-Martinez, K. Boschmans, J.-P. Kruth, J. Van Humbeeck, K. Vanmeensel, Microstructure evolution of 316L produced by HP-SLM (high power selective laser melting), Additive Manufacturing 23 (2018) 402–410. https://doi.org/10.1016/j.addma.2018.08.028.
[18] R. Esmaeilizadeh, A. Keshavarzkermani, U. Ali, B. Behravesh, A. Bonakdar, H. Jahed, E. Toyserkani, On the effect of laser powder-bed fusion process parameters on quasi-static and fatigue behaviour of Hastelloy X: A microstructure/defect interaction study, Additive Manufacturing 38 (2021) 101805. https://doi.org/10.1016/j.addma.2020.101805.
[19] D. Du, A. Dong, D. Shu, G. Zhu, B. Sun, X. Li, E. Lavernia, Influence of build orientation on microstructure, mechanical and corrosion behavior of Inconel 718 processed by selective laser melting, Materials Science and Engineering: A 760 (2019) 469–480. https://doi.org/10.1016/j.msea.2019.05.013.
[20] L.C. Araújo, A.H.G. Gabriel, E.B. Da Fonseca, J.A. Avila, A.L. Jardini, R. Seno Junior, É.S.N. Lopes, Effects of build orientation and heat treatments on the tensile and fracture toughness properties of additively manufactured AlSi10Mg, International Journal of Mechanical Sciences 213 (2022) 106868. https://doi.org/10.1016/j.ijmecsci.2021.106868.
[21] W. Beard, R. Lancaster, N. Barnard, T. Jones, J. Adams, The influence of surface finish and build orientation on the low cycle fatigue behaviour of laser powder bed fused stainless steel 316L, Materials Science and Engineering: A 864 (2023) 144593. https://doi.org/10.1016/j.msea.2023.144593.
[22] M. Simonelli, Y.Y. Tse, C. Tuck, Effect of the build orientation on the mechanical properties and fracture modes of SLM Ti–6Al–4V, Materials Science and Engineering: A 616 (2014) 1–11. https://doi.org/10.1016/j.msea.2014.07.086.
[23] A. Keshavarzkermani, R. Esmaeilizadeh, U. Ali, P.D. Enrique, Y. Mahmoodkhani, N.Y. Zhou, A. Bonakdar, E. Toyserkani, Controlling mechanical properties of additively manufactured hastelloy X by altering solidification pattern during laser powder-bed fusion, Materials Science and Engineering: A 762 (2019) 138081. https://doi.org/10.1016/j.msea.2019.138081.
[24] Z. Zheng, B. Sun, L. Mao, Effect of Scanning Strategy on the Manufacturing Quality and Performance of Printed 316L Stainless Steel Using SLM Process, Materials 17 (2024) 1189. https://doi.org/10.3390/ma17051189.
[25] C. Zhao, Y. Bai, Y. Zhang, X. Wang, J.M. Xue, H. Wang, Influence of scanning strategy and building direction on microstructure and corrosion behaviour of selective laser melted 316L stainless steel, Materials & Design 209 (2021) 109999. https://doi.org/10.1016/j.matdes.2021.109999.
[26] M. Prior, Safran 3D Prints a Titanium Nose Landing Gear Component For a Business Jet, 3Dnatives (2021). https://www.3dnatives.com/en/safran-3d-prints-a-titanium-nose-landing-gear-component-070420216/ (accessed June 11, 2024).
[27] The Raptor Reloaded, Enabling The Future (2015). https://enablingthefuture.org/upper-limb-prosthetics/raptor-reloaded/ (accessed June 11, 2024).

[28] Impression 3D de pistons - Porsche Innovations, (n.d.). https://media.porsche.com/mediakit/porsche-innovationen/fr/porsche-innovationen/3d-printed-pistons (accessed June 11, 2024).
[29] 3D by flow, (n.d.). https://www.3dbyflow.com/ (accessed June 11, 2024).
[30] ISO/ASTM 52900:2021(en), Additive manufacturing — General principles — Fundamentals and vocabulary, (n.d.). https://www.iso.org/obp/ui/#iso:std:iso-astm:52900:ed-2:v1:en (accessed June 11, 2024).
[31] E. Haapa, A. Gopaluni, H. Piili, A. Ganvir, A. Salminen, J. Ottelin, Validation of powder layering simulation via packing density measurement for laser-based powder bed fusion, IOP Conference Series: Materials Science and Engineering 1296 (2023) 012020. https://doi.org/10.1088/1757-899X/1296/1/012020.
[32] P.K. Gokuldoss, S. Kolla, J. Eckert, Additive Manufacturing Processes: Selective Laser Melting, Electron Beam Melting and Binder Jetting—Selection Guidelines, Materials 10 (2017) 672. https://doi.org/10.3390/ma10060672.
[33] G. Marion, L'impression 3D par fusion de faisceau d'électrons (EBM), on vous explique tout !, 3Dnatives (2019). https://www.3dnatives.com/impression-3d-faisceau-electrons/ (accessed June 11, 2024).
[34] Les mystères de la fusion par faisceau d'électrons (EBM), MetalBlog (2022). https://metalblog.ctif.com/2022/01/24/les-mysteres-de-la-fusion-par-faisceau-delectrons-ebm/ (accessed June 11, 2024).
[35] La fabrication additive des alliages métalliques 1 - Procédés, matière première et simulation numérique, ISTE Editions, 2022.
[36] M. Lelievre, Elaboration de l'alliage Ni 20 wt. % Cr par fusion sélective laser : effet des paramètres de fabrication sur la microstructure, le comportement mécanique en traction et la stabilité thermique, Thèse de doctorat, Université de Caen Normandie, 2021.
[37] E. Hug, M. Lelièvre, C. Folton, A. Ribet, M. Martinez-Celis, C. Keller, Additive manufacturing of a Ni-20 wt%Cr binary alloy by laser powder bed fusion: Impact of the microstructure on the mechanical properties, Materials Science and Engineering: A 834 (2022) 142625. https://doi.org/10.1016/j.msea.2022.142625.
[38] Q. Zhong, K. Wei, T. Ouyang, X. Li, X. Zeng, Effect of rotation angle on surface morphology, microstructure, and mechanical properties of Inconel 718 alloy fabricated by high power laser powder bed fusion, Journal of Materials Science & Technology 154 (2023) 30–42. https://doi.org/10.1016/j.jmst.2023.01.021.
[39] T. Ronneberg, C.M. Davies, P.A. Hooper, Revealing relationships between porosity, microstructure and mechanical properties of laser powder bed fusion 316L stainless steel through heat treatment, Materials & Design 189 (2020) 108481. https://doi.org/10.1016/j.matdes.2020.108481.
[40] J. Kangazian, M. Shamanian, A. Kermanpur, E. Foroozmehr, M. Badrossamay, Investigation of microstructure-tensile behavior relationship in Hastelloy X Ni-based superalloy processed by laser powder-bed fusion: Insights into the elevated temperature ductility loss, Materials Science and Engineering: A 823 (2021) 141742. https://doi.org/10.1016/j.msea.2021.141742.
[41] Y. Tian, D. Tomus, P. Rometsch, X. Wu, Influences of processing parameters on surface roughness of Hastelloy X produced by selective laser melting, Additive Manufacturing 13 (2017) 103–112. https://doi.org/10.1016/j.addma.2016.10.010.
[42] J.P. Oliveira, A.D. LaLonde, J. Ma, Processing parameters in laser powder bed fusion metal additive manufacturing, Materials & Design 193 (2020) 108762. https://doi.org/10.1016/j.matdes.2020.108762.

[43] C. Su, H. Yu, Z. Wang, J. Yang, X. Zeng, Controlling the tensile and fatigue properties of selective laser melted Ti–6Al–4V alloy by post treatment, Journal of Alloys and Compounds 857 (2021) 157552. https://doi.org/10.1016/j.jallcom.2020.157552.
[44] D. Tomus, T. Jarvis, X. Wu, J. Mei, P. Rometsch, E. Herny, J.-F. Rideau, S. Vaillant, Controlling the Microstructure of Hastelloy-X Components Manufactured by Selective Laser Melting, Physics Procedia 41 (2013) 823–827. https://doi.org/10.1016/j.phpro.2013.03.154.
[45] L. Wang, Q. Wei, Y. Shi, J. Liu, W. He, Experimental Investigation into the Single-Track of Selective Laser Melting of IN625, Advanced Materials Research 233–235 (2011) 2844–2848. https://doi.org/10.4028/www.scientific.net/AMR.233-235.2844.
[46] I. Yadroitsev, I. Yadroitsava, P. Bertrand, I. Smurov, Factor analysis of selective laser melting process parameters and geometrical characteristics of synthesized single tracks, Rapid Prototyping Journal 18 (2012) 201–208. https://doi.org/10.1108/13552541211218117.
[47] S.L. Campanelli, G. Casalino, N. Contuzzi, A. Angelastro, L. Antonio Domenico, Analysis of the molten/solidified zone in selective laser melted parts, in: 2014: p. 896311. https://doi.org/10.1117/12.2042170.
[48] J. Ciurana, L. Hernandez, J. Delgado Sanglas, Energy density analysis on single tracks formed by selective laser melting with CoCrMo powder material, The International Journal of Advanced Manufacturing Technology 68 (2013). https://doi.org/10.1007/s00170-013-4902-4.
[49] T. De Terris, O. Castelnau, Z. Hamouche, H. Haddadi, V. Michel, P. Peyre, Analysis of As-Built Microstructures and Recrystallization Phenomena on Inconel 625 Alloy Obtained via Laser Powder Bed Fusion (L-PBF), Metals 11 (2021). https://doi.org/10.3390/met11040619.
[50] U. Scipioni Bertoli, A.J. Wolfer, M.J. Matthews, J.-P.R. Delplanque, J.M. Schoenung, On the limitations of Volumetric Energy Density as a design parameter for Selective Laser Melting, Materials & Design 113 (2017) 331–340. https://doi.org/10.1016/j.matdes.2016.10.037.
[51] A. Paraschiv, G. Matache, M.R. Condruz, T.F. Frigioescu, L. Pambaguian, Laser Powder Bed Fusion Process Parameters' Optimization for Fabrication of Dense IN 625, Materials 15 (2022) 5777. https://doi.org/10.3390/ma15165777.
[52] Standard Guide for Characterizing Properties of Metal Powders Used for Additive Manufacturing Processes, (n.d.). https://www.astm.org/f3049-14r21.html (accessed June 11, 2024).
[53] S. Vock, B. Klöden, A. Kirchner, T. Weißgärber, B. Kieback, Powders for powder bed fusion: a review, Prog Addit Manuf 4 (2019) 383–397. https://doi.org/10.1007/s40964-019-00078-6.
[54] N. Li, T. Wang, L. Zhang, L. Zhang, Crack initiation mechanism of laser powder bed fusion additive manufactured Al-Zn-Mg-Cu alloy, Materials Characterization 195 (2023) 112415. https://doi.org/10.1016/j.matchar.2022.112415.
[55] F. Liu, Y. Chen, L. Li, C. Wang, Q. Wang, Y. Liu, Interior defect-induced crack initiation mechanism and initial growth behavior for Ti6Al4V alloy fabricated using laser powder bed fusion, Journal of Materials Research and Technology 21 (2022) 2089–2104. https://doi.org/10.1016/j.jmrt.2022.10.043.
[56] C. Du, Y. Zhao, J. Jiang, Q. Wang, H. Wang, N. Li, J. Sun, Pore defects in Laser Powder Bed Fusion: Formation mechanism, control method, and perspectives, Journal of Alloys and Compounds 944 (2023) 169215. https://doi.org/10.1016/j.jallcom.2023.169215.

[57] C. Zöller, N.A. Adams, S. Adami, Numerical investigation of balling defects in laser-based powder bed fusion of metals with Inconel 718, Additive Manufacturing 73 (2023) 103658. https://doi.org/10.1016/j.addma.2023.103658.
[58] J.V. Gordon, S.P. Narra, R.W. Cunningham, H. Liu, H. Chen, R.M. Suter, J.L. Beuth, A.D. Rollett, Defect structure process maps for laser powder bed fusion additive manufacturing, Additive Manufacturing 36 (2020) 101552. https://doi.org/10.1016/j.addma.2020.101552.
[59] T. De Terris, O. Andreau, P. Peyre, F. Adamski, I. Koutiri, C. Gorny, C. Dupuy, Optimization and comparison of porosity rate measurement methods of Selective Laser Melted metallic parts, Additive Manufacturing 28 (2019) 802–813. https://doi.org/10.1016/j.addma.2019.05.035.
[60] H. Attar, M. Calin, L.C. Zhang, S. Scudino, J. Eckert, Manufacture by selective laser melting and mechanical behavior of commercially pure titanium, Materials Science and Engineering: A 593 (2014) 170–177. https://doi.org/10.1016/j.msea.2013.11.038.
[61] W. Liu, C. Liu, Y. Wang, H. Zhang, J. Li, Y. Lu, L. Xiong, H. Ni, Tailoring the microstructural and mechanical properties of 316L stainless steel manufactured by laser powder bed fusion, Journal of Materials Research and Technology 25 (2023) 7389–7405. https://doi.org/10.1016/j.jmrt.2023.07.158.
[62] S. Li, J.Y. Li, Z.W. Jiang, Y. Cheng, Y.Z. Li, S. Tang, J.Z. Leng, H.X. Chen, Y. Zou, Y.H. Zhao, J.P. Oliveira, Y. Zhang, K.H. Wang, Controlling the columnar-to-equiaxed transition during Directed Energy Deposition of Inconel 625, Additive Manufacturing 57 (2022) 102958. https://doi.org/10.1016/j.addma.2022.102958.
[63] X. Qi, X. Liang, J. Wang, H. Zhang, X. Wang, Z. Liu, Microstructure tailoring in laser powder bed fusion (L-PBF): Strategies, challenges, and future outlooks, Journal of Alloys and Compounds 970 (2024) 172564. https://doi.org/10.1016/j.jallcom.2023.172564.
[64] Y.-L. Kuo, S. Horikawa, K. Kakehi, The effect of interdendritic δ phase on the mechanical properties of Alloy 718 built up by additive manufacturing, Materials & Design 116 (2017) 411–418. https://doi.org/10.1016/j.matdes.2016.12.026.
[65] D. Herzog, V. Seyda, E. Wycisk, C. Emmelmann, Additive manufacturing of metals, Acta Materialia 117 (2016) 371–392. https://doi.org/10.1016/j.actamat.2016.07.019.
[66] N. Nadammal, S. Cabeza, T. Mishurova, T. Thiede, A. Kromm, C. Seyfert, L. Farahbod, C. Haberland, J.A. Schneider, P.D. Portella, G. Bruno, Effect of hatch length on the development of microstructure, texture and residual stresses in selective laser melted superalloy Inconel 718, Materials & Design 134 (2017) 139–150. https://doi.org/10.1016/j.matdes.2017.08.049.
[67] I. Serrano-Munoz, T. Mishurova, T. Thiede, M. Sprengel, A. Kromm, N. Nadammal, G. Nolze, R. Saliwan-Neumann, A. Evans, G. Bruno, The residual stress in as-built Laser Powder Bed Fusion IN718 alloy as a consequence of the scanning strategy induced microstructure, Sci Rep 10 (2020) 14645. https://doi.org/10.1038/s41598-020-71112-9.
[68] D. Deng, R.L. Peng, H. Brodin, J. Moverare, Microstructure and mechanical properties of Inconel 718 produced by selective laser melting: Sample orientation dependence and effects of post heat treatments, Materials Science and Engineering: A 713 (2018) 294–306. https://doi.org/10.1016/j.msea.2017.12.043.
[69] La fabrication additive des alliages métalliques 2 - Microstructures, post-traitements et propriétés d'usage, ISTE Editions, 2022.
[70] Y.M. Wang, T. Voisin, J.T. McKeown, J. Ye, N.P. Calta, Z. Li, Z. Zeng, Y. Zhang, W. Chen, T.T. Roehling, R.T. Ott, M.K. Santala, P.J. Depond, M.J. Matthews, A.V. Hamza, T. Zhu, Additively manufactured hierarchical stainless steels with high strength and ductility, Nature Mater 17 (2018) 63–71. https://doi.org/10.1038/nmat5021.

[71] M. Ni, C. Chen, X. Wang, P. Wang, R. Li, X. Zhang, K. Zhou, Anisotropic tensile behavior of in situ precipitation strengthened Inconel 718 fabricated by additive manufacturing, Materials Science and Engineering: A 701 (2017) 344–351. https://doi.org/10.1016/j.msea.2017.06.098.
[72] D. Kong, X. Ni, C. Dong, L. Zhang, C. Man, X. Cheng, X. Li, Anisotropy in the microstructure and mechanical property for the bulk and porous 316L stainless steel fabricated via selective laser melting, Materials Letters 235 (2019) 1–5. https://doi.org/10.1016/j.matlet.2018.09.152.
[73] S.R. Ch, A. Raja, P. Nadig, R. Jayaganthan, N.J. Vasa, Influence of working environment and built orientation on the tensile properties of selective laser melted AlSi10Mg alloy, Materials Science and Engineering: A 750 (2019) 141–151. https://doi.org/10.1016/j.msea.2019.01.103.
[74] A. Banerjee, J. Rossin, M.-R. He, W.D. Musinski, P.A. Shade, M.E. Cox, E.J. Schwalbach, T. Pollock, K.J. Hemker, Decoupling build orientation-induced geometric and texture effects on the mechanical response of additively manufactured IN625 thin-walled elements, Materials Science and Engineering: A 870 (2023) 144826. https://doi.org/10.1016/j.msea.2023.144826.
[75] A. Leicht, C.H. Yu, V. Luzin, U. Klement, E. Hryha, Effect of scan rotation on the microstructure development and mechanical properties of 316L parts produced by laser powder bed fusion, Materials Characterization 163 (2020) 110309. https://doi.org/10.1016/j.matchar.2020.110309.
[76] R. Esmaeilizadeh, A. Keshavarzkermani, U. Ali, Y. Mahmoodkhani, B. Behravesh, H. Jahed, A. Bonakdar, E. Toyserkani, Customizing mechanical properties of additively manufactured Hastelloy X parts by adjusting laser scanning speed, Journal of Alloys and Compounds 812 (2020) 152097. https://doi.org/10.1016/j.jallcom.2019.152097.
[77] H. Pan, T. Dahmen, M. Bayat, K. Lin, X. Zhang, Independent effects of laser power and scanning speed on IN718's precipitation and mechanical properties produced by LBPF plus heat treatment, Materials Science and Engineering: A 849 (2022) 143530. https://doi.org/10.1016/j.msea.2022.143530.
[78] M.L. Montero-Sistiaga, S. Pourbabak, J. Van Humbeeck, D. Schryvers, K. Vanmeensel, Microstructure and mechanical properties of Hastelloy X produced by HP-SLM (high power selective laser melting), Materials & Design 165 (2019) 107598. https://doi.org/10.1016/j.matdes.2019.107598.
[79] D. Tomus, Y. Tian, P.A. Rometsch, M. Heilmaier, X. Wu, Influence of post heat treatments on anisotropy of mechanical behaviour and microstructure of Hastelloy-X parts produced by selective laser melting, Materials Science and Engineering: A 667 (2016) 42–53. https://doi.org/10.1016/j.msea.2016.04.086.
[80] O. Sanchez-Mata, X. Wang, J.A. Muñiz-Lerma, S.E. Atabay, M. Attarian Shandiz, M. Brochu, Dependence of mechanical properties on crystallographic orientation in nickel-based superalloy Hastelloy X fabricated by laser powder bed fusion, Journal of Alloys and Compounds 865 (2021) 158868. https://doi.org/10.1016/j.jallcom.2021.158868.
[81] N. Kladovasilakis, P. Charalampous, K. Tsongas, I. Kostavelis, D. Tzovaras, D. Tzetzis, Influence of Selective Laser Melting Additive Manufacturing Parameters in Inconel 718 Superalloy, Materials 15 (2022) 1362. https://doi.org/10.3390/ma15041362.
[82] J.-R. Zhao, F.-Y. Hung, T.-S. Lui, Microstructure and tensile fracture behavior of three-stage heat treated inconel 718 alloy produced via laser powder bed fusion process, Journal of Materials Research and Technology 9 (2020) 3357–3367. https://doi.org/10.1016/j.jmrt.2020.01.030.
[83] Y. Lu, S. Wu, Y. Gan, T. Huang, C. Yang, J. Lin, J. Lin, Study on the microstructure, mechanical property and residual stress of SLM Inconel-718 alloy manufactured by

differing island scanning strategy, Optics & Laser Technology 75 (2015) 197–206. https://doi.org/10.1016/j.optlastec.2015.07.009.
[84] H. Yang, L. Meng, S. Luo, Z. Wang, Microstructural evolution and mechanical performances of selective laser melting Inconel 718 from low to high laser power, Journal of Alloys and Compounds 828 (2020) 154473. https://doi.org/10.1016/j.jallcom.2020.154473.
[85] D.S. Watring, J.T. Benzing, N. Hrabe, A.D. Spear, Effects of laser-energy density and build orientation on the structure–property relationships in as-built Inconel 718 manufactured by laser powder bed fusion, Additive Manufacturing 36 (2020) 101425. https://doi.org/10.1016/j.addma.2020.101425.
[86] S. Heo, Y. Lim, N. Kwak, C. Jeon, M. Choi, I. Jo, Impact of Heat Treatment and Building Direction on Tensile Properties and Fracture Mechanism of Inconel 718 Produced by SLM Process, Metals 14 (2024) 440. https://doi.org/10.3390/met14040440.
[87] A. Popovich, V. Sufiiarov, I. Polozov, E. Borisov, Microstructure and Mechanical Properties of Inconel 718 Produced by SLM and Subsequent Heat Treatment, Key Engineering Materials 651–653 (2015) 665–670. https://doi.org/10.4028/www.scientific.net/KEM.651-653.665.
[88] G. Marchese, S. Parizia, M. Rashidi, A. Saboori, D. Manfredi, D. Ugues, M. Lombardi, E. Hryha, S. Biamino, The role of texturing and microstructure evolution on the tensile behavior of heat-treated Inconel 625 produced via laser powder bed fusion, Materials Science and Engineering: A 769 (2020) 138500. https://doi.org/10.1016/j.msea.2019.138500.
[89] M.A. Anam, Microstructure and mechanical properties of selective laser melted superalloy inconel 625., Thèse de doctorat, University of Louisville, 2018. https://doi.org/10.18297/etd/3029.
[90] M. Condruz, G. Matache, A. Paraschiv, T. Frigioescu, T. Badea, Microstructural and Tensile Properties Anisotropy of Selective Laser Melting Manufactured IN 625, Materials 13 (2020) 4829. https://doi.org/10.3390/ma13214829.
[91] N.P. Lavery, J. Cherry, S. Mehmood, H. Davies, B. Girling, E. Sackett, S.G.R. Brown, J. Sienz, Effects of hot isostatic pressing on the elastic modulus and tensile properties of 316L parts made by powder bed laser fusion, Materials Science and Engineering: A 693 (2017) 186–213. https://doi.org/10.1016/j.msea.2017.03.100.
[92] A. Fedorenko, B. Fedulov, Y. Kuzminova, S. Evlashin, O. Staroverov, M. Tretyakov, E. Lomakin, I. Akhatov, Anisotropy of Mechanical Properties and Residual Stress in Additively Manufactured 316L Specimens, Materials 14 (2021) 7176. https://doi.org/10.3390/ma14237176.
[93] S. Dixit, S. Liu, H.A. Murdoch, P.M. Smith, Investigating build orientation-induced mechanical anisotropy in additive manufacturing 316L stainless steel, Materials Science and Engineering: A 880 (2023) 145308. https://doi.org/10.1016/j.msea.2023.145308.
[94] H. Sohrabpoor, V. Salarvand, R. Lupoi, Q. Chu, W. Li, B. Aldwell, W. Stanley, S. O'Halloran, R. Raghavendra, C.-H. Choi, D. Brabazon, Microstructural and mechanical evaluation of post-processed SS 316L manufactured by laser-based powder bed fusion, Journal of Materials Research and Technology 12 (2021) 210–220. https://doi.org/10.1016/j.jmrt.2021.02.090.
[95] N. Diaz Vallejo, C. Lucas, N. Ayers, K. Graydon, H. Hyer, Y. Sohn, Process Optimization and Microstructure Analysis to Understand Laser Powder Bed Fusion of 316L Stainless Steel, Metals 11 (2021) 832. https://doi.org/10.3390/met11050832.
[96] I. Hacısalihoğlu, F. Yıldiz, A. Çelik, The effects of build orientation and hatch spacing on mechanical properties of medical Ti–6Al–4V alloy manufactured by selective laser

melting, Materials Science and Engineering: A 802 (2021) 140649. https://doi.org/10.1016/j.msea.2020.140649.
[97] S. Cao, Z. Chen, S. Lim, K. Yang, Q. Jia, T. Jarvis, D. Tomus, X. Wu, Defect, Microstructure, and Mechanical Property of Ti-6Al-4V Alloy Fabricated by High-Power Selective Laser Melting, JOM 69 (2017) 2684–2692. https://doi.org/10.1007/s11837-017-2581-6.
[98] B. Vrancken, L. Thijs, J.-P. Kruth, J. Van Humbeeck, Heat treatment of Ti6Al4V produced by Selective Laser Melting: Microstructure and mechanical properties, Journal of Alloys and Compounds 541 (2012) 177–185. https://doi.org/10.1016/j.jallcom.2012.07.022.
[99] W. Xu, M. Brandt, S. Sun, J. Elambasseril, Q. Liu, K. Latham, K. Xia, M. Qian, Additive manufacturing of strong and ductile Ti–6Al–4V by selective laser melting via in situ martensite decomposition, Acta Materialia 85 (2015) 74–84. https://doi.org/10.1016/j.actamat.2014.11.028.
[100] T. Maconachie, M. Leary, J. Zhang, A. Medvedev, A. Sarker, D. Ruan, G. Lu, O. Faruque, M. Brandt, Effect of build orientation on the quasi-static and dynamic response of SLM AlSi10Mg, Materials Science and Engineering: A 788 (2020) 139445. https://doi.org/10.1016/j.msea.2020.139445.
[101] J. Fiocchi, C. Biffi, C. Colombo, L. Vergani, A. Tuissi, Ad Hoc Heat Treatments for Selective Laser Melted AlSi10mg Alloy Aimed at Stress-Relieving and Enhancing Mechanical Performances, JOM 72 (2020). https://doi.org/10.1007/s11837-019-03973-z.
[102] E. Padovano, C. Badini, A. Pantarelli, F. Gili, F. D'Aiuto, A comparative study of the effects of thermal treatments on AlSi10Mg produced by laser powder bed fusion, Journal of Alloys and Compounds 831 (2020) 154822. https://doi.org/10.1016/j.jallcom.2020.154822.
[103] R. Casati, M. Hamidi Nasab, M. Coduri, V. Tirelli, M. Vedani, Effects of Platform Pre-Heating and Thermal-Treatment Strategies on Properties of AlSi10Mg Alloy Processed by Selective Laser Melting, Metals 8 (2018) 954. https://doi.org/10.3390/met8110954.
[104] E. Sert, L. Hitzler, S. Hafenstein, M. Merkel, E. Werner, A. Öchsner, Tensile and compressive behaviour of additively manufactured AlSi10Mg samples, Progress in Additive Manufacturing 5 (2020). https://doi.org/10.1007/s40964-020-00131-9.
[105] Q. Tan, J. Zhang, N. Mo, Z. Fan, Y. Yin, M. Bermingham, Y. Liu, H. Huang, M.-X. Zhang, A novel method to 3D-print fine-grained AlSi10Mg alloy with isotropic properties via inoculation with LaB6 nanoparticles, Additive Manufacturing 32 (2020) 101034. https://doi.org/10.1016/j.addma.2019.101034.
[106] F. Geiger, K. Kunze, T. Etter, Tailoring the texture of IN738LC processed by selective laser melting (SLM) by specific scanning strategies, Materials Science and Engineering: A 661 (2016) 240–246. https://doi.org/10.1016/j.msea.2016.03.036.
[107] H. Yang, L. Meng, S. Luo, Z. Wang, Microstructural evolution and mechanical performances of selective laser melting Inconel 718 from low to high laser power, Journal of Alloys and Compounds 828 (2020) 154473. https://doi.org/10.1016/j.jallcom.2020.154473.
[108] J. Besson, J. Bleyer, S. Feld-Payet, A.-F. Gourgues-Lorenzon, F. Hannard, T. Helfer, J. Hure, D. Kondo, V. Lazarus, C. Le Bourlot, H. Maitournam, C. Maurini, N. Moes, T. Morgeneyer, L. Morin, T. Petit, A. Simar, MEALOR II Damage Mechanics and Local Approach to Fracture, (2023). https://doi.org/10.5281/ZENODO.10125169.
[109] F. Dominique, Essais de mesure de la ténacité, Techniques de l'Ingénieur (n.d.). https://www.techniques-ingenieur.fr/base-documentaire/materiaux-th11/essais-

mecaniques-sur-les-metaux-et-alliages-42531210/essais-de-mesure-de-la-tenacite-m4166/ (accessed July 4, 2024).
[110] Loading Modes I, II, III, (n.d.). https://www.fracturemechanics.org/modes123.html (accessed August 28, 2024).
[111] G.R. Irwin, Analysis of Stresses and Strains Near the End of a Crack Traversing a Plate, Journal of Applied Mechanics 24 (1957) 361–364. https://doi.org/10.1115/1.4011547.
[112] J. Rice, A Path Integral and the Approximate Analysis of Strain Concentration by Notches and Cracks, Journal of Applied Mechanics 35 (1968) 379–386. https://doi.org/10.1115/1.3601206.
[113] ISO 12135:2021 Metallic Materials — Unified Method of Test for the Determination of Quasistatic Fracture Toughness, (2021).
[114] ASTM E1820-21 Standard Test Method for Measurement of Fracture Toughness, (2021). https://doi.org/10.1520/E1820-21.
[115] BS 74448 Fracture mechanics toughness tests - Method for determination of KIc, critical CTOD and critical J values of metallic materials, (n.d.). https://doi.org/10.3403/BS7448.
[116] S. Zhang, S. Zhou, M. Li, B. Fu, Calculation and comparison on fracture toughness of specific reliability between ASTM and ISO standards, Materials Research Express 7 (2020). https://doi.org/10.1088/2053-1591/ab6c21.
[117] H.E. Ostergaard, J.D. Pribe, M. Tarik Hasib, A.M. Paradowska, T. Siegmund, J.J. Kruzic, Near-threshold fatigue crack growth in laser powder bed fusion produced alloy 718, International Journal of Fatigue 163 (2022) 107041. https://doi.org/10.1016/j.ijfatigue.2022.107041.
[118] R. Jones, A. Ang, D. Peng, V.K. Champagne, A. Michelson, A. Birt, Modelling Crack Growth in Additively Manufactured Inconel 718 and Inconel 625, Metals 13 (2023) 1300. https://doi.org/10.3390/met13071300.
[119] J.-R. Poulin, A. Kreitcberg, P. Terriault, V. Brailovski, Long fatigue crack propagation behavior of laser powder bed-fused inconel 625 with intentionally-seeded porosity, International Journal of Fatigue 127 (2019) 144–156. https://doi.org/10.1016/j.ijfatigue.2019.06.008.
[120] W. Zhu, Z. Moumni, J. Zhu, Y. Zhang, Y. You, W. Zhang, A multi-scale experimental investigation on fatigue crack propagation rate behavior of powder bed fusion-laser beam 316L stainless steel subjected to various heat treatments, Engineering Fracture Mechanics 302 (2024) 110064. https://doi.org/10.1016/j.engfracmech.2024.110064.
[121] X. Tian, Q. Li, G. Zhao, Z. Qu, S. Ai, Fatigue behavior of selective laser melted 316L stainless steel: Experiments and modeling, Engineering Fracture Mechanics 298 (2024) 109942. https://doi.org/10.1016/j.engfracmech.2024.109942.
[122] R. Konečná, L. Kunz, G. Nicoletto, A. Bača, Long fatigue crack growth in Inconel 718 produced by selective laser melting, International Journal of Fatigue 92 (2016) 499–506. https://doi.org/10.1016/j.ijfatigue.2016.03.012.
[123] K. Gruber, P. Szymczyk-Ziółkowska, S. Dziuba, S. Duda, P. Zielonka, S. Seitl, G. Lesiuk, Fatigue crack growth characterization of Inconel 718 after additive manufacturing by laser powder bed fusion and heat treatment, International Journal of Fatigue 166 (2023) 107287. https://doi.org/10.1016/j.ijfatigue.2022.107287.
[124] X.F. Ma, H.L. Zhai, L. Zuo, W.J. Zhang, S.S. Rui, Q.N. Han, J.S. Jiang, C.P. Li, G.F. Chen, G.A. Qian, S.J. Zhao, Fatigue short crack propagation behavior of selective laser melted Inconel 718 alloy by in-situ SEM study: Influence of orientation and temperature, International Journal of Fatigue 139 (2020) 105739. https://doi.org/10.1016/j.ijfatigue.2020.105739.
[125] A. Riemer, S. Leuders, M. Thöne, H.A. Richard, T. Tröster, T. Niendorf, On the fatigue crack growth behavior in 316L stainless steel manufactured by selective laser melting,

Engineering Fracture Mechanics 120 (2014) 15–25. https://doi.org/10.1016/j.engfracmech.2014.03.008.
[126] X. Hu, Z. Xue, T. Ren, Y. Jiang, C. Dong, F. Liu, On the fatigue crack growth behaviour of selective laser melting fabricated Inconel 625: Effects of build orientation and stress ratio, Fatigue & Fracture of Engineering Materials & Structures 43 (2020). https://doi.org/10.1111/ffe.13181.
[127] M.R. Khosravani, F. Berto, M.R. Ayatollahi, T. Reinicke, Fracture behavior of additively manufactured components: A review, Theoretical and Applied Fracture Mechanics 109 (2020) 102763. https://doi.org/10.1016/j.tafmec.2020.102763.
[128] E. de Sonis, Evolution microstructurale de l'acier 316L élaboré par fabrication additive (LPBF et WAAM) et influence sur son comportement à rupture, Thèse de doctorat, 2024.
[129] B. Vieille, C. Keller, M. Mokhtari, H. Briatta, T. Breteau, J. Nguejio, F. Barbe, M. Ben Azzouna, E. Baustert, Investigations on the fracture behavior of Inconel 718 superalloys obtained from cast and additive manufacturing processes, Materials Science and Engineering: A 790 (2020) 139666. https://doi.org/10.1016/j.msea.2020.139666.
[130] Y. Zhao, B. Gong, Y. Wang, Y. Gu, Effects of microstructure anisotropy on dynamic fracture behaviors of a selective laser melting nickel-based superalloy, Materials Science and Engineering: A 858 (2022) 144133. https://doi.org/10.1016/j.msea.2022.144133.
[131] B. Vieille, A. Duchaussoy, S. Benmabrouk, R. Henry, C. Keller, Fracture behavior of Hastelloy X elaborated by laser powder bed fusion: Influence of microstructure and building direction, Journal of Alloys and Compounds 918 (2022) 165570. https://doi.org/10.1016/j.jallcom.2022.165570.
[132] M.J. Paul, Q. Liu, J.P. Best, X. Li, J.J. Kruzic, U. Ramamurty, B. Gludovatz, Fracture resistance of AlSi10Mg fabricated by laser powder bed fusion, Acta Materialia 211 (2021) 116869. https://doi.org/10.1016/j.actamat.2021.116869.
[133] D. Roucou, T. Corre, G. Rolland, V. Lazarus, Effect of the deposition direction on fracture propagation in a Duplex Stainless Steel manufactured by Directed Energy Deposition, Materials Science and Engineering: A 878 (2023) 145176. https://doi.org/10.1016/j.msea.2023.145176.
[134] E. de Sonis, S. Dépinoy, P.-F. Giroux, H. Maskrot, P. Wident, O. Hercher, F. Villaret, A.-F. Gourgues-Lorenzon, Microstructure – Toughness relationships in 316L stainless steel produced by laser powder bed fusion, Materials Science and Engineering: A 877 (2023) 145179. https://doi.org/10.1016/j.msea.2023.145179.
[135] M. Peters, E.G. Brodie, S. Thomas, L. Djumas, M. Brameld, M. Salasi, Z. Quadir, M. Iannuzzi, J. Wang, T. Sercombe, C. Hutchinson, On the importance of nano-oxide control in laser powder bed fusion manufactured Ni-based alloys to enhance fracture properties, Materialia 32 (2023) 101958. https://doi.org/10.1016/j.mtla.2023.101958.
[136] M.J. Paul, J.J. Kruzic, U. Ramamurty, B. Gludovatz, The importance of fracture toughness evaluation for additively manufactured metals, Acta Materialia 276 (2024) 120061. https://doi.org/10.1016/j.actamat.2024.120061.
[137] M. Peters, E.G. Brodie, S. Thomas, L. Djumas, M. Brameld, M. Salasi, Z. Quadir, M. Iannuzzi, J. Wang, T. Sercombe, C. Hutchinson, On the importance of nano-oxide control in laser powder bed fusion manufactured Ni-based alloys to enhance fracture properties, Materialia 32 (2023) 101958. https://doi.org/10.1016/j.mtla.2023.101958.
[138] X. Wang, O. Sanchez-Mata, S.E. Atabay, J.A. Muñiz-Lerma, M. Attarian Shandiz, M. Brochu, Crystallographic orientation dependence of Charpy impact behaviours in stainless steel 316L fabricated by laser powder bed fusion, Additive Manufacturing 46 (2021) 102104. https://doi.org/10.1016/j.addma.2021.102104.
[139] Z. Zhang, B. Ter-Ovanessian, S. Marcelin, B. Normand, Investigation of the passive behavior of a Ni–Cr binary alloy using successive electrochemical impedance

measurements, Electrochimica Acta 353 (2020) 136531. https://doi.org/10.1016/j.electacta.2020.136531.
[140] B. Ter-Ovanessian, C. Alemany-Dumont, B. Normand, Electronic and transport properties of passive films grown on different Ni-Cr binary alloys in relation to the pitting susceptibility, Electrochimica Acta 133 (2014) 373–381. https://doi.org/10.1016/j.electacta.2014.04.067.
[141] L. Giorleo, G. Vecchia, E. Ceretti, Nd:YVO4 Laser Irradiation on Cr3C2-25(Ni20Cr) Coating Realized with High Velocity Oxy-Fuel Technology—Analysis of Surface Modification, Micromachines 12 (2021) 1477. https://doi.org/10.3390/mi12121477.
[142] F. Rubino, D. Merino, A.T. Silvestri, C. Munez, P. Poza, Mechanical properties optimization of Cr3C2-NiCr coatings produced by compact plasma spray process, Surface and Coatings Technology 465 (2023) 129570. https://doi.org/10.1016/j.surfcoat.2023.129570.
[143] G. Calvarin, R. Molins, A.M. Huntz, Oxidation Mechanism of Ni—20Cr Foils and Its Relation to the Oxide-Scale Microstructure, Oxidation of Metals 53 (2000) 25–48. https://doi.org/10.1023/A:1004578513020.
[144] G. Calvarin-Amiri, A.F. Gourgues, A.M. Huntz, R. Molins, Effect of environment on the mechanical behavior of Ni–20Cr thin strip, Materials Science and Engineering: A 298 (2001) 200–208. https://doi.org/10.1016/S0921-5093(00)01319-8.
[145] L. Lai, X. Fu, R. Sun, R. Du, Comparison of microstructure and electrical properties of NiCr alloy thin film deposited on different substrates, Surface and Coatings Technology 235 (2013) 552–560. https://doi.org/10.1016/j.surfcoat.2013.08.023.
[146] I.H. Kazi, P.M. Wild, T.N. Moore, M. Sayer, The electromechanical behavior of nichrome (80/20 wt.%) film, Thin Solid Films 433 (2003) 337–343. https://doi.org/10.1016/S0040-6090(03)00390-0.
[147] L. Lai, W. Zeng, X. Fu, R. Sun, R. Du, Annealing effect on the electrical properties and microstructure of embedded Ni–Cr thin film resistor, Journal of Alloys and Compounds 538 (2012) 125–130. https://doi.org/10.1016/j.jallcom.2012.05.102.
[148] M. Rudloff, Etude des mécanismes de transition volume/surface du comportement mécanique d'un alliage Ni20Cr, Thèse de doctorat, Université de Technologie de Compiègne, 2010. https://theses.hal.science/tel-00564947 (accessed April 24, 2024).
[149] A. Balan, M. Perez, T. Chaise, S. Cazottes, D. Bardel, F. Corpace, F. Pichot, A. Deschamps, F. De Geuser, D. Nelias, Precipitation of γ″ in Inconel 718 alloy from microstructure to mechanical properties, Materialia 20 (2021) 101187. https://doi.org/10.1016/j.mtla.2021.101187.
[150] D. Texier, A.C. Gómez, S. Pierret, J.-M. Franchet, T.M. Pollock, P. Villechaise, J. Cormier, Microstructural Features Controlling the Variability in Low-Cycle Fatigue Properties of Alloy Inconel 718DA at Intermediate Temperature, Metall Mater Trans A 47 (2016) 1096–1109. https://doi.org/10.1007/s11661-015-3291-8.
[151] L.-J. Yu, E.A. Marquis, Precipitation behavior of Alloy 625 and Alloy 625 plus, Journal of Alloys and Compounds 811 (2019) 151916. https://doi.org/10.1016/j.jallcom.2019.151916.
[152] J.-C. Zhao, M. Larsen, V. Ravikumar, Phase precipitation and time–temperature-transformation diagram of Hastelloy X, Materials Science and Engineering: A 293 (2000) 112–119. https://doi.org/10.1016/S0921-5093(00)01049-2.
[153] C. Slama, M. Abdellaoui, Precipitation kinetics of γ′ and γ″ particles in Inconel 718 and its influence on mechanical properties, Materials Today Communications 38 (2024) 108158. https://doi.org/10.1016/j.mtcomm.2024.108158.
[154] M. Jouiad, E. Marin, R.S. Devarapalli, J. Cormier, F. Ravaux, C. Le Gall, J.-M. Franchet, Microstructure and mechanical properties evolutions of alloy 718 during isothermal and

thermal cycling over-aging, Materials & Design 102 (2016) 284–296. https://doi.org/10.1016/j.matdes.2016.04.048.
[155] P. Nash, The Cr−Ni (Chromium-Nickel) system, Bulletin of Alloy Phase Diagrams 7 (1986) 466–476. https://doi.org/10.1007/BF02867812.
[156] B. Song, S. Dong, P. Coddet, H. Liao, C. Coddet, Fabrication of NiCr alloy parts by selective laser melting: Columnar microstructure and anisotropic mechanical behavior, Materials & Design 53 (2014) 1–7. https://doi.org/10.1016/j.matdes.2013.07.010.
[157] S.S. Joshi, Investigation of the link between mechanical properties and microstructure of Ni20Cr alloy manufactured by laser powder bed fusion, Thèse de doctorat, Normandie Université, 2023.
[158] S.S. Joshi, C. Keller, L. Mas, W. Lefebvre, E. Hug, J.-P. Couzinie, On the origin of the strain hardening mechanisms of Ni20Cr alloy manufactured by laser powder bed fusion, International Journal of Plasticity 165 (2023) 103610. https://doi.org/10.1016/j.ijplas.2023.103610.
[159] S.S. Joshi, C. Keller, E. Hug, W. Lefebvre, Quantifying microstructural contribution to yield stress and strain hardening of Ni20Cr alloy manufactured by laser powder bed fusion with different volumetric energy densities, Journal of Alloys and Compounds 968 (2023) 172241. https://doi.org/10.1016/j.jallcom.2023.172241.
[160] T. Delacroix, F. Lomello, F. Schuster, H. Maskrot, C. Baslari, U. Gaumet, Y. Flici, J.-P. Garandet, Influence of build characteristics and chamber oxygen concentration on powder degradation in laser powder bed fusion, Powder Technology 416 (2023) 118231. https://doi.org/10.1016/j.powtec.2023.118231.
[161] K. Dietrich, J. Diller, S. Dubiez, D. Bauer, P. Forêt, G. Witt, The influence of oxygen on the chemical composition and mechanical properties of Ti-6Al-4V during laser powder bed fusion (L-PBF), Additive Manufacturing 32 (2019) 100980. https://doi.org/10.1016/j.addma.2019.100980.
[162] H.Y. Chia, L. Wang, W. Yan, Influence of oxygen content on melt pool dynamics in metal additive manufacturing: High-fidelity modeling with experimental validation, Acta Materialia 249 (2023) 118824. https://doi.org/10.1016/j.actamat.2023.118824.
[163] D. François, Essais mécaniques des métaux - Essais de dureté, Techniques de l'Ingénieur (n.d.). https://www.techniques-ingenieur.fr/base-documentaire/mecanique-th7/surfaces-42463210/essais-mecaniques-des-metaux-m4160/ (accessed June 4, 2024).
[164] ISO 6892-1:2019 Metallic Materials — Tensile testing — Part 1: Method of Test at Room Temperature, (2019).
[165] ISO 178:2019 Plastics - Determination of flexural properties, (2019).
[166] T.L. Anderson, Fracture Mechanics: Fundamentals and Applications, Taylor & Francis, 2005.
[167] H. Carassus, J.D. Guérin, H. Morvan, G. Haugou, T. Sadat, S. Guérard, E. Markiewicz, An experimental investigation into influences of build orientation and specimen thickness on quasi-static and dynamic mechanical responses of Selective Laser Melting 316L Stainless Steel, Materials Science and Engineering: A 835 (2022) 142683. https://doi.org/10.1016/j.msea.2022.142683.
[168] D. Forni, F. Mazzucato, A. Valente, E. Cadoni, High strain-rate behaviour of as-cast and as-build Inconel 718 alloys at elevated temperatures, Mechanics of Materials 159 (2021) 103859. https://doi.org/10.1016/j.mechmat.2021.103859.
[169] F. Khodabakhshi, M.H. Farshidianfar, A.P. Gerlich, M. Nosko, V. Trembošová, A. Khajepour, Microstructure, strain-rate sensitivity, work hardening, and fracture behavior of laser additive manufactured austenitic and martensitic stainless steel structures, Materials Science and Engineering: A 756 (2019) 545–561. https://doi.org/10.1016/j.msea.2019.04.065.

[170] M.A. Meyers, K.K. Chawla, Mechanical Behavior of Materials, Cambridge, 1998.
[171] T. Kobayashi, I. Yamamoto, M. Niinomi, Introduction of a New Dynamic Fracture Toughness Evaluation System, Journal of Testing and Evaluation; (United States) 21:3 (1993). https://doi.org/10.1520/JTE11763J.
[172] P.R. Sreenivasan, S.L. Mannan, Dynamic J-R curves and tension-impact properties of AISI 308 stainless steel weld, International Journal of Fracture 101 (2000) 229–249. https://doi.org/10.1023/A:1007621904164.
[173] J. Rice, P. Paris, J. Merkle, Some Further Results of J-Integral Analysis and Estimates, ASTM Special Technical Publication 536 (1973). https://doi.org/10.1520/STP49643S.
[174] S.J. Garwood, J.N. Robinson, C.E. Turner, The measurement of crack growth resistance curves (R-curves) using the J integral, Int J Fract 11 (1975) 528–530. https://doi.org/10.1007/BF00033539.
[175] J.A. Gonzalez, J. Mireles, S.W. Stafford, M.A. Perez, C.A. Terrazas, R.B. Wicker, Characterization of Inconel 625 fabricated using powder-bed-based additive manufacturing technologies, Journal of Materials Processing Technology 264 (2019) 200–210. https://doi.org/10.1016/j.jmatprotec.2018.08.031.
[176] A. Kumar Maurya, A. Kumar, Effect of building orientation & heat-treatment on microhardness & surface roughness of additive manufactured IN718 alloy, Materials Today: Proceedings 59 (2022) 628–635. https://doi.org/10.1016/j.matpr.2021.12.180.
[177] A. Kurdi, A. Aldoshan, F. Alshabouna, A. Alodadi, A. Degnah, H. Alnaser, T. Tabbakh, A.K. Basak, Investigation into the Microstructure and Hardness of Additively Manufactured (3D-Printed) Inconel 718 Alloy, Materials (Basel) 16 (2023) 2383. https://doi.org/10.3390/ma16062383.
[178] W.M. Tucho, P. Cuvillier, A. Sjolyst-Kverneland, V. Hansen, Microstructure and hardness studies of Inconel 718 manufactured by selective laser melting before and after solution heat treatment, Materials Science and Engineering: A 689 (2017) 220–232. https://doi.org/10.1016/j.msea.2017.02.062.
[179] M. Lelievre, Elaboration de l'alliage Ni 20 wt. % Cr par fusion sélective laser: effet des paramètres de fabrication sur la microstructure, le comportement mécanique en traction et la stabilité thermique, (n.d.) 227.
[180] V.A. Popovich, E.V. Borisov, A.A. Popovich, V.Sh. Sufiiarov, D.V. Masaylo, L. Alzina, Functionally graded Inconel 718 processed by additive manufacturing: Crystallographic texture, anisotropy of microstructure and mechanical properties, Materials & Design 114 (2017) 441–449. https://doi.org/10.1016/j.matdes.2016.10.075.
[181] Z. Li, B. He, Q. Guo, Strengthening and hardening mechanisms of additively manufactured stainless steels: The role of cell sizes, Scripta Materialia 177 (2020) 17–21. https://doi.org/10.1016/j.scriptamat.2019.10.005.
[182] S. Benmabrouk, B. Vieille, C. Keller, S.S. Joshi, E. Hug, Fracture behavior of a Ni-20 wt.%Cr binary alloy processed by Laser Powder Bed Fusion: Influence of the specimen building orientation and rotation angle between layers, Engineering Fracture Mechanics 307 (2024) 110340. https://doi.org/10.1016/j.engfracmech.2024.110340.
[183] P.K. Jena, K.S. Kumar, R.K. Mandal, A.K. Singh, An experimental study on the fracture behavior of different aluminium alloys subjected to ballistic impact, Procedia Structural Integrity 17 (2019) 957–964. https://doi.org/10.1016/j.prostr.2019.08.127.
[184] C. Li, S. Rasheed, A. Malik, F. Nazeer, J. Long, Study on ballistic impact behavior of Al alloys against two different shapes of steel core projectiles, Journal of Materials Research and Technology 20 (2022) 2489–2500. https://doi.org/10.1016/j.jmrt.2022.08.052.
[185] A.E. Medvedev, E.W. Lui, D. Edwards, M. Leary, M. Qian, M. Brandt, Improved ballistic performance of additively manufactured Ti6Al4V with α-β lamellar

microstructures, Materials Science and Engineering: A 825 (2021) 141888. https://doi.org/10.1016/j.msea.2021.141888.
[186] J.M. Pereira, B.A. Lerch, Effects of heat treatment on the ballistic impact properties of Inconel 718 for jet engine fan containment applications, International Journal of Impact Engineering 25 (2001) 715–733. https://doi.org/10.1016/S0734-743X(01)00018-5.
[187] J.J. DeMange, V. Prakash, J.M. Pereira, Effects of material microstructure on blunt projectile penetration of a nickel-based super alloy, International Journal of Impact Engineering 36 (2009) 1027–1043. https://doi.org/10.1016/j.ijimpeng.2009.01.007.
[188] T. Kobayashi, Y. Isamu, M. Niinomi, Evaluation of dynamic fracture toughness parameters by instrumented Charpy impact test, Engineering Fracture Mechanics 24 (1986) 773–782. https://doi.org/10.1016/0013-7944(86)90249-3.
[189] S. Cheng, Développement de méthodes et d'analyses pour l'étude de la ténacité sur petites éprouvettes, Thèse de doctorat, Université Paris sciences et lettres, 2024. https://pastel.hal.science/tel-04652203 (accessed August 30, 2024).
[190] K. Schmuck, M. Alfreider, D. Kiener, Crack length estimations for small-scale fracture experiments via image processing techniques, Journal of Materials Research 37 (2022) 2848–2861. https://doi.org/10.1557/s43578-022-00681-4.
[191] D. Rajpoot, P. Tandaiya, R.L. Narayan, U. Ramamurty, Size effects and failure regimes in notched micro-cantilever beam fracture, Acta Materialia 234 (2022) 118041. https://doi.org/10.1016/j.actamat.2022.118041.
[192] R. Pippan, S. Wurster, D. Kiener, Fracture mechanics of micro samples: Fundamental considerations, Materials & Design 159 (2018) 252–267. https://doi.org/10.1016/j.matdes.2018.09.004.
[193] P. Gruenewald, F. Schaefer, M. Thielen, M. Marx, C. Motz, Small scale fracture mechanics of ductile materials: Advantage of fatigue precracks and comparison of J-integral evaluations, Materialia 4 (2018) 104–108. https://doi.org/10.1016/j.mtla.2018.09.011.
[194] C. Bohnert, N.J. Schmitt, S.M. Weygand, O. Kraft, R. Schwaiger, Fracture toughness characterization of single-crystalline tungsten using notched micro-cantilever specimens, International Journal of Plasticity 81 (2016) 1–17. https://doi.org/10.1016/j.ijplas.2016.01.014.
[195] J. Ast, M. Ghidelli, K. Durst, M. Göken, M. Sebastiani, A.M. Korsunsky, A review of experimental approaches to fracture toughness evaluation at the micro-scale, Materials & Design 173 (2019) 107762. https://doi.org/10.1016/j.matdes.2019.107762.
[196] F. Iqbal, J. Ast, M. Göken, K. Durst, In situ micro-cantilever tests to study fracture properties of NiAl single crystals, Acta Materialia 60 (2012) 1193–1200. https://doi.org/10.1016/j.actamat.2011.10.060.
[197] B.D. Snartland, C. Thaulow, Fracture toughness testing at the micro-scale − The effect of the unloading compliance method, Engineering Fracture Mechanics 235 (2020) 107135. https://doi.org/10.1016/j.engfracmech.2020.107135.
[198] J. Ast, M. Göken, K. Durst, Size-dependent fracture toughness of tungsten, Acta Materialia 138 (2017) 198–211. https://doi.org/10.1016/j.actamat.2017.07.030.
[199] J. Ast, B. Merle, K. Durst, M. Göken, Fracture toughness evaluation of NiAl single crystals by microcantilevers—a new continuous J-integral method, Journal of Materials Research 31 (2016) 3786–3794. https://doi.org/10.1557/jmr.2016.393.
[200] O. Kolednik, M. Sistaninia, S. Kolitsch, J-integral testing on micro-scale cantilever beam specimens, Engineering Fracture Mechanics 292 (2023) 109636. https://doi.org/10.1016/j.engfracmech.2023.109636.
[201] M. Wurmshuber, M. Alfreider, S. Wurster, M. Burtscher, R. Pippan, D. Kiener, Small-scale fracture mechanical investigations on grain boundary doped ultrafine-grained

tungsten, Acta Materialia 250 (2023) 118878. https://doi.org/10.1016/j.actamat.2023.118878.
[202] J. Ast, M. N. Polyakov, G. Mohanty, J. Michler, X. Maeder, Interplay of stresses, plasticity at crack tips and small sample dimensions revealed by in-situ microcantilever tests in tungsten, Materials Science and Engineering: A 710 (2018) 400–412. https://doi.org/10.1016/j.msea.2017.10.096.
[203] B.D. Snartland, C. Thaulow, Fracture toughness testing at the micro-scale − The effect of the unloading compliance method, Engineering Fracture Mechanics 235 (2020) 107135. https://doi.org/10.1016/j.engfracmech.2020.107135.
[204] M. Alfreider, D. Kozic, O. Kolednik, D. Kiener, In-situ elastic-plastic fracture mechanics on the microscale by means of continuous dynamical testing, Materials & Design 148 (2018) 177–187. https://doi.org/10.1016/j.matdes.2018.03.051.

APPENDIX A
MATLAB code for three-point bending post-processing

This appendix presents the custom MATLAB script created in order to post-process the experimental data from the three-point bending tests. The initial script was created by Hugo BRIATTA during his master internship in 2019, and has been completed and improved throughout this PhD.

The post-processing consists of several steps: the first one is to collect, filter, and sort the experimental data in order to ease the data processing. The image processing parameters are then adjusted by the user to obtain the most accurate thresholding without undesired artifacts, to get the best image quality for crack propagation monitoring. The specimen's shape is automatically detected to locate the crack tip, as well as its dimensions. Each image is then analyzed, starting from the last to the first image taken during the test, and the crack tip is spotted on each image. The crack path is then recreated, and the overall crack extension calculated. From this point, all the parameters and curves of interest presented in this work are respectively computed and plotted.

```
% CRACK PROPAGATION ANALYSIS PROGRAM (for 3-point bending test)

% Creators : Hugo BRIATTA, Sélia BENMABROUK

% Parameters initialization
precracking = true;
autothresh = false;
thresh = 0;
autoOZ = true;
Lcursorpourcentage = 0.1;
Hcursorpourcentage = 0.2;
topOZpourcentage = 0.10;
heightOZpourcentage = 0.6;
widthOZpourcentage = 0.5;
proxiX = 20;
proxiY = 50;
gifspeed = 0.08;
numfig = 0;

W = 0.01004;
B = 0.01012;
L = 0.06501;
```

```
span = 0.04;
aini = 0.005;
aP = 0.00165;
a0 = aini+aP;
b0 = W-a0;

sigYS = 549;
sigUTS = 723;
sigY = (sigYS+sigUTS)/2;
E = 217992;
nu = 0.3;
Npl_ISO = 1.9;
Gpl_ISO = 0.5;

%--------------------------------------------------------------------------
%%                        DATA COLLECTION
%--------------------------------------------------------------------------

disp('Select the data file:');
[datafile,datafolder] = uigetfile('*.dat','Select the data file:');
specimenID = datafile(1:end-4);
disp(['Data file of specimen ' specimenID ' has been selected.']);
cd(datafolder)
disp(' '); disp('Select the first image taken:');
[imagefile] = uigetfile('*.*', 'Select the first image taken:');
[imagefilelast] = uigetfile('*.*', 'Select the last image taken:');
imageID = imagefile(1:end-11);
disp(['Image ' imageID ' has been selected.']);

fid = fopen(strcat((imageID), '.csv'));
imagedata = textscan(fid, '%s %s %s', 'Delimiter', ',', 'headerLines', 1);
fclose('all');
imagelist(:,1) = str2double(strrep(imagedata{3},',','.'));
imagelist(:,1) = imagelist(:,1)-imagelist(1,1);
imagelist(:,2) = str2double(imagedata{1})+1;
nbimage = size(imagelist,1);

if isfolder(['Results_' specimenID])
    delete(['Results_' specimenID '\*']);
else
    mkdir(datafolder,['Results_' specimenID]);
end

%--------------------------------------------------------------------------
%%                      TEST DATA PROCESSING
%--------------------------------------------------------------------------

if repairtest == 1
    openfile = fopen([datafolder strcat(specimenID, '_final.dat')]);
else
    openfile = fopen([datafolder strcat(specimenID, '.dat')]);
end
frewind(openfile);
if repairtest == 1
    data      =      textscan(openfile,'%s      %s      %s      %s','Delimiter','
','HeaderLines',0,'MultipleDelimsAsOne',1);
else
    data      =      textscan(openfile,'%s      %s      %s      %s','Delimiter','
','HeaderLines',8,'MultipleDelimsAsOne',1);
```

```
end
fclose(openfile);
disp(:,1) = str2double(strrep(data{1},',','.'));
disp(:,2) = str2double(strrep(data{2},',','.'))*(-0.001);
load(:,1) = str2double(strrep(data{1},',','.'));
load(:,2) = str2double(strrep(data{3},',','.'))*(-1000);
temp(:,1) = str2double(strrep(data{1},',','.'));
temp(:,2) = str2double(strrep(data{4},',','.'));

m = 1;
while m <= size(imagelist,1)
    imagelist(m,1)        =        imagelist(m,1)-(imagelist(size(imagelist,1),1)-
load(size(load,1),1));
    if imagelist(m,1) < 0
        imagelist(m,:) = [];
        m = m-1;
    end
    m = m+1;
end
numfirstimage = imagelist(1,2);
numlastimage = imagelist(size(imagelist,1),2);
nbimage = size(imagelist,1);

%--------------------------------------------------------------------------
%%               ADJUSTMENT OF IMAGE PROCESSING PARAMETERS
%--------------------------------------------------------------------------

[heightimage,lengthimage] = size(testimageB);
cursorX = floor(Lcursorpourcentage*lengthimage);
cursorY = 1;
if autoOZ == true
    while (testimageB(cursorY,cursorX) == 1) && (cursorY < heightimage)
        cursorY = cursorY+1;
    end
    topleft = cursorY;

    cursorX = floor((1-Lcursorpourcentage)*lengthimage);
    cursorY = 1;
    while (testimageB(cursorY,cursorX)) == 1 && (cursorY < heightimage)
        cursorY = cursorY+1;
    end
    topright = cursorY;
    topspecimen = floor(mean(topleft,topright));

    cursorX = floor(Lcursorpourcentage*lengthimage);
    cursorY = topleft;
    while (testimageB(cursorY,cursorX)) == 0 && (cursorY < heightimage)
        cursorY = cursorY+1;
    end
    bottomleft = cursorY;

    cursorX = floor((1-Lcursorpourcentage)*lengthimage);
    cursorY = topright;
    while (testimageB(cursorY,cursorX) == 0) && (cursorY < heightimage)
        cursorY = cursorY+1;
    end
    bottomright = cursorY;
    bottomspecimen = floor(mean(bottomleft,bottomright));
    Wpix = bottomspecimen-topspecimen;
```

```
    heightOZ = heightOZpourcentage*Wpix;
    widthOZ = widthOZpourcentage*Wpix;

    cursorX = floor(Lcursorpourcentage*lengthimage);
    cursorY    =    floor(topspecimen+(1-(Hcursorpourcentage+0.2))*(bottomspecimen-
topspecimen));
    while (testimageB(cursorY,cursorX) == 0) && (cursorX < lengthimage)
        cursorX = cursorX+1;
    end
    topleftnotch = cursorX;
    cursorX = floor(Lcursorpourcentage*lengthimage);
    cursorY      =      floor(topspecimen+(1-(Hcursorpourcentage))*(bottomspecimen-
topspecimen));
    while (testimageB(cursorY,cursorX) == 0) && (cursorX < lengthimage)
        cursorX = cursorX+1;
    end
    bottomleftnotch = cursorX;
    leftnotch = floor(mean(topleftnotch,bottomleftnotch));

    cursorX = topleftnotch;
    cursorY    =    floor(topspecimen+(1-(Hcursorpourcentage+0.2))*(bottomspecimen-
topspecimen));
    while (testimageB(cursorY,cursorX) == 1) && (cursorX < lengthimage)
        cursorX = cursorX+1;
    end
    toprightnotch = cursorX;
    cursorX = bottomleftnotch;
    cursorY      =      floor(topspecimen+(1-(Hcursorpourcentage))*(bottomspecimen-
topspecimen));
    while (testimageB(cursorY,cursorX) == 1) && (cursorX < lengthimage)
        cursorX = cursorX+1;
    end
    bottomrightnotch = cursorX;
    rightnotch = floor(mean(toprightnotch,bottomrightnotch));
    middlenotch = leftnotch+floor((rightnotch-leftnotch)/2);

    imshow(testimageB);
    hold on
    axis on
    scatter(floor((1-
Lcursorpourcentage)*lengthimage),bottomright,'b','LineWidth',2)
    scatter(floor(Lcursorpourcentage*lengthimage),bottomleft,'m','LineWidth',2)
    scatter(floor((1-Lcursorpourcentage)*lengthimage),topright,'c','LineWidth',2)
    scatter(floor(Lcursorpourcentage*lengthimage),topleft,'y','LineWidth',2)
    scatter(bottomrightnotch,floor(topspecimen+(1-
(Hcursorpourcentage))*(bottomspecimen-topspecimen)),'b','LineWidth',2)
    scatter(bottomleftnotch,                                    floor(topspecimen+(1-
(Hcursorpourcentage))*(bottomspecimen-topspecimen)),'m','LineWidth',2)
    scatter(toprightnotch,floor(topspecimen+(1-
(Hcursorpourcentage+0.2))*(bottomspecimen-topspecimen)),'c','LineWidth',2)
    scatter(topleftnotch,floor(topspecimen+(1-
(Hcursorpourcentage+0.2))*(bottomspecimen-topspecimen)),'y','LineWidth',2)
    yline(topspecimen,'--r','LineWidth',2);
    yline(bottomspecimen,'--r','LineWidth',2);
    xline(leftnotch,'--g','LineWidth',2);
    xline(rightnotch,'--g','LineWidth',2);
    plot(middlenotch,topspecimen+(1-
(Hcursorpourcentage+0.1))*Wpix,'r*','LineWidth',2);
    title('Positions'' determination: top, bottom, left edge, right edge & middle');
```

```
    disp(' '); disp('Check the positions determined.'); disp('If OK press enter,
else press Ctrl+C and adjust parameters again.');
    numfig = numfig+1;
    numfigstr=num2str(numfig);
    saveas(gcf, ['Results_' specimenID '\' numfigstr '_Positions_' specimenID
'.png']);
    close all

    imshow(testimageB);
    title('Observation Zone (OZ)');
    hold on
    axis on
    rectangle('Position',[(middlenotch-
widthOZ/2),(topspecimen+topOZpourcentage*Wpix),widthOZ/2,heightOZ],...
      'EdgeColor', 'b',...
      'LineWidth', 2,...
      'LineStyle','-');

rectangle('Position',[middlenotch,(topspecimen+topOZpourcentage*Wpix),widthOZ/2,he
ightOZ],...
     'EdgeColor', 'b',...
     'LineWidth', 2,...
     'LineStyle','-');
    disp(' '); disp('Check the Observation Zone determined.'); disp('If OK press
enter, else press Ctrl+C and adjust parameters again.');
    numfig = numfig+1;
    numfigstr=num2str(numfig);
    saveas(gcf, ['Results_' specimenID '\' numfigstr '_ObservationZone_' specimenID
'.png']);
    close all

else
    imshow(testimageB);
    hold on
    axis on
    disp(' '); disp('Click on the specimen''s top and press Enter.');
    [~,topspecimen] = getpts;
    disp(' '); disp('Click on the specimen''s bottom and press Enter.');
    [~,bottomspecimen] = getpts;
    disp(' '); disp('Click on notch''s left edge and press Enter.');
    [leftnotch,~] = getpts;
    disp(' '); disp('Click on notch''s right edge and press Enter.');
    [rightnotch,~] = getpts;
    middlenotch = leftnotch+floor((rightnotch-leftnotch)/2);
    Wpix = bottomspecimen-topspecimen;
    heightOZ = heightOZpourcentage*Wpix;
    widthOZ = widthOZpourcentage*Wpix;

    imshow(testimageB);
    hold on
    axis on
    scatter(rightnotch,floor(topspecimen+(1-(Hcursorpourcentage))*(bottomspecimen-
topspecimen)),'b','LineWidth',2)
    scatter(leftnotch, floor(topspecimen+(1-(Hcursorpourcentage))*(bottomspecimen-
topspecimen)),'m','LineWidth',2)
    yline(topspecimen,'--r','LineWidth',2);
    yline(bottomspecimen,'--r','LineWidth',2);
    xline(leftnotch,'--g','LineWidth',2);
    xline(rightnotch,'--g','LineWidth',2);
```

```
    plot(middlenotch,topspecimen+(1-
(Hcursorpourcentage+0.1))*Wpix,'r*','LineWidth',2);
    title('Positions'' determination: top, bottom, left edge, right edge & middle');
    disp(' '); disp('Check the positions determined.'); disp('If OK press enter,
else press Ctrl+C and adjust parameters again.');
    numfig = numfig+1;
    numfigstr=num2str(numfig);
    saveas(gcf, ['Results_' specimenID '\' numfigstr '_Positions_' specimenID
'.png']);
    close all

    imshow(testimageB);
    title('Observation Zone (OZ)');
    hold on
    axis on
    rectangle('Position',[(middlenotch-
widthOZ/2),topspecimen+topOZpourcentage*Wpix,widthOZ/2,heightOZ],...
      'EdgeColor', 'b',...
      'LineWidth', 2,...
      'LineStyle','-');

rectangle('Position',[middlenotch,topspecimen+topOZpourcentage*Wpix,widthOZ/2,heig
htOZ],...
     'EdgeColor', 'b',...
     'LineWidth', 2,...
     'LineStyle','-');
    disp(' '); disp('Check the Observation Zone determined.'); disp('If OK press
enter, else press Ctrl+C and adjust parameters again.');
    numfig = numfig+1;
    numfigstr=num2str(numfig);
    saveas(gcf, ['Results_' specimenID '\' numfigstr '_ObservationZone_' specimenID
'.png']);
    close all

end

%-------------------------------------------------------------------------
%%           IMAGE PROCESSING (CRACK PROPAGATION ANALYSIS)
%-------------------------------------------------------------------------

n = numlastimage;
n_idx = nbimage;
nlist = zeros(nbimage,1);
crackposX = zeros(nbimage,1);
crackposY = zeros(nbimage,1);

while (n >= numfirstimage)
    if (n-1) < 10
        imagename = strcat(imageID, '-000', int2str(n-1), '_0.tif');
    elseif (n-1) < 100
        imagename = strcat(imageID, '-00', int2str(n-1), '_0.tif');
    elseif (n-1) < 1000
        imagename = strcat(imageID, '-0', int2str(n-1), '_0.tif');
    else
        imagename = strcat(imageID, '-', int2str(n-1), '_0.tif');
    end
    image = imread(imagename);

    if autothresh == true
```

```
        imageB = 1-imbinarize(image);
    else
        imageB = 1-imbinarize(image,thresh);
    end
    imageOZ                                                                                    =
imageB(round(topspecimen+topOZpourcentage*Wpix):round(topspecimen+topOZpourcentage
*Wpix+heightOZ),round((middlenotch-
round(widthOZ)/2)):round((middlenotch+round(widthOZ/2))));
    imshow(imageOZ);

    found = false;
    for i=1:size(imageOZ,1)
        for j=1:size(imageOZ,2)
            if imageOZ(i,j) == 1
                if n == numlastimage
                    crackposY(n_idx) = i;
                    crackposX(n_idx) = j;
                    found = true;
                elseif  (n<numlastimage)  &&  (abs(i-crackposY(n_idx+1))<proxiY)  &&
(abs(j-crackposX(n_idx+1))<proxiX) && crackposY(n_idx+1)<=i
                    crackposY(n_idx) = i;
                    crackposX(n_idx) = j;
                    found = true;
                end
            end
        if found == true
            break
        end
        end
            if found == true
                break
            end
    end

    if found == false
       fprintf('\n Error, not possible to determinate the next position of the crack
tip');
       fprintf('\n Try to change the parameters \n');
    return;
    end

    squarelength = 4;
    f = figure(1);
    imshow(imageOZ);
    hold on
    rectangle('Position',[crackposX(n_idx)-squarelength,crackposY(n_idx)-
squarelength,squarelength*2,squarelength*2],...
          'EdgeColor', 'r',...
          'LineWidth', 1,...
          'LineStyle','-') ;
    frame = getframe(f);
    im{n_idx} = frame2im(frame);

    status = 100*(nbimage-n_idx)/nbimage;
    clc
    sprintf('Analyse en cours...%0.2f %%',status)
    sprintf('Image n°...%d',n)
    nlist(n_idx) = n;
    n = n-1;
```

```
    n_idx = n_idx-1;
end
status = 100*(nbimage-n_idx)/nbimage;
clc
sprintf('Analyse en cours...%0.2f %%',status)
sprintf('Image n°...%d',n)
close all

crackposX_m = zeros(nbimage,1);
crackposY_m = zeros(nbimage,1);
for n=1:length(crackposX)
    crackposX_m(n,1) = (crackposX(n)-crackposX(1))*(W/Wpix);
    crackposY_m(n,1) = -(crackposY(n)-crackposY(1))*(W/Wpix);
end

imagelistnew = zeros(nbimage,2);
m = 1;
n = 1;
while (n <= size(nlist,1)) && (m <= size(imagelist,1))
    if imagelist(m,2)== nlist(n)
        imagelistnew(n,:) = imagelist(m,:);
        n = n+1;
    end
    m = m+1;
end
export = zeros(nbimage,5);
atot_precleaning = a0;

for n=1:size(crackposX_m,1)
    if n~=1
        atot_precleaning  =  atot_precleaning  +  ((crackposX_m(n)-crackposX_m(n-
1)).^2+(crackposY_m(n)-crackposY_m(n-1)).^2).^0.5;
    end
    export(n,1)= imagelistnew(n,1);
    export(n,2)= imagelistnew(n,2);
    export(n,3) = atot_precleaning;
    export(n,4) = crackposY_m(n)+a0;
    export(n,5) = b0-crackposY_m(n);
end

a_precleaning = export(:,4);

%--------------------------------------------------------------------------
%%                              PRECRACKING ADJUSMENTS
%--------------------------------------------------------------------------

for i=1:size(export,1)
    if export(i,4)-export(1,4) < aP
       export(i,4) = a0;
       export(i,5) = W-export(i,4);
    else
       export(i,4) = export(i,4)-aP;
       export(i,5) = W-export(i,4);
    end
end

a = export(:,4);
b = export(:,5);
```

```
j = 1;
for i=1:size(export,1)
    while (j <= size(load,1)) && (load(j,1) <= export(i,1))
        a_data(j,1:4) = export(i,1:4);
        b_data(j,1) = export(i,5);
        j = j+1 ;
    end
end
crackpropagY = crackposY_m;

loadimage = zeros(nbimage,4);
dispimage = zeros(nbimage,4);
j = nbimage;
for i=size(load,1):-1:1
    if (i == size(load,1)) && (j >= 1)
        loadimage(j,1:2) = a_data(i,1:2);
        dispimage(j,1:2) = a_data(i,1:2);
        loadimage(j,3:4) = load(i,:);
        dispimage(j,3:4) = disp(i,:);
        j = j-1;
    elseif (a_data(i,2) ~= a_data(i+1,2)) && (j >= 1)
        loadimage(j,1:2) = a_data(i,1:2);
        dispimage(j,1:2) = a_data(i,1:2);
        loadimage(j,3:4) = load(i,:);
        dispimage(j,3:4) = disp(i,:);
        j = j-1;
    end
end

for i=1:size(crackposX_m,1)
    f = figure(1);
    hold on
    plot(crackposX_m(1:i,1)*10^3,crackposY_m(1:i,1)*10^3,':rs','LineWidth',1)
    title('Crack path')
    xlabel('x position (mm)')
    ylabel('y position (mm)')
    axis equal
    frame = getframe(f);
    img{i} = frame2im(frame);
    grid on
    grid minor
    box on;
end
numfig = numfig+1;
numfigstr=num2str(numfig);
saveas(f, ['Results_' specimenID '\' numfigstr '_CrackPath_' specimenID '.png']);
box off;

m = length(im);
numfig = numfig+1;
numfig2 = numfig+2;
numfigstr=num2str(numfig);
numfigstr2=num2str(numfig2);
for n=1:m
    [image,mapi] = rgb2ind(im{n},32);
    [graph,mapg] = rgb2ind(img{n},32);
    if n == 1
        imwrite(image,mapi,['Results_'   specimenID   '\'   numfigstr   '_CrackGif_'
specimenID '.gif'],'gif','LoopCount',Inf,'DelayTime',gifspeed);
```

```
        imwrite(graph,mapg,['Results_'  specimenID  '\'  numfigstr2  '_PropagGif_'
specimenID '.gif'],'gif','LoopCount',Inf,'DelayTime',gifspeed);
    else
        imwrite(image,mapi,['Results_'  specimenID  '\'  numfigstr  '_CrackGif_'
specimenID '.gif'],'gif','WriteMode','append','DelayTime',gifspeed);
        imwrite(graph,mapg,['Results_'  specimenID  '\'  numfigstr2  '_PropagGif_'
specimenID '.gif'],'gif','WriteMode','append','DelayTime',gifspeed);
    end

    status = 100*(n/m);
    clc
    sprintf('.gif file exportation... %0.2f %%',status)
end
close all

%--------------------------------------------------------------------------
%%                              DATA PROCESSING
%--------------------------------------------------------------------------

alldata = cat(2,export,loadimage,dispimage);

if precracking == false
    noduplicate = cat(2,export,loadimage,dispimage);
else
    noduplicate = alldata;
end
firstvalue = noduplicate(1,:);
noduplicate(any(diff(noduplicate(:,4))==0,2),:)=[];
noduplicate(1,:) = firstvalue;
export_nodup = noduplicate(:,1:5);
loadimage_nodup = noduplicate(:,6:9);
dispimage_nodup = noduplicate(:,10:13);

a_nodup = export_nodup(:,4);
crackextension = zeros(size(a_nodup,1),1);
for i=1:size(a_nodup,1)
    crackextension(i,1) = a_nodup(i,1)-a_nodup(1,1);
end
b_nodup = W-a_nodup;
aW = a_nodup/W;

Fig = figure();
numfig = numfig+1;
numfigstr=num2str(numfig);
hold on
plot(disp(:,2),load(:,2),':o','Color',[0, 0.4470, 0.7410],...
    'LineWidth',1,...
    'MarkerSize',5,...
    'MarkerEdgeColor',[0, 0, 0],...
    'LineWidth',0.5,...
    'MarkerFaceColor',[0, 0.4470, 0.7410])
title('Load-Displacement')
xlabel('Displacement (m)')
xlim([disp(1,2) inf])
ylabel('Load (N)')
ylim([load(1,2) inf])
grid on
box on;
```

```
saveas(Fig, ['Results_' specimenID '\' numfigstr '_LoadDisplacement_' specimenID
'.png']);
box off;

Fig = figure();
numfig = numfig+1;
numfigstr=num2str(numfig);
hold on
plot(loadimage_nodup(:,1),loadimage_nodup(:,4),':o','Color',[0.4660,        0.6740,
0.1880],...
    'LineWidth',1,...
    'MarkerSize',5,...
    'MarkerEdgeColor',[0, 0, 0],...
    'LineWidth',0.5,...
    'MarkerFaceColor',[0.4660, 0.6740, 0.1880])
title('Load-time')
xlabel('Time (s)')
xlim([min(loadimage_nodup(:,1)) max(loadimage_nodup(:,1))*(1+0.1)])
ylabel('Load (N)')
ylim([min(loadimage_nodup(:,4)) max(loadimage_nodup(:,4))*(1+0.1)])
grid on
box on;
saveas(Fig, ['Results_' specimenID '\' numfigstr '_LoadEvolution_' specimenID
'.png']);
box off;
close all

Fig = figure();
numfig = numfig+1;
numfigstr=num2str(numfig);
hold on
plot(loadimage_nodup(:,1),a_nodup*10^3,':o','Color',[0, 0.75, 0.75],...
    'LineWidth',1,...
    'MarkerSize',5,...
    'MarkerEdgeColor',[0, 0, 0],...
    'LineWidth',0.5,...
    'MarkerFaceColor',[0, 0.75, 0.75])
title('Crack propagation')
xlabel('Time (s)')
xlim([loadimage_nodup(1,1) inf])
ylabel('Crack propagation (mm)')
ylim([a_nodup(1)*10^3 inf])
grid on
box on;
saveas(Fig, ['Results_' specimenID '\' numfigstr '_CrackPropagation_' specimenID
'.png']);
box off;

Fig = figure();
numfig = numfig+1;
numfigstr=num2str(numfig);
plot(crackextension*10^3,loadimage_nodup(:,4),':o','Color',[0 0.4470 0.7410],...
    'LineWidth',1,...
    'MarkerSize',5,...
    'MarkerEdgeColor',[0, 0, 0],...
    'LineWidth',0.5,...
    'MarkerFaceColor',[0 0.4470 0.7410])
hold on
title('Load-Crack extension')
```

```
xlabel('Crack extension \Deltaa(Y) (mm)')
xlim([min(crackextension*10^3) max(crackextension*10^3)])
ylabel('Load (N)')
ylim([min(loadimage_nodup(:,4)) max(loadimage_nodup(:,4))*(1+0.1)])
grid on
box on;
saveas(Fig, ['Results_' specimenID '\' numfigstr '_LoadCrackExtension_' specimenID
'.png']);
box off;
close all

strain = zeros(size(load,1),2);
stress = zeros(size(load,1),2);
strain_notch_cst = zeros(size(load,1),2);
stress_notch_cst = zeros(size(load,1),2);
strain_notch_var = zeros(size(load,1),2);
stress_notch_var = zeros(size(load,1),2);
stress_notch_img = zeros(size(loadimage,1),2);
strain_notch_img = zeros(size(loadimage,1),2);
strain_notch_nodup = zeros(size(loadimage_nodup,1),2);
stress_notch_nodup = zeros(size(loadimage_nodup,1),2);

strain(:,1) = load(:,1);
stress(:,1) = load(:,1);
strain_notch_cst(:,1) = load(:,1);
stress_notch_cst(:,1) = load(:,1);
strain_notch_var(:,1) = load(:,1);
stress_notch_var(:,1) = load(:,1);
stress_notch_img(:,1) = loadimage(:,3);
strain_notch_img(:,1) = loadimage(:,3);
strain_notch_nodup(:,1) = loadimage_nodup(:,3);
stress_notch_nodup(:,1) = loadimage_nodup(:,3);

strain(:,2) = (6*disp(:,2)*W)/(span^2)*100;
stress(:,2) = (3*load(:,2)*span)/(2*B*(W.^2)*(10^6));
strain_notch_cst(:,2) = (6*disp(:,2)*b0)/(span^2)*100;
stress_notch_cst(:,2) = (3*load(:,2)*span)/(2*B*(b0.^2)*(10^6));
for i=1:size(load,1)
    strain_notch_var(i,2) = (6*disp(i,2)*b_data(i,1))/(span^2)*100;
    stress_notch_var(i,2) = (3*load(i,2)*span)/(2*B*(b_data(i,1)^2)*(10^6));
end

strain_notch_var_arch = strain_notch_var;

corr = 0;
for i=2:size(load,1)
    if (strain_notch_var(i,2) - strain_notch_var(i-1,2)) < 0
        corr = strain_notch_var(i-1,2)-strain_notch_var(i,2);
        strain_notch_var(i,2) = strain_notch_var(i-1,2);
        strain_notch_var(i+1:end,2) = strain_notch_var(i+1:end,2) + corr;
    end
end

count_img = 1;
count_nodup = 1;
i = 1;
while i <= size(load,1)
    if strain_notch_var(i,1) == strain_notch_img(count_img,1)
       strain_notch_img(count_img,2) = strain_notch_var(i,2);
```

```
        stress_notch_img(count_img,2) = stress_notch_var(i,2);
        count_img = count_img+1;
    end
    if strain_notch_var(i,1) == strain_notch_nodup(count_nodup,1)
        strain_notch_nodup(count_nodup,2) = strain_notch_var(i,2);
        stress_notch_nodup(count_nodup,2) = stress_notch_var(i,2);
        count_nodup = count_nodup+1;
    end
    i = i+1;
end

Fig = figure();
numfig = numfig+1;
numfigstr=num2str(numfig);
hold on
plot(strain(:,2),stress(:,2),':o','Color',[0.6350, 0.0780, 0.1840],...
    'LineWidth',1,...
    'MarkerSize',5,...
    'MarkerEdgeColor',[0, 0, 0],...
    'LineWidth',0.5,...
    'MarkerFaceColor',[0.6350, 0.0780, 0.1840])
title('Stress-Strain (no notch)')
xlabel('Strain (%)')
xlim([strain(1,2) inf])
ylabel('Stress (MPa)')
ylim([stress(1,2) inf])
grid on
box on;
saveas(Fig, ['Results_' specimenID '\' numfigstr '_StrainStress_' specimenID
'.png']);
box off;

Fig = figure();
numfig = numfig+1;
numfigstr=num2str(numfig);
hold on
plot(strain_notch_cst(:,2),stress_notch_cst(:,2),':o','Color',[0.6350,     0.0780,
0.1840],...
    'LineWidth',1,...
    'MarkerSize',5,...
    'MarkerEdgeColor',[0, 0, 0],...
    'LineWidth',0.5,...
    'MarkerFaceColor',[0.6350, 0.0780, 0.1840])
title('Stress-Strain (notch cst)')
xlabel('Strain (%)')
xlim([strain(1,2) inf])
ylabel('Stress (MPa)')
ylim([stress(1,2) inf])
grid on
box on;
saveas(Fig, ['Results_' specimenID '\' numfigstr '_StrainStressNotchCst_' specimenID
'.png']);
box off;

Fig = figure();
numfig = numfig+1;
numfigstr=num2str(numfig);
hold on
```

```
plot(strain_notch_var_arch(:,2),stress_notch_var(:,2),':o','Color',[0.6350,
0.0780, 0.1840],...
    'LineWidth',1,...
    'MarkerSize',5,...
    'MarkerEdgeColor',[0, 0, 0],...
    'LineWidth',0.5,...
    'MarkerFaceColor',[0.6350, 0.0780, 0.1840])
title('Stress-Strain (notch var) - before correction')
xlabel('Strain (%)')
xlim([strain(1,2) inf])
ylabel('Stress (MPa)')
ylim([stress(1,2) inf])
grid on
box on;
saveas(Fig, ['Results_' specimenID '\' numfigstr '_StrainStressNotchVar_' specimenID
'.png']);
box off;

Fig = figure();
numfig = numfig+1;
numfigstr=num2str(numfig);
hold on
plot(strain_notch_var(:,2),stress_notch_var(:,2),':o','Color',[0.6350,     0.0780,
0.1840],...
    'LineWidth',1,...
    'MarkerSize',5,...
    'MarkerEdgeColor',[0, 0, 0],...
    'LineWidth',0.5,...
    'MarkerFaceColor',[0.6350, 0.0780, 0.1840])
title('Stress-Strain (notch var) - with correction')
xlabel('Strain (%)')
xlim([strain(1,2) inf])
ylabel('Stress (MPa)')
ylim([stress(1,2) inf])
grid on
box on;
saveas(Fig,  ['Results_'  specimenID  '\'  numfigstr  '_StrainStressNotchVarCorr_'
specimenID '.png']);
box off;

Fig = figure();
numfig = numfig+1;
numfigstr=num2str(numfig);
hold on
plot(strain_notch_img(:,2),stress_notch_img(:,2),':o','Color',[0.6350,     0.0780,
0.1840],...
    'LineWidth',1,...
    'MarkerSize',5,...
    'MarkerEdgeColor',[0, 0, 0],...
    'LineWidth',0.5,...
    'MarkerFaceColor',[0.6350, 0.0780, 0.1840])
title('Stress-Strain (notch var-img) - after correction')
xlabel('Strain (%)')
xlim([strain(1,2) inf])
ylabel('Stress (MPa)')
ylim([stress(1,2) inf])
grid on
box on;
```

```
saveas(Fig, ['Results_' specimenID '\' numfigstr '_StrainStressnNotchVarImg_'
specimenID '.png']);
box off;

Fig = figure();
numfig = numfig+1;
numfigstr=num2str(numfig);
hold on
plot(strain_notch_nodup(:,2),stress_notch_nodup(:,2),':o','Color',[0.6350, 0.0780,
0.1840],...
    'LineWidth',1,...
    'MarkerSize',5,...
    'MarkerEdgeColor',[0, 0, 0],...
    'LineWidth',0.5,...
    'MarkerFaceColor',[0.6350, 0.0780, 0.1840])
title('Stress-Strain (notch var-img and nodup)')
xlabel('Strain (%)')
xlim([strain(1,2) inf])
ylabel('Stress (MPa)')
ylim([stress(1,2) inf])
grid on
box on;
saveas(Fig, ['Results_' specimenID '\' numfigstr '_StrainStressNotchVarImgNodup_'
specimenID '.png']);
box off;

for i=1:size(aW,1)
    faW_ISO(i,1)          =          (3*(aW(1)^(1/2))*(1.99-aW(1)*(1-aW(1))*(2.15-
3.93*aW(1)+2.7*(aW(1)^2))))/(2*(1+2*aW(1))*((1-aW(1))^(3/2)));
    K_ISO(i,1) = (((loadimage_nodup(i,4)*span)/(B*W^(3/2)))*faW_ISO(i,1))*10^(-6);
end

Fig = figure();
numfig = numfig+1;
numfigstr=num2str(numfig);
hold on
plot(loadimage_nodup(:,1),K_ISO,':o','Color',[0.9290 0.6940 0.1250],...
    'LineWidth',1,...
    'MarkerSize',5,...
    'MarkerEdgeColor',[0, 0, 0],...
    'LineWidth',0.5,...
    'MarkerFaceColor',[0.9290 0.6940 0.1250])
title('Stress Intensity Factor K (ISO)')
xlabel('Time (s)')
xlim([min(loadimage_nodup(:,1)) max(loadimage_nodup(:,1))*(1+0.1)])
ylabel('K (MPaVm)')
ylim([min(K_ISO) max(K_ISO)*(1+0.1)])
grid on
box on;
saveas(Fig, ['Results_' specimenID '\' numfigstr '_StressIntensityFactorISO_'
specimenID '.png']);
box off;
close all

Fig = figure();
numfig = numfig+1;
numfigstr=num2str(numfig);
hold on
plot(loadimage_nodup(:,1),faW_ISO,':o','Color',[0.9290, 0.6940, 0.1250],...
```

```
    'LineWidth',1,...
    'MarkerSize',5,...
    'MarkerEdgeColor',[0, 0, 0],...
    'LineWidth',0.5,...
    'MarkerFaceColor',[0.9290, 0.6940, 0.1250])
title('Geometric factor faW evolution (ISO)')
xlabel('Time (s)')
xlim([min(loadimage_nodup(:,1)) max(loadimage_nodup(:,1))*(1+0.1)])
ylabel('faW (-)')
grid on
box on;
saveas(Fig, ['Results_' specimenID '\' numfigstr '_GeometricFactorfaWISO_'
specimenID '.png']);
box off;
close all

C_ISO = C_ASTM*(1-nu^2);
dispimagepl_ISO = zeros(size(a_nodup,1),1);

for i=1:size(C_ISO,1)
    dispimagepl_ISO(i,1) = dispimage_nodup(i,4)-loadimage_nodup(i,4)*C_ISO(i,1);
end

Fig = figure();
numfig = numfig+1;
numfigstr=num2str(numfig);
plot(dispimage_nodup(:,3),C_ISO,':o','Color',[0.4940 0.1840 0.5560],...
    'LineWidth',1,...
    'MarkerSize',5,...
    'MarkerEdgeColor',[0, 0, 0],...
    'LineWidth',0.5,...
    'MarkerFaceColor',[0.4940 0.1840 0.5560])
hold on
title('Compliance variation (ISO)')
xlabel('time (s)')
xlim([disp(1,2) inf])
ylabel('Compliance (m/N)')
grid on
box on;
saveas(Fig, ['Results_' specimenID '\' numfigstr '_Compliance_ISO_' specimenID
'.png']);
box off;

Atot_ISO = zeros(size(a_nodup,1),1);
Apl_ISO = zeros(size(a_nodup,1),1);

for i=1:size(Apl_ISO,1)
    if i == 1
        Atot_ISO(i,1)= 0;
        Apl_ISO(i,1) = 0;
    else
        Atot_ISO(i,1) = Atot_ISO(i-1,1) + (dispimage_nodup(i,4)-dispimage_nodup(i-
1,4))*((loadimage_nodup(i-1,4)+loadimage_nodup(i,4))/2);
        Apl_ISO(i,1) = Atot_ISO(i,1) - (loadimage_nodup(i,4))^2*C_ISO(i,1)/2;
    end
end

Fig = figure();
numfig = numfig+1;
```

```
numfigstr=num2str(numfig);
hold on
plot(loadimage_nodup(:,1),Apl_ISO,':o','Color',[0.3010 0.7450 0.9330],...
    'LineWidth',1,...
    'MarkerSize',5,...
    'MarkerEdgeColor',[0, 0, 0],...
    'LineWidth',0.5,...
    'MarkerFaceColor',[0.3010 0.7450 0.9330])
title('Plastic area value evolution (ISO)')
xlabel('Time (s)')
xlim([min(loadimage_nodup(:,1)) max(loadimage_nodup(:,1))*(1+0.1)])
ylabel('Area (N.m)')
ylim([min(Apl_ISO) max(Apl_ISO)*(1+0.1)])
grid on
box on;
saveas(Fig, ['Results_' specimenID '\' numfigstr '_PlasticAreaISO_' specimenID
'.png']);
box off;
close all

Fig = figure();
numfig = numfig+1;
numfigstr=num2str(numfig);
numfig = numfig+1;
numfigstr=num2str(numfig);
hold on
plot(dispimagepl_ISO,loadimage_nodup(:,4),':o','Color',[0.3010, 0.7450, 0.9330],...
    'LineWidth',1,...
    'MarkerSize',5,...
    'MarkerEdgeColor',[0, 0, 0],...
    'LineWidth',0.5,...
    'MarkerFaceColor',[0.3010, 0.7450, 0.9330])
title('Load-Plastic displacement (ISO)')
xlabel('Plastic displacement (m)')
xlim([min(dispimagepl_ASTM) max(dispimagepl_ASTM)*(1+0.1)])
ylabel('Load (N)')
ylim([min(loadimage_nodup(:,4)) max(loadimage_nodup(:,4))*(1+0.1)])
grid on
box on;
saveas(Fig, ['Results_' specimenID '\' numfigstr '_Load-PlasticDisplacementISO_'
specimenID '.png']);
box off;
close all

for i=1:size(K_ISO,1)
    Jel_ISO(i,1) = ((K_ISO(i,1)^2)*(1-(nu^2)))/E;
    if i==1
        Jpl_ISO(i,1) = 0;
    else
    Jpl_ISO(i,1)          =          ((Npl_ISO/b_nodup(1,1))*(Apl_ISO(i,1)/B))*(1-
(Gpl_ISO*(a_nodup(i,1)-a_nodup(i-1,1))/b_nodup(1,1)));
    end
end
Jel_ISO = Jel_ISO*10^3;
Jpl_ISO = Jpl_ISO*10^(-3);

Fig = figure();
numfig = numfig+1;
numfigstr=num2str(numfig);
```

```
hold on
plot(a_nodup*10^3,Jel_ISO,':o','Color',[0 0.4470 0.7410],...
    'LineWidth',1,...
    'MarkerSize',5,...
    'MarkerEdgeColor',[0, 0, 0],...
    'LineWidth',0.5,...
    'MarkerFaceColor',[0 0.4470 0.7410])
plot(a_nodup*10^3,Jpl_ISO,':o','Color',[0.8500, 0.3250, 0.0980],...
    'LineWidth',1,...
    'MarkerSize',5,...
    'MarkerEdgeColor',[0, 0, 0],...
    'LineWidth',0.5,...
    'MarkerFaceColor',[0.8500, 0.3250, 0.0980])
legend('Jel','Jpl','Location','southeast')
title('Jel and Jpl contribution comparison (ISO)')
xlabel('Crack length a(Y) (mm)')
xlim([min(a_nodup*10^3) max(a_nodup*10^3)])
ylabel('J (kJ/m²)')
ylim([min(cat(1,Jel_ISO,Jpl_ISO)) max(cat(1,Jel_ISO,Jpl_ISO))])
grid on
box on;
saveas(Fig,  ['Results_'  specimenID  '\'  numfigstr  '_JelJplContributionISO_'
specimenID '.png']);
box off;
close all

J_ISO(:,1) = loadimage_nodup(:,1);
J_ISO(:,2) = Jel_ISO + Jpl_ISO;

Fig = figure();
plot(crackextension*10^3,J_ISO(:,2),':o','Color',[0.6350, 0.0780, 0.1840],...
    'LineWidth',1,...
    'MarkerSize',5,...
    'MarkerEdgeColor',[0, 0, 0],...
    'LineWidth',0.5,...
    'MarkerFaceColor',[0.6350, 0.0780, 0.1840])
hold on
plot(linspace(0,crackextension(end,1))*10^3,linspace(0,crackextension(end,1))*10^3
*(3.75*sigUTS),'k:')
plot(linspace(0,crackextension(end,1))*10^3+0.1,linspace(0,crackextension(end,1))*
10^3*(3.75*sigUTS),'k--')
plot(linspace(0,crackextension(end,1))*10^3+0.2,linspace(0,crackextension(end,1))*
10^3*(3.75*sigUTS),'k')
plot(linspace(0,crackextension(end,1))*10^3+2,linspace(0,crackextension(end,1))*10
^3*(3.75*sigUTS),'k')
legend('Resistance              curve','C-line','C-line              0.1mm','C-line
0.2mm','Location','southeast')
title('Resistance curve (ISO)')
xlabel('Crack extension \Deltaa(Y) (mm)')
xlim([min(crackextension*10^3) max(crackextension(end,1)*10^3)])
ylabel('J (kJ/m²)')
ylim([min(J_ISO(:,2)) max(J_ISO(:,2))*(1+0.1)])
grid on
box on;
saveas(Fig,  ['Results_'  specimenID  '\'  numfigstr  '_ResistanceCurvePropag_ISO_'
specimenID '.png']);
box off;
close all
```

APPENDIX B
Dendrite and nano-oxide observations

This appendix provides a more detailed analysis of two features observed at the sub-micro/nanoscale: the dendrites and the nano-oxides.

As discussed in Chapter 3, the dendrite structures resulting from the different manufacturing conditions exhibit more or less scatter in terms of size distribution. Figure 94 illustrates this phenomenon by presenting four representative images extracted from each dataset, all taken on a single surface. The influence of the manufacturing parameters on the dendrites can be classified into three categories of processing parameters: 90 J/mm^3 and 67° (H9067 and V9067), 90 J/mm^3 and 90° (H9090 and V9090), and 60 J/mm^3 and 67° (H6067 and V6067). Dendrites from H9067 and V9067 specimens are subjected to minimal variations, with sizes relatively uniform. On the other hand, H9090 and V9090 specimens display very heterogeneous sizes, going from very fine to very coarse dendrites. H6067 and V6067 specimens exhibit some scatter, but the amplitude falls in between the two configurations previously mentioned. The mean sizes have already been discussed, with the smallest dendrites for H6067 and V6067 specimens, and the biggest for H9090 and V9090 specimens. However, due to the small scale of these observations, which were also performed on a single specimen each time, further investigation is necessary to improve the statistical approach. This would be of the utmost importance to improve the reliability of the study on the relationship between dendrite size and yield stress.

Figure 95 presents a set of three images from each dataset obtained on the nano-oxides for each manufacturing condition. The unexpected presence of nano-oxides was already partially characterized by previous PhD works on L-PBF Ni20Cr [36,157]. These studies highlight that nano-oxides are located within interdendritic walls, and are Cr-rich particles. While it initially seems that a VED of 90 J/mm^3 results in bigger nano-oxides than a VED of 60 J/mm^3, previous discussion for a broader range of VEDs indicated that this trend was not statistically confirmed [36] and requires a larger dataset to be representative. Overall, the nano-oxides display a heterogeneous distribution in size, location, and shape regardless of the manufacturing conditions, particularly with specimens produced with a VED of 90 J/mm^3. Two

shapes are commonly observed as shown in Figure 96: circular precipitates (Figure 96a) and “blocky” precipitates (Figure 96b).

I. Dendrites observations

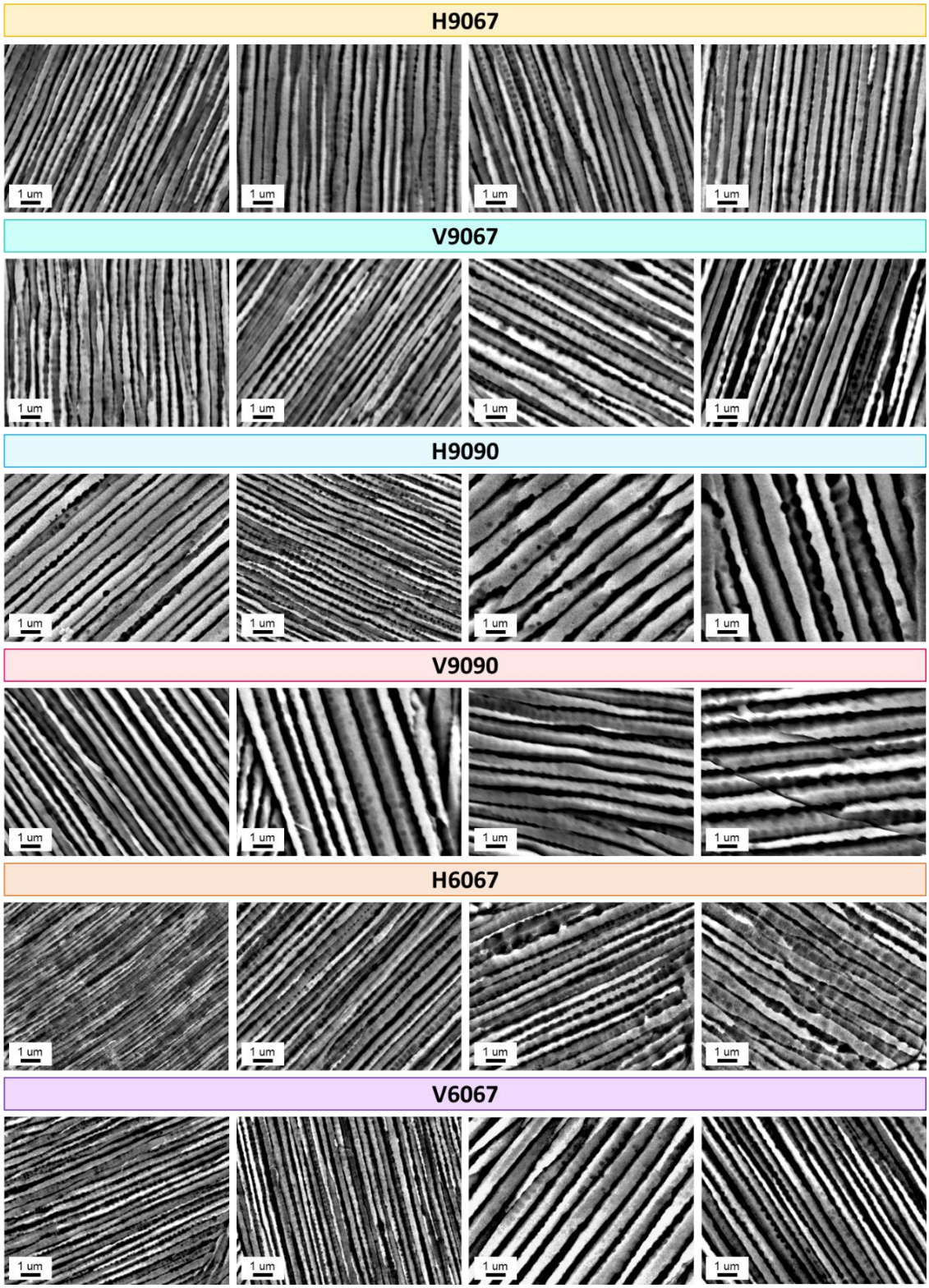

Figure 94: Dendrites SEM images for all the manufacturing conditions

II. Nano-oxides observations

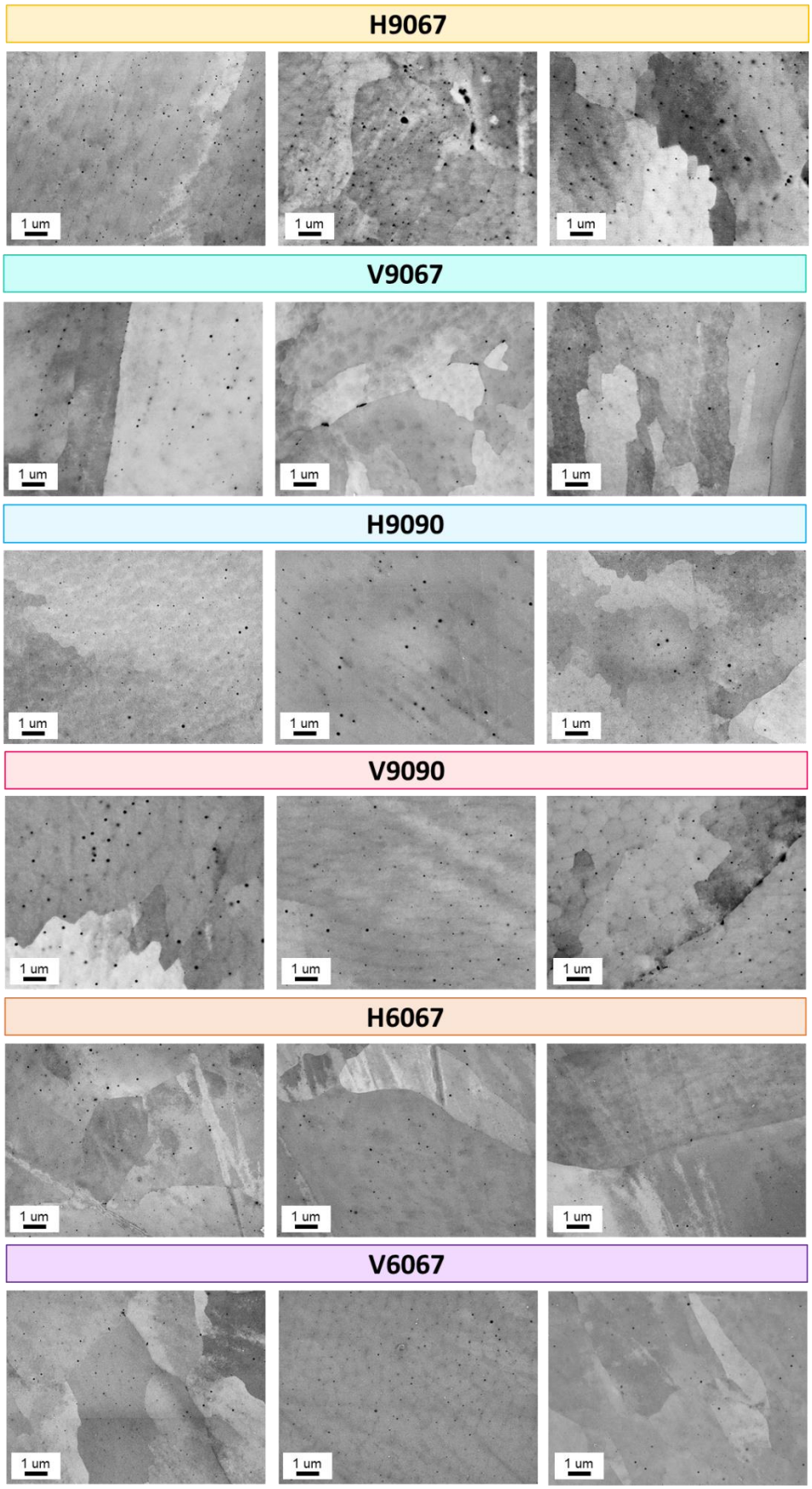

Figure 95: Nano-oxides SEM images for all the manufacturing conditions

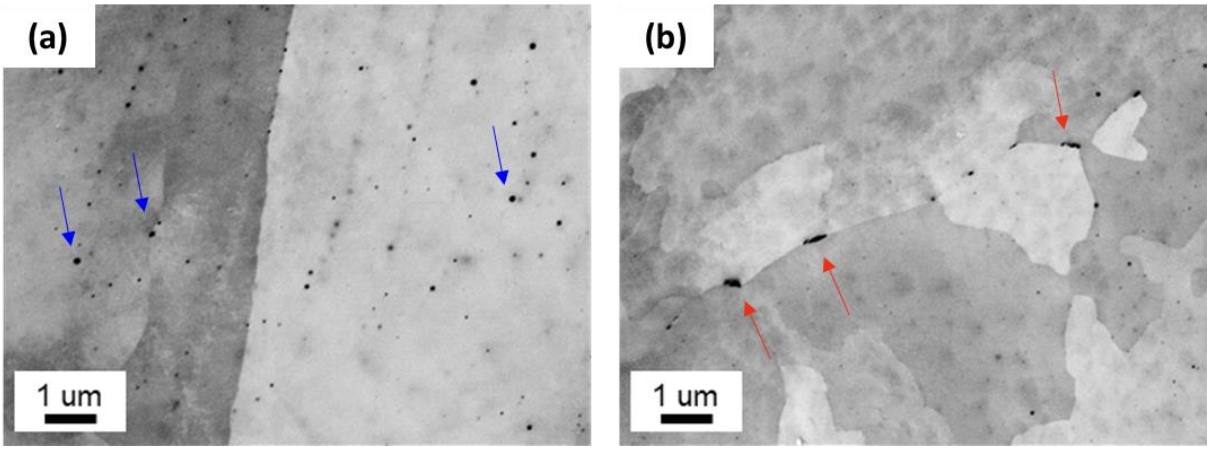

Figure 96: SEM images of the two types of precipitates observed
(a) Circular interdendritic precipitates (pointed by blue arrows)
(b) "Blocky" interdendritic precipitates (pointed by red arrows)

APPENDIX C

Three-point bending Load-Displacement & Stress-Strain curves

This appendix exhibits the load-displacement (Figure 97) and stress-strain (Figure 98) curves resulting from the three-point bending tests. The objective of this section is to give an idea of the little scattering observed for all the conditions tested. For each manufacturing configuration, at least 5 specimens were considered. The experimental curves are plotted in continuous lines, and the mean curves in dotted lines.

I. Load-Displacement curves

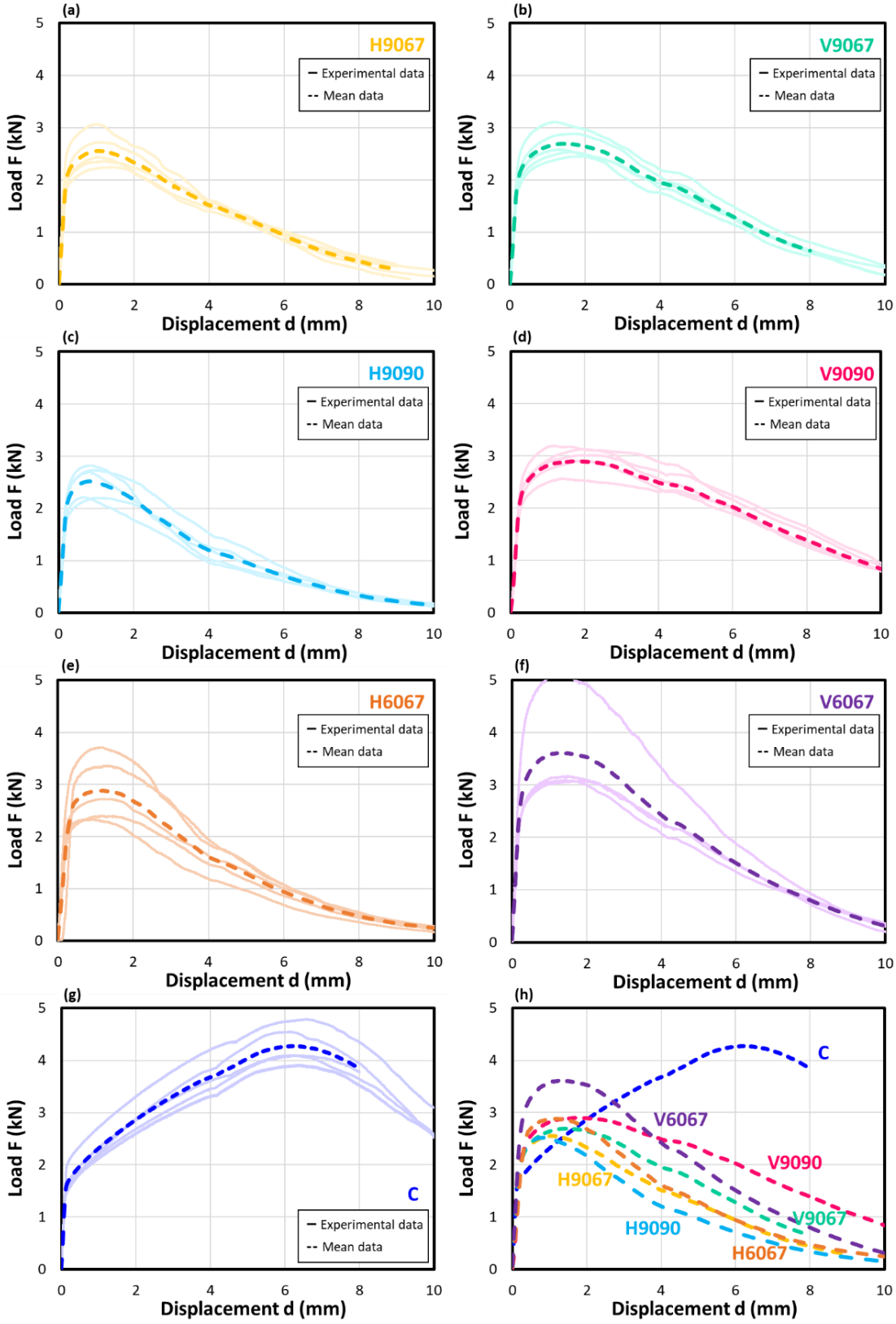

Figure 97: Load-Displacement curves for all manufacturing configurations
(a) H9067 (b) V9067 (c) H9090 (d) V9090 (e) H6067 (f) V6067 (g) C (h) Mean curves

II. Stress-Strain curves

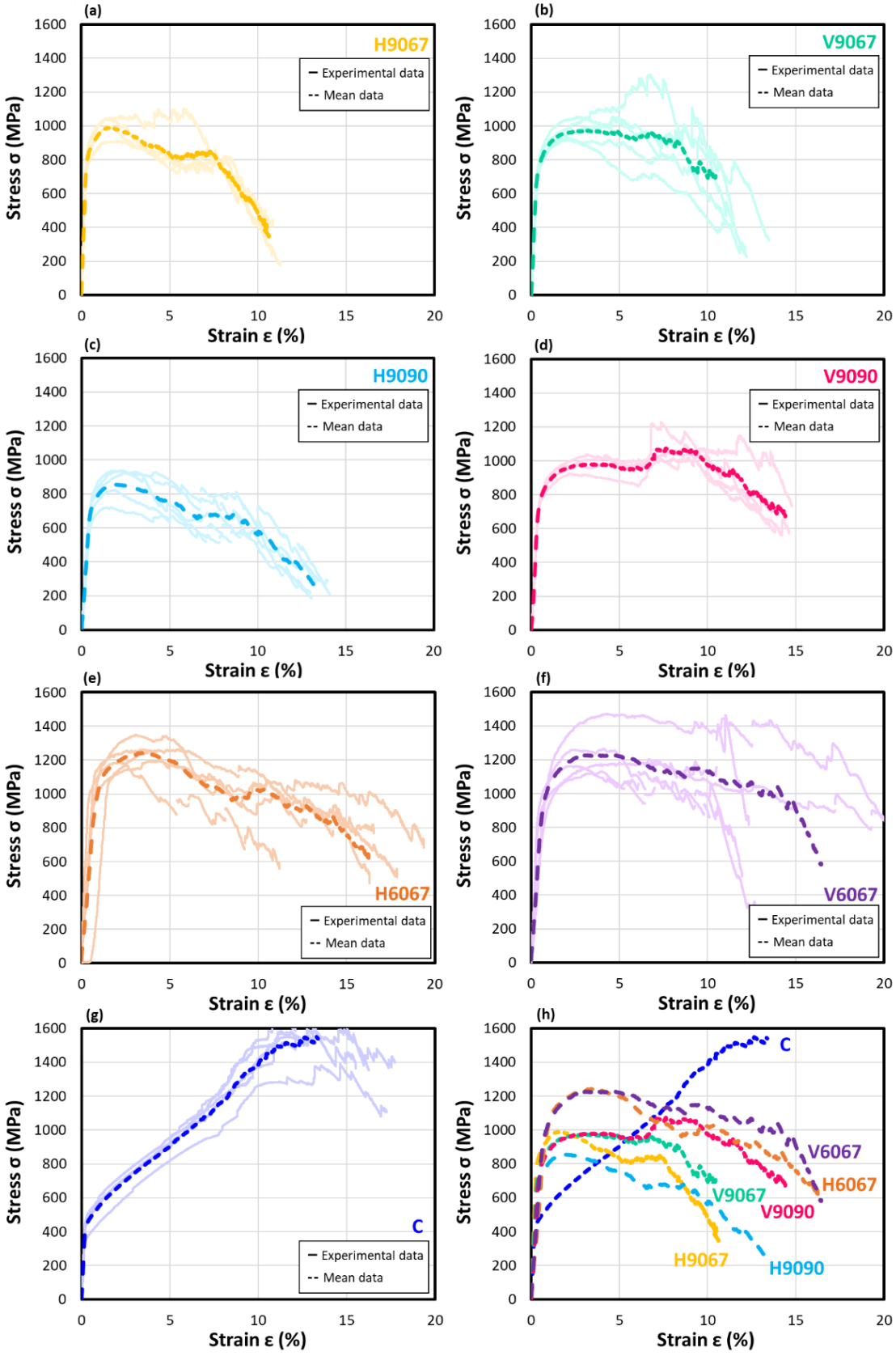

Figure 98: Stress-Strain curves for all manufacturing configurations

(a) H9067 (b) V9067 (c) H9090 (d) V9090 (e) H6067 (f) V6067 (g) C (h) Mean curves

APPENDIX D
Post-mortem observations

This appendix reports a more exhaustive set of post-mortem images obtained for each manufacturing configuration. Figure 99 and Figure 100 display fractographic observations carried out on both cast & wrought and L-PBF specimens, whereas Figure 101 shows fracture mechanisms observed near the crack tip, after etching was performed to reveal dendrites. This aims at showing the diversity of the observations obtained at smaller scales (10 µm scalebar and below), and the fracture mechanisms observed.

I. Fractographic observations

The fractographic observations obtained for all the specimens tested are displayed in both Figure 99 (L-PBF specimens) and Figure 100 (cast & wrought specimens).

L-PBF specimens overall exhibited the same fracture mechanisms, all of them consisting of ductile fracture mechanisms. The most obvious mechanism identified is transgranular void growth and coalescence, with the presence of several dimples all over the specimens' fracture surfaces as in Figure 99c. Plane slips were also observed, as shown in Figure 99l and m. Nonetheless, some fracture mechanisms are still yet to be clearly identified in the fractographic images due to the complexity of the fracture surfaces.

Cast & wrought specimens on the other hand, presented in Figure 100, were characterized by clear brittle fracture mechanisms, with mechanisms that are yet to be clearly identified at smaller scales (Figure 100a and b). However, it was already shown in Figure 72f that intergranular decohesion was also widely observed. Ductile transgranular void nucleation, growth, and coalescence was also identified in Figure 100c, with oxides clearly visible inside the dimples.

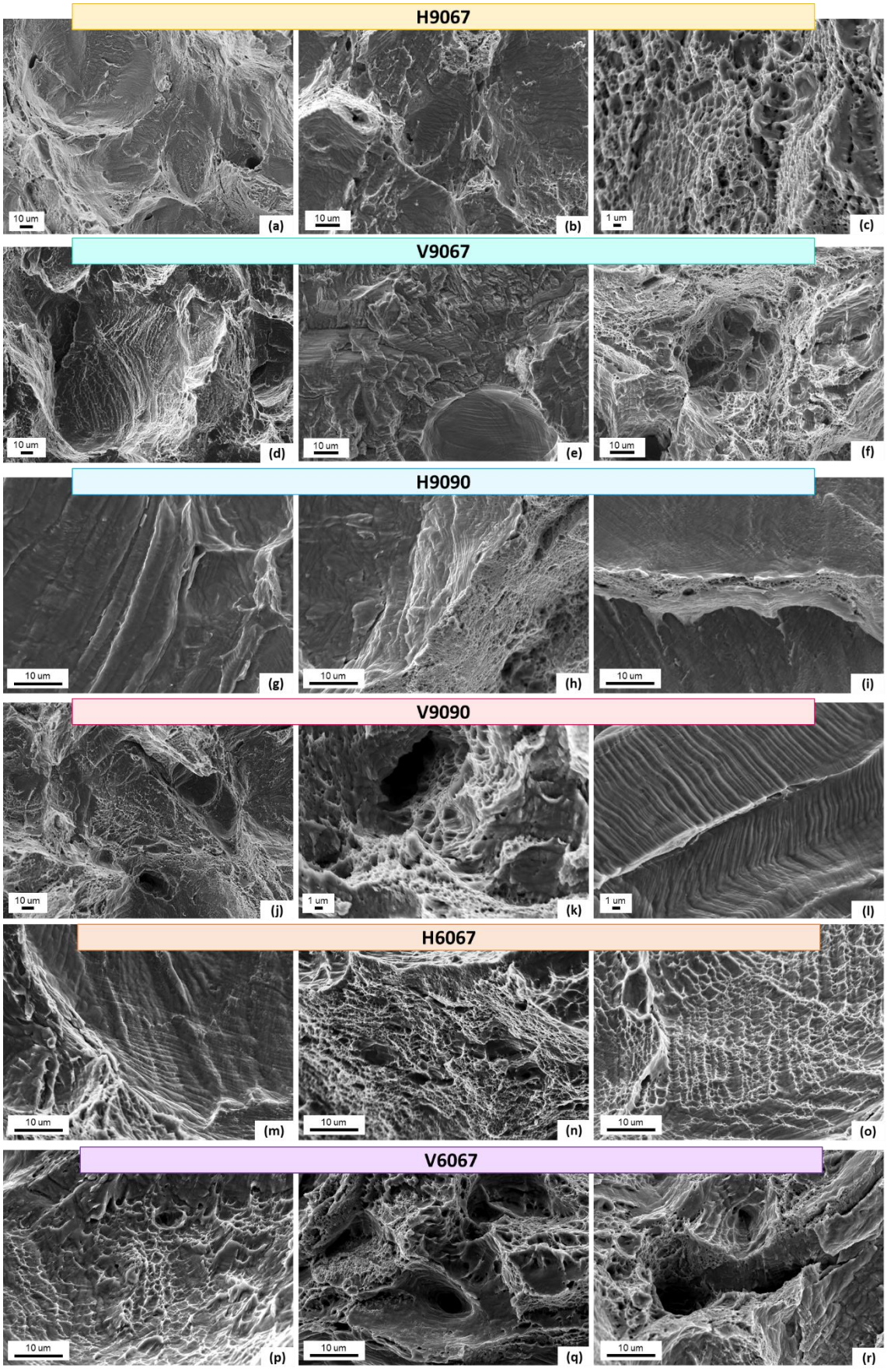

Figure 99: Fractographic images from all the L-PBF printing strategies

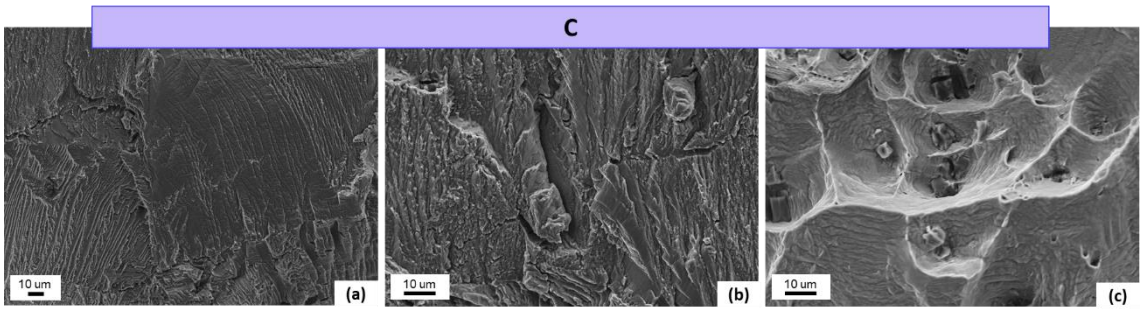

Figure 100: Fractographic images from cast & wrought specimens

II. Post-mortem observations at the crack tip

Figure 101 presents in more details the diversity of the post-mortem fracture mechanisms observed at the crack tip.

As already discussed in Chapter 4, different behaviors can be observed at the dendritic scale, with crack propagation along the dendritic arm spacings (Figure 101a, c…), straight through it (Figure 101e), between two different dendrite colonies (Figure 101f), or within the same colony (Figure 101j)… The presence of slip bands was also noticed (Figure 101e and h). Figure 101 highlights how several fracture surfaces have been observed for many specimens, making it difficult to clearly associate one mechanism with one printing strategy yet. These observations are highly dependent on the quality of the surface preparation, and may need more time and specimens to classify thoroughly the fracture mechanisms with respect to the processing parameters considered.

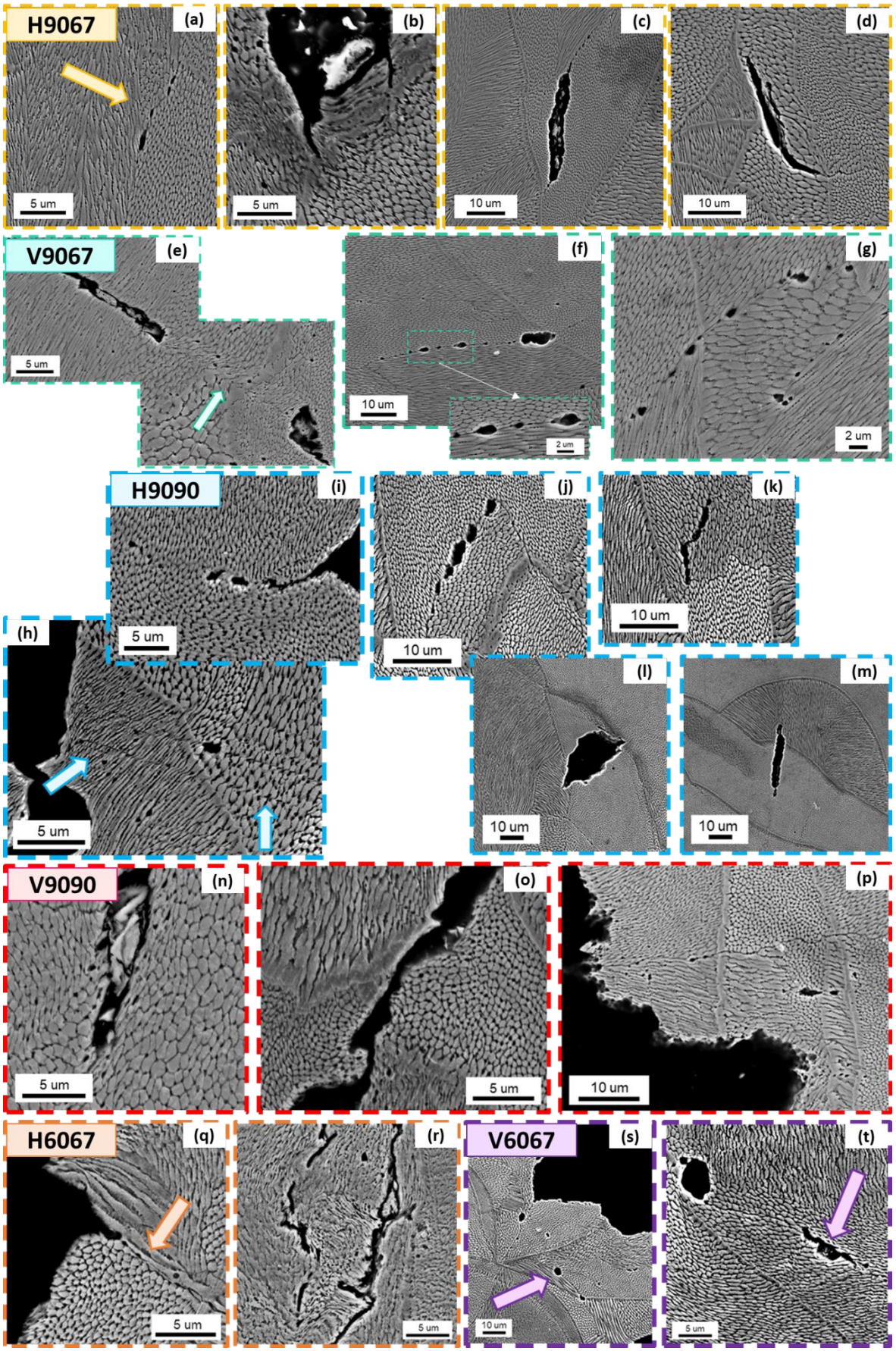

Figure 101: Fracture mechanisms observed at the sub-microscale

NOMENCLATURE

a	Crack length
A	Elongation to ultimate tensile stress
A_0	Initial section of the tensile specimen
A_f	Ultimate section of the broken tensile specimen
A_{pl}	Area under the load-plastic displacement curve
AM	Additive Manufacturing
b_0	Initial unbroken ligament
B	Specimen thickness
C	Fitting parameter of the Paris law or Compliance or J_{limit} criterion
C_{el}	Elastic compliance
CT	Compact Tension
d	Mean value between two diagonal length for microhardness
d_{max}	Maximum displacement
d_{pl}	Plastic displacement
dS	Length increment along the contour
e	Powder thickness
E	Young's Modulus or Energy Density
E_l	Linear energy density
E_p	Initial potential energy
E_s	Surface energy density
E_v	Volume energy density
E-PBF	Electron Beam Powder Bed Fusion
EPFM	Elasto-Plastic Fracture Mechanics
EBSD	Electron Back-Scattered Diffraction
F	Load
F_{ini}	Load associated with crack initiation
F_{gy}	Load associated with the start of the plastic behavior
F_{max}	Maximum load
FIB	Focused Ion Beam
FPZ	Fracture Process Zone
G	Strain energy release rate or Thermal gradient
G_{Ic}	Fracture toughness (LEFM)
h	Hatch spacing
HV	Vickers hardness
IPF	Inverse Pole Figure
J	Rice Integral
J_{el}	Elastic component of the J-integral

J_{Ic} / $J_{0.2}$	Fracture toughness (at an offset of 0.2 mm)
J_{limit}	Limit value for the fracture toughness
J_{pl}	Plastic component of the J-integral
k	Power law constant or compliance
K_{HP}	Hall-Petch coefficient (or slope)
k_H	Strength coefficient from the Hollomon law
k_i	Compliance for a given unloading time i
K	Stress intensity factor
K_I	Stress intensity factor for mode I loading
K_{Ic}	Fracture toughness (LEFM)
KV	Total fracture energy
KV_i	Fracture energy for crack initiation
KV_p	Fracture energy for crack propagation
L	Length (of the pendulum or microcantilever)
LEFM	Linear Elastic Fracture Mechanics
LOF	Lack Of Fusion
L-PBF	Laser Powder Bed Fusion
m	Fitting parameter of the Paris law or Power law constant
m_d	Dry weight
m_w	Wet weight
MEMS	Micro-electro-mechanical systems
M.R.D	Multiple Random Distribution
n_H	Strain hardening exponent from the Hollomon law
N	Number of cycles
P	Laser power
PBF	Powder Bed Fusion
PF	Pole Figure
VED	Volumetric Energy Density
r	Polar coordinate (radial distance)
r_p	Irwin plastic zone size
R	Solidification interface velocity or Load ratio
s	Laser beam diameter
S	Distance between the supporting rolls
SEM	Scanning Electron Microscope
SENB	Single Edge Notch Bend
t	Specimen thickness or Remaining ligament during the test
$\vec{t}$	Traction vector at a given point of the contour
T	Tearing modulus
$\vec{u}$	Displacement vector at a given point of the contour
U	Area under the load-displacement curve
v	Laser speed

W	Specimen height or Strain energy density
Y	Function of the specimen geometry and crack length
σ	Engineering stress or Applied stress
σ_t	True stress
σ_b	Bending stress
σ_{ij}	Component of the stress tensor
σ_0	Intrinsic yield stress
σ_{YS}	Yield stress
σ_{UTS}	Ultimate tensile stress
σ_Y	Flow stress (mean value of σ_{YS} and σ_{UTS})
Δa	Crack extension
ΔC	Compliance variation
Δd	Displacement variation
ΔF	Load variation
ΔK	Stress intensity factor variation
η	Plastic factor given by ISO 12135-21
ρ	Volumetric mass (density)
ρ_a	Air density
ρ_w	Water density
ε	Engineering strain
σ_t	True strain
ε_b	Bending strain
$\dot{\varepsilon}$	Strain rate
ν	Poisson ratio
γ	Plastic factor given by ISO 12135-21
Γ	Arbitrary contour defined around the crack tip
θ	Charpy pendulum angle or Polar coordinate (angle)

Investigation of the influence of the process parameters on the microstructure and fracture behavior of a Ni20wt.%Cr alloy produced by Laser Powder Bed Fusion

Résumé

Le comportement à rupture d'alliages base-nickel conventionnels (coulés, forgés…) est depuis longtemps étudié dans le cadre du dimensionnement des structures. Cependant, les microstructures complexes issues des procédés de fabrication additive métallique induisent des comportement mécaniques différents, compliquant la transposition des savoir-faire. Afin de contribuer à mieux comprendre les mécanismes de rupture issus de ces procédés, ces travaux de thèse s'intéressent au comportement à rupture de l'alliage Ni20wt.%Cr produit par Fusion Laser sur Lit de Poudre. L'influence de trois paramètres de fabrication est étudiée : l'orientation de fabrication (horizontale ou verticale), l'angle entre les couches de lasage (67° ou 90°), et la densité d'énergie volumique (60 J/mm^3 ou 90 J/mm^3). Des essais de propagation de fissure sont réalisés afin de déterminer et comparer les propriétés à rupture (ténacité et module de déchirure) de chaque stratégie de fabrication. Les microstructures initiale et post-mortem sont analysées pour identifier les mécanismes à rupture. Les résultats indiquent que la propagation de fissure est majoritairement pilotée à l'échelle microscopique, avec un rôle important de l'orientation, la morphologie et la taille des grains. La ductilité devient également un paramètre fondamental lorsque les caractéristiques microstructurales sont similaires entre deux configurations de fabrication.

Mots-clés : Fabrication additive, Ni20Cr, Propriétés à rupture, Microstructure

Abstract

The fracture behavior of conventional nickel-based alloys (cast, wrought…) has been studied for decades for structural design purposes. However, the complex microstructure induced by metallic additive manufacturing processes results in different mechanical behaviors, which hinders the use of existing knowledge. To better understand the fracture mechanisms associated with these processes, this PhD research investigates the fracture behavior of a Ni20wt.%Cr alloy produced by Laser Powder Bed Fusion. The influence of three manufacturing parameters is studied: the building orientation (horizontal or vertical), the rotation angle between layers (67° or 90°), and the volumetric energy density (60 J/mm^3 or 90 J/mm^3). Crack propagation tests are conducted to determine and compare the fracture properties (fracture toughness and tearing modulus) of each printing strategy. Initial and post-mortem microstructures are analyzed to identify the fracture mechanisms. Results demonstrate that the crack propagation is mainly governed at the microscale, with a strong influence from the grain's orientation, morphology, and size. Ductility also becomes a key parameter when few differences are noted between the microstructural features of two given printing strategies.

Keywords: Additive manufacturing, Ni20Cr, Fracture properties, Microstructure